UNIVERSITY OF SOUTHAMPTON

FACULTY OF ENGINEERING, SCIENCE AND MATHEMATICS

Optoelectronics Research Centre

Integration of glass microspheres and planar waveguides for microsphere lasers

by

Yuwapat Panitchob

Thesis for the degree of Doctor of Philosophy

November 2008

UNIVERSITY OF SOUTHAMPTON

ABSTRACT

FACULTY OF ENGINEERING, SCIENCE AND MATHEMATICS
OPTOELECTRONICS RESEARCH CENTRE

Doctor of Philosophy

by Yuwapat Panitchob

Microsphere resonators with sizes in the micrometer range are reported to support very high Q's of more than 10^9 for a fused silica microsphere. This high Q value represents many promising characteristics such as low cavity loss, long cavity life time, and narrow band width. With their remarkable characteristics, microsphere resonators can be used in various applications such as the narrow band filter, add-drop multiplexer, microlasers, and etc. In this work, the integration of microspheres with planar waveguides is the main focus. High quality neodymium-doped BK7 microspheres are fabricated and characterised to observe laser oscillation at 1.06 μm from the $^4F_{3/2}$ - $^4I_{11/2}$ transition.

Theoretical calculation of the microsphere mode and field and the characteristic equation which describes the relation of the sphere mode numbers l, m, n to the wavelength, are obtained. The theoretical expressions of the microsphere WGM can be described with the sphere mode numbers based on spherical Bessel and Hankel functions. Coupling and quality factors of the waveguide-coupled system are obtained by integrating the overlapped fields of the microsphere and waveguide, and the study of Q factors as a function of sphere/waveguide separation are elaborated. Theoretical models to calculate the total loss and gain of the microsphere lasers and the Q which is required for lasing action, are developed. The expressions for power threshold in the microsphere and in the input waveguide are derived, and the threshold pump power as a function of sphere/waveguide separation is obtained.

Experimental work to observe the WGM propagation of a passive microsphere has been carried out, and results obtained at wavelengths in the 800 nm and 1550 nm regions, and modal assignment including the evaluation of Q for each system are carried out. The experiments to observe the fluorescence and the lasing oscillation of the neodymium-doped BK7 microspheres are demonstrated. The measurement of the fluorescence lifetime of a neodymium-doped BK7 microsphere, is obtained. A laser oscillation is demonstrated with the free-space pump excitation, with the threshold pump power of 8 mW at $\lambda = 808$ nm.

Contents

List of Figures

List of Tables

List of Symbols

$\psi_r(r)$	Field in radial direction
$\psi_\phi(\phi)$	Field in azimuthal direction
$\psi_\theta(\theta)$	Field in angular direction
N_s	Normalisation constant of the volume integration
l, m, n	Sphere mode numbers
k	Wave number
n_s	Refractive index of sphere
α_s	Decay constant of the field in sphere
β_l	Propagation constant parallel to the surface of sphere
R_o	Sphere radius
D	Sphere diameter
$\mathrm{R}_{\mathrm{eff}}$	Effective radius of the path that light is propagating in microsphere
n_{eff}	Effective refractive index of light propagating in a channel waveguide
$j_n(x)$	Spherical Bessel function of x of order n
$J_n(x)$	Bessel function of x of order n
$H_N(x)$	Hermite polynomial of x of order N
κ	Coupling factor
Q	Quality factor
G	Cavity round-trip gain
L	Cavity round-trip loss
δ_c	Loss fraction microsphere cavity
σ_p	Pump absorption cross-section
σ_s	Emission cross-section
τ	Fluorescence lifetime
λ_p	Pump wavelength
λ_s	Signal wavelength
ν_p	Pump frequency
η_q	Quantum efficiency
c	Speed of light
N_o	Ion density
β_p	Absorption coefficient
a_p	Propagation loss in sphere cavity per unit length

α_p	Loss factor associated with propagation loss per unit length a_p
h	Planck's constant
α_{Nd}	Loss fraction due to Nd absorption
I_p	Pump intensity
P_p	Pump power
S_p	Pump mode distribution
I_s	Signal intensity
P_s	Signal power
S_s	Signal mode distribution
P_{th}	Power threshold
$P_{\mathrm{th\text{-}sphere}}$	Power threshold at microsphere
$P_{\mathrm{th\text{-}wg}}$	Power threshold at waveguide input
$\epsilon_{\mathrm{thermal}}$	Thermal expansion coefficient

List of Abbreviations

FSR	Free spectral range
FWHM	Full-width at half-maximum
Nd_2O_3	Neodymium oxide
OSA	Optical spectrum analyser
OPL	Optical path length
TE	Transverse electric
TM	Transverse magnetic
WGM	Whispering-gallery mode

Acknowledgements

I would like to express my sincere gratitude to all who made this thesis possible. My deepest gratitude is to my supervisor, Prof. James Wilkinson. I have been privileged to work with my supervisor who has significantly provided guidance, support and encouragement in numerous ways. I would like to express my deep gratitude to Prof. Mikhail Zervas for his guidance and helpful discussion. Also I would like to thank the people from the Optoelectronics Research Centre, Physics, Chemistry departments and National Oceanography Centre of Southampton; Prof. Phil Bartlett, Prof. Dan Hewak, Dr. Senthil Ganapathy, Dr. Eleanor Tarbox, Dr. Elizabeth Tull, Dr. Peter Horak, Dr. Christos Grivas, Dr. Andy Milton, Ping Hua and Greg Elliott for all discussions and support in the most useful ways. I wish to acknowledge the assistance for all technical issues from Dave Sager, Neil Session, Edwin Weatherby, Mark Lessy, Kenton Knight, Trevor Austin and Zondy Webber.

I wish to thank post doctoral researchers and postgraduate students from the Integrated Photonic Devices group for valuable feedback and discussions.

My warm thanks are due to Dr. Daniel Jaque and Antonio Benayas from Universidad Autónoma de Madrid, Spain for assistance during my visit in Madrid. I would like to thank Dr. Gualtiero Conti from Italy for constructive comments via email.

I am grateful to thank Dr. Jaymin Amin for attracting me to the United Kingdom and convincing me to join the ORC.

The financial support from the ORC and the Higher Education Funding Council for England (HEFCE) through Overseas Research Students Awards Scheme (ORSAS) is gratefully acknowledged.

Lastly, I would like to thank my family including my brother, Nuttanont Panitchob, for the courage and support in many ways. I want to express my gratitude to my uncle and aunt for their inspiration and for believing that I was able to pursue this degree. I ultimately dedicate my thesis to my grandmother, and my parents, Yupa Panitchob and Dr. Supat Panitchob, in honour of their tremendous amount of support, guidance, and making me the person I am today.

Declaration of Authorship

I, **Yuwapat Panitchob**, declare that the thesis entitled **Integration of glass microspheres and planar waveguides for microsphere lasers** and the work presented in the thesis are both my own, and have been generated by me as the result of my own original research. I confirm that:

- this work was done wholly or mainly while in candidature for a research degree at this University;
- where any part of this thesis has previously been submitted for a degree or any other qualification at this University or any other institution, this has been clearly stated;
- where I have consulted the published work of others, this is always clearly attributed;
- where I have quoted from the work of others, the source is always given. With the exception of such quotations, this thesis is entirely my own work;
- I have acknowledged all main sources of help;
- where the thesis is based on work done by myself jointly with others, I have made clear exactly what was done by others and what I have contributed myself;
- parts of this work have been published as shown in the List of Publications.

Signed:.....

Date:.....

List of Publications

- Y. Panitchob, G. Senthil Murugan, M. N. Zervas, and J. S. Wilkinson. Neodymium-doped BK7 microsphere laser. *to be submitted to Optics Express.*

- G. Senthil Murugan, Y. Panitchob, M. N. Zervas, and J. S. Wilkinson. Characterization of optical coupling between planar waveguide and microsphere resonator for integrated microsphere planar lightwave circuits. *to be submitted to Optics Express.*

- Y. Panitchob, G. Senthil Murugan, M. N. Zervas, P. Horak, S. Berneschi, S. Pelli, G. Nunzi Conti, and J. S. Wilkinson. Whispering gallery mode spectra of channel waveguide coupled microspheres. *Optics Express*, 16(15):11066-11076, 2008.

- James S. Wilkinson, G. Senthil Murugan, Yuwapat Panitchob, and Mikhail N. Zervas. Microsphere Resonators: a route to enhanced functionality in planar lightwave circuits. In *Norwegian Electro-Optics Meeting 2008*, Hurtigruten, Norway, 2008.

- A. Benayas, G. S. Murugan, Y. Panitchob, D. Jaque, and J. S. Wilkinson. Time resolved confocal luminescence of Nd^{3+} doped BK7 glass microspheres. In *The 15th International Conference on Luminescence and Optical Spectroscopy of Condensed Matter*, Lyon, France, 2008.

- Y. Panitchob, G. Senthil Murugan, M. N. Zervas, and J. S. Wilkinson. Q-Factor and Waveguide-Sphere Separation Effects in Waveguide-Coupled Microsphere Resonators. In *International Workshop and Conference on Photonics and Nanotechnology*, Pattaya, Thailand, 2007.

- Yuwapat Panitchob, G. Senthil Murugan, Mikhail N. Zervas and James S. Wilkinson. Control of Coupling between Waveguides and Microsphere Resonators. In *The 5th International Conference on Optics-Photonics Design Fabrication*, Nara, Japan, 2006.

- Senthil M. Ganapathy, Yuwapat Panitchob, Elizabeth J. Tull, Philip N. Bartlett, and James S. Wilkinson. Micropositioning of Microsphere Resonators on Planar Optical Waveguides. In *The 5th International Conference on Optics-Photonics Design Fabrication*, Nara, Japan, 2006.

Chapter 1

Introduction

1.1 Introduction

Microspheres can support a very high Quality factor, Q, of more than 10^9 and they have very compact sizes. These characteristics are very useful in many diverse high Q device applications [1, 2]. With the extremely low whispering-gallery mode (WGM) loss of the microspheres, a high Q resonator device is obtained. Besides the obvious application, which is for narrow band optical filters [3], with the high-Q WGM characteristics, there are many other applications, including microsphere lasers [4, 5], optical waveguides [6], and ultralow-threshold Raman lasers [7]. The application in this thesis is mainly focused on microsphere lasers using neodymium-doped glass microspheres. The optical transition from $^4F_{3/2}$ - $^4I_{11/2}$ around 1060 nm can be easily obtained by pumping at 808 nm ($^4I_{9/2}$ - $^4F_{5/2}$).

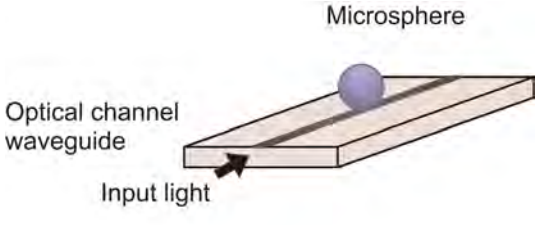

FIGURE 1.1: Optical channel waveguide coupling method

The method used to evanescently couple light into the microsphere is by exciting the evanescent field from the light propagating in a optical channel waveguide. The waveguide coupling method is considered particularly promising as it has the advantage of providing the possibility of more complex waveguide circuits, and has a low cost of fabrication with the potential for mass-production through photolithography. The evanescent field from the channel waveguide can be a useful source for exciting the WGM in microspheres, and light may be launched into the waveguide facet and coupled into the

microsphere without involving fragile devices such as a fibre optics, or bulky devices such as prisms (see Figure 1.3).

In this thesis, fabrication methods and techniques to obtain microspheres and waveguides will be described. The experimental work to observe the WGM characteristics from passive microspheres coupled to optical waveguides, and to demonstrate lasing oscillation from neodymium-doped BK7 microspheres by free-space and waveguide excitation, will be carried out. The sphere modal assignment to each resonance peak and the theoretical model that is used to identify microsphere diameter from the results obtained from experiments, will be elaborated. Theoretical work on the laser characteristics including threshold pump power and related emission power will be addressed.

1.2 Whispering-gallery modes

Whispering-gallery modes, WGM, are found in circular path resonant cavities. The whispering-gallery mode was discovered in 1910 when Lord Rayleigh was conducting experiments on acoustic waves in the dome of St. Paul's Cathedral [8]. The experiment was done by observing the propagation of the sound of the speaker in the oval shaped dome in the cathedral. The distant listeners at specific locations were able to hear the whispering voice from the speaker from the dome in the cathedral. This whispering sound was described as an acoustic wave travelling along the wall path. Recently whispering-gallery mode phenomena have been exploited in many research areas [1, 4, 7, 9–14].

When the incident ray travelling from the higher index medium to the lower one at an angle greater than the critical angle, there is an extended field decaying along the surface of the two media. The extended tail of the field at the resonator boundary decays exponentially away from the interface. This extended field is known as the evanescent field. Light travels inside the bounded cavity by repeated quasi-total internal reflection at the cavity boundaries, a concentric ring of the electromagnetic field occurs close to the cavity surface. This evanescent excitation is insufficient to obtain with the free-space excitation. Dielectric waveguides may be used to excite WGMs efficiently through evanescent coupling [13, 15]. The light that travels through the waveguide creates an evanescent field at its surface. This evanescent field can be coupled into the resonator cavities by whispering-gallery mode coupling, when the velocity of the field from the waveguide and the resonator cavity are under phase matching condition. The resonant condition will take place when the WGM propagations are supported by the resonator cavity at specific wavelengths. Depending on the resonant condition, the resonator cavity will selectively allow certain wavelengths of light to travel inside the cavity, these wavelengths are defined as resonant wavelengths.

1.3 Microsphere lasers

The essential elements of the laser system consist of the laser medium, pumping process, and feedback element. The population inversion occurs when the atoms are pumped from the ground level of the system to the upper level. The laser action is obtained when the atoms are decayed from the metastable level to the lower level by the stimulated emission, see Figure 1.2. The existence of forbidden transitions of the laser transitions in rare-earth doped media make upper-state lifetimes become relatively longer than those which decay via electric dipole transitions. These forbidden transitions have small oscillator strengths, thus a substantial amount of the energy can be stored in the media.

The demonstration of laser oscillation has been widely shown in microdroplets [16], polymer microspheres [17], glass microspheres [4, 9–12, 18–21] and crystal microspheres [22]. Micro-resonators, microsphere particles and microdroplets, doped with rare-earth (or lanthanide) ions or dyes, exhibit laser action when these active impurities in the host material are excited. Rare-earth ions in the form of trivalent ions such as neodymium (Nd^{3+}), thulium (Tm^{3+}), praesodymium (Pr^{3+}), erbium (Er^{3+}) and ytterbium (Yb^{3+}) are widely used as dopants, while the well known host materials are glasses and crystals. In this work, BK7 microspheres in the range of 30 μm to 200 μm in diameter, doped with neodymium, will be used to demonstrate laser oscillation for the free-space and ion-exchanged waveguide light coupling configurations. The experiments to observe laser oscillation at 1.06 μm from the $^4F_{3/2}$ - $^4I_{11/2}$ transition will be carried out.

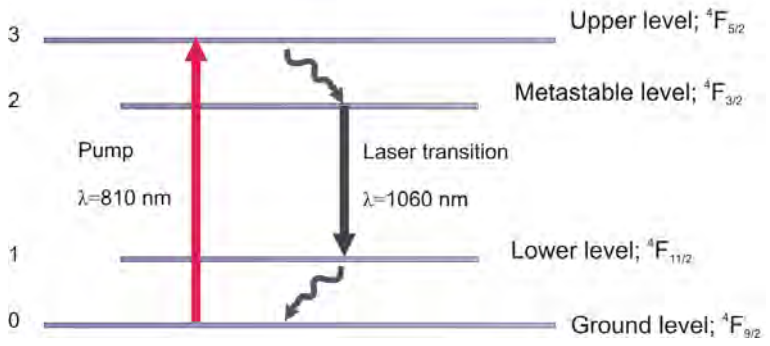

FIGURE 1.2: Schematic diagram of neodymium energy level [23]

1.4 Review of microsphere coupling techniques and pumping methods for microsphere lasers

This section contains a review of methods used for microsphere coupling, evanescent wave excitations of undoped-microspheres and microsphere lasers. The techniques require an inexpensive device, such as a prism or an optical fibre; however, difficulties and drawbacks for each method are covered in this section. At the end of this section, a review of the pumping method for microsphere lasers is given.

1.4.1 Microsphere coupling methods

Light can be coupled into a microsphere cavity efficiently by various evanescent techniques, such as the waveguide coupling [13, 15, 24], prism-to-sphere coupling [25–27], tapered fibre coupling [28], etch-eroded fibre coupling [29], fibre half-blocked coupling [14, 30–32] or angle-polished fibre coupling [33]. Each of the methods requires careful alignment, because the gap between the microsphere and the prism has to be at an optimum to achieve high coupling efficiency. In this section, various methods for evanescent coupling of light into microspheres are reviewed and discussed.

The prism light coupling method is among the earliest techniques used to couple the light into the spherical resonator. This method involves the use of the prism to allow the WGM propagation in the microsphere, see Figure 1.3. The light was directed to the surface of the prism to achieve the total internal reflection. The evanescent field was presented at the surface and was coupled into the spherical resonator.

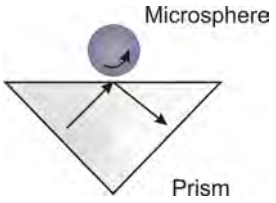

FIGURE 1.3: Prism coupling method [25, 27]

In 1989, Brakinsky et al. developed the prism coupling method by using a fused quartz microsphere of about 150 μm in diameter as a resonator that was placed in close proximity to the high refractive index prism. The gap between the prism and the resonator made a separation of about $(0.1-1.0)\lambda$. The quality factor was reported to have a value of up to 10^8 at the operating wavelength of 780 nm [25]. In 1993, Collot et al. reported a higher value of quality factor in a fused silica microsphere. The microsphere diameter in the range of 60 μm to 200 μm was formed by fusing the end of a short silica wire. The quality factor achieved for a 120 μm diameter microsphere was 2×10^9 at 632.8 nm [27]. The evidence showed that the surface scattering loss was reduced compared to the previous attempt on the quartz microsphere. The experimental work based on this

coupling configuration is found to be critical as the location of the microsphere and the prism need to be controlled to less than a 0.1λ, where the prism is a bulky device, and the control is difficult to achieve. A thin layer of low-index film may be coated on the prism face to allow the sphere to be placed in contact for ease of the alignment.

Tapered fibre coupling is a powerful method to achieve a high coupling efficiency, because the evanescent light, extending to the outer region of the tapered area, provides strong coupling to the micro-resonator devices. This method can be useful in optical fibre applications, because the fibre can be directly spliced to the readout devices easily. In 1997, Knight et al. [28] developed a tapered fibre in which the fibre was heated and stretched to achieve a very thin coupling region. Light travelled along the silica waist and coupled the evanescent field to the resonator that was in close proximity. In order to couple light into the silica microsphere of 170 μm in diameter, the waist radius of 1.7 μm was developed; and a quality factor of 2×10^6 was obtained at 1550 nm [28].

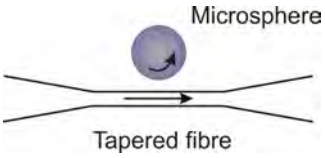

FIGURE 1.4: Tapered fibre coupling method [28]

Even though fibre tapered coupling is a promising method to couple light into the microsphere, there is a frustrating drawback for this method, the tapered area is very fragile and hard to handle. The high coupling efficiency of the resonator can only be achieved with the small diameter of the tapered fibre at the coupling region.

The angle-polished fibre coupler method [33] combines the use of an optical fibre and the advantage of the prism coupling method. This method is based on the idea of the previous prism coupling method, however, it is more convenient since the evanescent field at the angle-polished tip of the fibre is generated from the light that propagates through the fibre. This field can be used as an excitation source to the microsphere cavity as shown in Figure 1.5.

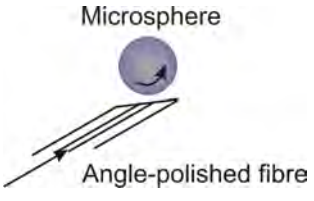

FIGURE 1.5: Angle-polished fibre coupling method [33]

In 1999, Ilchenko et al. developed the angle-polished fibre that had a core diameter of 8.3 μm and the polished angle of 77°. The silica microsphere had a lower index than the fibre core (which had a refractive index of 1.4505 at $\lambda = 1550$ nm and 1.4535 at $\lambda = 1310$ nm). Q-factors of 3×10^7 at 1550 nm, and 3.2×10^6 at 1310 nm, for

a microsphere of diameter of 470 μm, were reported [33]. The Q-factors obtained are relatively low compared with Q obtained from a prism coupler; this may be due to the strong coupling of the evanescent light at the surface, or the used of different sphere.

Another method for coupling light into a microsphere is by using the fibre half-block coupling method, where a fibre half-block coupler, which consists of a polished-to-core optical fibre that is buried in a metal block [30–32], is used for light WGM excitation in the microspheres. This method allows the microsphere to interact directly with the evanescent field from the fibre core, see Figure 1.6.

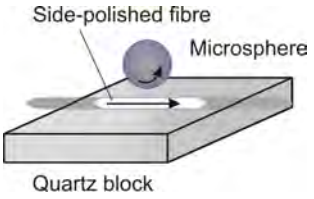

FIGURE 1.6: Fibre half-block coupling method [30–32]

In the fibre half-block coupling method, a microsphere as small as 30 μm in diameter was reported in 1995 by Serpengüzel et al. [30], to have a quality factor of 10^6. The microsphere was placed on the fibre that had a cladding layer polished down to about 0.7 μm. The fibre had a refractive index of 1.462 in the core and 1.457 in the cladding region at 632.8 nm. The microsphere was a polystyrene microsphere that had a refractive index of 1.59 at an operating wavelength in the 600 nm region. A higher Q factor was achieved later by Dubreuil et al. with a larger resonator size, that is 215 μm in diameter. The quality factor was reported to have a value up to 10^8 [32].

The downside of this method relates to the labour intensive cladding polishing process, because the cladding of the fibre must be polished to a certain thickness to achieve a proper coupling; thus this method is not suitable for complex circuits. Another downside of this method is the tunnelling loss to the cladding area and the surrounded block, hence a lower Q value is achieved.

The etch-eroded fibre coupling method eliminates the problem of the light leakage which may occur in the fibre half-block method. The interaction of the evanescent fields will take place only at the core of the coupling region, unlike the fibre half-block coupling method. As a result, the etch-eroded fibre coupling method yields a higher coupling efficiency than the fibre half-block coupling method.

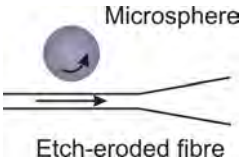

FIGURE 1.7: Etch-eroded fibre coupling method [29]

In 1999, Laine et al. completed an experiment on etch-eroded fibre coupling on silica

microspheres of diameter 280 μm. A Q factor of up to 8×10^8 was obtained at 1550 nm. The fibre cladding was chemically eroded, by using hydrofluoric acid as an etching solution, so that the core of the fibre could be exposed fully. The eroded fibre had a diameter of approximately 6 μm [29]. Q obtained from the etch-eroded fibre coupling method is larger compared to a tapered fibre coupling method, thus light interaction can be obtained without light coupling back to the cladding surface. This method has its main drawback in common with the tapered fibre method since the coupling area is small and fragile.

The waveguide coupling microsphere method provides a better coupling structure for complex circuit integration, compared to other methods. The theoretical model for this coupling technique is of interest in many research groups [24, 34–36], confirming that the coupling in this technique is versatile.

In 2000, Laine et al. introduced a stripline pedestal anti-resonant reflecting optical waveguide coupler to couple light into a microsphere [13, 15]. An alternate layer of Si and SiO_2 was used to isolate the sphere and substrate, this highly-reflective structure can minimise the leakage into the substrate. The microsphere was attached to a fibre tip to allow movement in vertical and lateral translation. Microspheres of 100 μm to 400 μm in diameter were fabricated by melting fibre tips. Q of 5×10^7 was obtained from the 220 μm diameter microsphere.

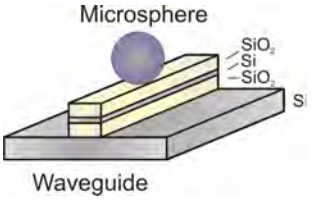

FIGURE 1.8: Stripline pedestal anti-resonant reflecting optical waveguide coupling method [13, 15]

In conclusion, microsphere coupling with half-block couplers suffered from light leakage into the substrate. Although the tapered fibre and etch-eroded fibre couplers provide promising coupling to achieve high Q characteristics, this is not practical for handling since the structure is very fragile and delicate. The prism coupling method is one of the promising techniques to couple the light into a microsphere, but the alignment is difficult to obtain and the prism is rather bulky. Waveguide coupling techniques are very robust and the optimisation to achieve a desired Q can be done with a properly designed structure and material. An ion-exchanged waveguide can be a good candidate for the microsphere coupling, because it can be simple to fabricate and it has low cost of fabrication. Thus, in this project, microsphere coupling to an ion-exchanged waveguide is explored.

1.4.2 Pumping methods for microsphere lasers

In this section, prior work on the technique for pumping microsphere lasers is reviewed. The early attempts at making microsphere lasers were accomplished with free-space excitation [9, 12, 16, 17, 22]. Evanescent wave excitation microsphere lasers were then developed in order to achieve a low laser threshold pump power. Light becomes efficiently trapped inside the microsphere cavity under the evanescent wave excitation, so that the pump light may be efficiently absorbed by the cavity. Consequently, the gain of the laser is easier to attain at the lower pump power. Thus, the laser can operate at a lower pump power compared to the free-space excitation case. Until now the evanescent fields were obtained from wave propagation in prisms [4, 10, 18, 22] or tapered fibres [11, 19–21].

In 1984, the experimental observation of laser oscillation on a single liquid droplet, by free-space pumping, was made by Tzeng et al. [16]. A Rhodamine 6G-ethanol droplet of 60 μm in diameter was pumped by an argon-ion laser at the wavelength of 514.5 nm, at room temperature. The droplets were formed by an aerosol generator, driven at a frequency of 62 kHz, that generated a droplet of 60 μm in diameter every 16 μsec. The pumped light was focused to a 200 μm diameter spot on the rim of the microdroplet. The emitted radiation from a single droplet was collected at 90° and 0° relative to the pump beam. The experiments to observe emission spectra, as well as the temporal behavior from a single Rhodamine 6G-ethanol droplet, were carried out. The emission spectra were observed by detecting the beam of radiation emitted at 90° using an optical multichannel analyzer (OMA), while the radiation at 0° was filtered out from the original beam and detected by a photomultiplier such that the measurements on the temporal behaviour of the droplet were obtained. It was reported that the emitted laser radiation emerged in all directions from a droplet, and that the pumping threshold power was about 10 mW.

The experimental observation of laser action on the crystal microsphere, by free-space excitation, was demonstrated by Baer et al. in 1987 [22]. The oscillation was achieved with a 5 mm Nd:YAG microsphere. A 810-nm-pump light was incident onto the microsphere and propagated along the rim by total internal reflection. Lasing oscillation at 1064 nm and pump power threshold of 100 mW were obtained. In 1991, laser emission from dye-doped polymer microspheres was demonstrated by Kuwata et al. [17]. The polymer microspheres, in the range of 10 μm to 92 μm in diameter, were doped with Nile Red dye with a concentration of 10^{-6} mol/g, the microspheres were individually pumped by a nanosecond pulsed dye laser at the wavelength of 520 nm. The temporal responses were observed and collected using a fast response microchannel plate photomultiplier. The lasing oscillation was obtained from a 41 μm diameter microsphere. A threshold pumping power of 20 W was obtained.

The laser action of a Nd^{3+}-doped fluoride microsphere was demonstrated by Miura et al. in 1997 [12]. The Nd^{3+}-doped fluoride microsphere was excited by a titanium:sapphire

laser at the wavelength of 800 nm. The emitted light was captured by the objective lens, and the emission spectra were obtained via a monochromator equipped with a photodiode. The simultaneous laser oscillations on $^4F_{3/2}$ - $^4I_{11/2}$ and $^4F_{3/2}$ - $^4I_{13/2}$ were obtained, with the corresponding emission wavelength of 1051 and 1334 nm, respectively. The emission at 1051 nm has a higher intensity than the emission in the 1334 nm region. The threshold pump power obtained for the emission in the 1051 nm region was 5 mW, while in the 1334 nm region the threshold pump power was 60 mW.

In 2002, the laser oscillations on Nd^{3+}-doped tellurite microspheres were demonstrated by Sasagawa et al. [9]. The incident beam was focused onto the Nd^{3+}-doped tellurite microsphere, of 140 μm in diameter, by a 20× microscope objective lens such that the focal point was located on the rim of the microsphere. The emitted light from the microsphere was coupled into an optical fibre. The emission at 1.06 μm was obtained with the pumping wavelength of 800 nm. A threshold pump power of about 81 mW was obtained.

The laser oscillations observed by free-space excitation suffer from high threshold pump power, and the modes are not selectable. Light coupling by the evanescent light coupling method is considered to be a good candidate to reduce the threshold and select the lasing mode.

The laser oscillations of Nd^{3+}-doped silica microspheres were observed by Sandoghdar et al. in 1996 [4]. Microspheres of 40 μm to 200 μm in diameter were formed by fusing a core of 0.2-wt% Nd^{3+}-doped silica fibre with a CO_2 laser. The WGM of the microsphere was excited by the evanescent field from a high index glass prism at a wavelength of 807 nm. The fluorescence spectrum and the laser spectrum from a $^4F_{3/2}$ - $^4I_{11/2}$ transition of the Nd^{3+}-doped silica microsphere, of 56 μm in diameter, were obtained. The threshold absorbed pump power of 200 nW was obtained for the incident pump power onto the prism face of 1 mW.

In 2000, whispering-gallery mode lasers were demonstrated using Er^{3+}-doped fluoride glass microspheres by Lissillour et al. [10, 18]. A 56 μm diameter fluoride glass microsphere was doped with 0.2% by weight of Er^{3+}, it was excited by the evanescent field from a prism so that the laser transition around 1.56 μm was obtained from a $^4I_{13/2}$ - $^4I_{15/2}$ transition of the Er^{3+}. The pump wavelength was chosen to be 1.48 μm, where a good overlap between the pump and the laser mode volume could be obtained. The separation between the prism and the Er^{3+}-doped fluoride glass microsphere was controlled by a piezo-actuator. A pump threshold power of 0.6 mW and a laser linewidth of 270 kHz were obtained. The prism coupling method provides a relatively low threshold pump power compared to the free-space excitation described previously. The drawback from this method is that it needed a complicated alignment tool in order to achieve the total internal reflection and also a complex method was required to readout the information from the devices when used with an optical fibre.

Laser oscillations of rare-earth-doped phosphate microspheres, with an evanescent field coupling from a tapered fibre, were observed by Cai et al. in 2000 [19]. Phosphate glass microspheres were doped with Yb^{3+} and Er^{3+}, with concentrations of 20% and 5% by weight respectively. The microspheres were excited with the evanescent field from the tapered fibre at a pump wavelength of 976 nm, and emissions in the 1500-nm band were obtained. Phase matching conditions between the mode of the tapered fibre and the whispering-gallery modes in the microsphere were obtained by adjusting the diameter of the tapered fibre. The microsphere of 57 μm in diameter was placed on the tapered fibre, and the lasing spectrum was collected with the tapered fibre. The results showed that a side-mode suppression of the system of about 26 dB was obtained, and the microsphere was lasing at 1535 nm. The threshold pump power of about 60 μW was obtained.

In 2003, laser oscillation on an Er^{3+}-doped tellurite microsphere was demonstrated by Peng et al. [20]. The glass microsphere was doped with erbium and the excitation of the whispering-gallery mode was attained via a tapered fibre. Pump light, at a wavelength of 975 nm, was coupled to a 33 μm-diameter microsphere by the tapered fibre with a diameter of 1.3 μm. A power threshold of less than 2 mW was obtained.

In 2005, laser action on an Er^{3+}-doped microsphere was demonstrated by Kalkman et al. [21]. The tips of Er^{3+}-doped silica fibres were melted and formed microspheres of about 22 μm in radius. The evanescent fields of the tapered fibre were used to excite the whispering-gallery modes. The lasing spectrum of the fundamental mode ($l = m$) was obtained. The pump threshold power was reported to have a value of about 150 μW at the pump wavelength of 1450 nm.

In 2006, Conti et al. demonstrated laser action from Er^{3+}-doped, modified-silica and phosphate glass microspheres [11]. A 980 nm pump laser was coupled through a tapered fibre, laser action of 1550 nm was obtained from the $^4I_{13/2}$-$^4I_{15/2}$ transition of a 0.5%-wt Er^{3+}-doped modified-silica glass (Baccarat glass) microsphere of 85 μm in diameter. The fluorescence and lasing spectra were also experimentally observed in an Er^{3+}/Yb^{3+} co-doped, phosphate glass, microsphere of 70 μm in diameter. Power thresholds of 2.5 mW were observed.

The microsphere lasers excited by a tapered fibre have a relatively low threshold level compared to the free-space excitation. The tapered fibre is an excellent method for coupling pump power in microsphere lasers except that the tapered area is very delicate and fragile, and these fibres become very delicate for handling and fabrication.

1.5 The approach adopted in this thesis

This work is focused on the planar waveguide coupling method [13, 24] for microsphere lasers. The evanescent field from a waveguide may then be coupled to the field at the surface of the resonator. The microsphere will be placed on top of the waveguide to allow the coupling interaction to take place, so that the observation of the power circulating in the microsphere will be exploited. The evanescent field that occurs at the spherical surface interacts with the evanescent field from the waveguide; and if a phase matching condition is met, coupling occurs. Thus, depending on the resonant condition, the resonator cavity will selectively let the light at certain wavelengths travel inside the cavity, while the rest of the non-selected wavelength will not excite a resonance inside the cavity.

There are no obvious prior attempts to achieve lasing oscillations of the rare-earth-doped microspheres in the waveguide configuration, while many research groups have demonstrated laser oscillation in microspheres by tapered fibre coupling and prism coupling techniques. The planar waveguide and microsphere laser can be a promising method to solve all the problems that may be found in microsphere laser and prism or tapered fibre configurations. Thus, waveguide coupling microsphere lasers is considered to be a promising method to pursue in this project.

1.6 Thesis structure

This thesis is divided into 7 chapters. The first chapter is the introduction of the topic. The remaining chapters of the thesis are organised as following, Chapter 2 includes the theoretical work on microsphere mode and fields and the waveguide. The method of obtaining the coupling efficiency of the microsphere and waveguide are discussed. The basic theoretical modelling on the power transfer functions of the microsphere resonators, and the waveguide are also included. Chapter 3 describes the method used for waveguide and microsphere fabrication, and the characterisation of the waveguide and the microspheres obtained based on the fabricated methods described. The experimental results on the passive microspheres will be discussed in detail in Chapter 4, and the theoretical work for the mode assignment will be carried out. Chapter 5 includes theoretical work on microsphere lasers, where loss and gain of the cavity are calculated. The calculated threshold pump power for lasing action of the microsphere coupled waveguide will also be discussed at the end of the chapter. Chapter 6 describes the experimental work on microsphere lasers. The discussion of the experimental results will be made in the chapter. Chapter 7 contains the conclusions, discussion, and reviews the work of the research, and suggestions for further work plans are also provided.

1.7 References

[1] M. L. Gorodetsky, A. A. Savchenkov, and V. S. Ilchenko. Ultimate Q of optical microsphere resonators. *Optics Letters*, 21:453–455, 1996.

[2] D. W. Vernooy, V. S. Ilchenko, H. Mabuchi, E. W. Streed, and H. J. Kimble. High-Q measurements of fused-silica microspheres in the near infrared. *Optics Letters*, 23:247–249, 1998.

[3] X. H. Jiao, P. Guillon, L. A. Bermijdez, and P. Auxemery. Whispering-gallery modes of dielectric structures: Applications to millimeter-wave bandstop filters. *IEEE Transactions on Microwave Theory and Techniques*, MTT-35:1169–1175, 1987.

[4] V. Sandoghdar, F. Treussart, J. Hare, V. Lefèvre-Seguin, J. M. Raimond, and S. Haroche. Very low threshold whispering-gallery-mode microsphere laser. *Physical Review A*, 54:R1777–R1780, 1996.

[5] S. L. McCall, A. F. J. Levi, R. E. Slusher, S. J. Pearton, and R. A. Logan. Whispering-gallery mode microdisk lasers. *Applied Physics Letter*, 60:289–291, 1992.

[6] A. D. Bristow, D. M. Whittaker, V. N. Astratov, M. S. Skolnick, A. Tahraoui, T. F. Krauss, M. Hopkinson, M. P. Croucher, and G. A. Gehring. Defect states and commensurability in dual-period Al_xGa_1-xAs photonic crystal waveguides. *Physical Review B*, 68:033303–1–033303–4, 2003.

[7] S. M. Spillane, T. J. Kippenberg, and K. J. Vahala. Ultralow-threshold Raman laser using a spherical dielectric microcavity. *Nature*, 415:620–623, 2002.

[8] Lord Rayleigh. *The problem of the whispering gallery.* Cambridge, England, 1912.

[9] K. Sasagawa, K. Kusawake, J. Ohta, and M. Nunoshita. Nd-doped tellurite glass microsphere laser. *Electronics Letters*, 38:1355–1357, 2002.

[10] P. Féron. Whispering gallery mode lasers in erbium doped fluoride glasses. *Annales de la Foundation Louis de Broglie*, 29:317–329, 2004.

[11] G. Nunzi Conti, A. Chiasera, L. Ghisa, S. Berneschi, M. Brenci, Y. Dumeige, S. Pelli, S. Sebastiani, P. Feron, M. Ferrari, and G. C. Righini. Spectroscopic and lasing properties of Er^{3+}-doped glass microspheres. *Journal of Non-Crystalline Solids*, 352:2360–2363, 2006.

[12] K. Miura, K. Tanaka, and K. Hirao. CW laser oscillation on both the $^4F_{3/2}$-$^4I_{11/2}$ and $^4F_{3/2}$-$^4I_{13/2}$ transitions of Nd^{3+} ions using a fluoride glass microsphere. *Journal of Non-crystalline Solids*, 213–214:276–280, 1997.

[13] B. E. Little, J. P. Laine, D. R. Lim, and H. A. Haus. Pedestal antiresonant reflecting waveguides for robust coupling to microsphere resonators and for microphotonics circuits. *Optics Letters*, 25:73–75, 2000.

[14] J. C. Knight, N. Dubreuil, V. Sandoghdar, J. Hare, V. Lefèvre-Seguin, J. M. Raimond, and S. Haroche. Mapping whispering-gallery modes in microspheres with a near-field probe. *Optics Letters*, 20:1515–1517, 1995.

[15] J. P. Laine, B. E. Little, D. R. Lim, H. C. Tapalian, L. C. Kimerling, and H. A. Haus. Microsphere resonator mode characterization by pedestal anti-resonant reflecting waveguide coupler. *IEEE Photonics Technology Letters*, 12:1004–1006, 2000.

[16] H. M. Tzeng, K. F. Wall, M. B. Long, and R. K. Chang. Laser emission from individual droplets at wavelengths corresponding to morphology-dependent resonances. *Optics Letters*, 9:499–501, 1984.

[17] M. Kuwata, K. Takeda, G. Yasuda, and K. Ema. Laser emission from dye-doped polystyrene microsphere. *Japanese Journal of Applied Physics*, 31:L99–L101, 1992.

[18] F. Lissillour, P. Féron, N. Dubreuil, P. Dupriez, M. Poulain, and G. M. Stéphan. Erbium-doped microspherical lasers at 1.56 μm. *Electronics Letters*, 36:1382–1384, 2000.

[19] M. Cai, O. Painter, and K. J. Vahala. Fiber-coupled microsphere laser. *Optics Letters*, 25:1430–1432, 2000.

[20] X. Peng, F. Song, S. Jiang, N. Peyghambarian, M. K. Gonokami, and L. Xu. Fiber-taper-coupled L-band Er^{3+}-doped tellurite glass microsphere laser. *Applied Physics Letters*, 82:1497–1499, 2003.

[21] J. Kalkman, A. Polman, T. J. Kippenberg, K. J. Vahala, and M. L. Brongersma. Erbium-implanted silica microsphere laser. *Nuclear Instruments and Methods in Physics Research B*, 242:182–185, 2006.

[22] T. Baer. Continuous-wave laser oscillation in a Nd:YAG sphere. *Optics Letters*, 12: 392–394, 1987.

[23] A. E. Siegman. *Lasers*. Univerity Science Books, California, 1986. ISBN 0-935702-11-3.

[24] A. Yariv, Y. Xu, R. K. Lee, and A. Scherer. Coupled-resonator optical waveguide: a proposal and analysis. *Optics Letters*, 24:711–713, 1999.

[25] V. B. Braginsky, M. L. Gorodetsky, and V. S. Ilchenko. Quality-factor and nonlinear properties of optical whispering-gallery modes. *Physics Letters A*, 137:393–397, 1989.

[26] M. L. Gorodetsky and V. S. Ilchenko. High-Q optical whispering-gallery microresonators: precession approach for spherical mode analysis and emission patterns with prism couplers. *Optics Communications*, 113:133–143, 1994.

[27] L. Collot, V. Lefèvre-Seguin, M. Brune, J. M. Raimond, and S. Haroche. Very high-Q whispering-gallery mode resonances observed on fused silica microspheres. *Europhysics Letters*, 23:327–334, 1993.

[28] J. C. Knight, G. Cheung, F. Jacques, and T. A. Birks. Phase-matched excitation of whispering-gallery mode resonances by a fiber taper. *Optics Letters*, 22:1129–1131, 1997.

[29] J. P. Laine, B. E. Little, and H. A. Haus. Etch-eroded fiber coupler for whispering-gallery-mode excitation in high-Q silica microspheres. *IEEE Photonics Technology Letters*, 11:1429–1430, 1999.

[30] A. Serpengüzel, S. Arnold, and G. Griffel. Excitation of resonances of microspheres on an optical fiber. *Optics Letters*, 20:654–656, 1995.

[31] G. Griffel, S. Arnold, D. Taskent, and A. Serpengüzel. Morphology-dependent resonances of a microsphere-optical fiber system. *Optics Letters*, 21:695–697, 1996.

[32] N. Dubreuil, J. C. Knight, D. K. Leventhal, V. Sandoghdar, J. Hare, and V. Lefèvre. Eroded monomode optical fiber for whispering-gallery mode excitation in fused-silica microspheres. *Optics Letters*, 20:813–815, 1995.

[33] V. S. Ilchenko, X. S. Yao, and L. Maleki. Pigtailing the high-Q microsphere cavity: a simple fiber coupler for optical whispering-gallery modes. *Optics Letters*, 24: 723–725, 1999.

[34] S. C. Hagness, D. Rafizadeh, S. T. Ho, and A. Taflove. FDTD microcavity simulations: Design and experimental realization of waveguide-coupled single-mode ring and whispering-gallery-mode disk resonators. *Journal of Lightwave Technology*, 15: 2154–2165, 1997.

[35] B. E. Little, J. P. Laine, and H. A. Haus. Analytic theory of coupling from tapered fibers and half-blocks into microsphere resonators. *Journal of Lightwave Technology*, 17:704–715, 1999.

[36] Z. Guo and H. Quan. Energy transfer to optical microcavities with waveguides. *Transactions of the ASME*, 129:44–52, 2007.

Chapter 2

Theoretical modelling of microspheres and waveguide-coupled microspheres

2.1 Introduction

The coupling factor and the quality factor of the system waveguide-coupled microsphere are key parameters that determine the parameters of the designed devices, as they dictate the circulating power and wavelength characteristics of the system. The determination of the coupling strength and the corresponding quality factor of the system of a sphere coupled to a waveguide will be explained in this chapter. The sphere resonator and waveguide modal calculations will be explored in detail in Section 2.2 and Section 2.3, respectively, to allow the description of the modal field distribution. In Section 2.4, the contributions of Q factor according to the various losses in the system will be explored. In Section 2.6, the transmittance and circulating power of the system will be determined by using the value of the coupling factor found in the former section, the results and discussion are also shown. The method of calculating the coupling factor, κ, and the Q factor of the system due to the coupling will be obtained in Section 2.5, as well as the Q as a function of useful parameters such as the sphere index and the waveguide width and depth and the sphere mode numbers, these will be explored.

2.2 Spherical modes and fields

The sphere whispering-gallery modes (WGM) derivations are determined in this section. The whispering-gallery modes are electromagnetic resonances that occur in a circular cavity. The modes propagate around the sphere resonator along the sphere equator. By convention, the modes of the spherical resonator can be identified from the three different integer mode numbers, namely, n, m, and l [1, 2]. The mode number n represents the electromagnetic field component in the radial direction, and the mode numbers m and l represent the electromagnetic field in azimuthal (equatorial) and polar (angular) directions. $2m$, $l - |m| + 1$, and n represent the number of the field extrema in the azimuthal, angular, and radial directions, respectively. These mode numbers are very important for the visualisation of many characteristics of the sphere resonator and also for understanding three-dimensional modes in the spheres. Figure 2.1 shows the spherical coordinates with distance of radius r from the origin, azimuthal angle, ϕ, that has the variation in the yz plane, and the angular angle, θ, that has the variation in the plane which is perpendicular to the yz plane.

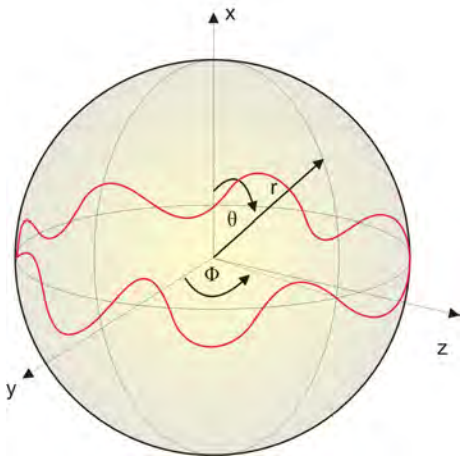

FIGURE 2.1: Spherical coordinates: radial, angular, azimuthal (r, θ, ϕ)

The field which represents either E_θ or H_θ components of the electromagnetic field of the WGM's can be described by the following equation.

$$\Psi_{l,m,n}(r, \theta, \phi) = N_s \psi_r(r) \psi_\theta(\theta) \psi_\phi(\phi), \tag{2.1}$$

where the fields in each dependency are,

$$\psi_\phi(\phi) = \exp[\pm jm\phi], \tag{2.2a}$$

$$\psi_\theta(\theta) = \exp\left[-\frac{m}{2}\theta^2\right] H_N(\sqrt{m}\theta), \tag{2.2b}$$

$$\psi_r(r) = \begin{cases} j_l(kn_s r) & \text{if } r \leq \mathrm{R}_o \\ j_l(kn_s \mathrm{R}_o) \exp[-\alpha_s(r - \mathrm{R}_o)] & \text{if } r > \mathrm{R}_o \end{cases}, \tag{2.2c}$$

and the normalisation constant is,

$$N_s = \sqrt{\frac{\pi}{m}} 2^{N-1} N! \mathrm{R}_o^2 \left[\left(1 + \frac{1}{\alpha_s \mathrm{R}_o} \right) j_l^2(k n_s \mathrm{R}_o) - j_{l-1}(k n_s \mathrm{R}_o) j_{l+1}(k n_s \mathrm{R}_o) \right]^{1/2}, \quad (2.3)$$

where $N = l - m$, and $k = \frac{2\pi}{\lambda}$.

The normalisation constant, N_s, is chosen so that the volume integral of the square of magnitude of the fields over the entire space in the sphere, divided by the sphere circumference is unity [2]. The normalised field obtained from this normalisation constant, N_s, is necessary for the calculation of the coupling factor (κ) to the waveguide, that is used in Section 2.5.

Figure 2.2 shows the angular distribution and the radial distribution of the fundamental mode in a three-dimensional view. The equatorial plane is perpendicular to the angular modal plane (or transverse plane).

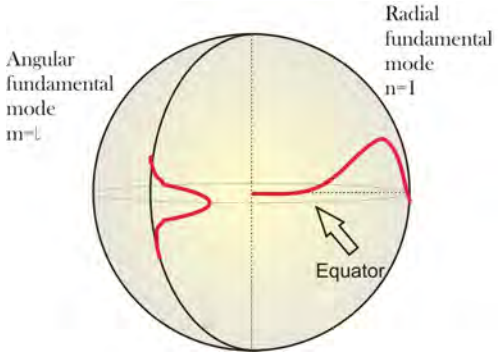

FIGURE 2.2: Spherical mode fields

$\psi_\phi(\phi)$ represents either E_θ or H_θ components of the electromagnetic field in the azimuthal direction; while $\psi_\theta(\theta)$ and $\psi_r(r)$ represent the fields in angular and radial directions, respectively.

The characteristic equation describes the relationship between the wave number, k, and the sphere mode numbers l and n. The characteristic equation can be determined by matching tangential electric and magnetic fields across the spherical surface [2]. By matching the tangential components of electric and magnetic fields, the characteristic equation can be obtained to be as follows.

$$\left(\eta_s \alpha_s + \frac{l}{\mathrm{R}_o} \right) j_l(k n_s \mathrm{R}_o) = k n_s j_{l+1}(k n_s \mathrm{R}_o), \quad (2.4)$$

where

$$\eta_s = \begin{cases} 1 & \text{TE mode} \\ \frac{n_s^2}{n_o^2} & \text{TM mode} \end{cases}, \tag{2.5a}$$

$$\alpha_s = \sqrt{\beta_l^2 - k^2 n_o^2}, \tag{2.5b}$$

$$\beta_l = \frac{\sqrt{l(l+1)}}{\mathrm{R}_o}, \tag{2.5c}$$

$$k = \frac{2\pi}{\lambda}, \tag{2.5d}$$

α_s is the decay constant away from the sphere in the radial direction. β_l is the propagation constant parallel to the surface of the sphere. k is the wavenumber. R_o is the sphere radius, n_s is the refractive index of the sphere, and n_o is the refractive index of outside medium.

The characteristic equation (Equation 2.4) can be used to find the fields of the WGM's of the spheres. Modal solutions exist where

$$f(\lambda) = \left(\eta_s \alpha_s + \frac{l}{\mathrm{R}_o}\right) j_l(k n_s \mathrm{R}_o) - k n_s j_{l+1}(k n_s \mathrm{R}_o) = 0, \tag{2.6}$$

and $f(\lambda)$ is plotted as a function of wavelength in Figure 2.3 using the values given in Table 2.1.

The zero crossing at the longest wavelength corresponds to the modal solution where n is equal to 1, and the second zero crossing represents $n = 2$, respectively. This n value is the mode number that indicates number of maxima and minima in the field in the radial direction, representing the fundamental mode when $n = 1$. The sphere of radius 15 μm with a refractive index of 1.51 is surrounded by air ($n_o = 1$). The sphere mode number l is an integer number that indicates the numbers of modes of the fields that propagate along the sphere in an azimuthal direction. The value of the resonant wavelength is obtained according to the sphere mode number l, which is supported by the sphere cavity of radius, R_o. l is inversely proportional to the wavelength, λ. For ease of presentation, the sphere mode number l is chosen to have a small value, however, the sphere mode number l must be large enough such that the high order mode in radial direction can be supported by the spherical cavity. Thus, the sphere mode number l is chosen to be 25 and the corresponding value of the resonant wavelengths become 4.77 μm, 4.13 μm and 3.71 μm for $n = 1$, $n = 2$ and $n = 3$, respectively for the TE polarisation.

Resonance occurs when the optical path length of the WGM around the equator is equal to an integer multiple of wavelengths, so that for a large sphere (compared with the wavelength λ), l can be obtained from the relation shown in Equation 2.7.

Parameters	Value
Sphere index, n_s	1.51
Medium index, n_o	1.00
Sphere radius, R_o (μm)	15
Sphere mode number, l	25

TABLE 2.1: Parameters and their values for the sphere mode and field calculations

$$l = 2\pi R_o \frac{n_{\text{eff}}}{\lambda}, \tag{2.7}$$

where l is the sphere mode number, λ is the operating wavelength, n_{eff} is the effective refractive index which corresponds to the cavity path length for each sphere mode. The value of the effective refractive index of the sphere must lie below the value of the refractive index of the sphere, however, the field that is extended to the outer region of the sphere for each mode is significantly small.

The exact resonant wavelengths may then be found by finding zeros of Equation 2.6; the plot for $l = 25$ is shown in Figure 2.3.

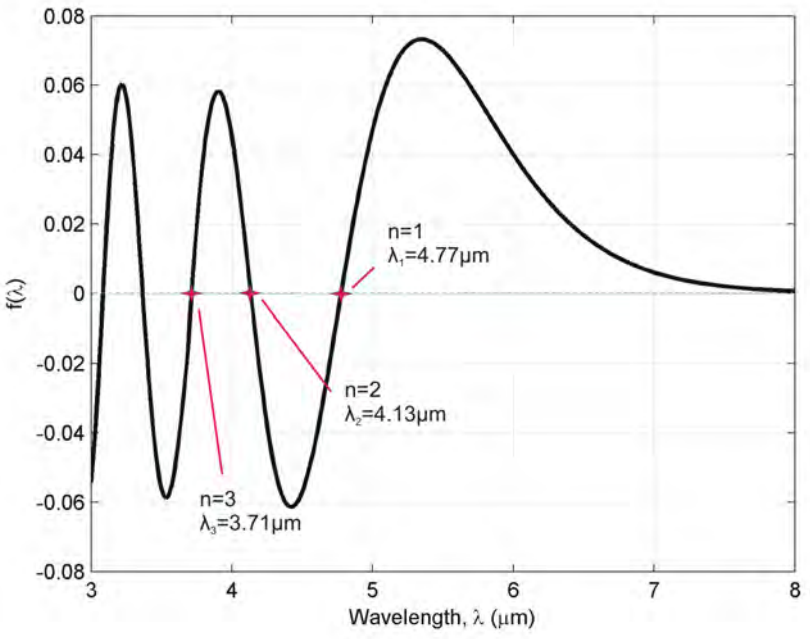

FIGURE 2.3: Plot of characteristic equation as a function of wavelength, for a sphere of 15 μm in radius, $n_s = 1.51$, $l = 25$

The radial dependence of the modal field distribution, $\psi_r(r)$, is described by the Spherical Bessel function, $j_l(x)$, which is defined by [3, 4],

$$j_l(x) = (-1)^l x^l \left(\frac{d}{xdx}\right)^l \frac{\sin(x)}{x}, \tag{2.8}$$

The Spherical Bessel function can be related to a well known Bessel function as shown in Equation 2.9.

$$j_l(x) = \sqrt{\frac{\pi}{2x}} J_{l+0.5}(x), \tag{2.9}$$

where $J_l(x)$ is a Bessel Function of the first kind of order l.

The first few terms of the Spherical Bessel function can be described as shown in Equation 2.10 [3, 4];

$$j_0(x) = \frac{\sin(x)}{x}, \tag{2.10a}$$

$$j_1(x) = \frac{\sin(x)}{x^2} - \frac{\cos(x)}{x}, \tag{2.10b}$$

$$j_2(x) = \left(\frac{3}{x^3} - \frac{1}{x}\right)\sin(x) - \frac{3}{x^2}\cos(x). \tag{2.10c}$$

In the radial dependence, the wavelengths that correspond to the fundamental and the 2^{nd} modes are 4.77 μm and 4.13 μm, respectively. Plots of the electric fields in the radial direction of the fundamental and the 2^{nd} order modes are shown in Figure 2.4. The fields inside and outside the sphere are plotted. Figure 2.4 shows that the field maximum of the fundamental mode in the radial direction is located close to the sphere interface, and the highest peak is moved toward the center of the sphere as mode number, n, is increased. It can also be seen from the figure that the field outside the sphere decays in a near-exponential way in order of wavelengths from the sphere interface.

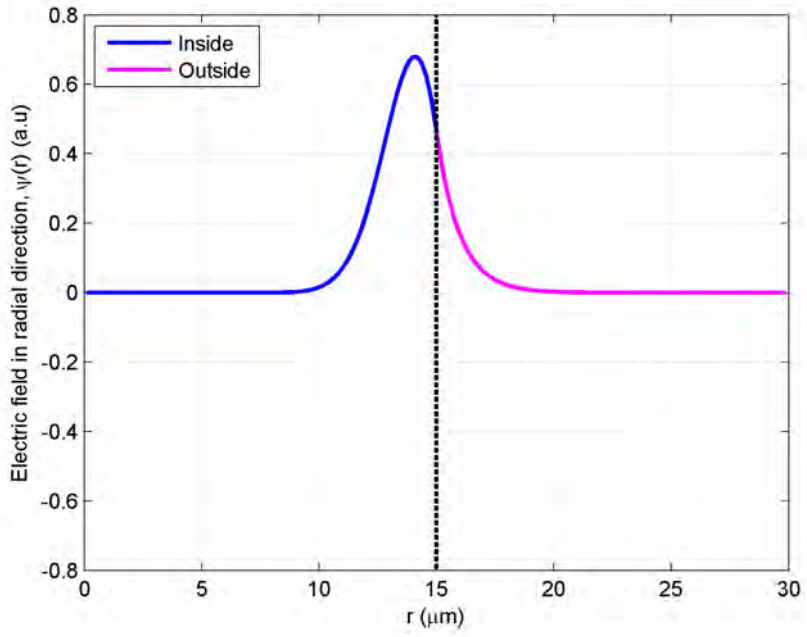

a)

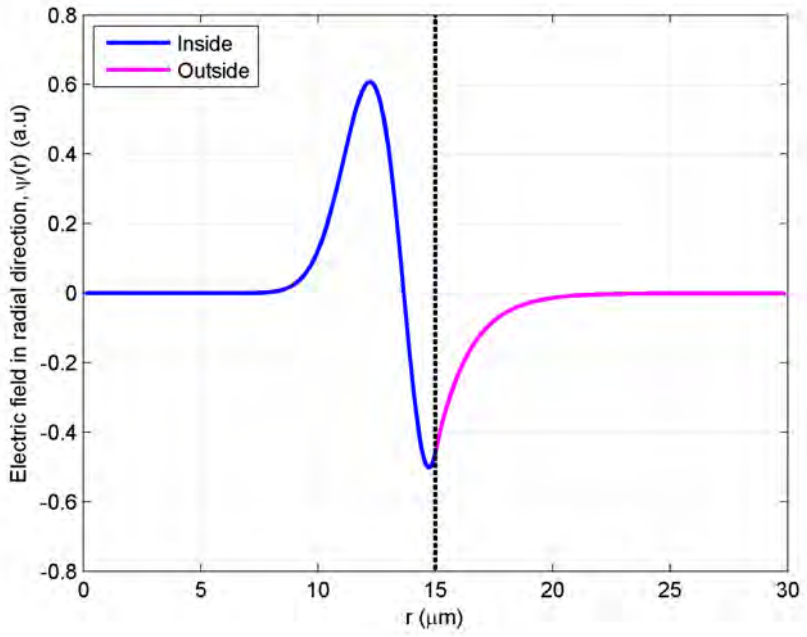

b)

FIGURE 2.4: Electric field in radial direction, $l = 25$, a) $n = 1$ ($\lambda = 4.77$ μm) and b) $n = 2$ ($\lambda = 4.13$ μm), sphere radius 15 μm

The field in the angular direction, $\psi_\theta(\theta)$, is described by the Hermite-Gaussian function $\exp[-\frac{m}{2}\theta^2]H_N(\sqrt{m}\theta)$, where $H_N(\sqrt{m}\theta)$ are the Hermite polynomials. If $x = \sqrt{m}\theta$, the Hermite polynomials are defined by equation 2.11.

$$H_N(x) = (-1)^N \exp(x^2)\frac{d^N}{dx^N}\exp(x^2). \tag{2.11}$$

The first four terms of the Hermite polynomials can be described as shown in Equation 2.12 [4, 5];

$$\begin{aligned} H_0(x) &= 1, && \text{(2.12a)} \\ H_1(x) &= 2x, && \text{(2.12b)} \\ H_2(x) &= 4x^2 - 2, && \text{(2.12c)} \\ H_3(x) &= 8x^3 - 12x, && \text{(2.12d)} \end{aligned}$$

The electric field in the angular direction depends on the sphere mode numbers l and m. The integer m can range from -l to l, and when m equals l, the fundamental mode is obtained. All of these modes, however, are degenerate under the same wavelength. The plots of the first four modes that are degenerate under the same wavelength ($\lambda = 4.77\mu$m) are shown in Figure 2.5. The figure shows that when the value of m is decreasing the number of lobes is increasing. For example, when $m = l$, the wave function has 1 peak; while when $m = l-1$, $m = l-2$, and $m = l-3$ there are 2, 3 and 4 extrema, respectively.

The field in the azimuthal direction, $\psi_\phi(\phi)$, is described by a simple sine function. Figure 2.6 shows the field of the wave along the equatorial direction. The number of field maxima, which depends on the value of m (or l for the fundamental case), is $2m$.

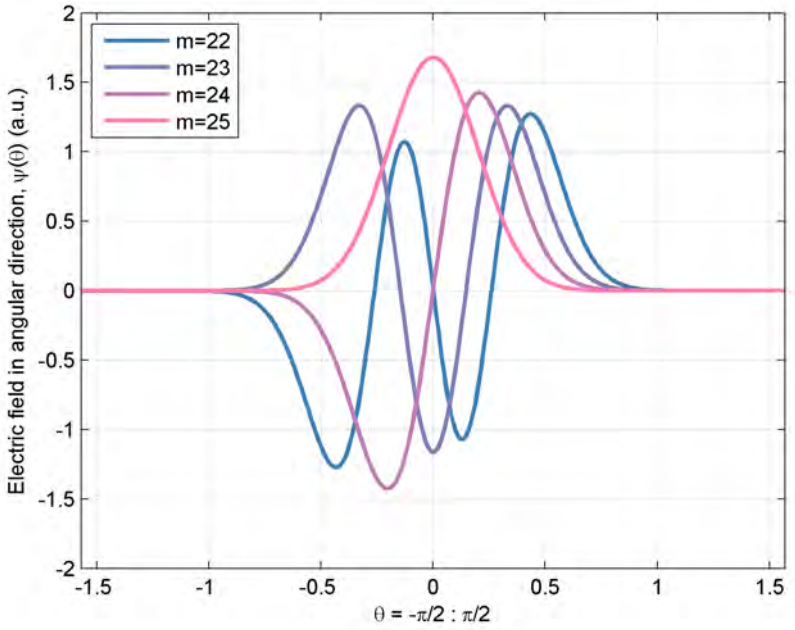

FIGURE 2.5: Electric field in angular direction, $l = 25$, $m = 22, ..., 25$, $n = 1$

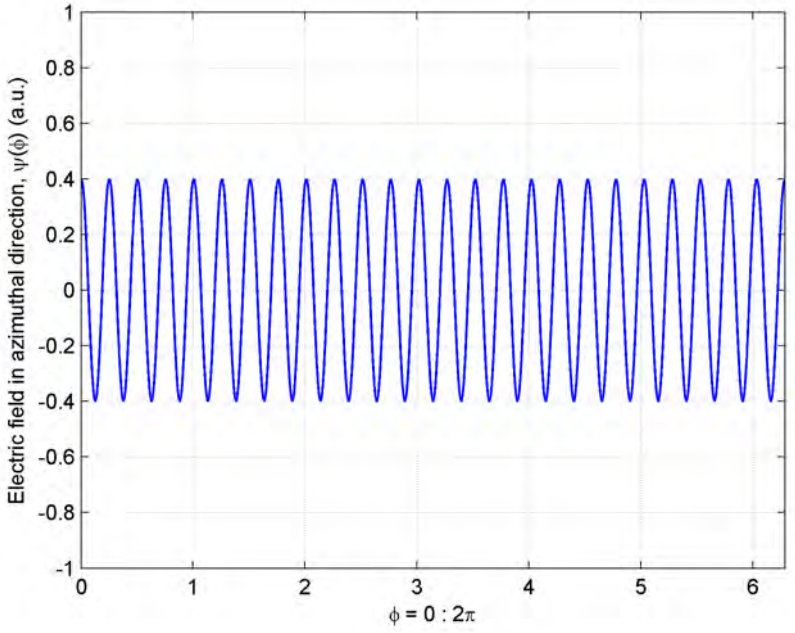

FIGURE 2.6: Electric field in azimuthal direction, $l = 25$, $m = 25$, $n = 1$

A contour plot of the field distribution inside and outside the sphere resonator in the radial and azimuthal directions, $\psi(r, \phi)$, in an equatorial plane of the sphere size of radius 15 μm, with the refractive index of 1.51, is shown in the Figure 2.7. The electric field of the sphere mode in a plane perpendicular to the equatorial plane is shown in Figure 2.8, showing a contour plot of the wave function in radial and angular directions, $\psi(r, \theta)$. For ease of visualisation, the fields that are shown in the figures are plotted based on relatively small spherical mode numbers l of 25. In Figure 2.7 and 2.8, the sphere boundary is located at 15 μm, the sphere mode numbers are $l = 25$, $m = 25$ and $n = 1$. The corresponding wavelength of the mode described is 4.77 μm. The fields inside and outside the sphere are matched at the boundary as expected. Figure 2.7 shows that the field of the fundamental mode in the radial direction has a maximum peak located close to the sphere interface, and the field in an azimuthal direction has 50 peaks. Figure 2.8 shows the fundamental mode of the fields in radial and angular directions, the field has one peak in both directions. As a conclusion, it can be seen that the numbers of field extrema in the azimuthal, angular and radial directions are 50, 1, and 1, respectively. These results agree with the previous explanation on the mode numbers, that the number of extrema in azimuthal direction is $2m$ $(2 * 25 = 50)$, the number of extrema in the angular direction is $l - |m| + 1$ $(25 - |25| + 1 = 1)$ and the number of extrema in the radial direction is n (1).

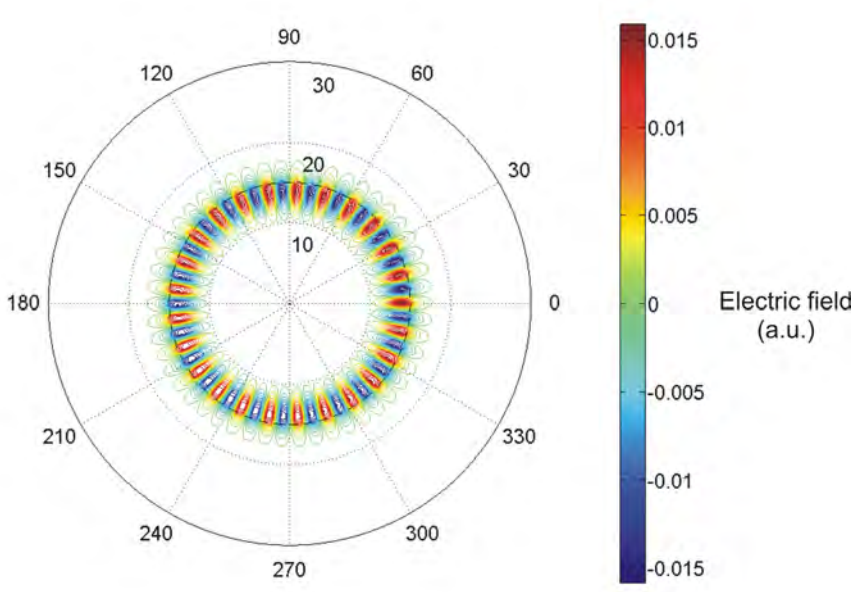

FIGURE 2.7: Electric field in $\hat{r}$-$\hat{\phi}$ plane, $l = 25$, $m = 25$, $n = 1$, $\lambda = 4.77$ μm, $R_o = 15$ μm

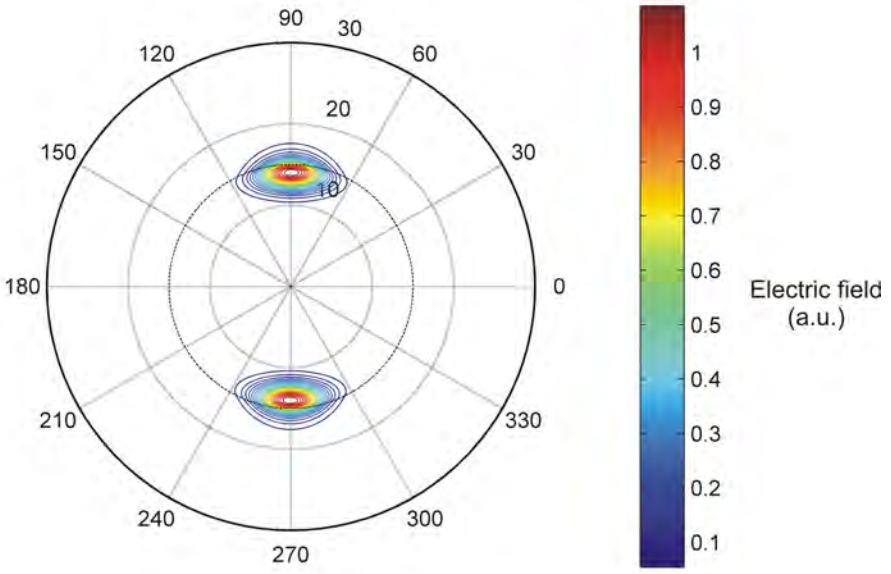

FIGURE 2.8: Electric field in $\hat{r}$-$\hat{\theta}$ plane, $l = 25$, $m = 25$, $n = 1$, $\lambda = 4.77$ μm, $R_o = 15$ μm

In this section, the contour plots of the next two higher order modes in the radial direction, (when $n = 2, n = 3$) in an equatorial plane, are shown in Figure 2.9 - 2.10. The figures shows that there are 2, 3 maxima in the radial direction, respectively; this number of maxima is equal to the sphere mode number n. Not only the observation in the radial direction can be achieved, in this equatorial plane, the azimuthal mode dependency can also be observed. The number of maxima in this direction can be obtained from the mode number m multiplied by 2. For example, Figure 2.11 shows that when the sphere mode number m is 22, the numbers of maxima in the azimuthal direction is 44; while Figure 2.12 shows that when the sphere mode number m is 24, the numbers of maxima in the azimuthal direction is 48.

In a transverse plane, which is the plane perpendicular to the equatorial plane, the contour plots of the next three higher order modes in the angular direction (when $m = l-1, \ldots, m = l-3$) are shown in Figure 2.13 to Figure 2.15. The contour plots show that the number of maxima in an angular direction and the angle of the field propagation to the equatorial plane are increasing as the mode number m is decreasing, respectively. In the transverse plane, the variations of the modal intensity distribution can be seen in both the radial and angular directions. The contour plots in Figure 2.16 and Figure 2.17 show the variations of the mode in radial and angular dependencies in the same plot. The modes with sphere mode numbers $l = 25$, $n = 2$, $m = l$ and $l = 25$, $n = 2$, $m = l-2$ are plotted in Figure 2.16 and 2.17, respectively. The mode with sphere mode number $n = 2$ has 2 peaks (counted from the origin of the sphere toward the sphere boundary), while the mode in angular dependent can be obtained from different sphere

mode number m. Figure 2.16 shows that when $m = l$, the number of maxima in angular dependent is 1; while Figure 2.17 shows that when $m = l - 2$, there are 3 maxima in the angular direction.

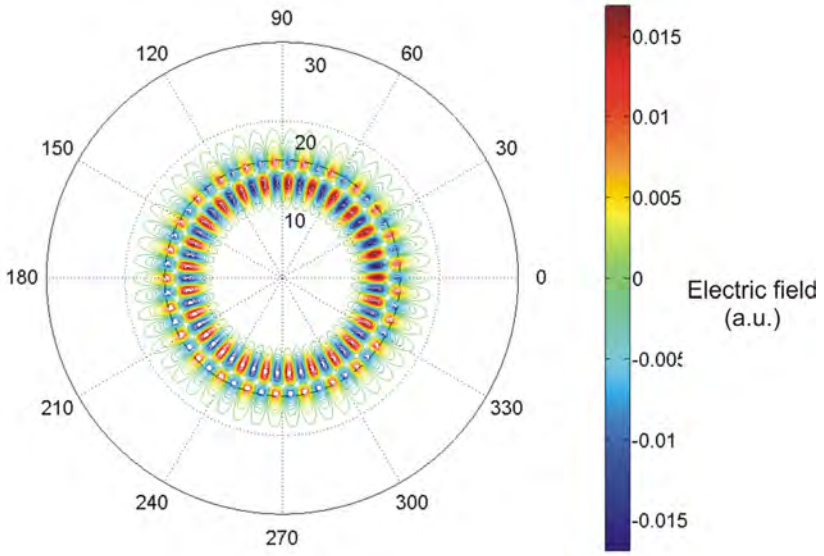

FIGURE 2.9: Electric field in $\hat{r}$-$\hat{\phi}$ plane, $l = 25$, $m = 25$, $n = 2$, $\lambda = 4.13$ μm, $R_o = 15$ μm

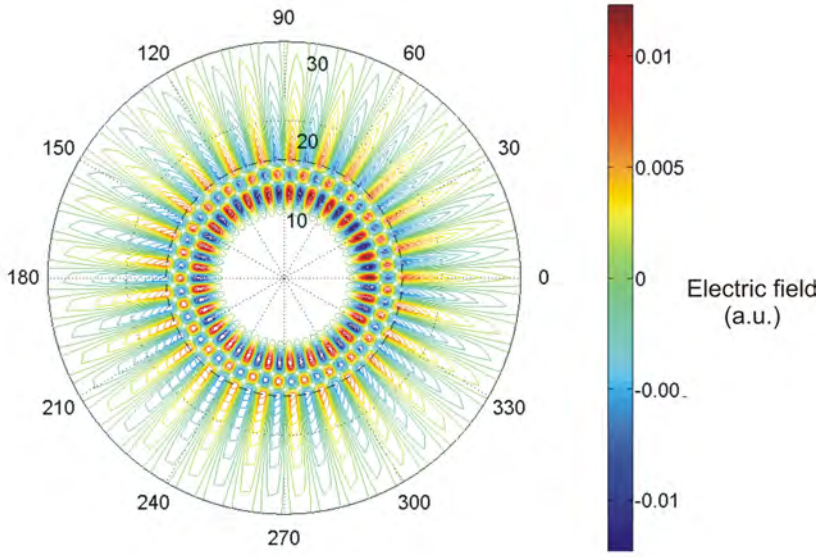

FIGURE 2.10: Electric field in $\hat{r}$-$\hat{\phi}$ plane, $l = 25$, $m = 25$, $n = 3$, $\lambda = 3.71$ μm, $R_o = 15$ μm

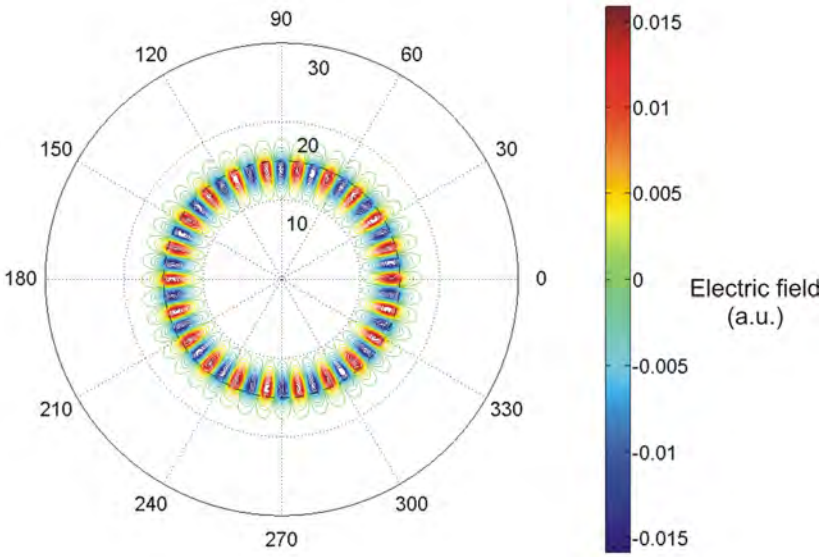

FIGURE 2.11: Electric field in $\hat{r}$-$\hat{\phi}$ plane, $l = 25$, $m = 22$, $n = 1$, $\lambda = 4.77$ μm, $R_o = 15$ μm

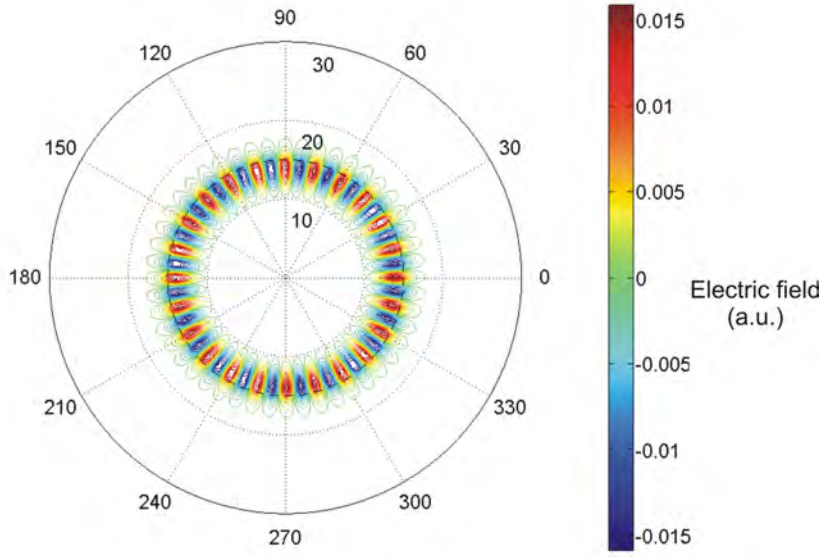

FIGURE 2.12: Electric field in $\hat{r}$-$\hat{\phi}$ plane, $l = 25$, $m = 24$, $n = 1$, $\lambda = 4.77$ μm, $R_o = 15$ μm

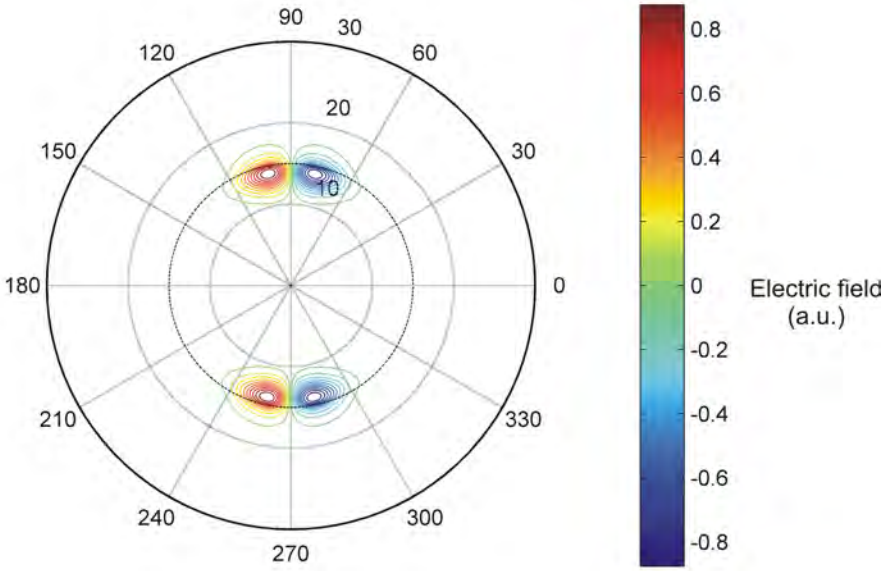

FIGURE 2.13: Electric field in $\hat{r}$-$\hat{\theta}$ plane, $l = 25$, $m = 24$, $n = 1$, $\lambda = 4.77$ μm, $R_o = 15$ μm

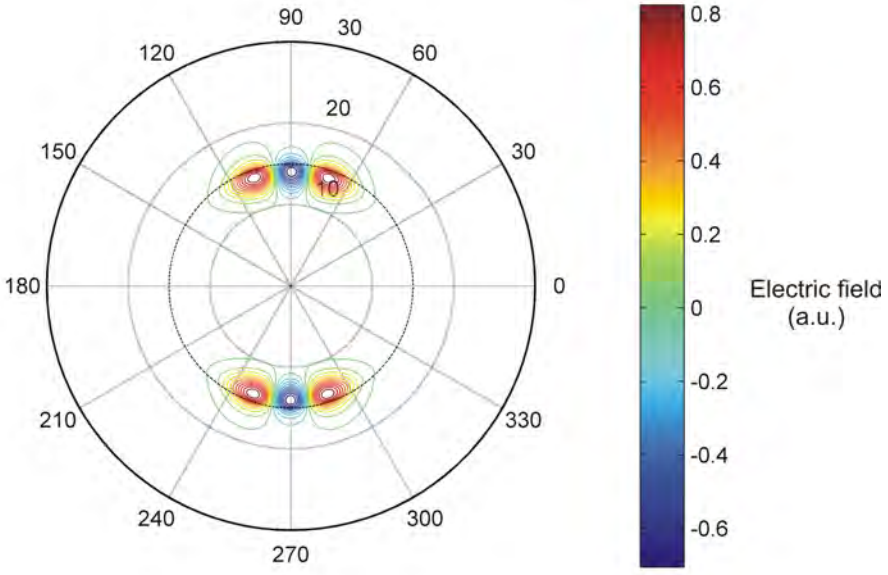

FIGURE 2.14: Electric field in $\hat{r}$-$\hat{\theta}$ plane, $l = 25$, $m = 23$, $n = 1$, $\lambda = 4.77$ μm, $R_o = 15$ μm

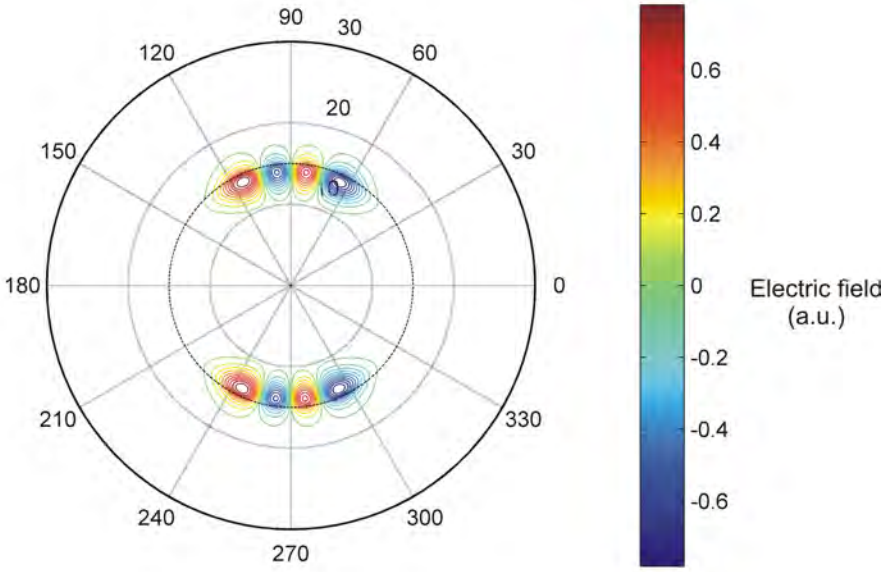

FIGURE 2.15: Electric field in $\hat{r}$-$\hat{\theta}$ plane, $l = 25$, $m = 22$, $n = 1$, $\lambda = 4.77$ μm, $R_o = 15$ μm

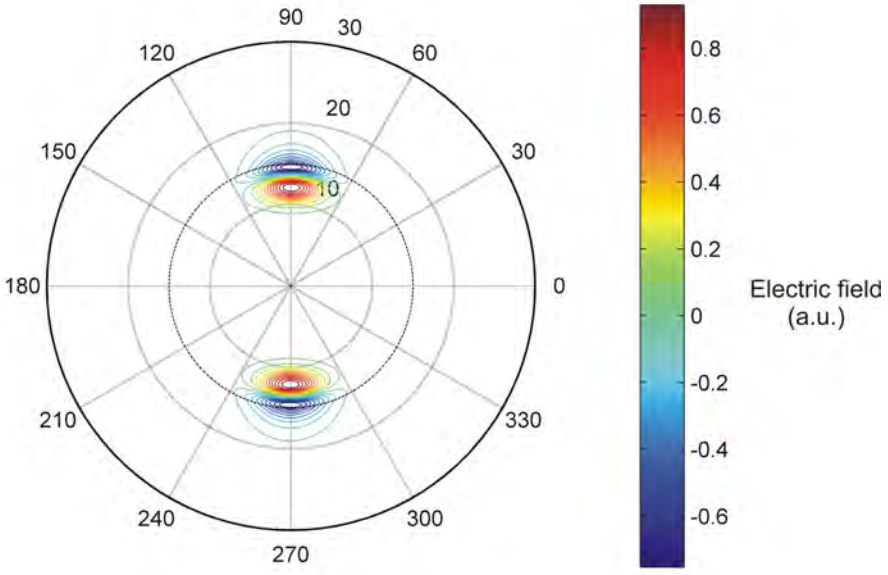

FIGURE 2.16: Electric field in $\hat{r}$-$\hat{\theta}$ plane, $l = 25$, $m = 25$, $n = 2$, $\lambda = 4.13$ μm, $R_o = 15$ μm

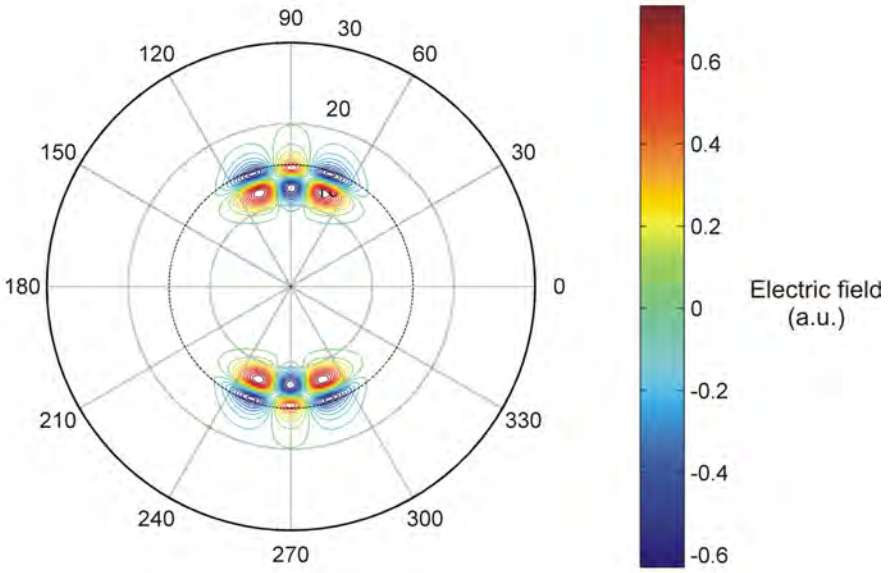

FIGURE 2.17: Electric field in $\hat{r}$-$\hat{\theta}$ plane, $l = 25$, $m = 23$, $n = 2$, $\lambda = 4.13$ μm, $R_o = 15$ μm

The WGM fields have been found in this section with a complete description of the fields in the three directions of the spherical coordinates. These fields are described by the spherical mode numbers with refractive index, the radius of the sphere and wavelength being the parameters required to determine the fields. The values of wavelengths that correspond to the spherical mode numbers are found by solving the characteristic equation, Equation 2.4. The examples of the basic mode numbers which describe WGMs have been pointed out and illustrative examples are given in this section. Some of these modes are the modes that have the same mode number of n and l (with different m value); they are generated under the same operating wavelength. The coupling strength from the optical waveguide into these modes can now be addressed.

2.3 Waveguide modal calculation

In order to determine the coupling factor, κ, which is an important parameter used to determine the coupling efficiency between the waveguide and the sphere resonator, the fields of both the sphere modes and the waveguide mode must be determined. The Q-factor of the system can also be calculated from the coupling factor and other loss mechanisms [2, 6]. In the previous section, the fields of the sphere modes were determined using analytical solutions. In this section an example of the waveguide modal derivation by using a Beamprop modelling package is discussed.

As an example in this section, the waveguide width and height are chosen to have the value of 5 and 3 μm, respectively (see figure 2.18). These values are chosen based on the value obtained from potassium-sodium-ion exchanged waveguide in BK7 with an opening width of 3 μm and diffusion time of 4 hours. The detailed discussion on the fabrication, will be given in Chapter 3. The background refractive index, n_{b}, which corresponds to the refractive index of the surrounding medium, is 1, substrate refractive index, n_s, is 1.51 and the index change, Δn, is 0.0094. The selection of Δn is chosen based on the value in the literature for potassium-sodium ion exchanged waveguide in BK7 [7]. The values of the parameters that are used in this waveguide modal calculation are shown in Table 2.2. The example of the electric field, E_y^2, plot in the transverse plane of the TE fundamental mode is shown in Figure 2.19. It shows the field distribution of the fundamental mode of the waveguide which has a corresponding effective index of 1.511517 at the operating wavelength of 750 nm.

Parameters	Values
Background refractive index, n_{b}	1.00
Substrate refractive index, n_s	1.51
Index change, Δn	0.0094
Waveguide width (μm)	5
Waveguide height (μm)	3

TABLE 2.2: Waveguide parameters

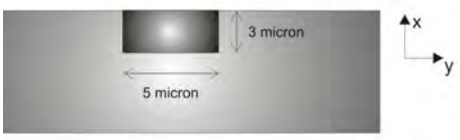

FIGURE 2.18: Waveguide cross-section

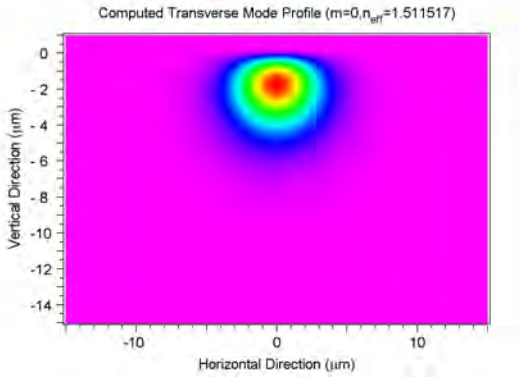

FIGURE 2.19: Waveguide transverse mode profile

The field outputted by the BPM has arbitrary amplitude, it is therefore normalised so that the integral of $|\mathrm{E}|^2$ over the area of the mode distribution in the cross-sectional plane is unity, see Equation 2.13.

$$N_{\mathrm{wg}}^2 \int_x \int_y |\mathrm{E}_{\mathrm{wg}}|^2 \, dx \, dy = 1, \tag{2.13}$$

where E_{wg} is the electric field strength (V/m), and N_{wg} is the waveguide normalisation constant. The sphere WGM's and the waveguide mode field are normalised to allow the subsequent calculation of the WGM's and the waveguide coupling factor.

2.4 Q and its components

The quality factor of the mode describes the relationship between the energy stored (E_s) in the resonator cavity and the energy loss per cycle (E_L), and can be determined from

$$\mathrm{Q} = \frac{2\pi \cdot E_s}{E_L}, \tag{2.14}$$

The relation in Equation 2.14, expresses the fact that the more energy that is lost per cycle, the smaller Q becomes.

The total Quality factor of the system is composed of several loss contributions, which are intrinsic material absorption, scattering loss, surface absorption loss, loss due to the intrinsic radiative loss from WG mode propagation and the external coupling loss. $\mathrm{Q_{ext}}$ is defined as the quality factor that depends on the external coupling loss, this value of Q varies with the separation of the sphere and waveguide, as described in the last section. $\mathrm{Q_{WGM}}$, $\mathrm{Q_{surf}}$ and $\mathrm{Q_{matl}}$ are the Q factors of the system corresponding to the loss due to intrinsic radiative loss from WG mode propagation, material absorption and scattering loss due to surface roughness, respectively, these Q values do not depend on the gap separation of the sphere and waveguide. The total Q is obtained from the relation shown in Equation 2.15 [8].

$$\mathrm{Q}^{-1} = \mathrm{Q}_{\mathrm{WGM}}^{-1} + \mathrm{Q}_{\mathrm{surf}}^{-1} + \mathrm{Q}_{\mathrm{matl}}^{-1} + \mathrm{Q}_{\mathrm{ext}}^{-1}, \tag{2.15}$$

where $\mathrm{Q_{WGM}}$ can be obtained from Equation 2.16 [2].

$$\begin{aligned}
\mathrm{Q_{WGM}} &= \frac{l^2 n_s}{k^3 c\epsilon_o N_s^2 n_o^2 \mathrm{R}_o^5 \mathrm{Z}_o} \\
&\quad \times [n_o \left(\frac{\pi}{\gamma_1}\right)^{1/4} j_l(kn_s\mathrm{R}_o) j_{l+1}(kn_o\mathrm{R}_o) \\
&\quad - n_s \left(\frac{\pi}{\gamma_2}\right)^{1/4} j_{l-1}(kn_s\mathrm{R}_o) j_l(kn_o\mathrm{R}_o)]^{-2}, && \text{(2.16a)} \\
\gamma_1 &= l - \frac{1}{2} - kn_o\mathrm{R}_o \frac{j_l(kn_o\mathrm{R}_o)}{j_{l-1}(kn_o\mathrm{R}_o)} + \frac{(kn_o\mathrm{R}_o)^2}{l}, && \text{(2.16b)} \\
\gamma_2 &= l + \frac{1}{2} - kn_o\mathrm{R}_o \frac{j_{l+1}(kn_o\mathrm{R}_o)}{j_l(kn_o\mathrm{R}_o)} + \frac{(kn_o\mathrm{R}_o)^2}{l}, && \text{(2.16c)}
\end{aligned}$$

Where c is the speed of light in vacuum, ϵ_o is the permittivity in free space, Z_o is the impedance of free space, and N_s is the normalisation constant that was previously obtained in Section 2.2.

Q_{matl} is the quality factor that is associated with the material absorption of the spherical cavity. It can be calculated from the following equation [8].

$$Q_{matl} = \frac{2\pi n_s}{\lambda \alpha_{matl}^{dB}}, \tag{2.17}$$

where α_{matl}^{dB} is the loss in dB per unit length, n_s is the sphere index, and λ is the wavelength.

Q_{surf} is the quality factor that is associated with the surface roughness of the spherical cavity. It can be calculated as follows [8, 9].

$$Q_{surf} = \frac{D\lambda^2}{2L_{corr}\pi^2\sigma^2}, \tag{2.18}$$

where D is the sphere diameter, λ is the wavelength, L_{corr} is the surface correlation length, and σ is the root mean square of the surface roughness.

Figure 2.20 shows the Q_{WGM} as a function of sphere diameter for the spheres of refractive index of 1.51 at the operating wavelength of $\lambda = 750$ nm. It can be seen from Figure 2.20 that, at the operating wavelength of 750 nm, spheres of diameter greater than 10 μm have Q_{WGM} of greater than 10^{11}.

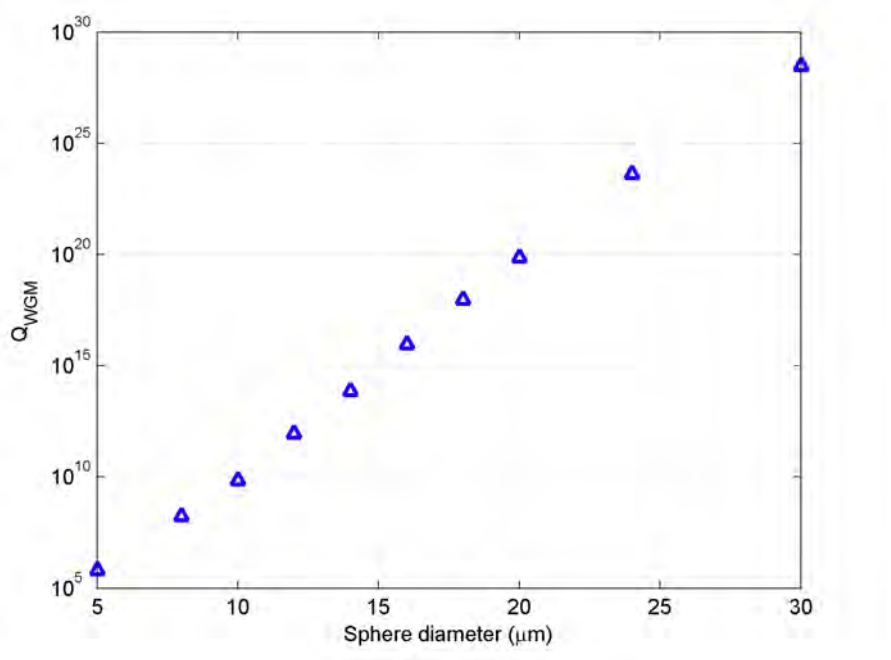

FIGURE 2.20: Q_{WGM} vs sphere diameter, D, for the sphere of refractive index 1.51 at the operating wavelength of $\lambda = 750$ nm

Figure 2.21 shows that for the sphere of refractive index of 1.51 at the operating wavelength of 750 nm, the quality factor due to material loss has value of more than 10^9 with

the value of material loss per unit length ($\alpha_{\text{matl}}^{\text{dB}}$) of less than 10 dB/km. It has been found that the material loss for fused silica is about 5 dB/km at wavelength near 750 nm [9], which corresponds to Q_{matl} of about 10^9.

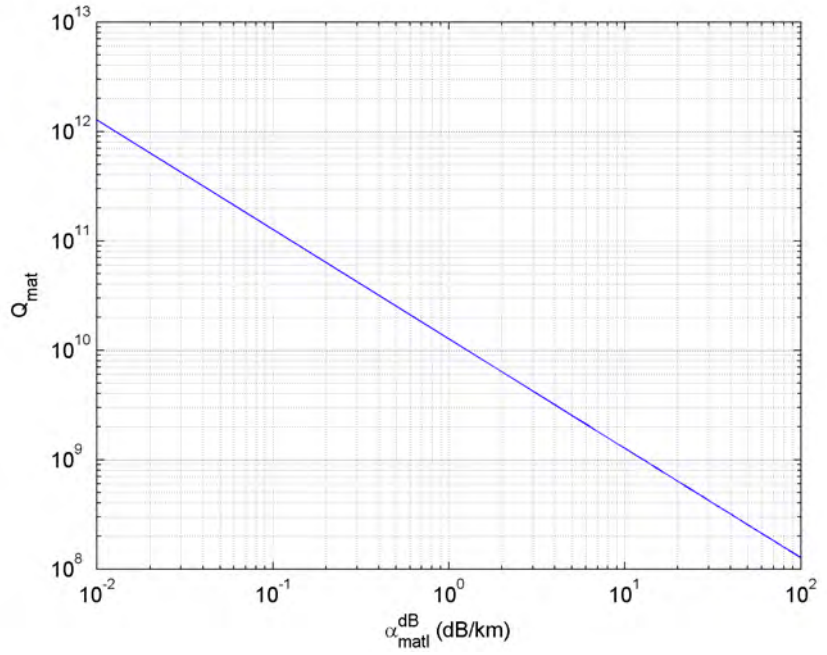

FIGURE 2.21: Q_{matl} vs material loss in dB per unit length, $\alpha_{\text{matl}}^{\text{dB}}$, for the sphere of refractive index of 1.51 at the operating wavelength of $\lambda = 750$ nm

Typical values of the surface correlation length, L_{corr}, and the rms of the surface roughness, σ, are $L_{\text{corr}} \approx 5$ nm and $\sigma \approx 1$ nm, respectively [8–11]. Figure 2.22 shows the plots of Q_{surf} vs surface correlation length, L_{corr}, for a 30 μm diameter sphere at the operating wavelength of $\lambda = 750$ nm. It can be seen that, at the point where $L_{\text{corr}} = 5$ nm and $\sigma = 1$ nm, the quality factor due to the surface roughness is about 1×10^8. It also can be seen that, at the fixed value of L_{corr}, the value of Q_{surf} is greater as σ gets smaller, and vice versa.

Thus, it can be concluded that, for the typical value of roughness for a 30 μm diameter sphere with the index of 1.51 at the operating wavelength of 750 nm, the losses that are associated with Q_{WGM} and Q_{matl} are relatively small compared to the loss that is introduced by the roughness of the sphere. The loss due to the surface roughness is a major loss of the system.

The study of coupling factor and Q_{ext} as a function of gap separation will be explored in the next section.

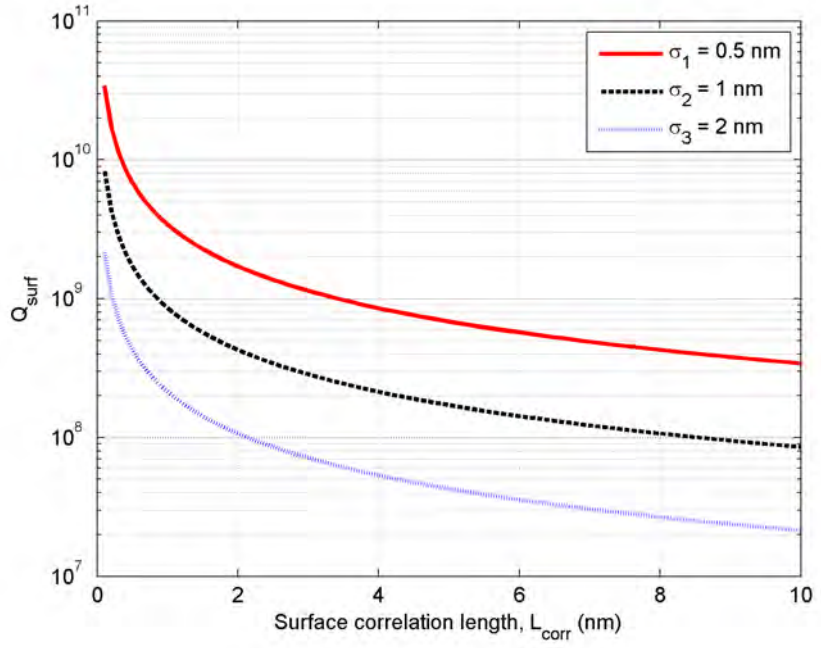

FIGURE 2.22: Q_{surf} vs surface correlation length, L_{corr}, as a function of σ, for a 30 μm diameter sphere at the operating wavelength of $\lambda = 750$ nm

2.5 Determination of coupling factor and Q_{ext}

2.5.1 Introduction

In this section, the evaluation of the cross-coupling factor, κ, through overlap integration of the evanescent field of the waveguide and the field distribution in the sphere will be described, allowing the determination of the coupling strength from a waveguide into a sphere WGM as a function of sphere-waveguide separation. The microsphere resonator is placed on or close to the surface of the waveguide so that WGMs may be evanescently excited.

2.5.2 Method to calculate coupling factor and Q_{ext}

Coupling factor of the system can be determined through the overlap integration of the waveguide field and the field in microsphere resonator. In this chapter, the coupling factors are calculated from the overlap integration between the evanescent fields of the waveguide over the transverse cross-section of the sphere resonator. The transverse plane of the sphere resonator and the transverse plane of the waveguide are defined as the plane that is perpendicular to the direction of the waveguide mode propagation. The field of the sphere resonator is normalised so that the modulus squared of field distribution of the mode integrated over the transverse plane sums to unity. Likewise, the field distribution of the waveguide is normalised so that the integration of $|\mathrm{E_{wg}}|^2$ over the waveguide cross-section is unity. These normalised fields will be denoted as $\tilde{\mathrm{E}}_{\mathrm{sphere}}$ and $\tilde{\mathrm{E}}_{\mathrm{wg}}$, respectively. Figure 2.23 shows the electric field distribution of the fundamental mode of the sphere, as well as the evanescent field of the waveguide in a transverse plane.

The overlap integral of these normalised fields is used to calculate the coupling strength between the waveguide and the sphere. The interaction strength between the waveguide mode and the sphere mode at the minimum separation, K_o, is shown in Equation 2.19 [2].

$$K_o = \frac{\pi}{\lambda n_{\mathrm{eff}}} \int_x \int_y (n_s^2 - n_o^2) \tilde{\mathrm{E}}_{\mathrm{sphere}} \tilde{\mathrm{E}}_{\mathrm{wg}} \, dx \, dy, \tag{2.19}$$

where $\tilde{\mathrm{E}}_{\mathrm{sphere}}$ is the normalised electric fields of the sphere, and $\tilde{\mathrm{E}}_{\mathrm{wg}}$ is the normalised waveguide field. n_{eff} is the effective refractive index of the mode propagating along the waveguide. n_s is the sphere refractive index and n_o is an air index, the term $(n_s^2 - n_o^2)$ indicates that the field overlap outside the sphere is zero.

When light travels into the system along the z direction, there is a phase mismatch due to the difference in velocity of the light propagation in the sphere and the waveguide.

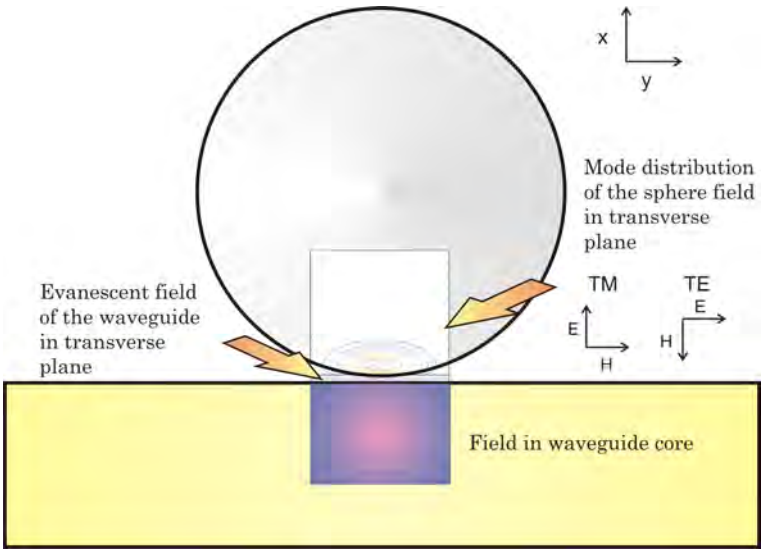

FIGURE 2.23: Electric field distribution of the fundamental mode of the sphere and waveguide

The net coupling amplitude is obtained from integrating K_o along the curved surface of the sphere along the z direction over the entire region of the interaction while taking the phase mismatch into account. Due to the curvature of the sphere, a decrease of the interaction strength between the fields is introduced as the light is travelling away from the minimum separation, the decay constant of the waveguide must be included to obtain a net coupling efficiency. The coupling factor, κ is found from Equation 2.20 [2].

$$\kappa = \left[K_o^2 \frac{2\pi \mathrm{R}_o}{\gamma_{\mathrm{wg}}} \exp\left(\frac{-\mathrm{R}_o \Delta\beta^2}{\gamma_{\mathrm{wg}}} \right) \right]^{1/2}, \tag{2.20}$$

where

$$\Delta\beta = \beta_{\mathrm{wg}} - \frac{m}{\mathrm{R}_o}, \tag{2.21a}$$

$$\gamma_{\mathrm{wg}} = \frac{2\pi}{\lambda} \sqrt{n_{\mathrm{eff}}^2 - n_o^2}, \tag{2.21b}$$

$\Delta\beta$ is the difference in propagation constants. γ_{wg} is the waveguide mode decay constant away from the waveguide surface.

The relationship of the coupling factor and the Quality factor of the system that is due to the coupling to the waveguide, $\mathrm{Q}_{\mathrm{ext}}$, assuming there is no other loss, can be found from Equation 2.22 [2].

$$\mathrm{Q}_{\mathrm{ext}} = \frac{m\pi}{\kappa^2}, \tag{2.22}$$

where m is the sphere mode number in the angular direction and κ^2 is proportional to

the power coupled into the sphere per revolution.

2.5.3 Validation against literature

In this thesis, the Beamprop (BPM) package will be used to obtain the electric fields in the waveguide. To confirm that the modal fields from the BPM package agree with the analytical results obtained from literature [2], the Q_{ext} from the two approaches are compared.

The parameters in the calculation are based on the system coupling from a 5 μm tapered fiber into a sphere resonator of 500 μm in diameter at a wavelength of 1550 nm. The refractive index of the sphere and fiber are 1.45. The intensity of the fundamental mode of a 5 μm diameter fibre was obtained and normalised to unity. Figure 2.24 shows that the Q_{ext} obtained from the two approaches have the same values. The overlap integral of the fibre field and the field in the sphere was carried out. The results in Figure 2.24 show a good agreement on a calculated fiber field from the BPM method and the analytical solutions approach. Thus, the results from Beamprop are reliable and they will be used to describe the field distribution in the waveguide substrate throughout this thesis.

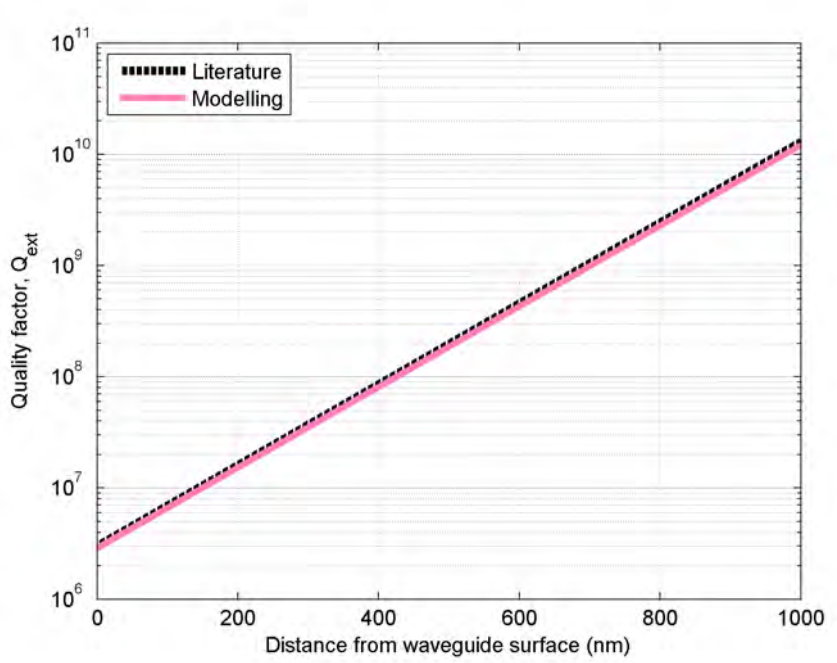

FIGURE 2.24: Comparison of Q_{ext} vs S_o of the literature and modelling results

2.5.4 Q_{ext} as a function of separation between a sphere and a waveguide

As the sphere is placed further away from the waveguide surface, the waveguide evanescent field reaching the sphere is reduced. Figure 2.25 shows the fields of the sphere and the evanescent field of the waveguide as the sphere is placed further away from the waveguide substrate.

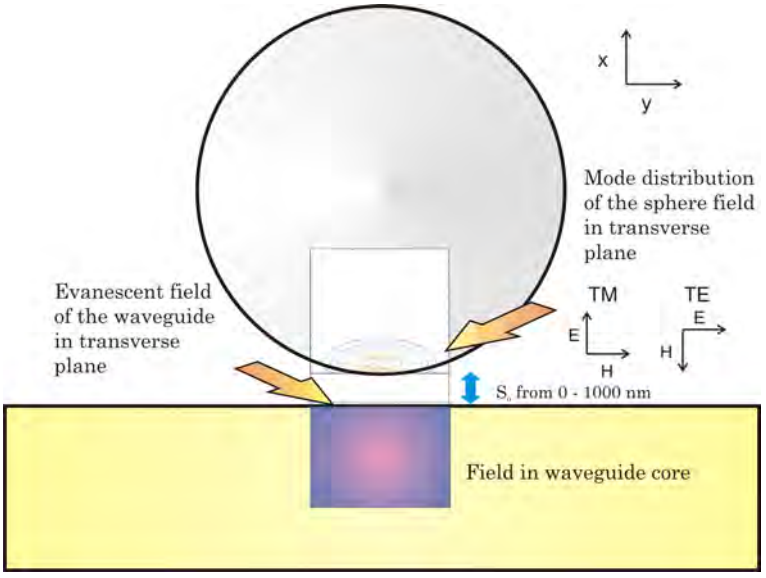

FIGURE 2.25: Electric field distribution of the fundamental mode of the sphere and waveguide

K_o as a function of waveguide-sphere separation can be found from the equation below.

$$K_o(S_o) = \frac{\pi}{\lambda n_{\text{eff}}} \int_x \int_y (n_s^2 - n_o^2) \tilde{\text{E}}_{\text{sphere}} \tilde{\text{E}}_{\text{wg}}(S_o)\, dx\, dy, \tag{2.23}$$

where $\tilde{\text{E}}_{\text{sphere}}$ is the normalised electric fields of the sphere, and $\tilde{\text{E}}_{\text{wg}}(S_o)$ is the normalised waveguide field as a function of gap separation.

Coupling factor as a function of gap separation, $\kappa(S_o)$, is found from Equation 2.24 [2].

$$\kappa(S_o) = \left[K_o^2(S_o) \frac{2\pi \text{R}_o}{\gamma_{\text{wg}}} \exp\left(\frac{-\text{R}_o \Delta\beta^2}{\gamma_{\text{wg}}} \right) \right]^{1/2}, \tag{2.24}$$

Figure 2.26 shows results of K_o as a function of waveguide-sphere separation, S_o, of a 30 μm diameter sphere with refractive index of 1.51 at 750 nm. The calculations are based upon the fundamental mode for both sphere and waveguide. The coupling efficiency decreases exponentially as the distance of the sphere and the waveguide surface, S_o, is increased. The results of the coupling factor as a function of the distance from the waveguide surface are shown in Figure 2.27, with a similar manner to K_o, the graph shows that at the zero separation, the coupling factor has a maximum value, and

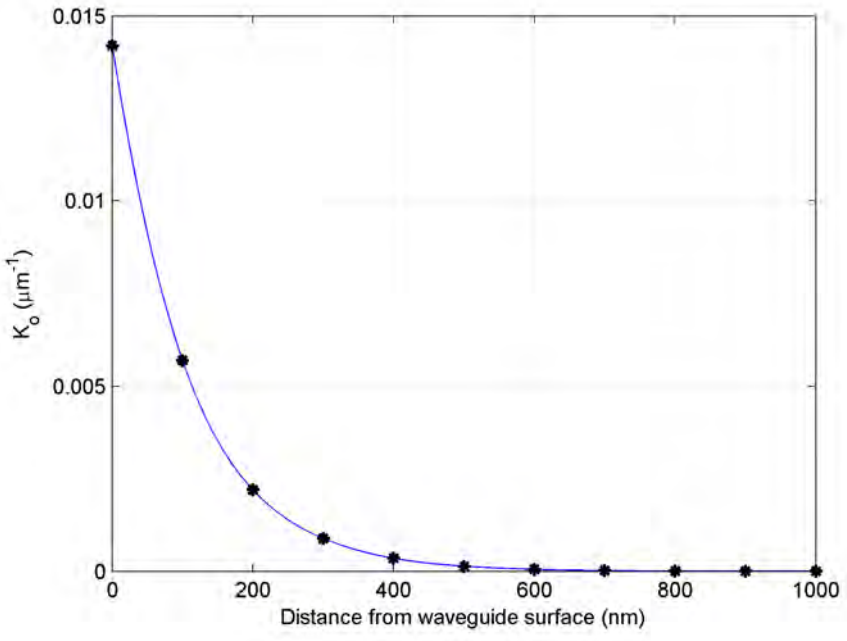

FIGURE 2.26: K_o as a function of gap separation

decreases in fast decay manner as the separation increases toward 1000 nm away from the waveguide surface.

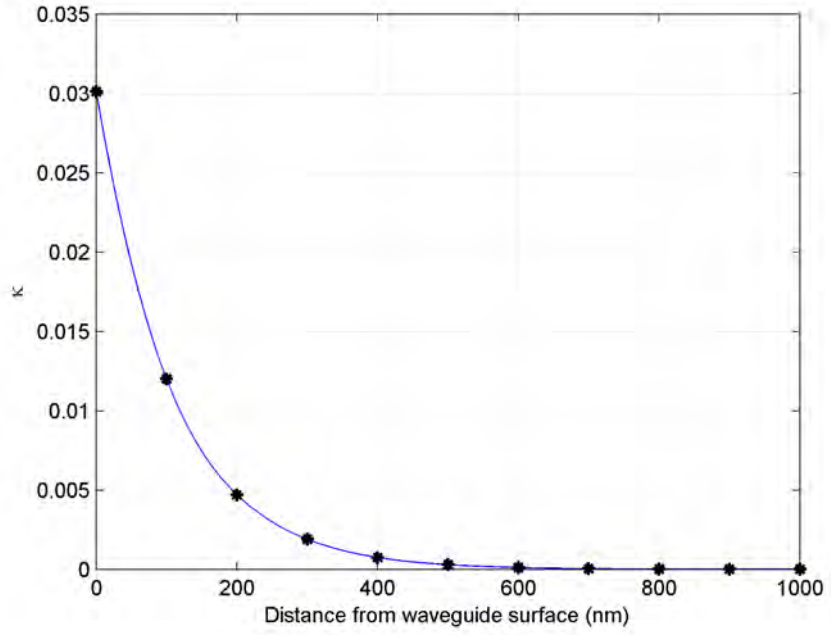

FIGURE 2.27: κ as a function of gap separation, S_o

It is clear that, as expected, the coupling factor is reduced as the sphere is placed at a further distance from the waveguide surface. Q as a function of the separation is shown in Figure 2.28. Q of the system due to the coupling is increasing as the waveguide-

sphere separation, S_o, is increasing. In order to obtain higher Q, the coupling factor of the system must be decreased. It is important to note that if other sources of loss are taken into account, the total Q will be limited to the value of Q of the maximum loss.

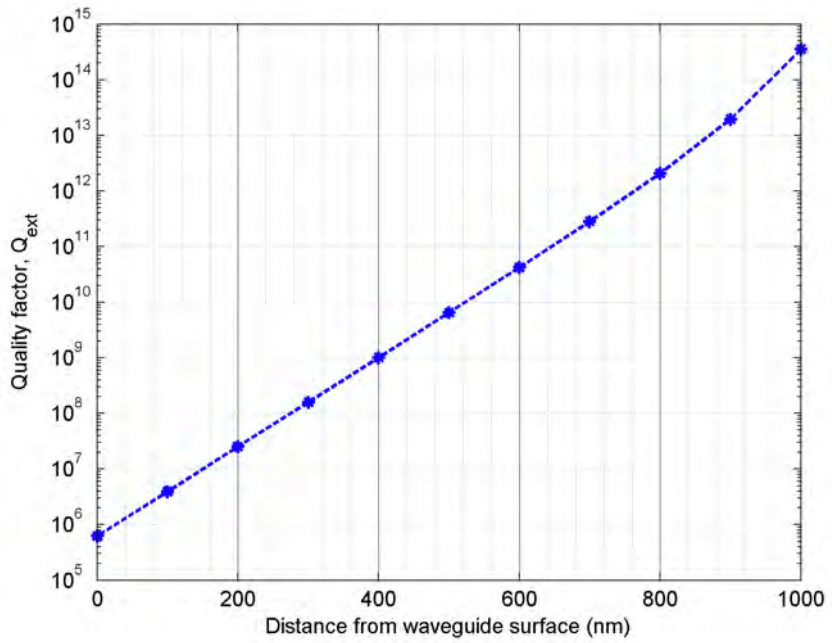

FIGURE 2.28: Q_{ext} as a function of gap separation, S_o

2.5.5 Q_{ext} of various sphere modes

In this section, the quality factors of the waveguide coupled spheres for various mode numbers m and n are determined. Figure 2.29 shows the contour plots in the transverse plane of the waveguide mode and some of the examples of sphere modes, which are a) $n = 1$, $m = l$, b) $n = 2$, $m = l$, c) $n = 1$, $m = l - 1$, and d) $n = 1$, $m = l - 2$, where $l = 180$, $n = 1$ corresponds to $\lambda = 750$ nm, and $n = 2$ to $\lambda = 720$ nm, respectively. Quality factors of these sphere modes are shown in Figure 2.31 and 2.33 as a function of waveguide-sphere separation. The resultant Q of the system of other degenerate modes is plotted in Figure 2.31. It can be seen that the fundamental mode in an angular direction ($|m| = l$) has a highest field overlap, resulting in low Q, while the other modes in the angular direction ($|m| \neq l$) have a relatively high Q compared to the fundamental mode. These results can simply be explained by observing the variation of the field overlap of the sphere mode and the waveguide field, where the fundamental mode has the highest overlap.

When $m = l - (2n + 1)$, where $n = 0, 1, \ldots, l/2$, the modes that are asymmetrical in amplitude are obtained. It is very obvious to observe that, in an ideal case, these "asymmetric" modes have zero coupling efficiency, due to the field maxima and minima

in the overlap integral cancelling. Accordingly, the Q value of the system is unmeasurable using this evanescent excitation configuration.

When $m = l-(2n)$, where $n = 1, 2, \ldots, l/2$, the modes that are symmetrical in amplitude are obtained. In these cases, the field maxima of the main lobe have a smaller field distribution compared to the fundamental mode ($m = l$). Thus, the overlap of the fields of these modes is less (see Figure 2.30), consequently, Q of the systems for these configurations are higher.

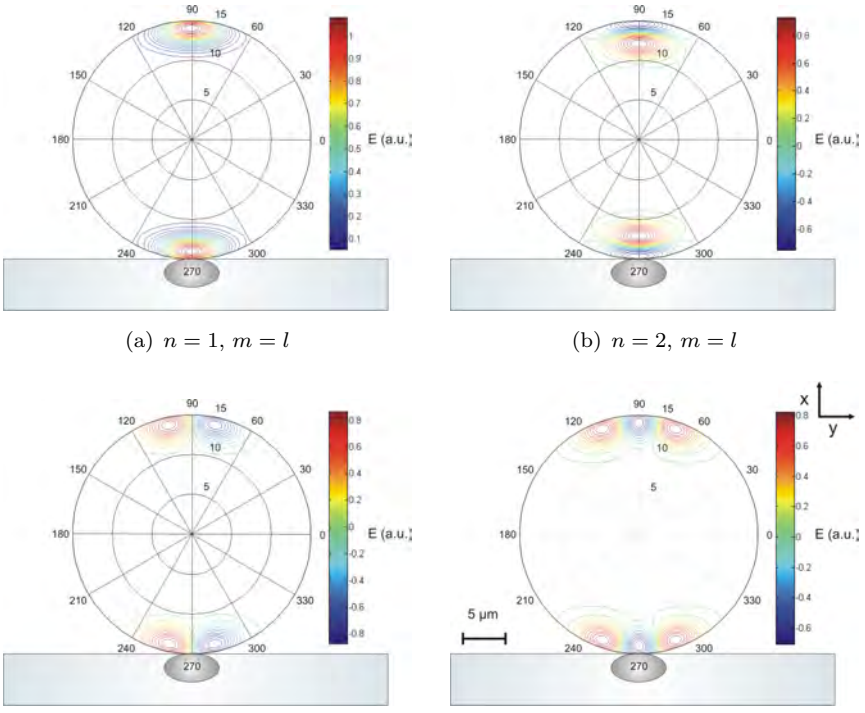

(a) $n = 1$, $m = l$ (b) $n = 2$, $m = l$

(c) $n = 1$, $m = l - 1$ (d) $n = 1$, $m = l - 2$

FIGURE 2.29: Sphere resonator of 30 μm in diameter with different mode numbers

The Q of the waveguide-sphere system for the different radial order modes is now considered. The fundamental mode in the radial direction ($n = 1$) has a higher field overlap with the evanescent field of the waveguide due to the fact that the field of the main lobe is extended more to the sphere interface. As n increases, the main lobe moves toward the centre of the sphere, the higher Q is obtained due to weaker coupling with the waveguide. The coupling factor of the fundamental mode ($n = 1$) and the next high order mode in the radial direction ($n = 2$) of the field is plotted in Figure 2.32, and the Q-factor of the system with a different sphere mode number n is shown in Figure 2.33. Coupling factor, κ, of the radial fundamental mode is greater than κ of $n = 2$, Q of the fundamental mode is lower than Q of $n = 2$, as expected.

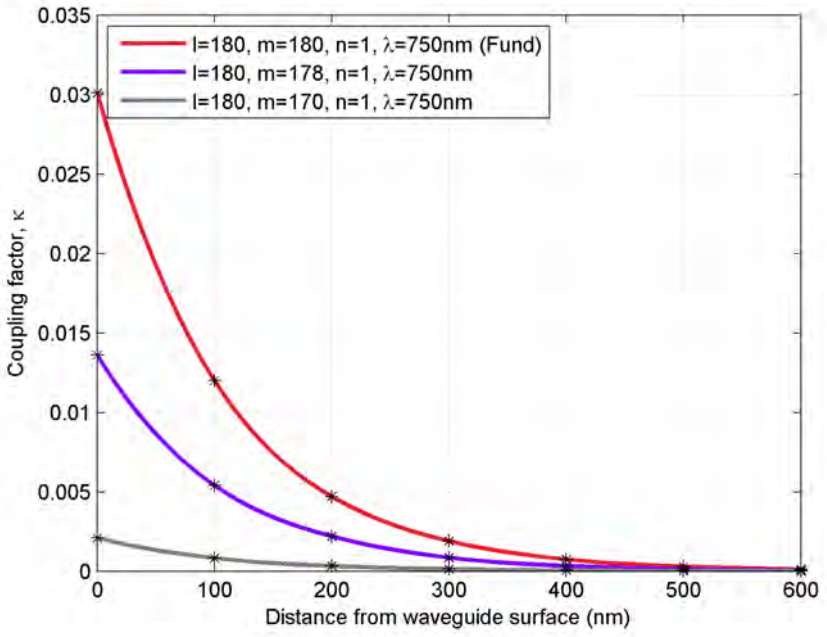

FIGURE 2.30: κ vs S_o of sphere of fundamental ($m = l = 180$) and higher order angular modes ($m = 178, 170$)

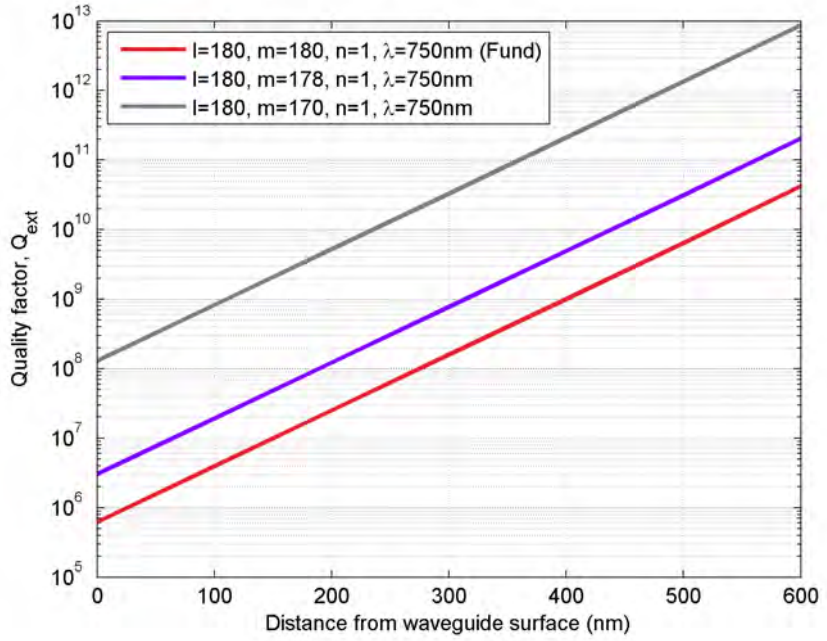

FIGURE 2.31: Q vs S_o of sphere of fundamental ($m = l = 180$) and higher order angular modes ($m = 178, 170$)

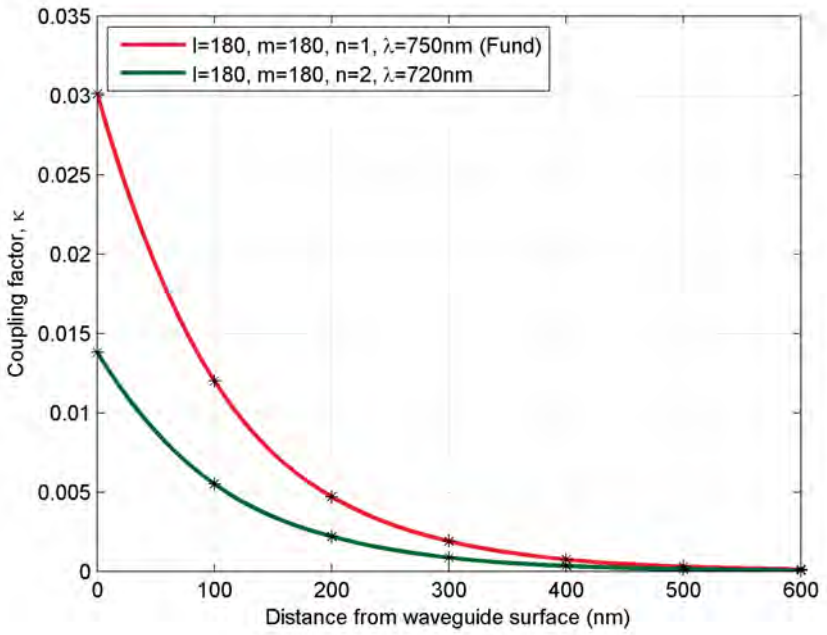

FIGURE 2.32: κ vs S_o of sphere of fundamental and higher order radial modes (n=1,2)

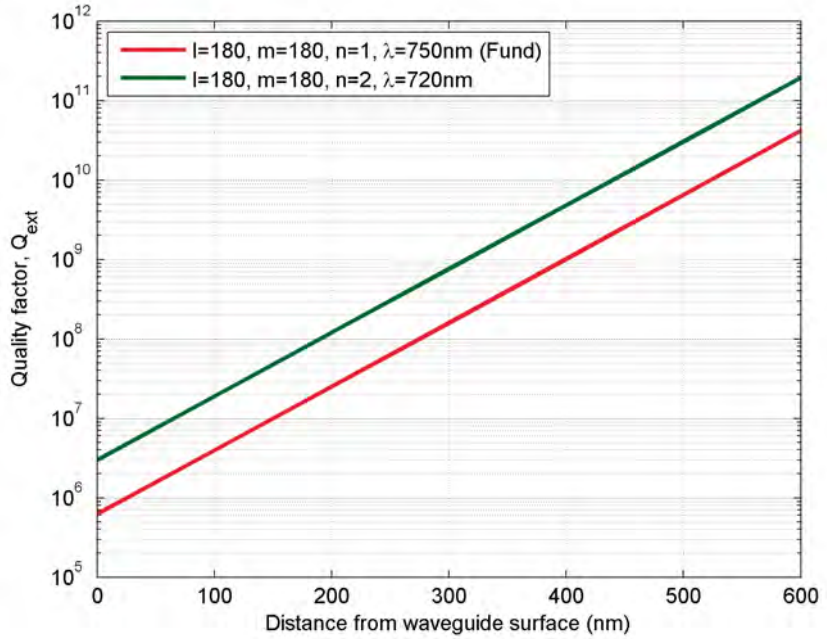

FIGURE 2.33: Q vs S_o of sphere of fundamental and higher order radial modes (n=1,2)

2.5.6 Q_{ext} as a function of sphere index

The determination of the Q_{ext} as a function of sphere refractive index, n_s, is described in this section. Sphere index is varied from 1.3 - 2.4, while the waveguide index is chosen to be 1.51. When the sphere index is changed, in order to obtain the fundamental WGM at the same operating wavelength of 750 nm, the value of l must be adjusted to satisfy the characteristic equation. In this model, the fundamental modes of a sphere of 30 μm diameter are calculated. The values of l were obtained according to each sphere index and are shown in the following table, along with the deduced coupling factors for a zero separation from the waveguide surface.

Sphere index, n_s	Sphere mode number l	Coupling factor, κ
1.3	155	4.0617×10^{-4}
1.4	167	0.0059
1.51	180	0.0301
1.6	190	0.0285
1.8	215	0.0070
1.9	228	7.3307×10^{-4}
2.0	240	2.0533×10^{-5}
2.2	265	7.6416×10^{-10}
2.4	290	3.7280×10^{-16}

TABLE 2.3: Values of sphere mode number l and corresponding κ with different sphere index ($m = l$, $n = 1$)

Figure 2.34 shows the results for Q_{ext} as a function of the sphere index with different gap separations between the sphere and waveguide, which are S_o= 0 nm, 100 nm and 300 nm. The system with the higher separation exhibits higher Q, while at the zero separation Q of the system is at the lowest, as described in Section 2.5.4. At the points where the difference in refractive index of the sphere and the waveguide are relatively large, Q of the system is large. This is because there is less interaction between the two fields. At the points where the Q of the system becomes large, where n_s is less than 1.3 and greater than 1.8, the corresponding coupling factors are relatively small, see Table 2.3.Thus, it can be concluded that in order to obtained the maximum coupling strength (Q is minimum), the index of the designed devices must be matched. However, these values will be limited by the Q limiting described in Section 2.4, depending upon the dominant loss mechanism.

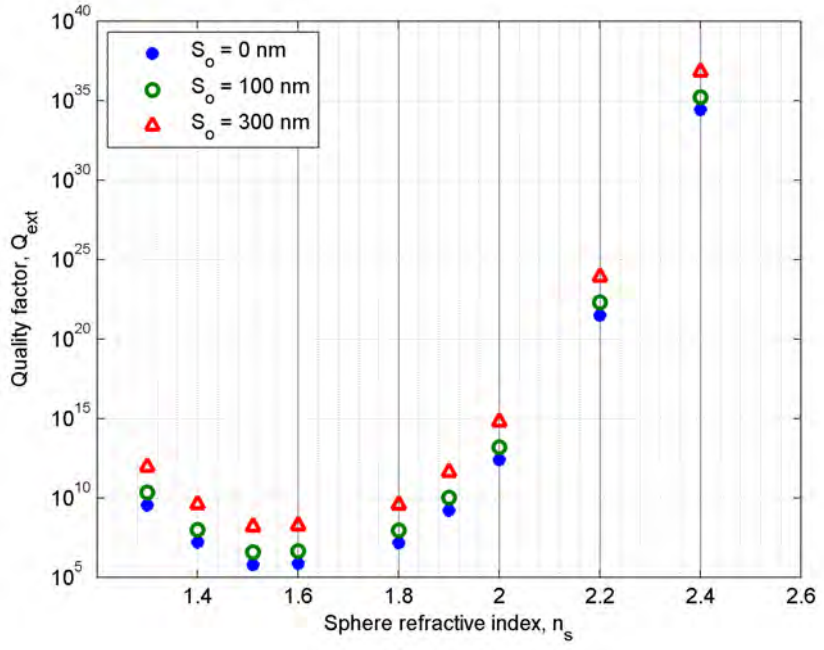

FIGURE 2.34: Q as a function of sphere index with three different value of gap separation ($S_o = 0, 100, 300$ nm), $n_{\text{wg}} = 1.51$

2.5.7 Q_{ext} as a function of waveguide width and height

In this section, the variation of Q_{ext} with waveguide size and structure is described. The fundamental WGM of a sphere of 30 μm diameter and a refractive index of 1.51, which corresponds to the sphere number (l, m, n) of (180,180,1) and $\lambda = 750$ nm, is used in this calculation. The refractive index of the waveguide is 1.51. The waveguide width is varied from 3 μm to 7 μm with 1 μm increments, while the waveguide height (or depth) is 3 μm. Figure 2.35 shows the results of the Q factor as a function of waveguide width with three different values of gap separation between the waveguide and the sphere ($S_o = 0, 100, 300$ nm).

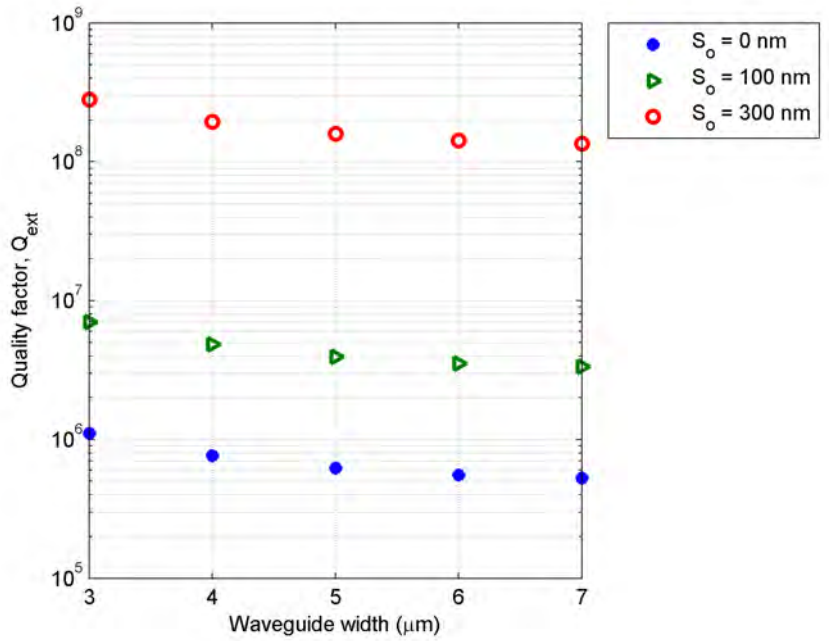

FIGURE 2.35: Q as a function of waveguide width with three different values of $S_o = 0, 100, 300$ nm of a 30 μm diameter sphere with a refractive index of 1.51

As the width of the waveguide is increasing, Q factor is decreasing, because the coupling strength increases as the width increases as the field overlap increases, and the waveguide width increases. Table 2.4 shows the variation of κ as a function of waveguide width with three different value of S_o.

Waveguide width (μm)	$\kappa@S_o = 0$ nm	$\kappa@S_o = 100$ nm	$\kappa@S_o = 300$ nm
3	0.0226	0.0090	0.0014
4	0.0272	0.0108	0.0017
5	0.0301	0.0120	0.0019
6	0.0319	0.0127	0.0020
7	0.0328	0.0130	0.0020

TABLE 2.4: Values of κ as a function of waveguide width with three different values of $S_o = 0, 100, 300$ nm of a 30 μm diameter sphere with a refractive index of 1.51

Figure 2.36 shows the field amplitude of the waveguide mode of three waveguides, with the values of width of 3, 5 and 7 μm. It can be confirmed from Figure 2.36 that the field at the waveguide surface (located at x = 0) of the 7 μm wide waveguide is greater than the one with 3 μm width. This is because the peak field in the waveguide core is pushed toward the substrate in an asymmetrical manner as the width of the waveguide is smaller, so that the field outside the waveguide is lower, resulting in low coupling efficiency and high Q.

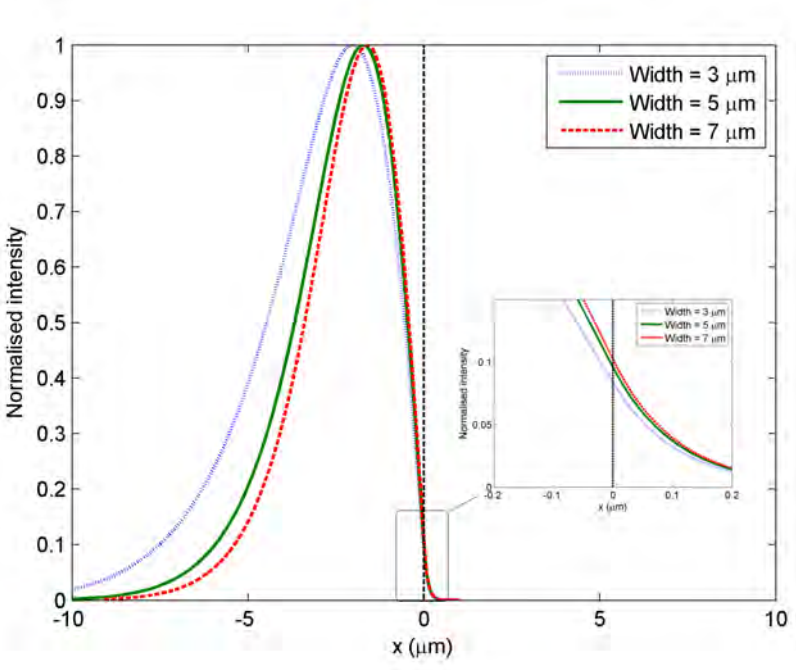

FIGURE 2.36: Normalised intensity distribution in the depth direction at the centre of the waveguide (at y = 0) for waveguide widths of 3, 5 and 7 μm, waveguide height of 3 μm, at λ = 750 nm. Inset: Normalised intensity distribution at waveguide surface

The calculation of Q as a function of the waveguide height (or depth) is also described in this section. The sphere that has a diameter of 30 μm and refractive index of 1.51 at $\lambda = 750$ nm, is used in the calculation. Figure 2.37 and Figure 2.38 show the results of the κ and Q_{ext} as a function of the waveguide height with three different values of waveguide-sphere separation of $S_o = 0, 100, 300$ nm, respectively.

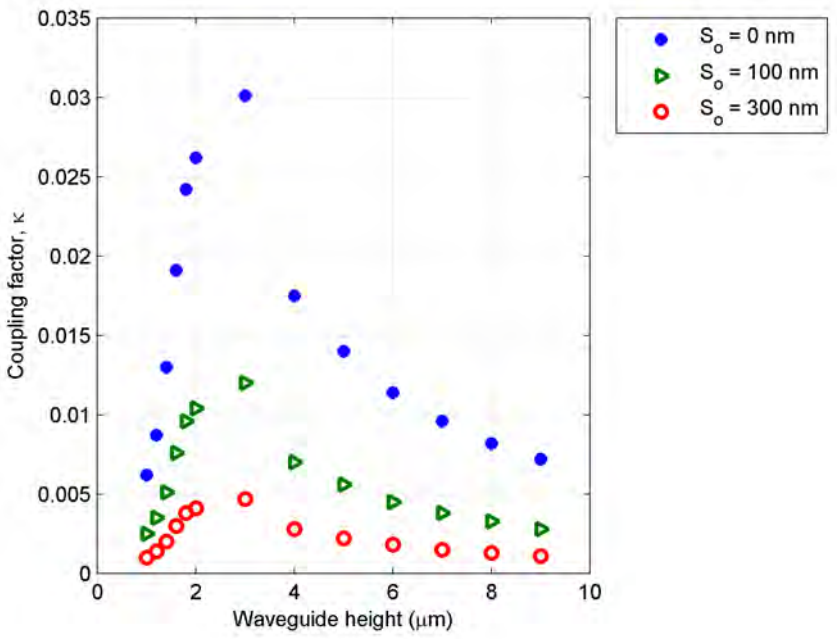

FIGURE 2.37: κ as a function of waveguide height with three different values of $S_o = 0, 100, 300$ nm, of a 30 μm diameter sphere with refractive index of 1.51 at $\lambda = 750$ nm

Figure 2.37 shows that, at a waveguide height of 3 μm, κ is maximum, as waveguide height becomes larger, the coupling is less, and as the waveguide height is reduced to 1 μm, the coupling is reduced. Figure 2.38 shows that at a waveguide height of 3 μm Q is at minimum, and it increases as the waveguide height increases, because the field overlap is less. Since, when the waveguide depth becomes small, the mode will be weakly confined within the core of the waveguide, resulting in less coupling factor or high Q. At the large depth, Q is significantly higher than at the smaller depth because the field is pulled down towards waveguide substrate as the height is increasing, as can be seen from Figure 2.39, where the field at the centre of the waveguide (when y = 0) of the 3 μm-depth waveguide is greater than the 7 μm depth.

The coupling factor and quality factor of the systems are calculated. The theoretical approach used in this work is found to be correlated with the model in literature. These calculated values of coupling and quality factors are useful for the calculation in the next section, where the information of the coupling factors is required to obtain the power-transfer function.

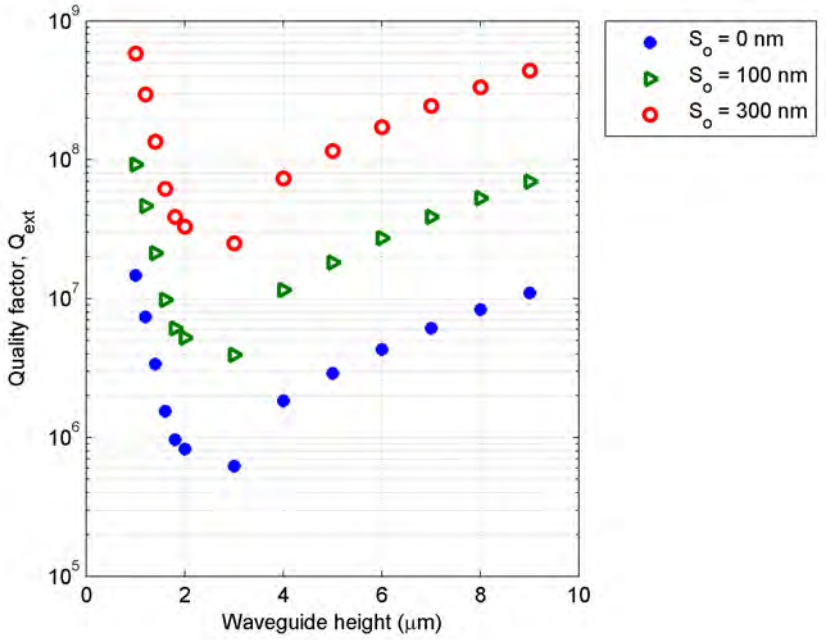

FIGURE 2.38: Q as a function of waveguide height with three different values of $S_o = 0, 100, 300$ nm, of a 30 μm diameter sphere with a refractive index of 1.51 at $\lambda = 750$ nm

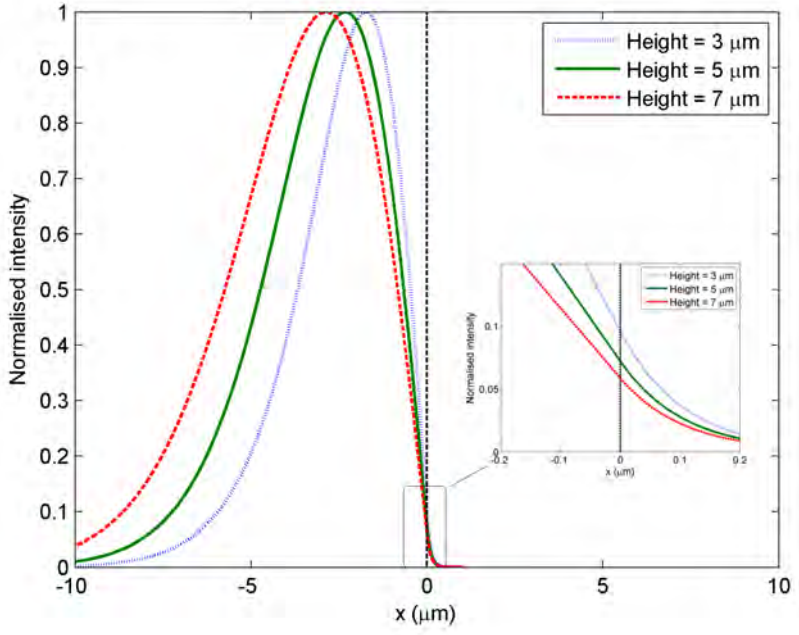

FIGURE 2.39: Normalised intensity distribution in the depth direction at the centre of the waveguide (at y = 0) for waveguide height of 3, 5 and 7 μm, waveguide width 5 μm, at $\lambda = 750$ nm. Inset: Normalised intensity distribution at waveguide surface

2.6 System power-transfer functions

In this section, the power in the sphere and the power transmitted past the sphere will be obtained from the power transfer functions. The transmittance and circulating power spectra will be shown and discussed in this chapter. κ that is used in this section is obtained from the previous section by the overlap integration method.

The power-transfer characteristics of the waveguide coupler and the microsphere resonator can be calculated using the unidirectional coupling method [12–15]. The method mainly depends upon two important coefficients; see Figure 2.40, the transmission coefficient, t, and the cross-coupling factor, κ, as calculated in Section 2.5.2. It is important to note in Figure 2.40 that t^* and κ^* are the complex conjugates of the transmission coefficient, t, and the cross-coupling factor, κ, respectively. Coefficients a_1, a_2, b_1 and b_2 are the field amplitudes that correspond to the incident field in the waveguide, the field that circulates along the sphere resonator, the field at the drop port of the waveguide, and the incident field to the sphere resonator, respectively.

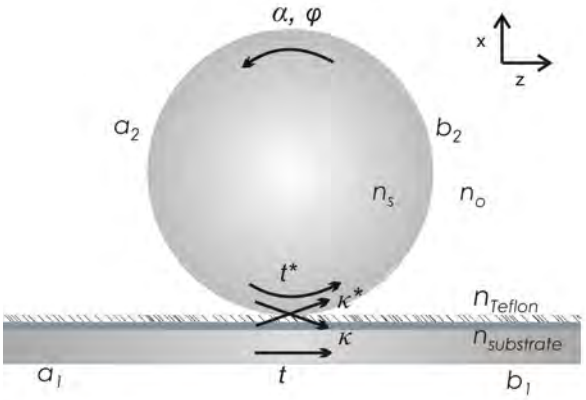

FIGURE 2.40: Cross-coupling factor and transmission coefficients

The transmission coefficient is the parameter that determines the transmission of the field through the waveguide from the region before to the region after the coupling region. The cross-coupling factor is the parameter that determines the coupling factor of the field from the waveguide to the sphere resonator, see Figure 2.40. The coupling matrix that relates these coefficients to the input and the output electromagnetic fields is shown in Equation 2.25 [14].

$$\begin{vmatrix} b_1 \\ b_2 \end{vmatrix} = \begin{vmatrix} t & \kappa \\ -\kappa^* & t^* \end{vmatrix} \cdot \begin{vmatrix} a_1 \\ a_2 \end{vmatrix}, \tag{2.25}$$

From energy conservation,

$$1 = |t|^2 + |\kappa|^2, \tag{2.26}$$

$$a_2 = \alpha \cdot e^{i\varphi} b_2, \tag{2.27}$$

The transmission coefficient, t, can be expressed as,

$$|t| = \sqrt{1 - |\kappa|^2}, \tag{2.28}$$

and, α is the inner circulation factor in the cavity, which can be described by Equation 2.29.

$$\alpha = 1 - \pi \mathrm{R}_o(\alpha_{\mathrm{surf}} + \alpha_{\mathrm{matl}} + \alpha_{\mathrm{WGM}}), \tag{2.29}$$

where α_{surf}, α_{matl}, α_{WGM} are the material, surface scattering and the curvature loss per unit length of the sphere. α_{WGM} is negligibly small for the sphere size of about 15 times greater than the wavelength of operation [8]. The surface scattering loss in dB per unit length is the dominant loss in the cavity, it can be defined as,

$$\alpha_{\mathrm{surf}}^{\mathrm{dB}} = \frac{2\mathrm{L}_{\mathrm{corr}}\pi^2\sigma^2}{\mathrm{D}\lambda^2} \cdot \frac{2\pi n_s}{\lambda}, \tag{2.30}$$

where $\mathrm{L}_{\mathrm{corr}}$ and σ are defined in Section 2.4.

The power-transfer functions for transmission through the waveguide and the total circulating power inside the resonator cavity are described in the following equations.

$$\frac{\mathrm{P}_t}{\mathrm{P}_i} = \left|\frac{b_1}{a_1}\right|^2 = \frac{\alpha^2 - 2\alpha|t|\cos(\varphi) + |t|^2}{1 - 2\alpha|t|\cos(\varphi) + \alpha^2|t|^2}, \tag{2.31a}$$

$$\frac{\mathrm{P}_r}{\mathrm{P}_i} = \left|\frac{a_2}{a_1}\right|^2 = \frac{\alpha^2(1 - |t|^2)}{1 - 2\alpha|t|\cos(\varphi) + \alpha^2|t|^2}, \tag{2.31b}$$

where P_i is the waveguide input power, P_t is the power at the waveguide through port, P_r is the circulating power inside the sphere cavity and φ is the circulation phase shift. The circulation phase shift can be obtained from the equation shown below [13].

$$\varphi = \frac{2\pi^2 \mathrm{D} n_{\mathrm{eff}}}{\lambda}, \tag{2.32}$$

where D is the sphere diameter and n_{eff} corresponds to the effective refractive index of the WGM.

At the resonant wavelengths the phase factor, φ, equals $2\pi l$, where l is an integer value, thus the power-transfer functions for transmission through the waveguide and the total circulating power inside the resonator cavity become,

$$\frac{\mathrm{P}_t}{\mathrm{P}_i} = \left|\frac{b_1}{a_1}\right|^2 = \frac{(\alpha - |t|)^2}{(1-\alpha|t|)^2}, \tag{2.33a}$$

$$\frac{\mathrm{P}_r}{\mathrm{P}_i} = \left|\frac{a_2}{a_1}\right|^2 = \frac{\alpha^2(1-|t|^2)}{(1-\alpha|t|)^2}. \tag{2.33b}$$

The ratio of P_r and P_i can be defined as an enhancement factor, ϵ, which can be expressed as follows:

$$\epsilon = \frac{\mathrm{P}_r}{\mathrm{P}_i}. \tag{2.34}$$

Figure 2.41 shows the plots of enhancement factor, ϵ, as a function of coupling factor, where circulating loss factor, α, is varied from 0.9 to 0.9946.

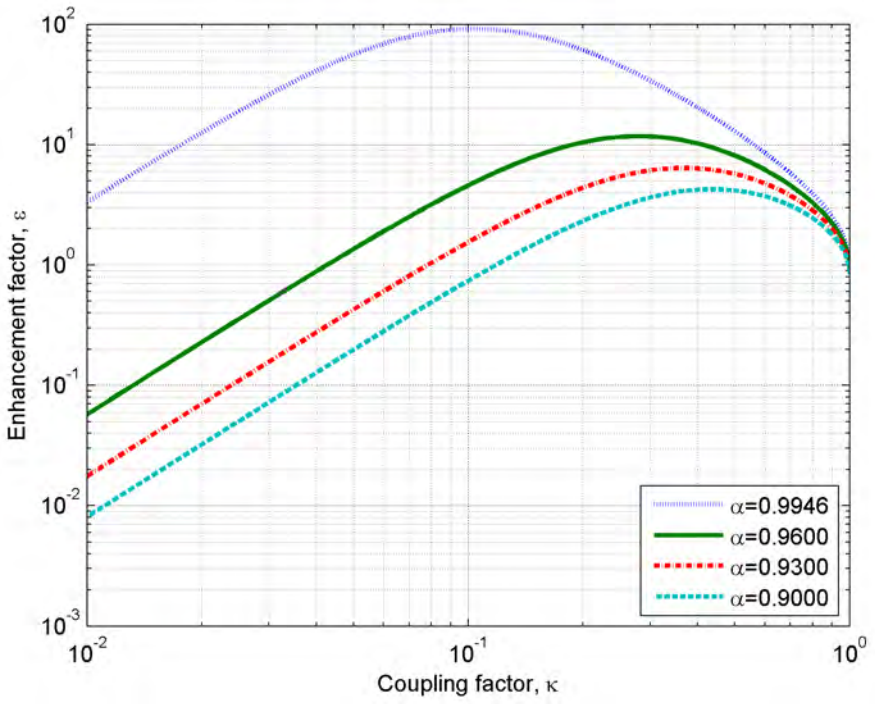

FIGURE 2.41: Enhancement factor vs κ as a function of α from 0.9 to 0.9946

It can be seen that in the low loss system, where the α is 0.9946, the enhancement factor is larger than the high loss case, where $\alpha = 0.9$. In the low coupling factor regime, the enhancement factor increases as κ increases. At the critical coupling, where $|\kappa| = \sqrt{1-|\alpha|^2}$, the enhancement factor is at a maximum, and lastly, at the higher

coupling regime, the enhancement factor decreases as κ increases. This indicates that the maximum power in the sphere is obtained at the critical coupling point.

The important parameters observed from Figure 2.42 are the widths of the resonator mode at the full-width at half maximum ($\delta\lambda_{\mathrm{FWHM}}$) and the Quality factor (Q-factor). The Q-factor of a resonator is a measurement of the sharpness of the resonance, defined as the time averaged stored energy per optical cycle divided by power loss. Q and $\delta\lambda_{\mathrm{FWHM}}$ can be calculated by using the following equations [15]:

$$\mathrm{Q}_{\mathrm{total}} = \frac{\pi^2 \mathrm{D} n_{\mathrm{eff}}}{\lambda} \cdot \frac{\sqrt{\alpha t}}{(1-\alpha t)}, \tag{2.35a}$$

$$\delta\lambda_{\mathrm{FWHM}} = \frac{\lambda^2}{\pi^2 \mathrm{D} n_{\mathrm{eff}}} \cdot \frac{(1-\alpha t)}{\sqrt{\alpha t}}, \tag{2.35b}$$

$\mathrm{Q}_{\mathrm{total}}$ is the actual Q of a resonator which can be calculated from the coupling loss and the total loss within the cavity (see Equation 2.36).

$$\frac{1}{\mathrm{Q}_{\mathrm{total}}} = \frac{1}{\mathrm{Q}_{\mathrm{ext}}} + \frac{1}{\mathrm{Q}_o}, \tag{2.36}$$

where $\mathrm{Q}_{\mathrm{ext}}$ is the external quality factor that is associated with the loss due to coupling, Q_o is the intrinsic quality factor of the isolated sphere associated with the absorption loss of the material of the cavity. $\mathrm{Q}_{\mathrm{ext}}$ and Q_o can be calculated as shown in Equation 2.37a and 2.38a, respectively.

$$\mathrm{Q}_{\mathrm{ext}} = \frac{\pi^2 \mathrm{D} n_{\mathrm{eff}}}{\lambda(1-|t|)}, \tag{2.37a}$$

$$\delta\lambda_{\mathrm{FWHM\,(ext)}} = \frac{\lambda^2}{\pi^2 \mathrm{D} n_{\mathrm{eff}}} \cdot (1-|t|), \tag{2.37b}$$

$$\mathrm{Q}_o = \frac{\pi^2 \mathrm{D} n_{\mathrm{eff}}}{\lambda(1-|\alpha|)}, \tag{2.38a}$$

$$\delta\lambda_{\mathrm{FWHM}(o)} = \frac{\lambda^2}{\pi^2 \mathrm{D} n_{\mathrm{eff}}} \cdot (1-|\alpha|), \tag{2.38b}$$

where D is the sphere diameter, α is the circulation loss factor and t is the transmission coefficient. In this chapter the results comparison will be made mainly on the calculated parameters which are based upon the coupling loss.

In order to obtain the power-transfer functions for transmission through the waveguide and the total circulating power inside the resonator cavity plots, the transmission coefficient, t, and the circulation loss factor in the spherical cavity, α, must be identified. By performing the overlap integration described in Section 2.5.2, the values of coupling factor, κ, are obtained. The corresponding transmission coefficient, t, can be calculated using equation 2.28 ($|t| = \sqrt{1 - |\kappa|^2}$). α is obtained from Equation 2.29, in this section α is arbitrary and is chosen to be 0.90. At the zero separation between the waveguide surface and the sphere resonator (i.e. $S_o = 0$ nm) where Q due to the coupling is dominant, for a sphere resonator of 30 μm in diameter and a refractive index of 1.51, the value of the coupling factor, κ is 0.0301, yielding a transmission coefficient, t, of 0.9995.

Figure 2.42 shows the plots of transmission and circulating power when input power is unity, as a function of wavelength.

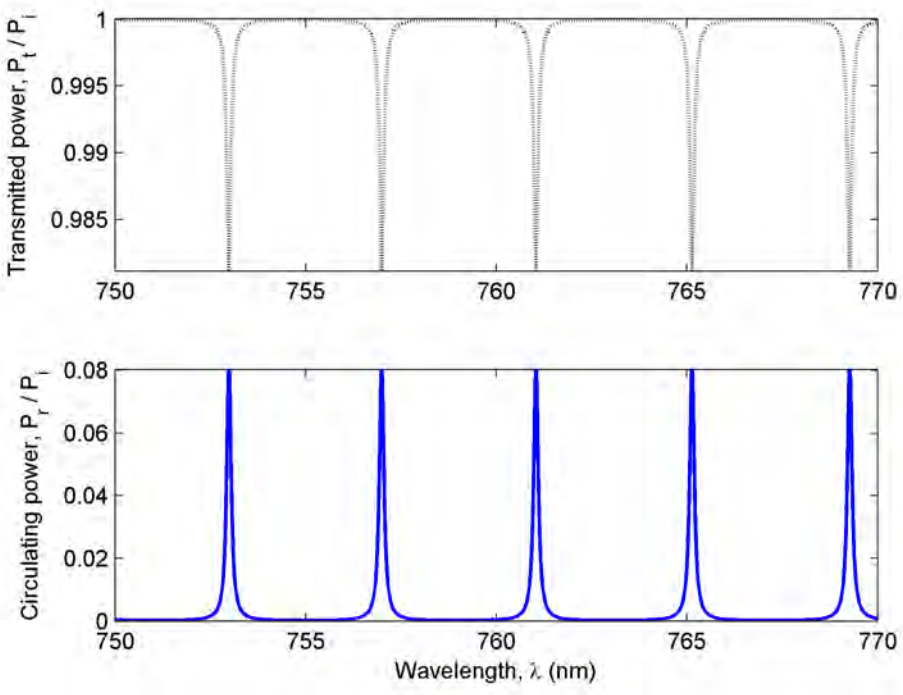

FIGURE 2.42: Transmission and circulating powers as a function of wavelength for a 30μm diameter microsphere with index of 1.51 at zero separation from the waveguide surface, $\kappa = 0.0301$ and $\alpha = 0.90$

It can be seen from Figure 2.42 that the resonant wavelengths are located at 752.98 nm, 756.99 nm, 761.04 nm, 765.13 nm, and 769.27 nm. The resonant wavelength separation between two consecutive resonances is found to be 4.07±0.002 nm at $\lambda = 761$ nm. This peak separation can be defined as a free spectral range, FSR, and it can be expressed as follows [14]:

$$\mathrm{FSR} = \frac{\lambda^2}{\pi n_{\mathrm{eff}} \mathrm{D}}, \tag{2.39}$$

where D is the sphere diameter. FSR is inversely proportional to the sphere diameter, a smaller sphere cavity yields a larger free spectral range, see Equation 2.39. Figure 2.43 shows the free spectral range as a function of sphere diameter for a sphere that has a refractive index of 1.51, note that for the simplification, n_{eff} is chosen to be 1.51.

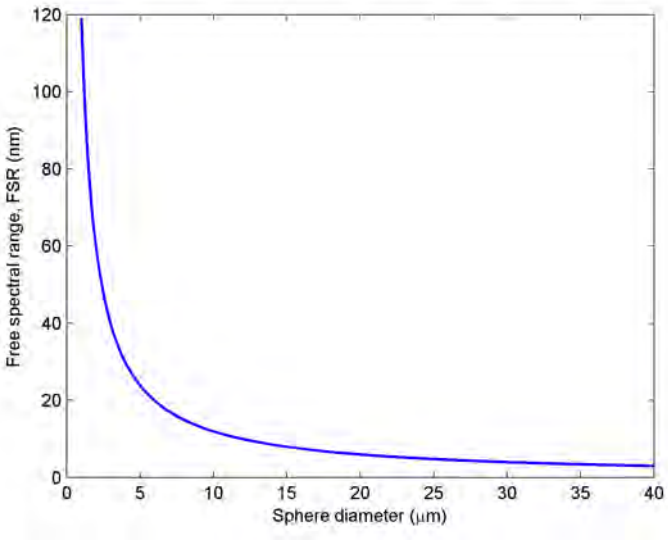

FIGURE 2.43: Free spectral range as a function of sphere diameter ($\lambda = 750$ nm)

It can be seen from Figure 2.43 that, for the sphere of 30 μm in diameter, FSR has the value of about 4 nm. The calculated values of Q_{ext} and $\delta\lambda_{FWHM(ext)}$ are found to be $Q_{ext} = 5.6 \times 10^3$ and $\delta\lambda_{FWHM(ext)} = 0.13$ nm at $\lambda = 753$ nm, respectively.

From this point until the end of this chapter, the discussion and the comparison will be made based upon the parameters obtained from the total losses associated with the systems. The assumption for the total circulating loss in the cavity for a lossless case is made, the value of $\alpha = 0.99999 \sim 1$ will be used. Q as function of various parameters, such as sphere diameter, circulation loss factor, α, transmission coefficient, t, and coupling factor, κ, will be explored.

First, by substituting the value of κ from Equation 2.26 and $\alpha = 0.99999 \sim 1$ into Equation 2.35a, Q can be plotted as a function of sphere diameter with three different values of cross-coupling factor, $\kappa = 0.0301$,0.0136 ,0.0054 and $\kappa = 0.0019$, 8.54×10^{-4}, 3.37×10^{-4}, at the gap separation of 0 and 300 nm, as shown in Figure 2.44 a) and b), respectively. These values of κ correspond to the 30 μm diameter sphere with the index of 1.51 at the operating wavelength of 750 nm with the mode numbers l, m, n of $(180, 180, 1)$, $(180, 178, 1)$, $(180, 176, 1)$, respectively, see Table 2.5, that are obtained from the field distributions of the different modes that vary in angular and azimuthal dependency.

From Figure 2.44, it can be seen that the smaller spheres have lower Q compared to the larger spheres.

Sphere mode number l, m, n	κ @ $S_o = 0$ nm	κ @ $S_o = 300$ nm
180,180,1	0.0301	0.0019
180,178,1	0.0136	8.54×10^{-4}
180,176,1	0.0054	3.37×10^{-4}
180,174,1	0.0027	1.68×10^{-4}
180,180,2	0.0138	8.64×10^{-4}

TABLE 2.5: κ with various sphere mode numbers l, m, n for zero and 300 nm separations

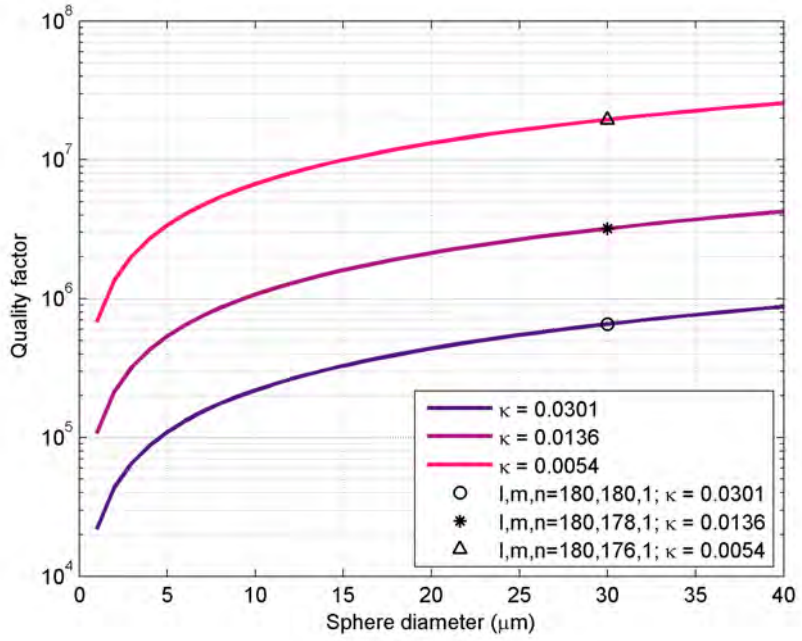

a)

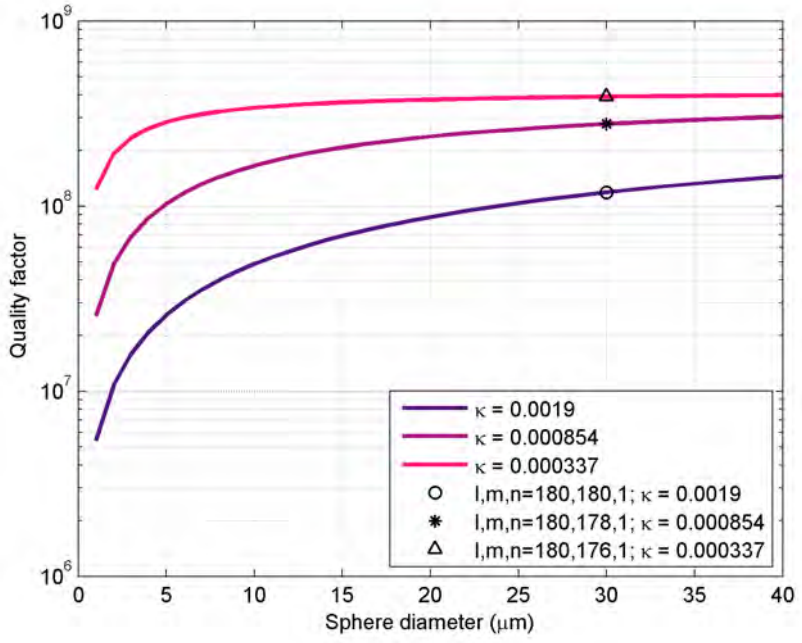

b)

FIGURE 2.44: Quality factor as a function of sphere diameter for different modes in angular and azimuthal dependencies a) $S_o = 0$ nm, and b) $S_o = 300$ nm

The further investigation on Q of the same sphere with different mode distribution in radial dependency are shown in Figure 2.45. At the zero separation, the values of κ are 0.0301 and 0.0138, these values correspond to sphere mode numbers l, m, n of $(180, 180, 1)$ and $(180, 180, 2)$, respectively, see Table 2.5, and κ that correspond to the same sphere mode number at 300 nm separation of the sphere from the waveguide surface are 0.0019 and 8.64×10^{-4}, respectively.

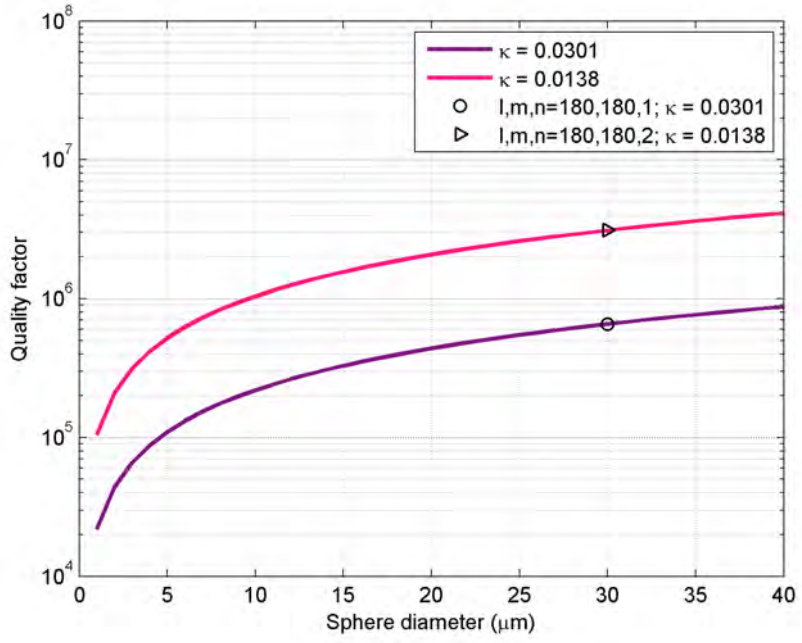

a)

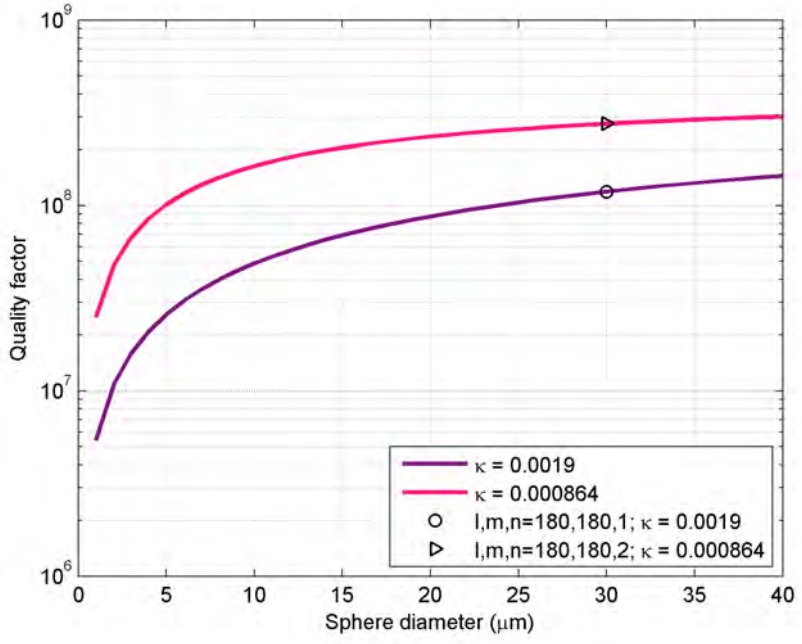

b)

FIGURE 2.45: Quality factor as a function of sphere diameter for different modes in radial dependency a) $S_o = 0$ nm, and b) $S_o = 300$ nm

Figure 2.46 shows plots of Q-factor as a function of circulation loss in dB per unit length,

α^{dB}, in dB/cm for a sphere of diameter 30 μm and $n_s = 1.51$ at the wavelength of 750 nm with the zero separation of the sphere from the waveguide surface for four different coupling efficiencies, κ ($\kappa = 0.0301$, 0.0136, 0.0054 and 0.0027). These values correspond to the sphere mode number l, m, n of $(180, 180, 1)$, $(180, 178, 1)$, $(180, 176, 1)$, $(180, 174, 1)$, respectively. These modes have the variations in both angular and azimuthal directions. It shows that the Q-factor increases as α^{dB} gets smaller and that Q-factor values saturate at very low loss values corresponding to a level resulting from the coupling. The results confirm that Q of the fundamental mode is the lowest compared to the higher order modes.

The results of the further calculation of Q of the same system described for the different mode variations in radial dependency as a function of α^{dB}, are shown in Figure 2.47. The values of κ are 0.0301 and 0.0138, which correspond to the sphere mode numbers l, m, n of $(180, 180, 1)$ and $(180, 180, 2)$, respectively.

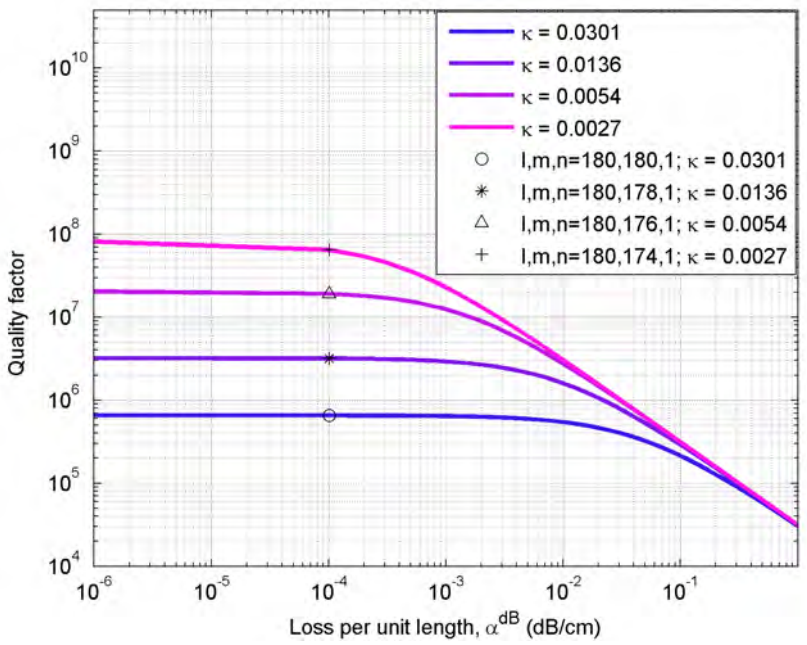

FIGURE 2.46: Quality factor as a function of loss in dB per unit length for different modes in angular and azimuthal dependencies, D = 30 μm

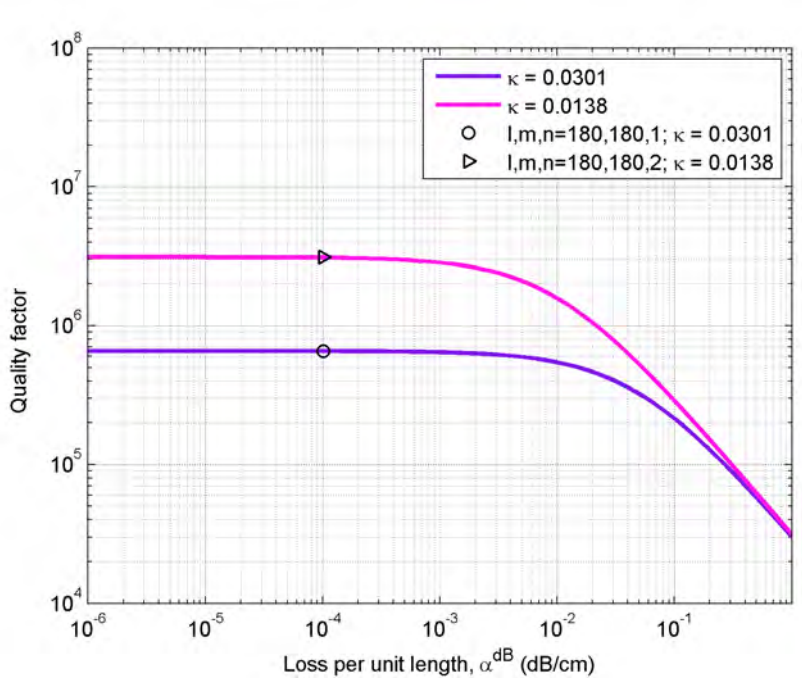

FIGURE 2.47: Quality factor as a function of loss in dB per unit length for different modes in radial dependency, D = 30 μm

The relationship of the quality factor to the transmission coefficient, t, is shown in Figure 2.48 - Figure 2.49. The values of quality factor of the system of the three diffrent modes which have the variations in both angular and azimuthal directions, as well as the ones that have the variations in the radial direction, are shown in Figure 2.48 and Figure 2.49, respectively, for the circulation loss factor of $\alpha = 0.99999$.

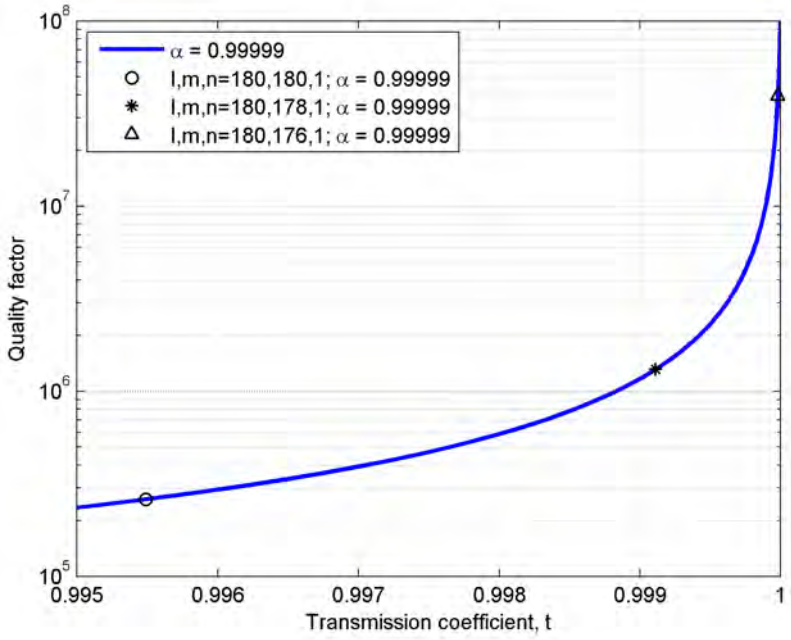

FIGURE 2.48: Quality factor as a function of transmission coefficient ($t = 0.995 - 1.0$), circulation factor $\alpha = 0.99999$, D = 30 μm for different modes in angular and azimuthal dependencies

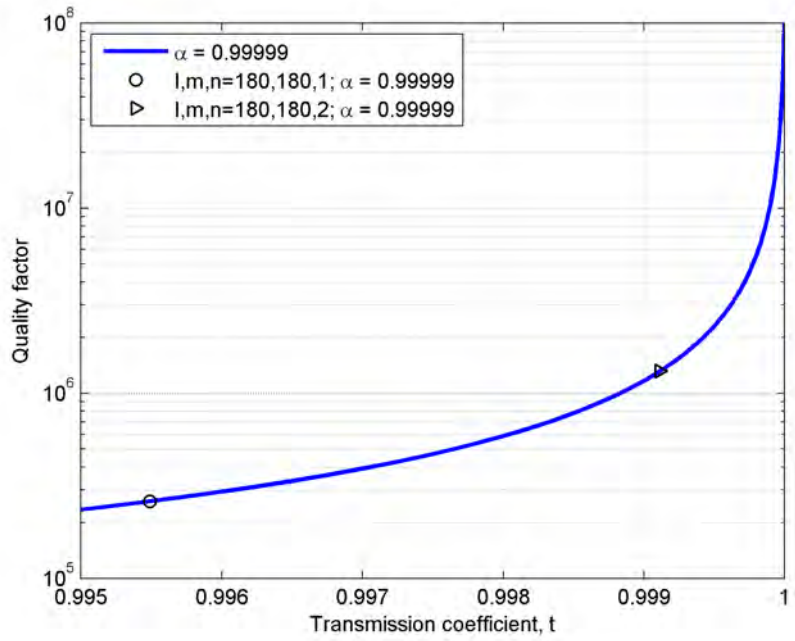

FIGURE 2.49: Quality factor as a function of transmission coefficient ($t = 0.995 - 1.0$), circulation factor $\alpha = 0.99999$, D = 30 μm for different modes in radial dependency

2.7 Conclusions

The modes and fields of the sphere and waveguide have been determined. The WGM fields of the sphere are described in three-dimensional spherical coordinates, they are determined from the spherical mode numbers, l, m, n. By matching tangential electric and magnetic fields across the spherical surface, with the use of the characteristic equation, the resonant wavelengths that are related to the sphere mode numbers l and n. The example of the electric field plot in radial, polar and azimuthal directions, and the contour plots of the fields in $\hat{r}$-$\hat{\theta}$ and $\hat{r}$-$\hat{\phi}$ planes have been shown.

The modelling calculation of the field of the waveguide mode has been derived by the BPM method. The waveguide core, of dimensions 5 by 3 μm, is used to determine the field in the waveguide. Q variations due to the various losses such as the radiative loss, material absorption loss, and the loss due to surface roughness have been discussed. Q variations due to the coupling is determined via overlap integration of the fields of the waveguide and sphere in two-dimension in the transverse plane. The overlap integrals of the fields have been performed in the transverse cross-section of the fields of the waveguide and WGM of the sphere. This overlap integral of the interaction fields has been used to determine the coupling efficiency from the physical parameters of the waveguide, the sphere and their separation. The determination of the coupling and quality factors as a function of the sphere separation from the waveguide has been performed, and the information of the coupling factors has been obtained to be used for the power-transfer function derivation. The unidirectional coupling method, which is used for basic modelling, has been discussed. The transmitted and the circulating power plots in this chapter are useful for comparison with the experimental results in Chapter 4.

2.8 References

[1] V. S. Ilchenko, P. S. Volikov, V. L. Velichansky, F. Treussart, V. Lefèvre-Seguin, J. M. Raimond, and S. Haroche. Strain-tunable high-Q optical microsphere resonator. *Optics Communications*, 145:86–90, 1998.

[2] B. E. Little, J. P. Laine, and H. A. Haus. Analytic theory of coupling from tapered fibers and half-blocks into microsphere resonators. *Journal of Lightwave Technology*, 17:704–715, 1999.

[3] http://mathworld.wolfram.com/SphericalBesselFunctionoftheFirstKind.html.

[4] M. Abramowitz and I. A. Stegun. *Handbook of Mathematical Functions with Formulas, Graphs, and Mathematical Tables*. Dover, New York, ninth Dover printing, tenth GPO printing edition, 1964. ISBN 0-486-61272-4.

[5] http://mathworld.wolfram.com/HermitePolynomial.html.

[6] B. E. Little, S. T. Chu, H. A. Haus, J. F., and J. P. Laine. Microring resonator channel dropping filters. *Journal of Lightwave Technology*, 15:998–1005, 1997.

[7] J. E. Gortych and D. G. Hall. Fabrication of planar optical waveguide by K^+-ion exchange in BK7 and Pyrex glass. *IEEE Journal of Quantum Electronics*, QE-22: 892–895, 1986.

[8] M. L. Gorodetsky, A. A. Savchenkov, and V. S. Ilchenko. Ultimate Q of optical microsphere resonators. *Optics Letters*, 21:453–455, 1996.

[9] M. Rosenblit, P. Horak, S. Helsby, and R. Folman. Single-atom detection using whispering-gallery modes of microdisk resonators. *Physical Review A*, 70:053808–1–053808–10, 2004.

[10] K. K. Lee, D. R. Lim, L. C. Kimerling, J. Shin, and F. Cerrina. Fabrication of ultralow-loss Si/SiO_2 waveguides by roughness reduction. *Optics Letters*, 26:1888–1890, 2001.

[11] K. H. Guenther, P. G. Wierer, and J. M. Bennett. Surface roughness measurements of low-scatter mirrors and roughness standards. *Applied Optics*, 23:3820–3836, 1984.

[12] G. Griffel, S. Arnold, D. Taskent, and A. Serpengüzel. Morphology-dependent resonances of a microsphere-optical fiber system. *Optics Letters*, 21:695–697, 1996.

[13] J. M. Choi, R. K. Lee, and A. Yariv. Control of critical coupling in a ring resonator-fiber configuration: application to wavelength-selective switching, modulation, amplification, and oscillation. *Optics Letters*, 26:1236–1238, 2001.

[14] A. Yariv. Universal relations for coupling of optical power between microresonators and dielectric waveguides. *Electronics Letters*, 36:321–322, 2000.

[15] M. Cai and K. Vahala. Highly efficient optical power transfer to whispering-gallery modes by use of a symmetrical dual-coupling configuration. *Optics Letters*, 25: 260–262, 2000.

Chapter 3

Waveguide and microsphere fabrication and characterisation

3.1 Introduction

In this chapter, fabrication processes of potassium-sodium-ion, K^+-Na^+-ion, and silver-sodium-ion, Ag^+-Na^+-ion, exchanged channel waveguides suitable for microsphere excitation, and glass microspheres will be discussed. Section 3.2 will describe the method and background of the fabrication processes for potassium-sodium-ion exchanged channel waveguides. The potassium-sodium-ion exchanged waveguide will be prepared so that single mode operation in the 800 nm region is obtained. The potassium-sodium-ion exchanged waveguide is an ideal candidate for low loss, single-mode, optical waveguide applications [1–4]. It has good reproducibility characteristics, since it has a relatively low diffusion rate, thus the diffusion depth can be easily controlled. Waveguide characterisation, such as measuring the effective refractive index of the waveguide mode propagation and waveguide cut-off wavelengths, will be described at the end of the section. Section 3.3 will describe the fabrication processes for silver-sodium-ion exchanged waveguides, that will be fabricated to use in the 1550 nm wavelength region. Silver-sodium-ion exchanged waveguides provide a compact modal size for long wavelength operation compared to the potassium-sodium-ion exchanged waveguide, this increases the field enhancement at the waveguide surface and provides stronger coupling to microspheres. The ion-exchange technique was first demonstrated by Giallorenzi in 1973 [5] and, since then, it has become important in waveguide fabrication research, as the fabrication process is straightforward and low cost.

Section 3.4 will describe the microsphere production processes and detailed quality measurements of the microspheres. Glass microspheres can be fabricated in various methods, such as a chemical etching, fibre-tip melting, sphere annealing on carbon substrate [6, 7], fusion of glass particles with a microwave plasma torch [8–11], and rapid quenching of

melted glass for microsphere formation [12].

There are two techniques for microsphere fabrication used in this work. In the first technique, microspheres are placed on a glassy carbon plate and heated, so that surface tension forms them into microspheres. This method is simple and a good surface quality can be obtained. However, one drawback of this technique is that, when large microspheres (above about 80 μm in diameter) are fabricated, gravity may create a flattened shape at the bottom of microsphere that is in contact with the carbon substrate. Further, the quantity of the microspheres obtained from this technique is limited by the area of the substrate. A good alternative technique for microsphere fabrication is to pass microparticles through a hot zone of a vertically oriented quartz furnace liner [13], where the temperature is set to above the glass melting temperature, and to allow the particles to fall slowly in an inert atmosphere during the sphere formation process. An inert atmosphere is applied so that the interaction of the micro-particles with the oxygen and water in the air is minimised, in order to prevent possible contamination and also to maintain a good surface quality of the microspheres produced and to control the dropping rate of the particles. Thus, good surface quality of microspheres fabricated in this manner can be obtained. The production is straightforward to perform, by carefully controlling the flow rate of an inert gas in the setup and selecting an appropriate operating temperature for the particular glass. Another advantage of microsphere production using this technique is that mass production of the microsphere can be obtained. The methods and techniques for particle preparation and microsphere separation are described in detail in this section. At the end of Section 3.4, quality factor measurements of the microspheres will be carried out, and a comparison will be made between the surface quality of the microspheres fabricated in this work and the commercial microspheres [14].

3.2 Potassium-sodium-ion exchanged channel waveguide fabrication

The fabrication method for potassium-sodium-ion exchanged channel waveguides involves exchanging potassium ions, K^+, in a molten salt with the sodium ions, Na^+, in a glass substrate. Potassium ions are easy to obtain from potassium nitrate, KNO_3, and this can be used as a molten salt for the ion exchange process. BK7 is a high quality optical glass that is rich in sodium, which makes the exchange of ions feasible. Moreover, BK7 is one of the most popular optical glasses as it has a broad transmission window in the visible and the near infrared. The refractive indices of BK7 glass as a function of wavelength can be calculated by using the dispersion formula (Sellmeier equation) and the dispersion constants obtained from the Schott handbook on optical glass [15], see Table 3.1.

By exchanging the heavy ions, that is potassium ions, with the lighter sodium ions of

Wavelength, λ (nm)	BK7 refractive index
587.56	1.51680
632.80	1.51509
656.27	1.51432
700.00	1.51306
750.00	1.51184
800.00	1.51078
850.00	1.50984
1000.00	1.50750
1100.00	1.50616
1300.00	1.50370
1550.00	1.50065

TABLE 3.1: Calculated refractive indices of BK7 glass as a function of wavelength

the glass substrate, the refractive index in the exchanged area is modified and has a higher value. The change of the refractive index of the glass substrate depends on the diffusion temperature and the diffusion time, thus, the diffusion temperature and time are parameters that need close control to achieve the required single mode waveguide. Diffusion through a patterned mask may be used to realise a strip of high-index material which acts as a channel waveguide.

The next section describes the method used for waveguide fabrication.

3.2.1 Waveguide fabrication process

Preparation of the glass substrate for ion exchange is carried out by photolithography, which is the process of transferring the pattern from a mask onto the surface of the required substrate. The waveguide fabrication procedure, which is carried out in a cleanroom environment, is as follows.

BK7 glass substrates having dimensions of $50 \times 50 \times 1$ mm^3, were cleaned in a hydrogen peroxide:sulfuric acid solution (H_2O_2:H_2SO_4=1:4) in a heated ultrasonic bath at 85°C, then the substrates were washed with deionised water. In order to prevent moisture remaining on the surface of samples, the samples were placed in the oven at 120°C for 20 minutes. An aluminium, Al, layer about 200 nm thick was then evaporated in a vacuum chamber onto the glass substrate to form a barrier layer. S1813 positive photoresist was then coated onto the substrate (see Figure 3.1) by spin coating at a speed of 6000 rpm for 30 seconds, to achieve a uniform layer of thickness 1 μm. The coated substrate was placed in an oven for 30 minutes at 90°C to soft-bake the photoresist.

The waveguide patterns, which are the straight channels with widths ranging from 3-12 μm, were transferred to the substrate by aligning the designed mask to the desired area, and exposing the photoresist to the ultraviolet (UV) light of intensity level of 18 mW/cm^2 at λ = 365 nm so that the exposed photoresist was soluble and could

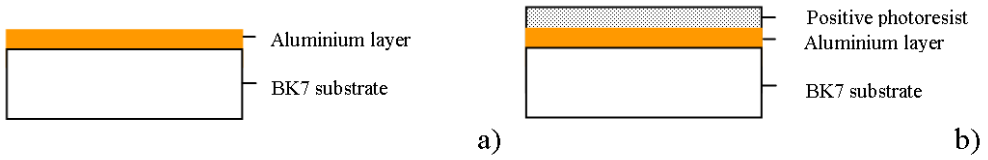

FIGURE 3.1: Photolithography: Surface preparation; a) Glass substrate with Al layer, b) Glass substrate with Al and positive photoresist layers

be removed in a developer. The exposure time to the UV light was set to about 5 seconds; this parameter was chosen from an optimised value estimated from the prior work [16]. The sample was then placed in Microposit MF 319 developer to remove the photoresist in the exposed areas, hence only the material underneath the masked areas remained. The sample was then placed in an oven at 120°C for 30 minutes to hard-bake the photoresist. The aluminium etchant solution was used to etch away the unwanted part of the aluminium layer, forming narrow channels in the aluminium layer. Al etchant was heated up to 50 °C, and an etch time of 90 seconds was used to etch away the unwanted part. The remaining photoresist layer was washed away with acetone and isopropanol, leaving the aluminium patterns remaining on the glass substrate. At this stage, the sample was ready for the ion exchange process. The areas exposed to the molten salt, not covered by the aluminium patterns, would become channel waveguides when the process of ion-exchanging was completed.

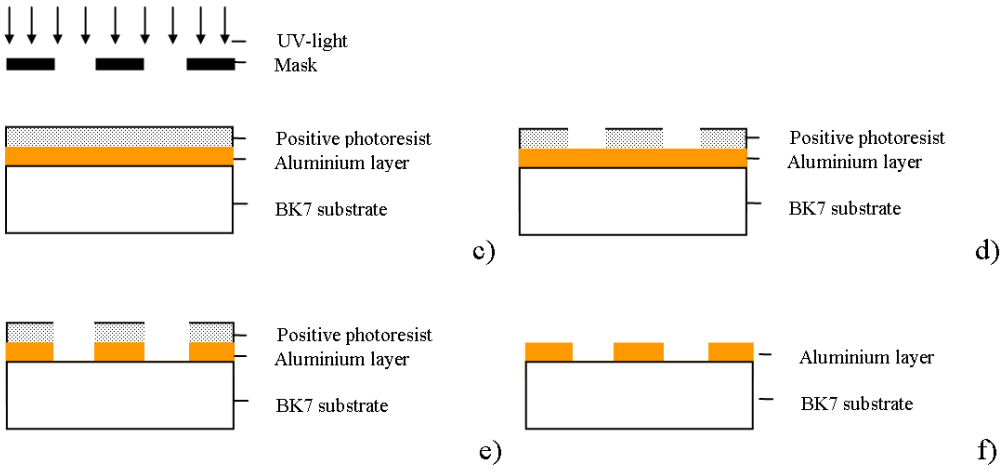

FIGURE 3.2: Photolithography: Pattern transferring; c) High intensity UV light exposure, d) Glass substrate with Al and positive photoresist pattern, e) Glass substrate with Al and positive photoresist pattern, f) Glass substrate with Al pattern

In order to obtain a single mode waveguide at a wavelength of 800 nm, for the waveguide that has a mask width of 3 μm, the diffusion time was set to about 4 hours; and molten KNO_3 for ion exchange was placed in an ion exchanging furnace with the temperature set to 400°C [17]. After completing the ion exchange process, in order to prevent cracking of the glass, the substrates were removed slowly from the molten salt. The residual salt

on the glass substrates was immediately washed away in deionised water. At this stage, the index modified areas, as shown in Figure 3.3, had been formed in the substrates, and comprised the channel waveguides.

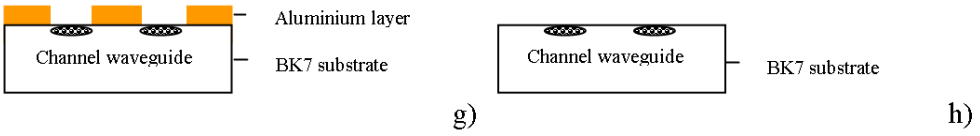

FIGURE 3.3: Ion exchanging; g) Glass substrate with channel waveguide and Al pattern, h) Glass substrate with channel waveguide

The edges of the waveguide were polished to obtain smooth surface ends for input/output coupling. Polishing was carried out as follows. Waveguide substrates were placed between two other glass substrates by using some heated wax for adhesion, in order to prevent the edges cracking when performing the cutting process. After the cutting process, the substrates were placed firmly in a holder with a sufficient loading weight to maintain the substrates in contact with the rotation plate while rotating. Nine-micron calcined aluminium oxide suspension was used to condition the rotational iron plate (as it required conditioning prior to its use). The lapping processes, with 9-μm and 3-μm-calcined aluminium oxide solutions, were consequently performed for 60 minutes and 30 minutes to achieve the removal of approximately 1000 μm and 300 μm, respectively. Lastly, a chemical removal was completed with Syton solution (0.125 μm silica particles in aqueous solution). Syton solution was applied onto the rotational plate, while the plate was rotating at a constant rate at 20 rpm for 20 minutes to achieve a uniform surface removal. The dropping rate of the Syton liquid was carefully controlled to prevent crystallisation of the Syton solution occurring if the substrates or the rotational plate were too dry. After the polishing process, in order to prevent crystallisation of the Syton solution, the glass substrates required an immediate and thorough cleansing in deionised water. At this stage, a waveguide substrate with high quality polished ends was obtained. Wax contaminant was washed away with Ecoclear. Aluminium pattern removal was achieved by placing samples into a 50°C aluminium etchant solution for about 5 minutes. At this stage, the K^+-Na^+-ion channel waveguide was ready to be used. The typical value of the waveguide propagation loss was found to be about less than 0.8 dB/cm [17].

3.2.2 Prism coupling: N_{eff} determination

In this section, the characterisation of the effective refractive index of the mode propagation in the waveguide, N_{eff}, is described. The prism coupling method [18] is a simple approach used to measure the effective refractive index of the mode that propagates along the waveguide. This method is convenient and easy to set up, the effective refrac-

tive index measurement of the mode is obtained by observing the angle of incident light onto the prism face. The value will be compared with the value found from literature, and used to inform the choice of paramters in theoretical models, when compares with experimental results.

The laser beam from a helium neon, HeNe, laser (λ = 632.8 nm) entered the prism with an incident angle, α, so that the light at the incident angle at the prism base, θ, is reflected by total internal reflection, see Figure 3.5. The waveguide was placed parallel in proximity to the prism base. The condition for the coupling is that the incident beam must enter the prism with an appropriate angle such that the evanescent field in the gap between the prism base and the waveguide has the same phase velocity. The angle that matches the incident velocity in the x-direction to the phase velocity of one of the guided propagation modes is called the "synchronous angle" [18]. It is also useful to note that the gap between the prism base and the waveguide is normally of the order of half a wavelength in order to obtain sufficient light coupling into the waveguide, see Figure 3.4.

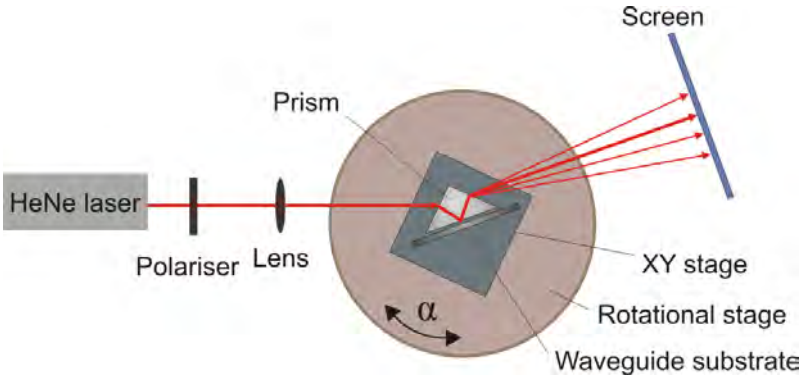

FIGURE 3.4: Prism coupling: Apparatus [18]

Monomode channel waveguides are very small, and light coupling from a prism to a small channel can be very complicated in this setup. Thus, the effective refractive index of the mode from the slab waveguide is measured. This effective refractive index is the upper limit of the effective refractive index of the mode in the channel waveguide. The effective refractive index of the mode in the channel waveguide is between the substrate refractive index and N_{eff} of the slab.

The measurement is done at the back of the substrate where the slab waveguide was formed. The evidence for light coupling into the slab waveguide can be observed on a screen, where the output light is coupling out at the exit face of the prism. At the angle, α, where the light is coupled into the slab waveguide, the scattered light from the waveguide substrate reflects back to the prism and couples out at the exit face, then bright lines appear on the screen. By measuring this angle of incidence, which is the angle at which light enters the prism, with respect to the perpendicular plane normal to the prism entrance face, the value of the effective refractive index of the mode can be

obtained.

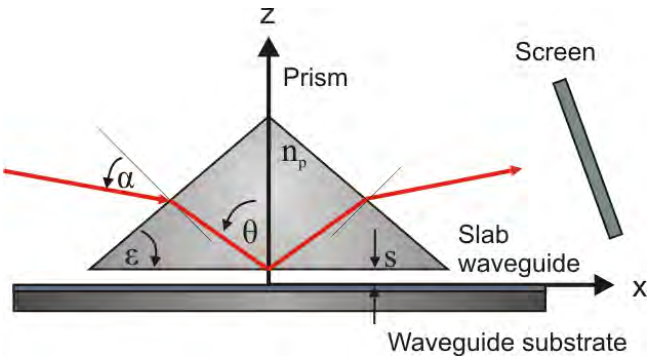

FIGURE 3.5: Prism coupling: Ray tracing

The effective refractive index of the excited mode can be calculated from the ray tracing method, using Snell's law, as described in the following formula.

$$\mathrm{N_{eff}} = n_\mathrm{p} \cdot \sin\left(\epsilon + \left(\sin^{-1}\left(\frac{\sin\alpha}{n_\mathrm{p}}\right)\right)\right), \tag{3.1}$$

where n_p is the refractive index of the prism, ϵ is the prism angle, and α is the incident angle, see Figure 3.5.

Measurement of the effective refractive index of the waveguide modes was carried out on a BK7 waveguide. K^+-Na^+-ion exchanged waveguides, that were fabricated based on the detailed discussion in Section 3.2, were characterised. The refractive index and the angle of the prism, that were used in the prism coupling apparatus for the measurement, were $n_\mathrm{p} = 1.79884$ and $\epsilon = 55.068°$, respectively. Light from a HeNe laser was launched through a polariser so that light in TE or TM polarisation was obtained, light was then focused onto the prism face via a lens such that it coupled into a slab waveguide which was placed in proximity to the prism base. The rotation stage was rotated to the point where the strongest power output at the output waveguide end was observed on a screen, the measured incident angle was obtained. TE light was launched to couple to a slab waveguide, the incident angle obtained was $\alpha = 5.107°$. The effective refractive index of the waveguide mode was calculated, according to Equation 3.1, and was found to have the value of $\mathrm{N_{eff}} = 1.5239$, corresponding to $\Delta n_\mathrm{eff} = 0.0073$. This Δn_eff is smaller than a typical value of refractive index difference, $\Delta n = 0.0094$ [2], for the K^+-Na^+-ion exchanged waveguide on BK7 at 400°C, at the operating wavelength of 632.8 nm, where the diffusion depth of about 4 μm [2] was obtained.

It is to be noted that the effective refractive index measurement of the mode in the waveguide was carried out with a HeNe laser at a wavelength of 632.8 nm. In order to obtain the values of the effective refractive indices of the waveguide modes at a required wavelength of operation, the apparatus must be setup with a laser source of the desired wavelength.

3.2.3 White light attenuation spectroscopy: Waveguide cut-off wavelength determination

In this section, the method of measuring waveguide cut-off wavelength, λ_c, is described. The waveguide cut-off wavelength, λ_c, is important since the range of single-mode operation can be obtained to ensure that the waveguide is appropriate for use at the specified wavelength. Waveguide cut-off wavelengths can be determined by measuring the loss spectrum of the waveguide in a white light attenuation spectroscopy setup. By measuring the transmission spectrum of the waveguide and comparing it to the one obtained from the input fibre alone, the spectral loss of the waveguide can be obtained. The cut-off wavelength corresponds to the wavelength at which the loss suddenly increases. At this wavelength, modes are no longer supported by the waveguide.

The experimental apparatus shown in Figure 3.6 is used to measure the waveguide attenuation spectra. Light from a white light source was coupled to the waveguide through an optical fibre. The waveguide output light was focused onto a monochromator and detector via a lens. This detector was connected to a lock-in amplifier and computer. The lock-in amplifier amplified the periodic square wave signal that was generated by the light source through the chopper. A polariser was placed in front of the monochromator to allow the selection of light propagation in the TE or TM mode. The output power spectra for the TE and TM polarisations were observed and compared to those obtained from the fibre, in order to determine the spectral loss due to the presence of the waveguide. Loss in decibels, as a function of wavelength, of the waveguide was obtained as follows,

$$\text{loss}_{\text{dB}}(\lambda) = -10 \log \left(\frac{\text{T}_{\text{waveguide}}(\lambda)}{\text{T}_{\text{fibre}}(\lambda)} \right), \tag{3.2}$$

where $\text{T}_{\text{fibre}}(\lambda)$ is the output power of the fibre and $\text{T}_{\text{waveguide}}(\lambda)$ is the output power of the waveguide as function of wavelength.

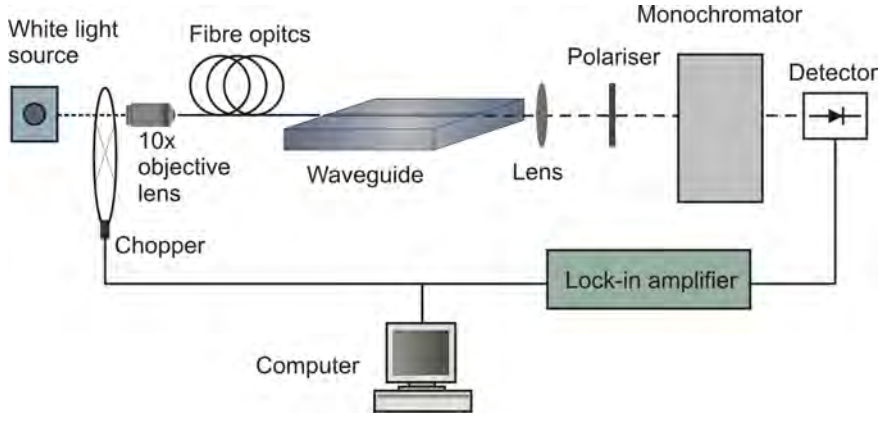

FIGURE 3.6: Apparatus for measuring absorption loss spectrum

The measurement of waveguide cut-off wavelengths for K^+-Na^+-ion exchanged channel waveguides made through mask widths of 3 μm, 6 μm and 10 μm, were carried out. Light was launched into each of these channel waveguides, the spectra of transmission signals from each of the waveguides and transmission spectra from the fibre without the waveguide were recorded. The value of the cut-off wavelengths are determined through the insertion loss of the waveguide to the fibre. Figure 3.7 shows the plots of the insertion loss in dB of the 3 μm-wide K^+-Na^+-ion exchanged waveguide to the fibre. The cut-off wavelengths for TE and TM polarisations of 1090 nm and 1089 nm, are determined, respectively. There is not much of a variation of the cut-off wavelength values in TE and TM cases, because the index difference in the potassium-sodium-ion exchanged waveguide is considered to be small. Figure 3.7 shows that there is a high background loss; this is due to misalignment or mode mismatch of the fibre and the waveguide.

Figure 3.8 shows the results of waveguide cut-off wavelengths of the K^+-Na^+-ion exchanged waveguide as function of mask widths in both polarisations. It can be seen that the waveguide cut-off wavelengths are larger for larger mask width, as expected, because the channel fabricated with a larger mask width would result in larger dimensions, and the larger waveguide can support light at a longer wavelength.

This method is appropriate for measuring the cut-off wavelengths of the waveguide. However, it is to be noted that this setup is not appropriate for waveguide propagation loss measurements because the loss measured in this manner includes various components such as insertion loss and loss due to mode mismatch.

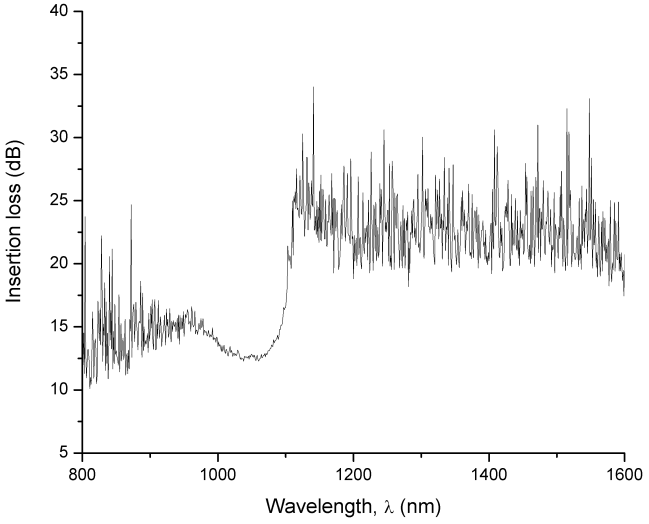

a)

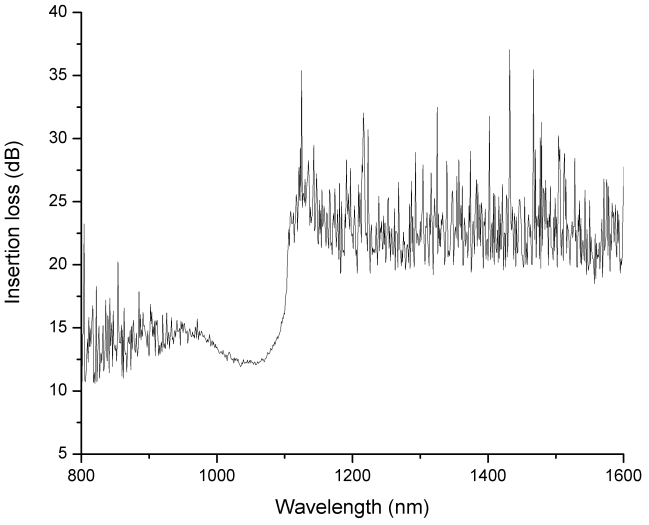

b)

FIGURE 3.7: Insertion loss of a K^+-Na^+-ion exchanged waveguide according to a mask width of 3 μm and the fibre in; a) TE mode, b) TM mode (wavelength resolution of 1 nm)

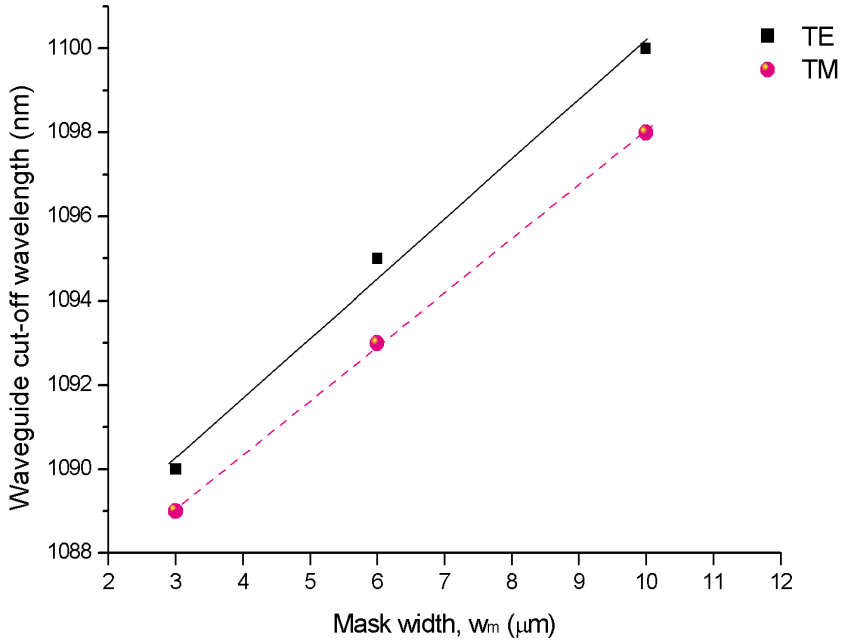

FIGURE 3.8: Waveguide cut-off wavelength of K^+-Na^+-ion exchanged waveguide as a function of the mask widths of 3 μm, 6 μm and 10 μm in TE and TM modes (*from the data with 1 nm wavelength resolution)

3.3 Silver-sodium-ion exchanged channel waveguide fabrication

In this section, fabrication of silver-sodium-ion, Ag^+-Na^+-ion, exchanged waveguides and the waveguide characterisation such as the measurement of the waveguide mode profile and waveguide cut-off wavelength, will be described. Single mode silver-sodium-ion exchanged waveguides for a wavelength in the 1550 nm region were fabricated by the collaborating team at "N. Carrara" Institute for Applied Physics, Optoelectronics and Photonics Department, Firenze, Italy [19], while the Optoelectronics Research Centre laboratories were out of action. Silver-sodium-ion exchanged waveguides [20] are obtained by modifying the glass substrate index by exchanging the Ag^+ from a molten salt with the Na^+ in the glass substrate, the areas that are affected by the ion-exchanging will form channel waveguides. Details of fabrication are described as follows.

3.3.1 Waveguide fabrication process

Surface preparation was carried out using a similar photolithography process as described in Section 3.2, to obtain patterned substrates for ion-exchange. BK7 glass substrates were immersed in a 350°C molten $AgNO_3$:$NaNO_3$:KNO_3 of 0.5:49.75:49.75 mol% for 4 hours to form a single mode channel waveguide with a mask width of 4 μm at a wavelength near 1550 nm. The diffusion depth of the waveguide channel, with the diffusion time of 4 hours in a 350°C molten $AgNO_3$:$NaNO_3$:KNO_3 of 0.5:49.75:49.75 mol% that has opening width of 4 μm, is expected to have a value of about 3.5 μm [19]. KNO_3 was included in the molten salt to prevent out-diffusion of the K^+ from the glass substrate which could cause tensile stress and microcracks on the surface [21]. The polishing processes was carried out using similar techniques as used for the potassium-sodium-ion exchanged waveguide, as described in Section 3.2, and to obtain channel waveguides with high quality polished ends.

3.3.2 Waveguide characterisation

In this section, the waveguide characterisation of the Ag^+-Na^+-ion exchanged waveguide is described. At the beginning of this section, the mode profile of the Ag^+-Na^+-ion exchanged channel waveguide measurement was obtained. The mode profile is determined so that the information of the physical width and depth of the fabricated waveguide channel can be obtained. These values are important as they are required to be used in a model in the theoretical sections. At the end of the section, the measurement of waveguide cut-off wavelength is included.

Mode profile measurements and cut-off wavelengths of the Ag^+-Na^+-ion exchanged waveguides that are fabricated according to Section 3.3.1, are described. A 1550 nm-light

in the TM polarisation was launched through a microscope objective lens and coupled into a 4 μm wide Ag^+-Na^+-ion exchanged waveguide. The modal profile of light in the waveguide was detected and recorded by a CCD camera. Figure 3.9 shows the mode profile of the 4 μm wide Ag^+-Na^+-ion exchanged waveguide. The measured width and height of the mode profile at full-width of half-maximum of 7.2 μm $\times$ 5.5 μm were obtained.

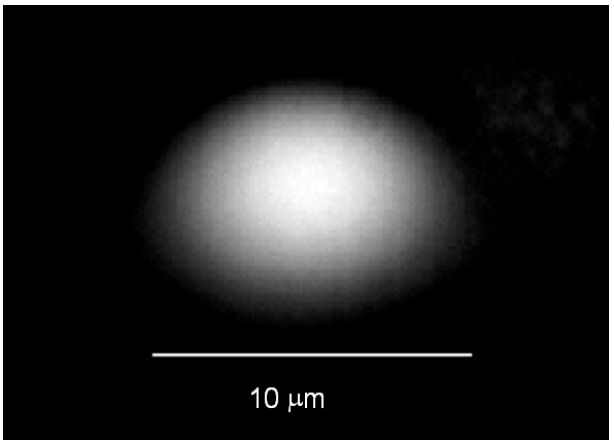

FIGURE 3.9: Mode profile of 1550 nm light in a 4 μm wide Ag^+-Na^+-ion exchanged waveguide

In order to estimate the physical width and depth of waveguide channel from this measured beam profile, Beamprop program was incorporated. The values of width and depth from the Beamprop model which make the corresponding full-width of half-maximum of the mode profile to have the values close to 7.2 μm $\times$ 5.5 μm are defined as the physical width and depth of the channel waveguide. The specific constants of $n_{\text{background}} = 1.0$, $n_{\text{substrate}} = 1.5$, $\lambda = 1550$ nm, and $\Delta n = 0.02$, were used in the model. The values of channel waveguide width and depth of 7.0 μm and 2.3 μm were obtained, for the TM polarisation.

It is to be noted that the channel waveguide width is larger than the mask width because, the nearby areas under the Al patterns were also affected by diffusion of the ions, yielding larger diffusion waveguide widths.

The measurement of waveguide cut-off wavelength of a 4 μm wide Ag^+-Na^+-ion exchanged channel waveguide was carried out in a similar way to the potassium-sodium-ion exchanged waveguide as described in Section 3.2.3. A cut-off wavelength could not be found as it is greater than the wavelength measurable by the current apparatus. However, the evidence of the second mode appeared at the wavelength below 1300 nm, so monomode operating of this waveguide at wavelength near 1550 nm was confirmed.

3.4 Microsphere fabrication

This section describes the microsphere production methods and the experimental work on measuring the quality of the microspheres. The production process consists of particle preparation, fabrication and microsphere separation.

3.4.1 Microsphere fabrication on a substrate

In this section, the microsphere fabrication by heating the desired micro-particles on a carbon substrate is described in detail.

Micro-particles were prepared in a clean environment. The glass was crushed with an agate pestle and mortar having highly polished surfaces and sieved into a range of sizes. Stainless steel mesh sieves were used for the particles' sieving because they do not introduce any impurities such as iron oxide onto particles during the sieving process. The sieving process involves two sizes of mesh sieves to obtain a range of particle sizes according to the sizes of the two mesh sieves. The crushed particles were firstly sieved with a large mesh sieve, the larger particles than the mesh size remained in the sieve, these particles were not used in the sphere formation process. The particles that passed through the first mesh were then sieved with a smaller mesh sieve. The particles remaining in the second mesh sieve were considered to be the particles of the required size range for the sphere formation process. The sieved particles were washed and cleaned, and the unwanted dust and contaminants were washed away using isopropanol. To prevent moisture forming on the particle surfaces, and the particles becoming attached to each other, the wet particles were dried in an oven and then sonicated for 2 to 3 minutes prior to the sphere formation process.

1.5-wt% Nd_2O_3-doped BK7 microspheres were prepared. Nd-doped glass was crushed into micro-particles and sieved into the range of sizes from 30 μm to 200 μm. The crushed particles were placed on to a highly polished carbon plate to prevent any adhesion that might be introduced between the contact substrate and the glass particles during the heating process. The particles on the carbon substrate were put in a closed high temperature furnace chamber in an argon atmosphere. The furnace temperature was set to 950°C with a ramping rate of 10°C/min. The micro-particles were heated with the duration of 45 minutes to promote the microsphere formation, microspheres were formed by allowing the surface tension of micro-particles to form spherical shapes. Then the temperature of the furnace was slowly ramping down to the room temperature, this process was taken place for about 8 to 10 hours. At this point, the microspheres were obtained.

Figure 3.10 shows an image of a 100±3 μm diameter microsphere obtained from this fabrication technique. The microspheres which are made from this technique have been

found to have a good spherical shape and to be transparent, however, the larger microspheres (>80 μm in diameter) have been found to suffer from a flattened surface at the contact area with the substrate, due to gravity pulling the particles downward during the sphere formation process.

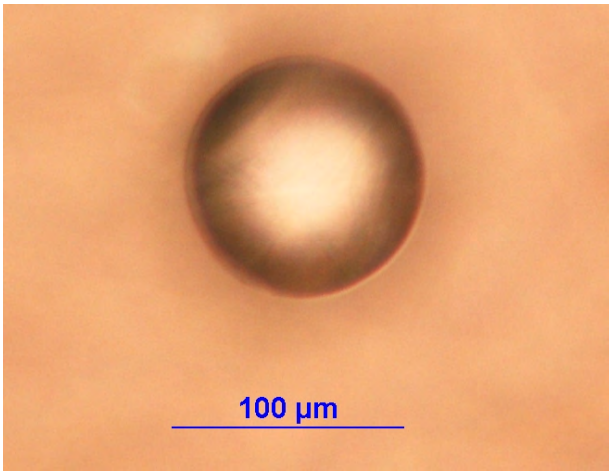

FIGURE 3.10: Nd-doped BK7 microsphere image, (heated on substrate)

3.4.2 Microsphere fabrication by dropping micro-particles through a hot zone in vertical furnace

This section describes techniques for microsphere formation by dropping micro-particles through a hot zone in vertical furnace. Particles for microsphere formation were prepared using the same process as described in Section 3.4.1.

Figure 3.11 shows the apparatus for microsphere fabrication established by Gregor Elliott [13]. A high temperature furnace from Lenton Thermal Designs Ltd. and a 90-cm-long quartz furnace liner, that has a diameter of 1.5 cm, were set in a vertical orientation to allow the particles to pass down vertically within the quartz furnace liner tube. The dried crushed particles were dropped into the liner tube, then while the particles travel from a hot to a cooler zone, the surface tension of the particle promotes the formation of a sphere. Argon gas flowed vertically upward from the bottom to the top of the furnace liner so that the appropriate dropping rate of the particles was obtained. An inert, argon, gas was used to prevent the melted particles from interacting with any oxygen and water in the atmosphere. The collection container was placed at the bottom of the furnace liner to collect all the particles which arrive at the bottom of the furnace liner. The particles were washed and collected from the container with the use of a suitable solvent (isopropanol or methanol). The particles collected were a mixture of microspheres and unformed particles. The last step of the microsphere production was to separate the microspheres from these non-spherical particles, by separating those particles which rolled down a shallow inclined plate from those that did not roll down. The particles that are left on the inclined plate are assumed to be the particles which did

not successfully form spheres. During the rolling process, an appropriated solvent was applied on the inclined plate to make sure that microspheres could freely roll down. The rolling process was carried out repeatedly (about five times) to ensure a good quality of microsphere from this separation method. The microspheres from the final round of rolling down process, were collected and kept in a bottle immersed in methanol.

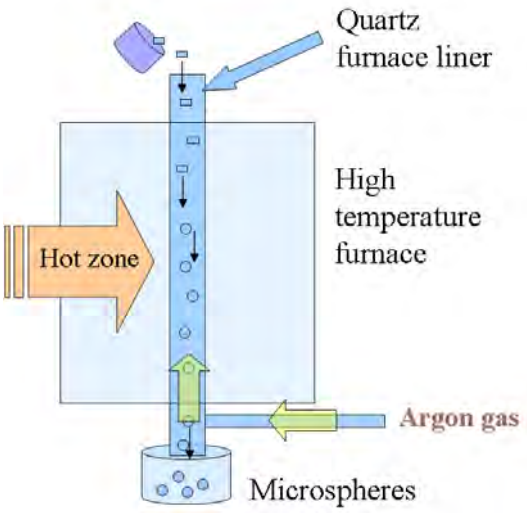

FIGURE 3.11: Apparatus for microsphere fabrication [13]

To form microspheres for laser measurements, 1.5-wt%-Nd_2O_3-doped BK7 glass was crushed and sieved into micro-particles ranging from 32 μm to 112 μm, according to the sizes of mesh sieves. In order to obtain Nd-doped BK7 microspheres, the furnace temperature was set to 1250°C. The temperature was set to above the melting temperature of the glass in order to make sure that the surrounding temperature in the furnace liner was sufficient for the sphere formation. The temperature was limited to 1250°C to avoid melting the quartz liner. An argon gas flow of 1 litre/min was applied to maintain the time in the hot zone and to slow the dropping rate of the particles.

The microspheres obtained were found to be between 60 μm to 200 μm in diameter. Particles smaller than 60 μm were not heavy enough to successfully drop through the furnace liner. It is proposed that microspheres with smaller sizes will be produced in the opposite manner, where particles will be carried by the argon flow to the top of the furnace liner and microspheres will be collected at the top [13]. Larger microspheres than expected were formed because, during the particle preparation process, unevenly shaped particles were introduced. These unevenly shaped particles may include cigar-shape particles with one dimension larger than the mesh size, these uneven shape particles would form themselves into larger microspheres than expected.

Figure 3.12 shows the image of a 135±3 μm diameter microsphere obtained from this process, using an optical microscope with a magnification of 20×. The image shows that the microsphere is clearly spherical in shape and that the surface quality is very promising. To quantitatively assess the quality of the microsphere, the Q-factor measurement

will be described in the next section.

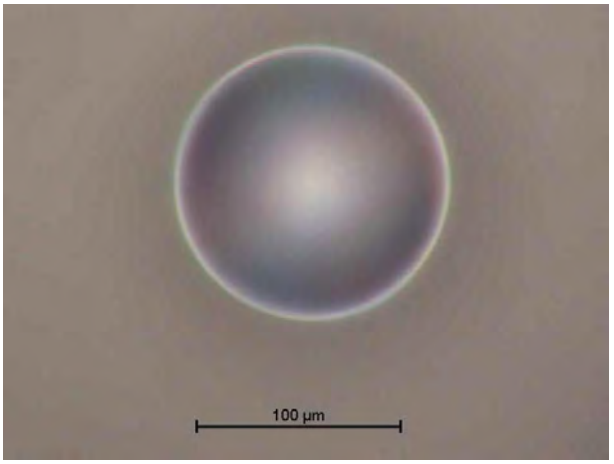

FIGURE 3.12: Nd-doped BK7 microsphere image, (dropped through furnace)

3.4.3 Quality factor measurement

Microsphere quality is most directly assessed by Q-factor measurement and in this section, Q-factor measurement of an in-house made microsphere fabricated on a glassy carbon plate, an in-house made microsphere obtained from the dropping technique and a commercial microsphere, are described. The Q-factor measurement of the microsphere was achieved by evanescently coupling the light from an optical planar waveguide into the microsphere and monitoring the scattered light from the microsphere as a function of wavelength. The Q factor can be obtained by measuring the sharpness of the resonant peaks obtained, as described in Section 2.5 in Chapter 2. Q-factor can be obtained from,

$$\mathrm{Q} = \frac{\lambda}{\delta\lambda_{\mathrm{FWHM}}}, \tag{3.3}$$

where λ is the resonant wavelength, and $\delta\lambda_{\mathrm{FWHM}}$ is the width at full-width at half-maximum power of the resonant lobe.

Light from a tunable source (Agilent 81600B), at a power of 8 dBm in the TM polarisation, was launched into the 4-μm-wide planar silver-sodium-ion exchanged waveguide, coated with a Teflon layer of 400 nm thick (Section 3.2), via a polarisation maintaining fibre. The scattered light, as a function of wavelength, was monitored and recorded by an InGaAs detector connected with a computer, as shown in Figure 3.13. A single microsphere was placed onto the waveguide and the alignment was adjusted such that the maximum scattered power was obtained.

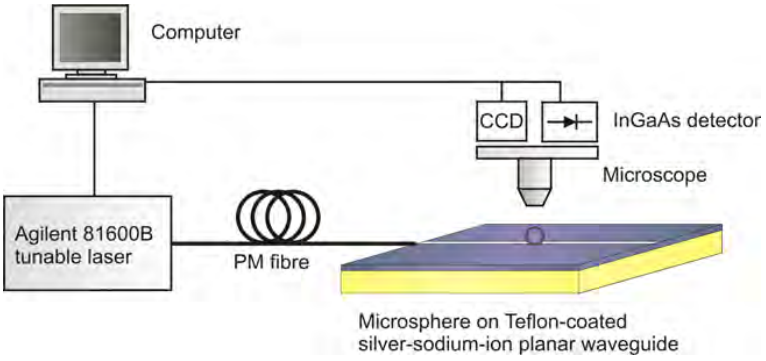

FIGURE 3.13: Experimental apparatus for Q-factor measurement

First, Q-factor measurement of the commercial microsphere was carried out. Figure 3.14 shows the scattered power as a function of wavelength obtained from the commercial Nd-doped BK7 microsphere with the size of 30±3 μm in diameter [14] when coupled to the same waveguide. The $\delta\lambda_{\mathrm{FWHM}}$ of 0.38 nm was obtained at a wavelength near 1550 nm, hence a Q-factor of 4×10^3.

Secondly, Q-factor measurement of a microsphere that was fabricated on a carbon substrate, as described in Section 3.4.1, was carried out. Figure 3.15 shows the scattered

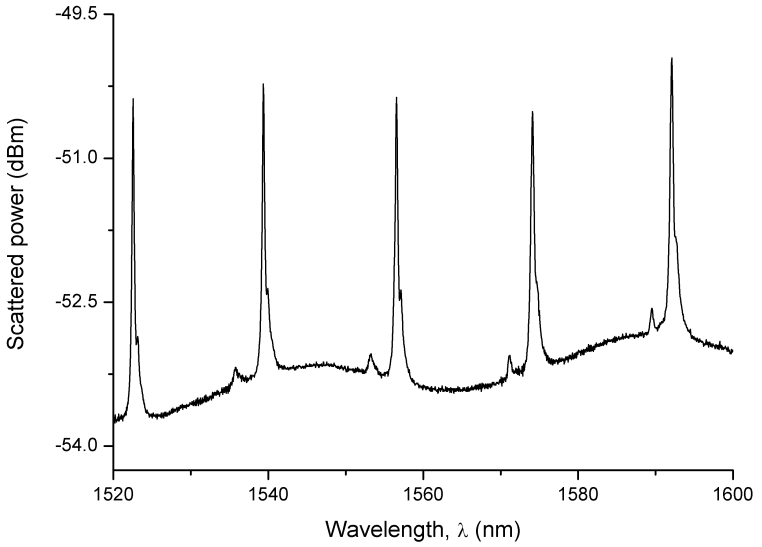

FIGURE 3.14: Scattered power of the commercial microsphere on the waveguide, Q-factor of 4×10^3 at $\lambda = 1550$ nm

power as a function of wavelength of a microsphere of about 80 μm in diameter that was fabricated on a glassy carbon plate, when coupled with the evanescent field of the silver-sodium-ion exchanged waveguide coated with a 400 nm thick Teflon layer.

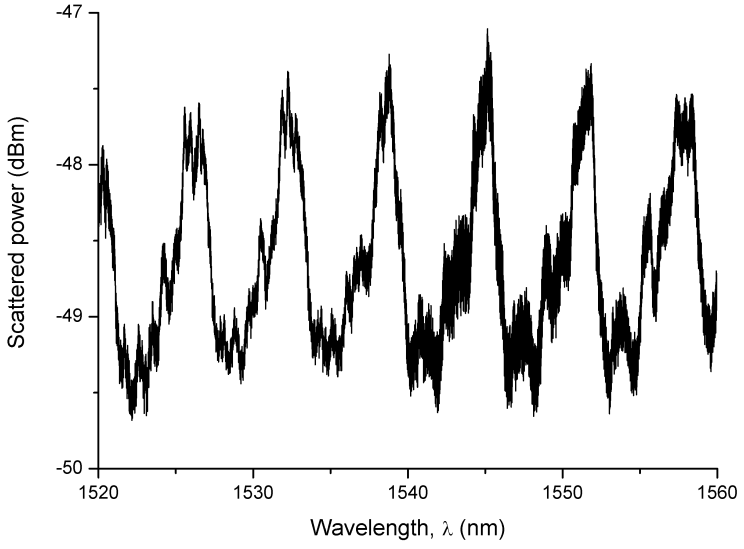

FIGURE 3.15: Scattered power of the in-house made microsphere as described in Section 3.4.1 on the waveguide, Q-factor of 1×10^3 at $\lambda = 1550$ nm

Q-factor of 1×10^3, at a wavelength near 1550 nm, is obtained. The Q-factor obtained is relatively small, this may be due to the fact that the flattened surface of the microsphere might be in the propagation path of WGM.

Lastly, an in-house made microsphere, formed using a dropping technique described in Section 3.4.2, was characterised. Figure 3.16 shows the scattered power obtained from the microsphere, that has a diameter of around 160 μm, as a function of wavelength when coupled to the silver-sodium-ion exchanged waveguide coated with a 400 nm thick Teflon layer. Q-factor of 6.2×10^4, at a wavelength near 1550 nm, was obtained, with the corresponding $\delta\lambda_{\mathrm{FWHM}}$ of 0.025 nm.

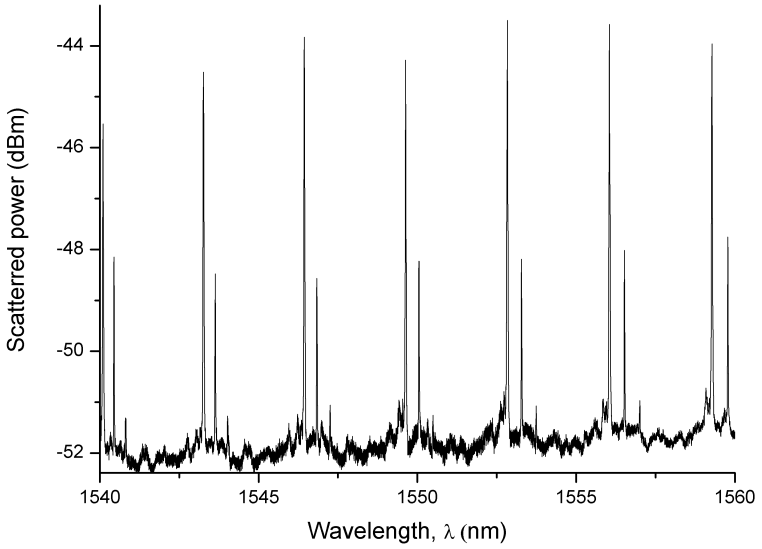

FIGURE 3.16: Scattered power of the in-house made microsphere as described in Section 3.4.2 on the waveguide, Q-factor of 6.2×10^4 at $\lambda = 1550$ nm

It has been found that the Q-factor measured from the in-house fabricated microsphere using the dropping technique is found to have a larger value than the Q-factor measured from the commercial microsphere.

It is to be emphasised that, as described in Section 2.4, losses due to the whispering-gallery propagation [22] and material absorption, are negligible compared to loss due to surface roughness, for a microsphere that has a diameter of more than 15 times larger than the operating wavelength [23], for the current configuration of the glass microsphere in an air medium [24]. Thus, it can be concluded that, the higher value of Q-factor obtained from the in-house fabricated microsphere, using a dropping technique, suggests that the in-house fabricated microspheres using dropping technique have a better surface quality than the commercial microspheres. These microspheres are chosen to be used for further study.

3.5 Conclusions

Waveguides suitable for microsphere excitation have been successfully fabricated and characterised. The single mode potassium-sodium-ion waveguide devices, for an operating wavelength of less than 1100 nm, were made by diffusing patterned BK7 glass (that has mask widths of 3 μm to 12 μm as prepared by a photolithography process into molten KNO_3) and controlling the diffusion time to 4 hours at 400°C. The silver-sodium-ion exchanged waveguide has been fabricated to operate as single mode in the 1550 nm region. The appropriate molten salt $AgNO_3$:$NaNO_3$:KNO_3 of 0.5:49.75:49.75 mol% and temperature of 350°C have been chosen, and the diffusion time of 4 hours has been used so that the silver-sodium-ion exchanged waveguide, that has a mask width of 4 μm, can operate as single mode at wavelengths in the 1550 nm region. The modal profile of the light in the channel of the silver-sodium-ion exchanged waveguide has thereby been found, and the values of physical width and depth of the waveguide have been found. These values are useful in the theoretical comparisions with experiment for waveguide modal calculation. The waveguide cut-off wavelengths for the potassium-sodium-ion exchanged waveguides have been obtained.

Good surface quality microspheres have been fabricated. The microspheres obtained from the carbon plate have been found to have good surface quality when compared with the commercial microspheres. The microspheres have also been found to have good spherical shapes with the value of the discrepancy of mean diameters among the major axes of less then 5% of their average diameters. However, it has been found that the microspheres of a larger diameter (of more than about 80 μm) have suffered from a flattened surface. It has been found that the amount of microspheres produced from this technique is limited by the area of the carbon plate. An alternative way of fabricating the microsphere has been developed by carefully preparing the glass micro-particles and controlling the flow rate of the argon gas to 1 liter/min, and the furnace operating temperature to 1250°C, microspheres ranging from 60 μm to 200 μm diameter have been obtained. This method is a good technique to obtain a mass microsphere production and it has also overcome the issue of the flattened shape of the microspheres obtained from the carbon plate. However, the gas flow rate must be properly controlled to prevent the small-size particles (nominal size of $<$50 μm) from floating upward the furnace liner tube. The Q-factor measurements of the microspheres, on a silver-sodium-ion exchanged channel waveguide coupling system, have been carried out. The high Q-factor measured from the microspheres fabricated by the dropping technique confirms that they have a promising surface quality, Q-factor values as high as 6.2×10^4 have been obtained. Q-factors of microspheres fabricated on the carbon plate have been found to be very low, because the microsphere has a flattened surface at the side in contact with the substrate holder, preventing a strong WGM to occur. Q-factor measurement of commercially available microspheres has been completed. The comparison of the Q-factor of these microspheres against the value obtained from the commercial microspheres has been

done, the result indicates that the microspheres fabricated in-house have a better surface quality. The improvement on surface quality of the microspheres fabricated in this manner can be made with proper control of the inert gas flow rate and the furnace temperature.

3.6 References

[1] G. L. Yip and J. Albert. Characterization of planar optical waveguide by K^+-ion exchange in glass. *Optics Letters*, 10:151–153, 1985.

[2] J. E. Gortych and D. G. Hall. Fabrication of planar optical waveguide by K^+-ion exchange in BK7 and Pyrex glass. *IEEE Journal of Quantum Electronics*, QE-22: 892–895, 1986.

[3] R. V. Ramaswamy and R. Srivastava. Ion-exchanged glass waveguide: A review. *Journal of Lightwave Technology*, 6:984–1002, 1988.

[4] A. Miliou, H. Zhenguang, H. C. Cheng, R. Srivastava, and R. V. Ramaswamy. Fiber-compatible K^+-Na^+ ion-exchanged channel waveguides: Fabrication and characterization. *IEEE Journal of Quantum Electronics*, 25:1889–1897, 1989.

[5] T. G. Giallorenzi, E. J. West, R. Kirk, R. Ginther, and R. A. Andrews. Optical waveguide formed by thermal migration of ions in glass. *Applied Optics*, 12:1240–1245, 1973.

[6] G. S. Murugan, J. S. Wilkinson, and M. N. Zervas. Waveguide coupling to size-mismatched bispheres. In *The 13th Microoptics Conference (MOC '07)*, Sunport Takamatsu, Takamatsu, Japan, October 2007. Microoptics Group, Optical Society of Japan, The Japan Society of Applied Physics.

[7] T. Kishi, S. Shibata, and T. Yano. Preparation of micrometer-size super-spherical glasses for optical resonator. In *XX. ICG International Congress on Glass*, Kyoto, Japan, September 2004.

[8] M. Mortier, P. Goldner, P. Féron, G. M. Stephan, H. Xu, and Z. Cai. New fluoride glasses for laser applications. *Journal of Non-Crystalline Solids*, 326–7:505–509, 2003.

[9] F. Lissillour, D. Messager, G. M. Stéphan, and P. Féron. Whispering-gallery-mode laser at 1.56 μm excited by a fiber taper. *Optics Letters*, 26:1051–1053, 2001.

[10] P. Féron. Whispering gallery mode lasers in erbium doped fluoride glasses. *Annales de la Foundation Louis de Broglie*, 29:317–329, 2004.

[11] G. Nunzi Conti, A. Chiasera, L. Ghisa, S. Berneschi, M. Brenci, Y. Dumeige, S. Pelli, S. Sebastiani, P. Feron, M. Ferrari, and G. C. Righini. Spectroscopic and lasing properties of Er^{3+}-doped glass microspheres. *Journal of Non-Crystalline Solids*, 352:2360–2363, 2006.

[12] X. Peng, F. Song, S. Jiang, N. Peyghambarian, M. K. Gonokami, and L. Xu. Fiber-taper-coupled L-band Er^{3+}-doped tellurite glass microsphere laser. *Applied Physics Letters*, 82:1497–1499, 2003.

[13] G. R. Elliott, D. W. Hewak, G. S. Murugan, and J. S. Wilkinson. Chalcogenide glass microspheres; their production, characterization and potential. *Optics Express*, 15: 17542–17553, 2007.

[14] http://www.mo-sci.com.

[15] http://www.schott.com.

[16] P. Hua, J. P. Hole, J. S. Wilkinson, G. Proll, J. Tschmelak, G. Gauglitz, M. A. Jackson, R. Nudd, H. M. T. Griffith, R. A. Abuknesha, J. Kaiser, and P. Kraemmer. Integrated optical fluorescence multisensor for water pollution. *Optics Express*, 13: 1124–1130, 2005.

[17] E. Mwarania. *PhD thesis on Planar ion-exchange waveguide lasers in glass.* University of Southampton, Southampton, 1992.

[18] R. Ulrich and R. Torge. Measurement of thin film parameters with a prism coupler. *Applied Optics*, 12:2901–2908, 1973.

[19] S. Sebastiani, S. Berneschi, M. Brenci, G. Nunzi Conti, S. Pelli, and G. C. Righini. Simple approach to calculate the refractive index profile of ion-exchanged waveguides. *Optical Engineering*, 44:054602–054605, 2005.

[20] H. Zhenguang, R. Srivastava, and R. V. Ramaswamy. Low-loss small-mode passive waveguides and near-adiabatic tapers in BK7 glass. *Journal of Lightwave Technology*, 7:1590–1596, 1989.

[21] A. Bradenburg. Stress in ion-exchanged glass waveguides. *Journal of Lightwave Technology*, 4:1580–1593, 1986.

[22] B. E. Little, J. P. Laine, and H. A. Haus. Analytic theory of coupling from tapered fibers and half-blocks into microsphere resonators. *Journal of Lightwave Technology*, 17:704–715, 1999.

[23] M. L. Gorodetsky, A. A. Savchenkov, and V. S. Ilchenko. Ultimate Q of optical microsphere resonators. *Optics Letters*, 21:453–455, 1996.

[24] M. Rosenblit, P. Horak, S. Helsby, and R. Folman. Single-atom detection using whispering-gallery modes of microdisk resonators. *Physical Review A*, 70:053808–1–053808–10, 2004.

Chapter 4

Experimental characterisation of waveguide-coupled microspheres

4.1 Introduction

The aim of the work in this chapter is to measure waveguide-coupled WGM spectra, determine Q-factors, assign the sphere mode numbers and confirm agreement with the model to determine microsphere diameter. The appropriate model will be applied to identify sphere mode numbers and they will be assigned to the corresponding resonant wavelengths in the experimental results, then the corresponding microsphere diameter can be obtained accordingly. The experimental data will be analysed to confirm that the model is accurate such that the extraction of these useful parameters can be precisely obtained. Q-factors, which are the values that measure the sharpness of the resonant peaks, can be used to help quantify the efficiency of the light coupling from the waveguide to the microsphere. The determination of the quality factor of a microsphere coupled to a planar waveguide will be carried out with various types of microspheres including sodalime, Nd-doped and Er-doped BK7 microspheres. The Nd-doped BK7 microspheres, fabricated as described in Chapter 3, will also be characterised so that the comparison with commercially available microspheres [1] can be made. The study of Q-factors of a microsphere coupled waveguide as a function of microsphere location with respect to the centre of the waveguide will be carried out. This study is useful to indicate trends of Q as a function of microsphere location with respect to the centre of the waveguide.

Straightforward experiments for the observation of the change of the signal (that is proportional to the light circulated in the microsphere on a planar waveguide) as a function of wavelength will be carried out to visualise the behaviour of the scattered power of a microsphere coupled to a waveguide as a function of wavelength. The microspheres will be excited by evanescent fields from potassium-sodium-ion and silver-sodium-ion exchanged waveguides, for which details of fabrication were discussed in Chapter 2. Ti-

tanium:sapphire, Ti:Al_2O_3, and Agilent 81600B tunable lasers will be used as tunable light sources so that the scattered light from the microsphere as a function of wavelength can be observed. The titanium:sapphire laser is a solid-state laser medium that has a broad range of tunability from 680 nm to 1025 nm, and it produces TEM_{00} output profile in TM polarisation. The tunability of the titanium:sapphire laser covers an absorption wavelength region of Nd-doped microspheres (800 nm to 825 nm), thus, it is selected because is a suitable pump source for the experimental work in Chapter 6 on Nd-doped microsphere lasers. The experimental data will be compared to the theoretical modelling, and the data is required to be accurate so that the comparison can be done with minimal error. The Agilent 81600B tunable laser is selected for the experiments in operating wavelength of the 1550 nm region, because it has a fast and accurate sweep across the entire wavelength range from 1440 nm to 1640 nm, with a scan resolution of 1 pm. With automated wavelength tunability, the experiment allows measurements with high wavelength resolution to be done quickly.

In Section 4.2, WGM propagation in microspheres will be observed. The experimental apparatus employed for microsphere excitation from 750 nm to 830 nm will be shown and the experimental results and observations will be discussed. The quality factors of the microsphere will be obtained and the relative comparison of microsphere surfaces can be done accordingly. Section 4.4 includes the experimental setup, method and results on a microsphere coupled waveguide when the microsphere is translating across the waveguide, the Q-factors as a function of the position of the microsphere with respect to the waveguide centre will be obtained. Section 4.5 includes the method, approaches and the discussion of the procedure employed to fit the experimental data to the model. Section 4.5 contains examples of the data fitting method, which explain the results obtained from Section 4.3 and Section 4.4.

4.2 Microsphere excitation at wavelengths between 750 nm and 830 nm

In this section, the experimental work on the observation of scattered light from microspheres on a planar waveguide as a function of wavelength, at wavelength of 750 nm to 830 nm, is discussed. A titanium:sapphire laser is used as a tunable light source so that the tunability from 750 nm to 830 nm can be obtained. Section 4.2.1 includes the experimental apparatus for measuring the scattered light from microspheres coupling with a planar waveguide by imaging the illuminated microsphere with a CCD camera, while the experimental apparatus and procedure of an alternative way of measuring the scattered light from the microsphere by directly measuring the scattered power with a silicon detector is described in Section 4.2.2. Results, including the derivation of quality factor, Q, of the microsphere due to the coupling with the waveguide, will be discussed at the end of the section.

4.2.1 Microsphere excitation in the 750 nm region

In this section, the measurements of the scattered light as a function of wavelength from a 30±2 μm diameter sodalime microsphere [2] coupled with a potassium-sodium-ion exchanged channel waveguide (that was fabricated in Section 3.2) are described. Light collection is carried out by imaging the scattered intensity of the microsphere using a microscope connected with a CCD camera, at each wavelength. In order to obtain the relative power of the scattered power from the microsphere as a function of wavelength, a straightforward image processing method is applied to the images. The experimental apparatus and the image processing technique, of obtaining the net power of the scattered light from the microsphere, are discussed as following.

4.2.1.1 Experimental apparatus

A 512-nm output beam from an argon-ion laser was directed to an input aperture of a titanium:sapphire laser. The output beam of the titanium:sapphire laser was directed to a mirror, and it was then reflected to the second and third mirror. The collimated beam of about 2 mm in diameter at FWHM was focused onto the potassium-sodium-ion exchanged channel waveguide, by the microscope objective lens of 10× magnification, to allow light to travel along the waveguide path. The evanescent field from the potassium-sodium-ion exchanged waveguide is coupled into a sodalime microsphere [2] which located on top of the waveguide channel, where the interactions are observed. The tunable laser was tuned so that the scattered power as a function of wavelength was obtained.

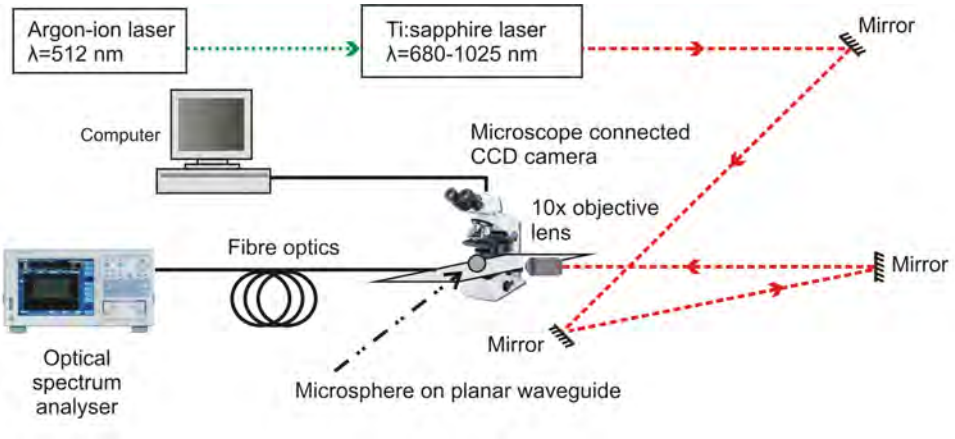

FIGURE 4.1: Experimental setup

The images of the scattered light of the microsphere were taken as function of wavelength, as the laser wavelength was tuned. The exposure time of the CCD camera was set to ensure that the CCD camera was not saturated over the complete wavelength range of the experiment. To prevent the interference from the surrounding light, the experiment was

done in a dark environment. Wavelength measurements were performed by monitoring the output spectrum from the through-port of the waveguide on an optical spectrum analyser, OSA, see Figure 4.1. The following sections will describe the analysis technique and the experimental results obtained from the setup described.

4.2.1.2 Analytical techniques

Light from a titanium:sapphire laser was end-fire coupled into the waveguides, the wavelength was recorded using an optical spectrum analyser, and each individual microsphere was imaged on a CCD camera through a microscope. Images of the microsphere were captured as the input wavelength was tuned from 745 nm to 765 nm, in order to observe their resonances. The power falling on the CCD, due to scattering and radiation, was proportional to the circulating WGM power, and this was calculated by integrating over the pixels in a rectangular area surrounding the microsphere and subtracting a background signal taken from a similar area away from the microsphere; this was then normalised to the output power of the laser.

The wavelength was manually tuned with a wavelength scan resolution of about 0.1 nm over the range of 745 nm to 765 nm, sufficient to observe four resonant peaks. Photographs of the microsphere were taken at each wavelength. The scattered intensities obtained in this chapter were proportional to the circulating intensities obtained in Chapter 2.

Figure 4.2 shows an image of microspheres above a waveguide corresponding to a resonant wavelength (753.97 nm). There are two microspheres located on the substrate; one is on the centre of the waveguide and the other one is off centre of the waveguide. At the resonant condition, the microsphere located on the waveguide has a higher intensity than the microsphere located off the waveguide. This indicates that the microsphere resonator on the waveguide is excited by the guided light from the waveguide.

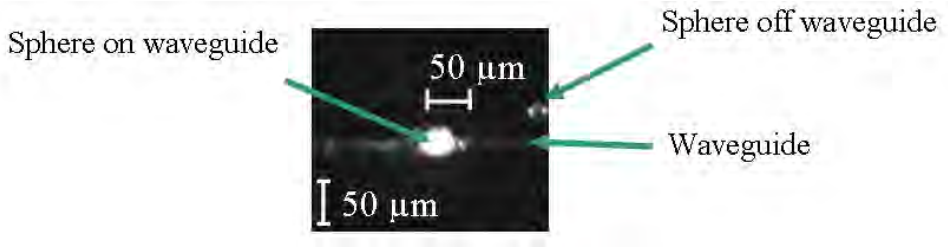

FIGURE 4.2: Image description ($\lambda = 753.97$ nm)

Figure 4.3 shows 24 sample images with their corresponding wavelengths. It can be seen from the figure that wavelengths that are supported by the resonator under the resonant condition are 749.90 nm, 753.97 nm, 758.01 nm and 762.13 nm. These wavelengths are defined as resonant wavelengths. At the resonant wavelengths, the microsphere has

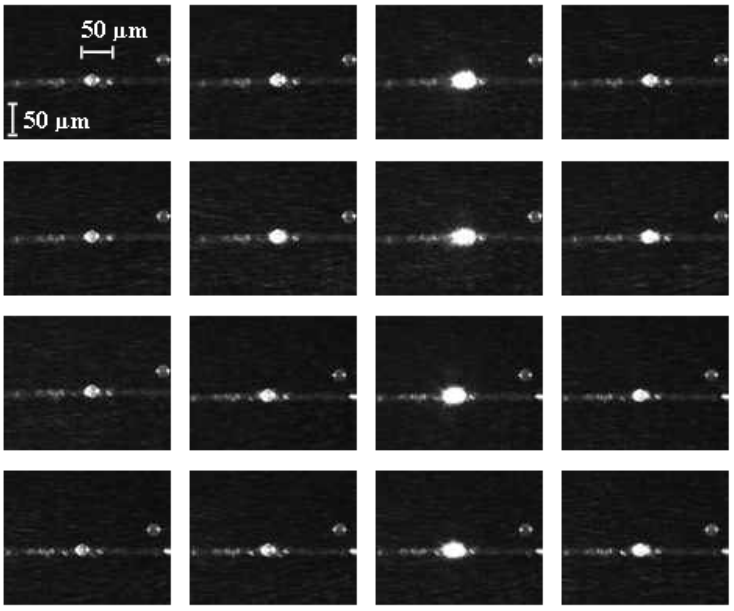

FIGURE 4.3: 24-sample image with 16 corresponding wavelengths:
749.70 nm, 749.80 nm, 749.90 nm, 749.96 nm,
751.35 nm, 753.86 nm, 753.97 nm, 754.04 nm,
755.24 nm, 757.93 nm, 758.01 nm, 758.50 nm,
759.92 nm, 762.06 nm, 762.13 nm, 762.24 nm.

a relatively higher intensity than at other wavelengths. Quantitative determination of the microsphere power was performed by applying a straightforward method of image processing. A signal, proportional to the intensity of the light circulating in the microsphere, was calculated by integrating the power falling on each pixel over an area of $m \times n$ pixels including the resonator. Each pixel has a specific power value, and the integration of the power for all pixels within this area is considered as the signal that is proportional to the scattered intensity of the microsphere, see Equation 4.1.

$$\mathrm{P}_{\mathrm{scattered}} \propto \sum_{y=0}^{m} \sum_{x=0}^{n} \mathrm{P}(x, y), \tag{4.1}$$

where n, m are the numbers of pixels in the x, y direction respectively. $\mathrm{P}(x, y)$ is the pixel power at (x, y).

Then the elimination of the background signal was done by subtracting it from the scattered power for each wavelength, see Figure 4.4. The net power, $\mathrm{P}_{\mathrm{net}}$, for each wavelength was simply obtained from Equation 4.2.

$$\mathrm{P}_{\mathrm{net}}(\lambda) = \mathrm{P}_{\mathrm{scattered}}(\lambda) - \mathrm{P}_{\mathrm{background}}(\lambda) \tag{4.2}$$

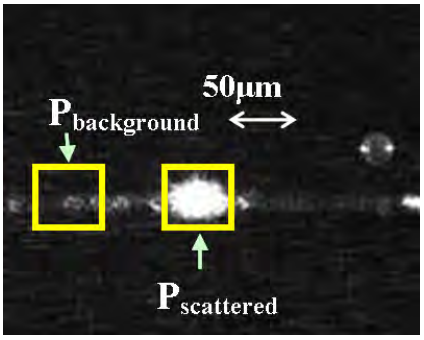

FIGURE 4.4: Microsphere scattered and background power

4.2.1.3 Experimental results and discussion

An example of collected scattered power as a function of wavelength, $P_{net}(\lambda)$, is shown in Figure 4.5. Each point of the plot in Figure 4.5 indicates the collected scattered power (P_{net}), which was calculated by using Equation 4.1 and Equation 4.2, at each wavelength. The resonant wavelengths obtained from the experimental results were 749.90 nm, 753.97 nm, 758.01 nm and 762.13 nm.

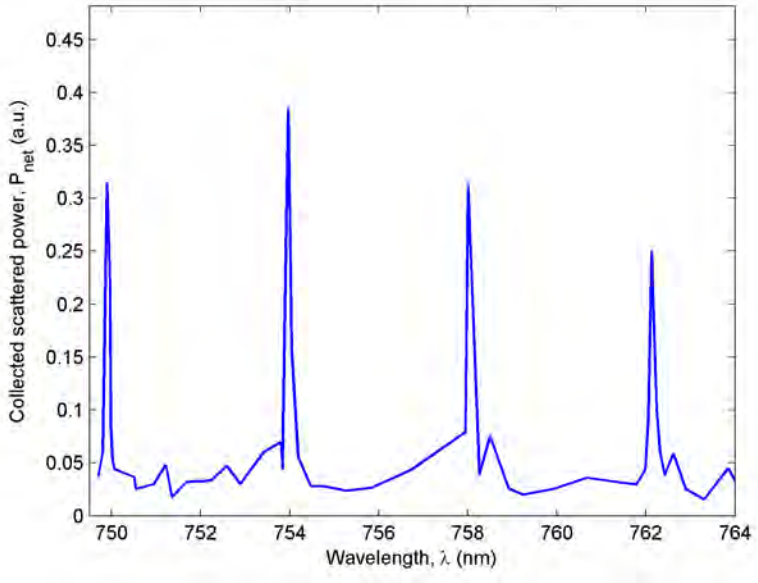

FIGURE 4.5: Collected scattered power as a function of wavelength, $P_{net}(\lambda)$ (wavelength resolution 0.1 nm)

From the experimental results shown in Figure 4.5, the resonant peaks separation (FSR) is 4.107±0.013 nm and the width of the resonant lobe at full-width of half-maximum ($\delta\lambda_{FWHM}$) is about 0.12 nm at the centre wavelength of around 762 nm. The value of $\delta\lambda_{FWHM}$ can be used to determine the quality factor of the resonant peaks, where Q can be obtained by dividing the resonant wavelength with $\delta\lambda_{FWHM}$, the relation is shown as following,

$$Q = \frac{\lambda}{\delta\lambda_{FWHM}}. \tag{4.3}$$

At the resonant wavelength of 754.00 nm, the quality factor is found to have a value about 6×10^3. It is to be noted that this value of Q is a worst-case value due to the large data point spacing. The information obtained from the experimental data can be used to determine the optical path length of the WGM and consequently the actual size of the microsphere can be obtained. The detail will be given in Section 4.5.

4.2.2 Microsphere excitation in the 800 nm region

In this section, the scattered power from a commercial 1.5-wt% Nd_2O_3-doped BK7 microsphere (D = 30±3 μm, $n_s \sim 1.50$ @ 800 nm) [1] coupled to a potassium-sodium-ion exchanged planar waveguide is detected and recorded with a silicon detector as a function of wavelength. Net scattered powers as a function of wavelength are obtained. The experimental apparatus, results and discussion are shown as follows.

4.2.2.1 Experimental apparatus

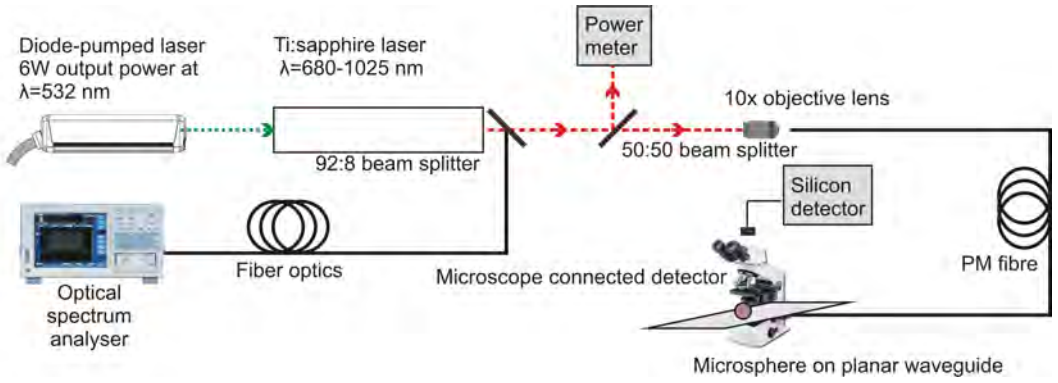

FIGURE 4.6: Experimental apparatus: Scattered light collecting with silicon detector

A 532-nm output beam from the diode-pump laser of 6 Watts was launched into the input aperture of the Ti:sapphire laser. The output, in TM polarisation, from the titanium:sapphire laser was 8% tapped to the optical spectrum analyser for wavelength monitoring. The remaining light was split by a 50:50 beam splitter, where 50% of the light was focused into a polarisation maintaining fibre and launched into the waveguide input end via a 10× microscope objective lens, and the rest of the light was launched into the power meter for real time power monitoring of the input power prior to the objective lens, see Figure 4.6. A Nd-doped microsphere was placed ontop of the potassium-sodium-ion exchanged waveguide. The scattered light was collected and recorded as a function of wavelength via the silicon detector as the input wavelength was tuned. The detector was connected to the microscope, so that the position of the microsphere was monitored.

4.2.2.2 Experimental results and discussion

Figure 4.7 shows the experimental results obtained from the Nd-doped BK7 microsphere. There are "strong" and "weak" resonant peaks shown in the results, where the FSR of the two families are 4.65±0.05 nm and 4.75±0.08 nm, respectively, as expected for the microsphere of about 30 μm diameter at the centre wavelength of around 818 nm. Q values of the two family peaks are found to be about 1.5×10^3 and 1×10^3, respectively, with the corresponding lobe widths at half maximum of 0.52 and 0.80 nm, respectively. The discussion and explanation on the occurrence of each family of peaks and the modal assignment will be given in Section 4.5.

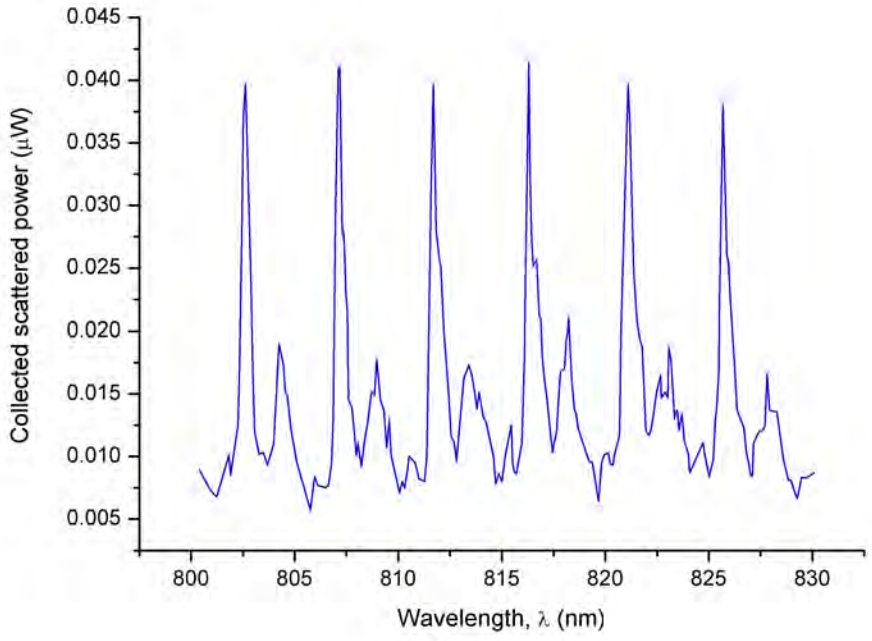

FIGURE 4.7: Experimental results: Nd-doped BK7 microsphere on uncoated-waveguide (wavelength resolution 0.1 nm)

The experiment was done in a dark environment to exclude the background noise, however, the background level which is shown in Figure 4.7 might occur due to the light from instruments. To prevent this from happening instruments should be covered with opaque screens.

4.3 Characterisation of commercial and in-house made Nd-doped BK7 microspheres

The aim of the experimental work in this section is to characterise the commercial Nd-doped BK7 microspheres and the in-house made Nd-doped BK7 microspheres obtained from the dropping technique, as described in Section 3.4.2. These in-house made microspheres will be used for microsphere laser experiments that will be described in Chapter 6. In this section, the comparison of the characteristics of the commercial and the in-house made Nd-doped microspheres will be explored. At the beginning of the section, commercial Nd-doped BK7 microsphere of 30±3 μm in diameter [1] will be characterised and the explanation of the results will be included, while the results from the experiment on an in-house made Nd-doped BK7 microsphere, with nominal diameter 200 μm, will be obtained at the latter part of the section. The discussion on the comparison of these results will be given at the end of the section. A silver-sodium-ion exchanged waveguide, which operates single mode at 1550 nm will be used to evanescently excite the microsphere. The experiments are carried out with a tunable Agilent 81600B laser, so the automatic sweep with fine resolution of tunability in the 1550 nm region can be obtained. The accurate data is obtained for sphere mode assignment, and the comparison of the experimental data will be described in Section 4.5.

4.3.1 Experimental apparatus

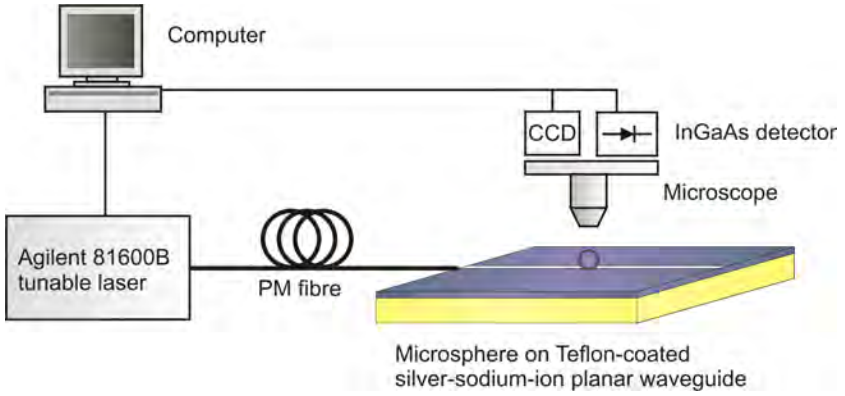

FIGURE 4.8: Experimental apparatus: Agilent 81600B tunable laser

Laser light (linewidth of 100kHz), in the TM polarisation, was focused into a polarisation maintaining fibre and coupled into the waveguide by butt-coupling. A microscope with CCD camera was used to monitor the position of the microsphere and a microscope connected InGaAs detector was used to measure and record the light scattered from the microsphere. The position of the microsphere was optimised by translating it across the waveguide and maximising the scattered power detected on resonance. The tuning resolution of 1pm was used in the experiment. In this experiment, the microsphere Q

was limited by surface roughness and therefore the power scattered from the microsphere was presumed to be proportional to the circulating power for a given mode. Both the power scattered and the power emerging from the waveguide were recorded as a function of laser wavelength.

4.3.2 Experimental results and discussion

Figure 4.9 shows the scattered power collected from a 30 μm diameter microsphere through the microscope by the InGaAs detector as a function of wavelength. The experimental data show both high amplitude strong resonance and a family of weak resonances. The FSR of these two families are 17.380±0.005 nm and 18.138±0.002 nm at the centre wavelength respectively.

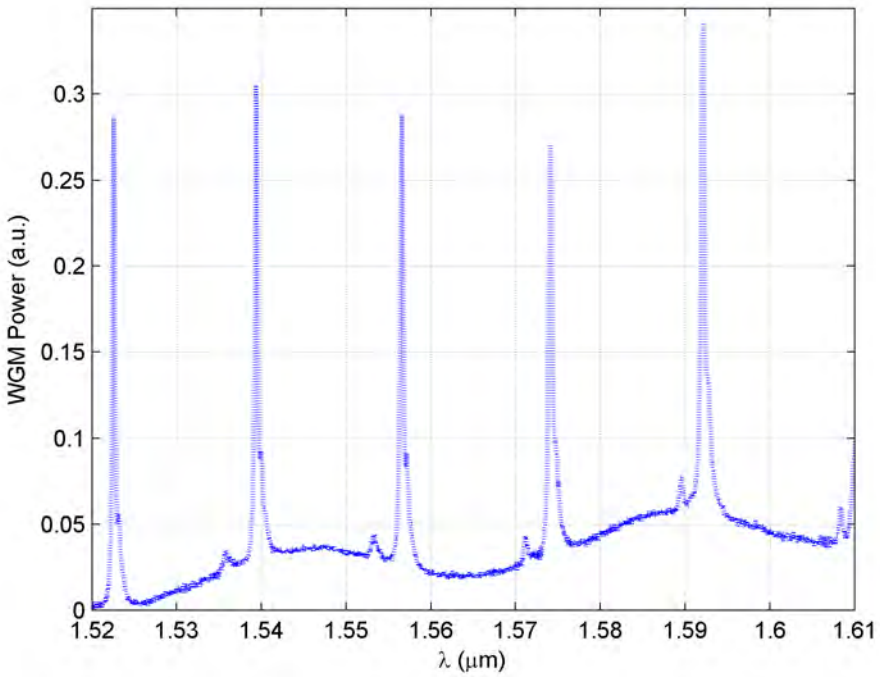

FIGURE 4.9: Experimental results: 30 μm Nd-doped BK7 microsphere on an uncoated-waveguide, 1550 nm laser source (wavelength resolution 10 pm)

In order to study the excitation of higher-order radial modes, larger microspheres were studied as, for the present geometry, the larger diameter leads to a larger circulating power in each mode due to the increased coupling factor, as shown in the coupling factor equation in Chapter 2, primarily due to the longer effective coupling region. Nd-doped BK7 microspheres that have nominal diameters of 200 μm, made by the dropping through a furnace technique described in Chapter 3, are used in this section.

Figure 4.10 shows the experimental results obtained for scattered WGM power vs wavelength for an in-house made microsphere with a nominal diameter of 200 μm, obtained

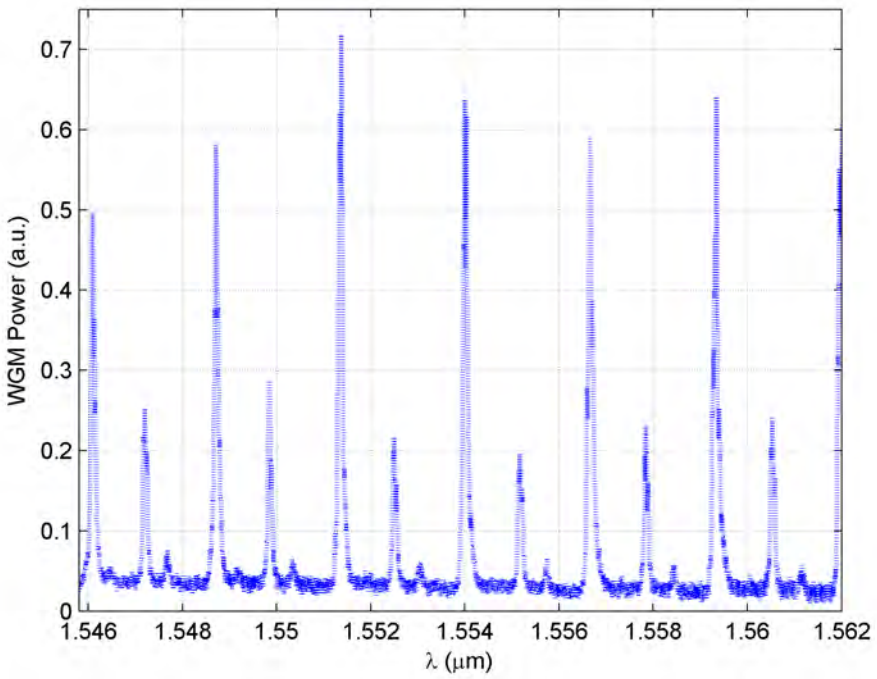

FIGURE 4.10: Experimental results: 200 μm Nd-doped BK7 microsphere on a 460 nm-Teflon-coated waveguide, 1550 nm laser source (wavelength resolution 10 pm)

in the same way as the spectra in Figure 4.25. The experimental data show the evidence of three families of resonances. This is because, in the larger microspheres, the higher κ were found for high order modes, thus, the high order modes were excited. The free spectral range of the strongest ($n = 1$) family of peaks is found to be 2.655±0.003 nm at the centre wavelength, and these modes showed Q-factors of 2.3×10^4. Two other families of peaks are observed, and the FSR of the second and third families are 2.671±0.001 nm and 2.70±0.01 nm at the centre wavelengths, respectively. The detailed discussion of mode assignment for these sets of data will be given in Section 4.5.

4.4 Measurement of Q-factor as a function of vertical and lateral displacement of an in-house made Er-doped BK7 microsphere

The experimental apparatus in this section is set up so that the measurement to confirm how the Q-factor of the scattered light from a microsphere coupled waveguide relates to the separation displacement or the position of the microsphere with respect to the waveguide centre can be obtained. An Agilent 81600B tunable laser source which provides a narrow linewidth is used, because the data comparison (made in Section 4.5), and the results must be sufficiently precise so that the information extracted from the model can be accurate. This section includes experimental data sets obtained by Dr. Senthil Ganapathy. The experimental setup and procedures on the variation of vertical and lateral positions of the Er-doped BK7 microsphere to the waveguide centre will be shown. An Er-doped BK7 microsphere of 130 μm in diameter (with ± 2 μm tolerance), that was fabricated based on the method described in Section 3.4.1, will be used. Various thicknesses of Teflon layer ($n_{\text{Teflon}} \sim 1.29$), ranging from 70 nm to 740 nm ($\pm$ 5%), were evaporated onto the silver-sodium-ion exchanged waveguide substrate across the channels of the waveguides, as a buffer layer to separate the microsphere from the waveguide surface in the vertical direction. The explanation of experiments on measuring the scattered light as a function of wavelength, at various lateral displacements with respect to the centre of the waveguide, will be given. The section will include the results on the quality factors of the microsphere at various separations in both vertical and lateral displacements with respect to the centre of the waveguide.

4.4.1 Experimental apparatus

Light, in the TM polarisation, from an Agilent tunable laser source was launched into polarisation maintaining fibre, so that it was butt-coupled to the waveguide input facet. Light propagated along the waveguide channel, and the evanescent light was coupled into the microsphere which was positioned on the waveguide surface. The separating distance in the vertical direction was controlled by the thickness of Teflon, D_{Teflon}, and the separating distance in the lateral direction, D_{lateral}, was manually varied with a precision nano-translation stage. The microsphere was monitored with two microscopes connected to CCD cameras which were setup in the vertical and lateral orientations, see Figure 4.11, so that the position of the microsphere in both orientations could be confirmed. The microsphere was attached to the fibre tip such that the flattened area was in contact with the fibre tip, so that the path of WGM propagation could be controlled to avoid propagating along the flattened area. The microsphere on the fibre stem attachment was also useful such that an identical microsphere was used throughout the experiment, in order to maintain the same orientation of the microsphere while

translating it vertically upward from the waveguide surface, and to maintain the same condition of the cavity loss due to the roughness and non-sphericity of the microsphere. The scattered light from the microsphere was detected by an InGaAs detector and recorded as a function of wavelength. Q as a function of position of the microsphere was extracted from the spectra.

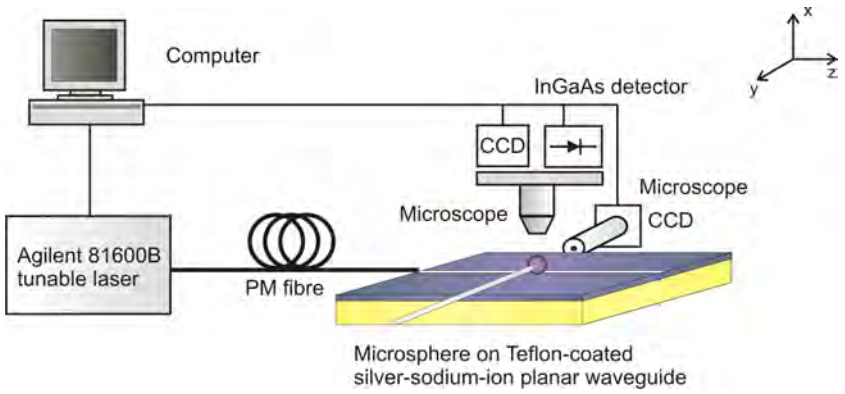

FIGURE 4.11: Experimental apparatus for Q measurement of the microsphere when it was translated in various positions in vertical and lateral displacements with respect to the waveguide centre

4.4.2 Experimental results and discussion

The measurement of the scattered light of the microsphere, when it was located at the centre of the waveguide, as a function of vertical displacement from the waveguide surface was carried out. The vertical direction is defined as the direction along the perpendicular plane (xy-plane) with respect to the waveguide surface, and the lateral displacement is the direction which is parallel to the waveguide surface across the waveguide channels (y-axis). The variation of the position of the microsphere in a vertical direction was controlled by the corresponding thickness of Teflon on the waveguide surface, D_{Teflon}.

Figure 4.12 shows plots in linear scale of the scattered light from $\lambda = 1440 - 1640$ nm of the microsphere as a function of vertical displacement from the waveguide surface. The figure shows overall variation of the scattered WGM amplitude as a function of sphere/waveguide separation. The featured characteristics of the spectra in detail from $\lambda = 1540 - 1560$ nm are displayed in a log scale. Figure 4.13 and Figure 4.14 show the plots in log scale of the scattered power as a function of the Teflon thickness, when the microsphere was located at centre and 6 μm away to the right-hand side from the centre of the waveguide (y = +6 μm), respectively. The values of width of the resonant lobes at full-width of half-maximum, $\delta\lambda_{\text{FWHM}}$, as a function of Teflon thickness at $\lambda = 1550$ nm are determined and shown in Table 4.1. The first column shows the values of the $\delta\lambda_{\text{FWHM}}$ of the resonant peaks when the microsphere was located at the centre of the waveguide, while in the second column, the values of $\delta\lambda_{\text{FWHM}}$, that correspond to the results when the position of the microsphere was 6 μm away from the centre of the

waveguide, are shown. At the Teflon thicknesses of more than 740 nm, no interaction was observed, this might be due to the fact that the microsphere was located further away from the waveguide surface where there was no interaction taking place.

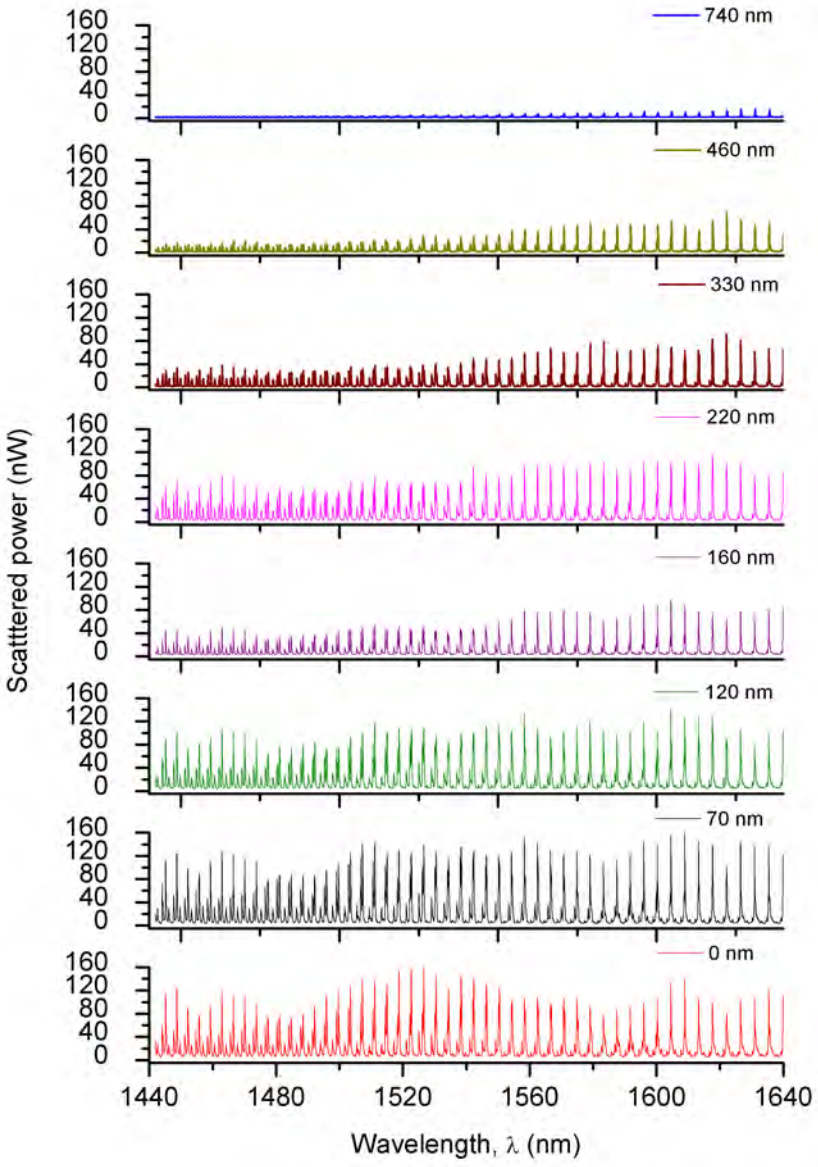

FIGURE 4.12: Scattered power of microsphere in linear scale as a function of Teflon thickness in the vertical displacement (microsphere located at the centre of the waveguide), $\lambda = 1440 - 1640$ nm (wavelength resolution 10 pm)

Q's are obtained from the $\delta\lambda_{\mathrm{FWHM}}$ shown in Table 4.1, plots of Q's from the scattered light of the microsphere located at the centre of the waveguide with a variation in the Teflon thickness from 0 nm to 740 nm, are shown in Figure 4.15. Q increases as the separation in the vertical direction of the microsphere with respect to the waveguide increases, as expected, because the coupling efficiency at the smaller separation is stronger

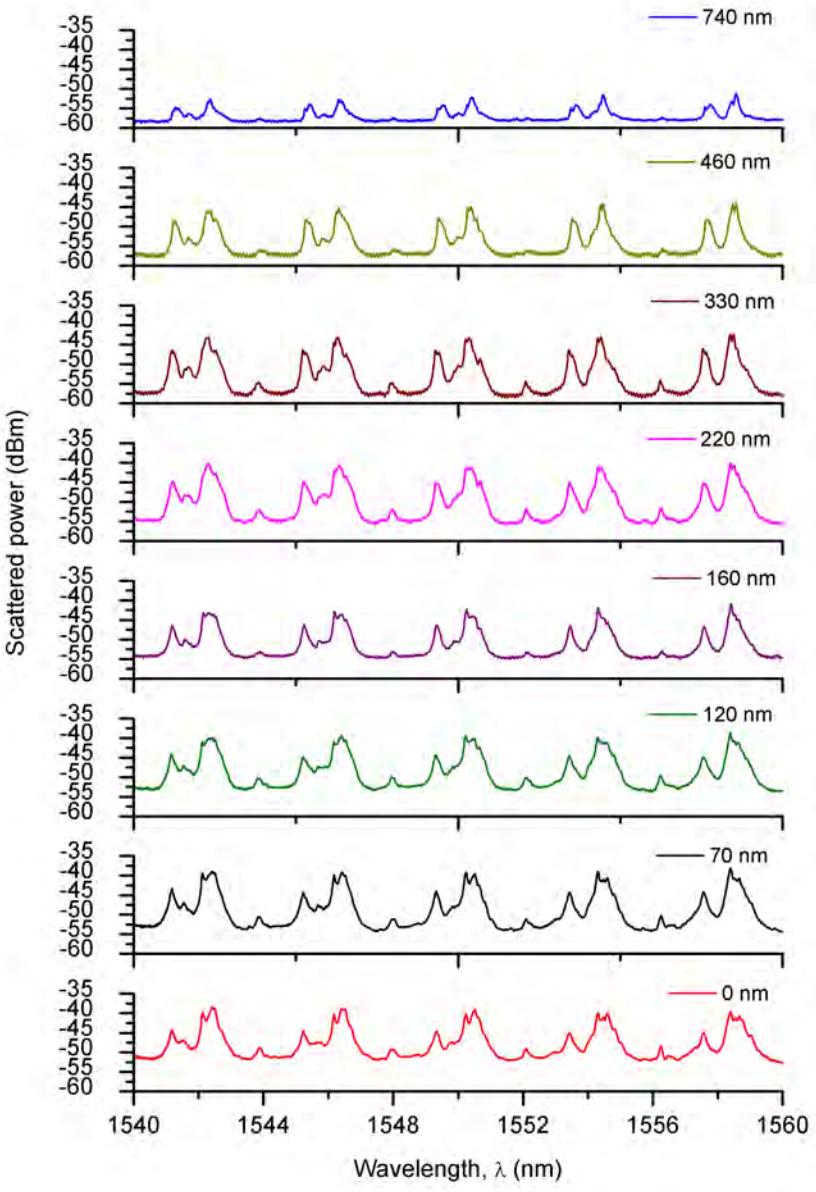

FIGURE 4.13: Scattered power of microsphere as a function of Teflon thickness in the vertical displacement (microsphere located at the centre of the waveguide), $\lambda = 1540 - 1560$ nm (wavelength resolution 10 pm)

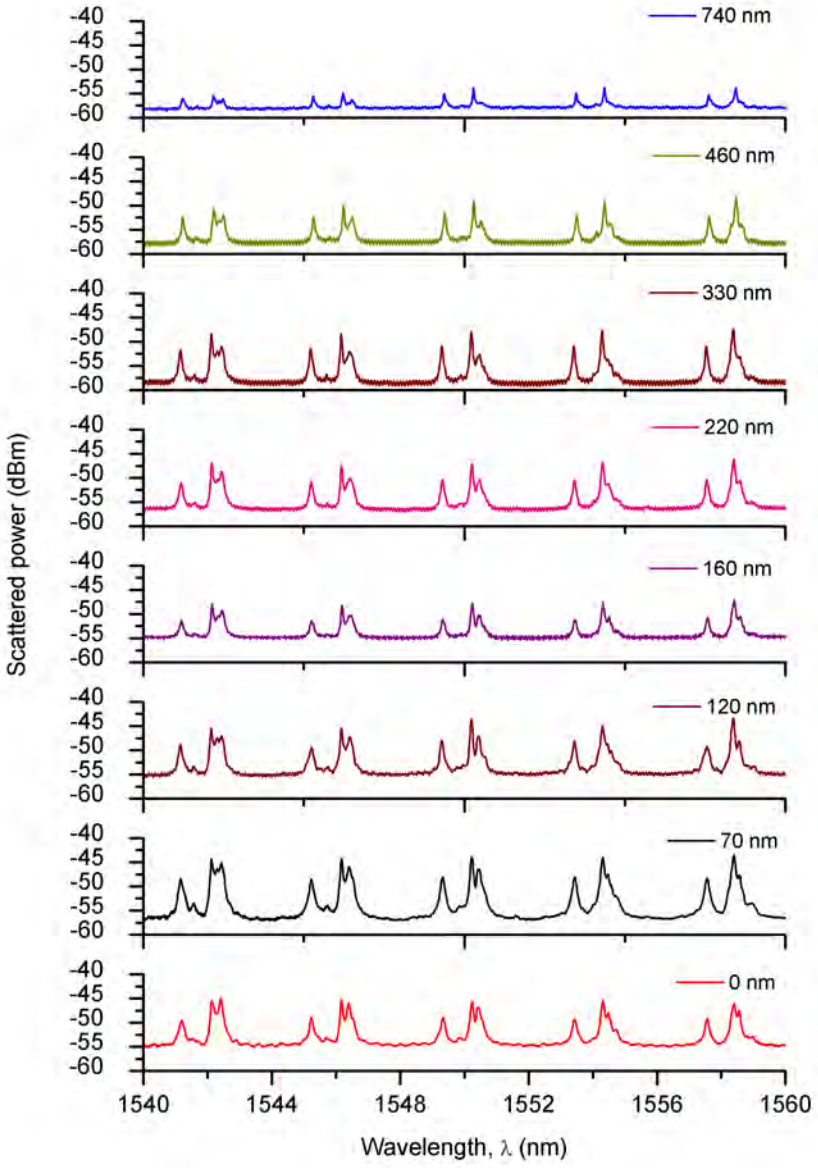

FIGURE 4.14: Scattered power of microsphere as a function of Teflon thickness in the vertical displacement (microsphere located at 6 μm away from the centre of the waveguide), $\lambda = 1540 - 1560$ nm (wavelength resolution 10 pm)

Teflon thickness (nm)	$\delta\lambda_{\mathrm{FWHM}}$ (nm) Microsphere located at centre of waveguide	$\delta\lambda_{\mathrm{FWHM}}$ (nm) Microsphere located at 6 μm away from waveguide
0	0.617	0.155
70	0.602	0.160
120	0.600	0.140
160	0.560	0.130
220	0.520	0.118
330	0.460	0.100
460	0.426	0.092
740	0.350	0.076

TABLE 4.1: Width of the resonant lobe at full-width of half-maximum power, $\delta\lambda_{\mathrm{FWHM}}$, as a function of Teflon thickness, at vertical separation of 330 nm, at $\lambda = 1550$ nm

compared to the larger separation. Figure 4.16 shows plots of Q as a function of $\mathrm{D_{Teflon}}$ of the scattered light from the microsphere located 6 μm away from centre of the waveguide. Q values obtained from Figure 4.15 are, respectively, smaller than the values found in the case where the microsphere was located at 6 μm away from the centre of the waveguide, because the microsphere couples more efficiently to the waveguide when it is located at the centre of the waveguide.

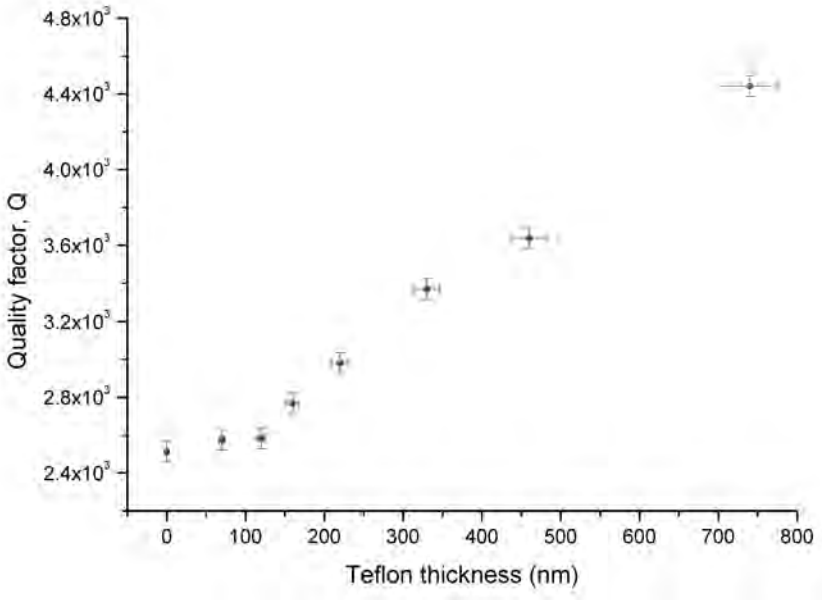

FIGURE 4.15: Q: Microsphere located at centre of waveguide as a function of Teflon thickness (in vertical variation), at $\lambda = 1550$ nm

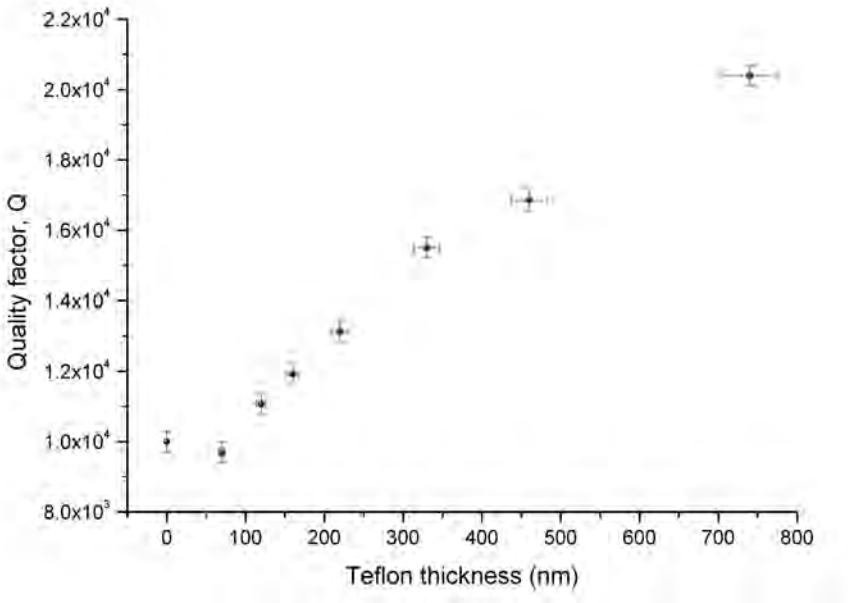

FIGURE 4.16: Q: Microsphere located 6 μm away from centre of waveguide as a function of Teflon thickness (in vertical variation), at $\lambda = 1550$ nm

In this section, microsphere WGM excitation as a function of lateral position is also characterised. The microsphere was precisely translated across the waveguide surface laterally for each different layer of the Teflon thickness, so that measurement of the scattered light as a function of lateral displacement of the microsphere with respect to the centre of the waveguide as a function of Teflon thickness, was obtained. The measurement was done with the same microsphere, which is the Er-doped BK7 microsphere on the fibre tip previously used in the vertical displacement measurement. Figure 4.17 shows the plot of the scattered light measured from the microsphere that was placed at 220 nm vertically away from waveguide surface as function of lateral displacement from -10 μm to 10 μm with respect to the centre of the waveguide (LHS to RHS). Figure 4.17, Figure 4.18 and Figure 4.19 show similar plots of the scattered light as a function of lateral displacement of the microsphere with respect to the waveguide centre, when the microsphere was located at 220 nm, 460 nm and 740 nm away from the waveguide surface respectively.

Table 4.2 shows the values of resonant width at half-maximum power, $\delta\lambda_{\mathrm{FWHM}}$, of the scattered powers measured from the microsphere which was located at 220 nm, 460 nm, and 740 nm vertically away from the waveguide surface as a function of the lateral displacement from -10 μm to 10 μm from the centre of the waveguide. The values of $\delta\lambda_{\mathrm{FWHM}}$ are used to obtained the corresponding Q-factors, where the plots of Q-factor as a function of lateral displacement, at different Teflon thicknesses, are shown in Figure 4.20.

Teflon thickness (nm)	Width of the resonant lobe at FWHM, $\delta\lambda_{\mathrm{FWHM}}$ (nm)						
	Lateral displacement from waveguide centre (μm)						
	LHS					RHS	
	-10	-6	-2	0	+2	+6	+10
220	0.29	0.39	0.52	0.60	0.49	0.16	0.08
460	0.19	0.28	0.40	0.46	0.40	0.12	0.07
	Lateral displacement from waveguide centre (μm)						
	LHS					RHS	
	-8	-6	-2	0	+2	+6	+8
740	0.13	0.16	0.26	0.32	0.24	0.11	0.08

TABLE 4.2: Width of the resonant lobe at full-width of half-maximum power, $\delta\lambda_{\mathrm{FWHM}}$, in lateral direction as a function of Teflon thickness, at $\lambda = 1550$ nm

It can be seen from Table 4.2 that, for the variation in lateral direction, as the separation of the microsphere from waveguide centre gets larger, the values of the width of the resonant lobe at half-maximum power are found to be smaller. Thus, for the microsphere located at the centre of the waveguide, Q-factors are found to be minimum and Q-factors increase as the separation in the lateral direction of the microsphere and waveguide are larger as shown in Figure 4.20. This is because as the separation gets larger, coupling efficiency of the microsphere to the waveguide is smaller, hence a higher Q-factor is

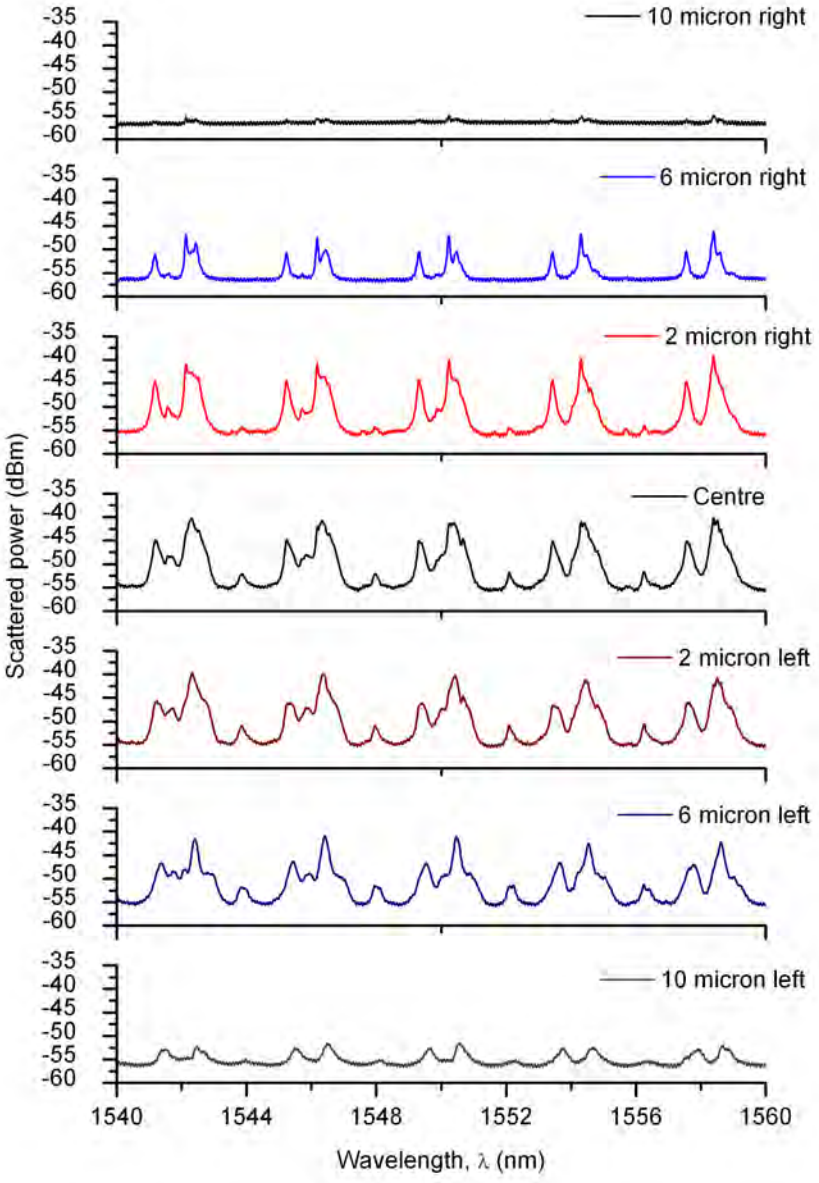

FIGURE 4.17: Scattered power of microsphere as a function of lateral displacement (microsphere located at 220 nm away from the waveguide), $\lambda = 1540 - 1560$ nm (wavelength resolution 10 pm)

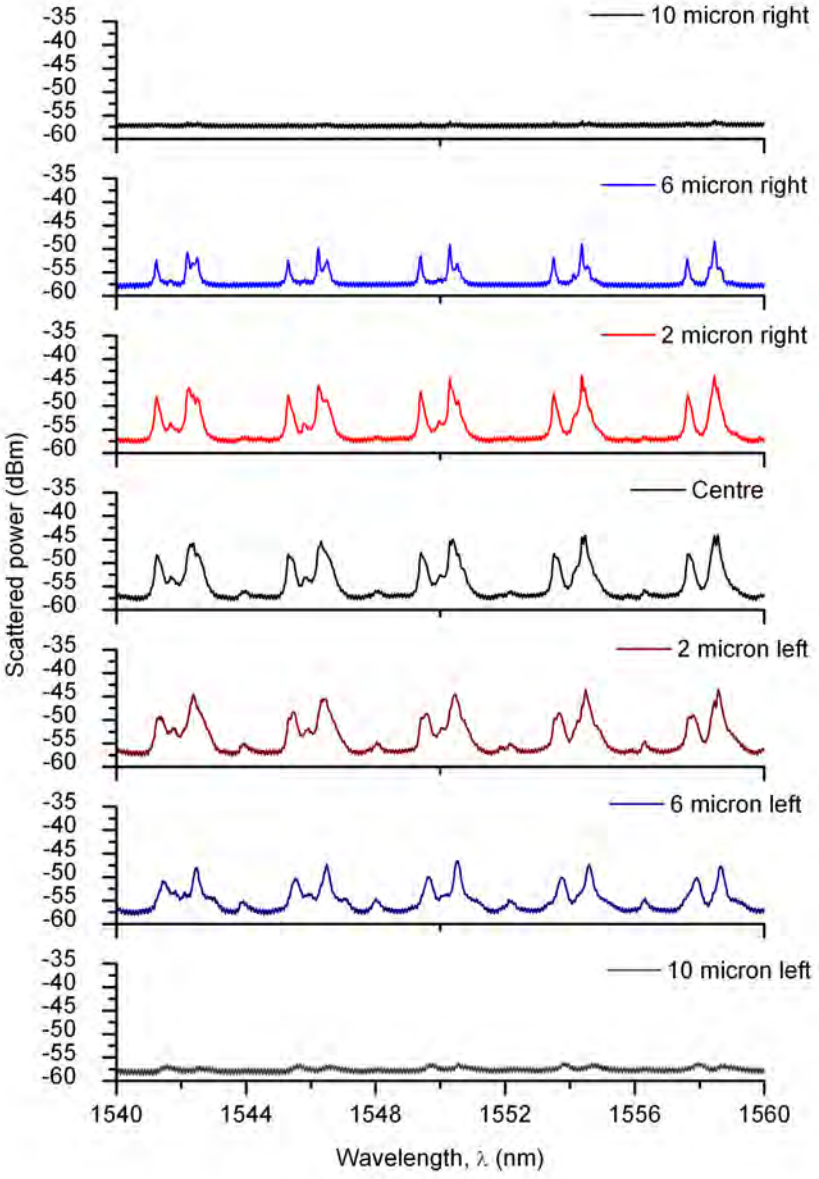

FIGURE 4.18: Scattered power of microsphere as a function of lateral displacement (microsphere located at 460 nm away from the waveguide), $\lambda = 1540 - 1560$ nm (wavelength resolution 10 pm)

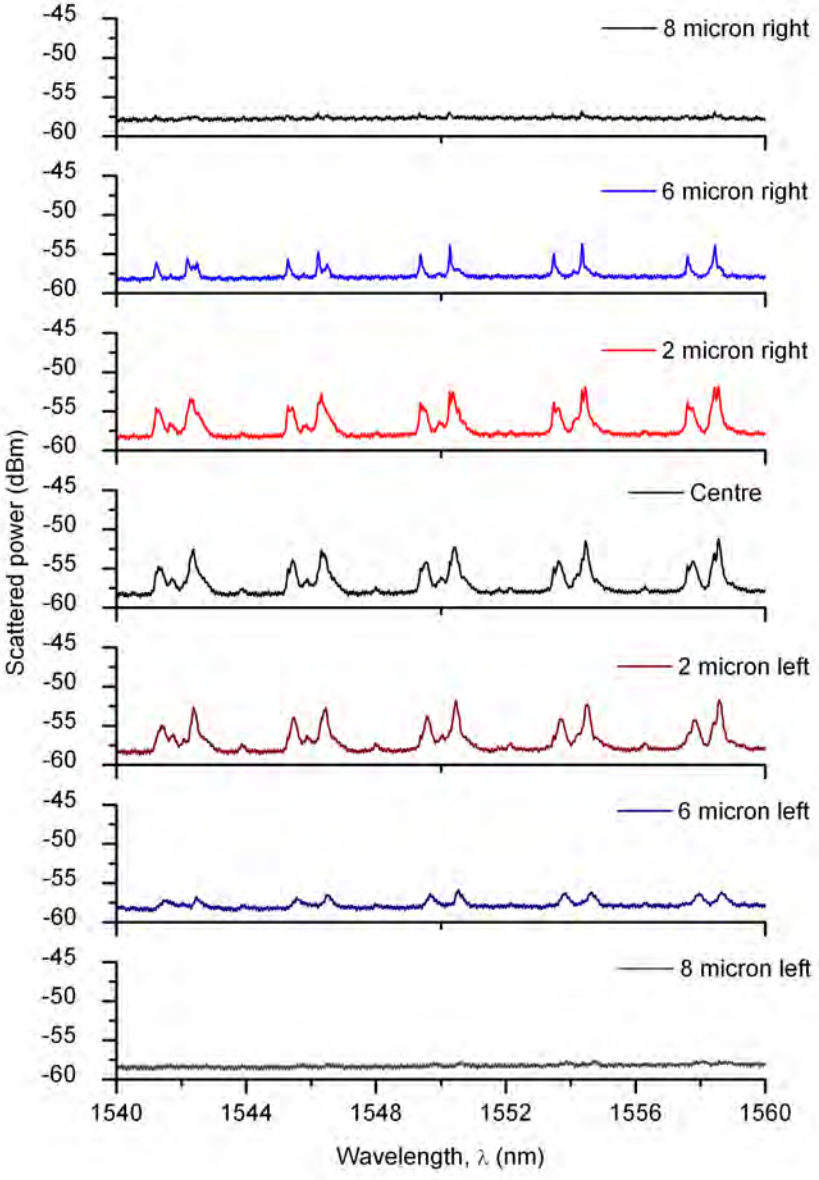

FIGURE 4.19: Scattered power of microsphere as a function of lateral displacement (microsphere located at 740 nm away from the waveguide), $\lambda = 1540 - 1560$ nm (wavelength resolution 10 pm)

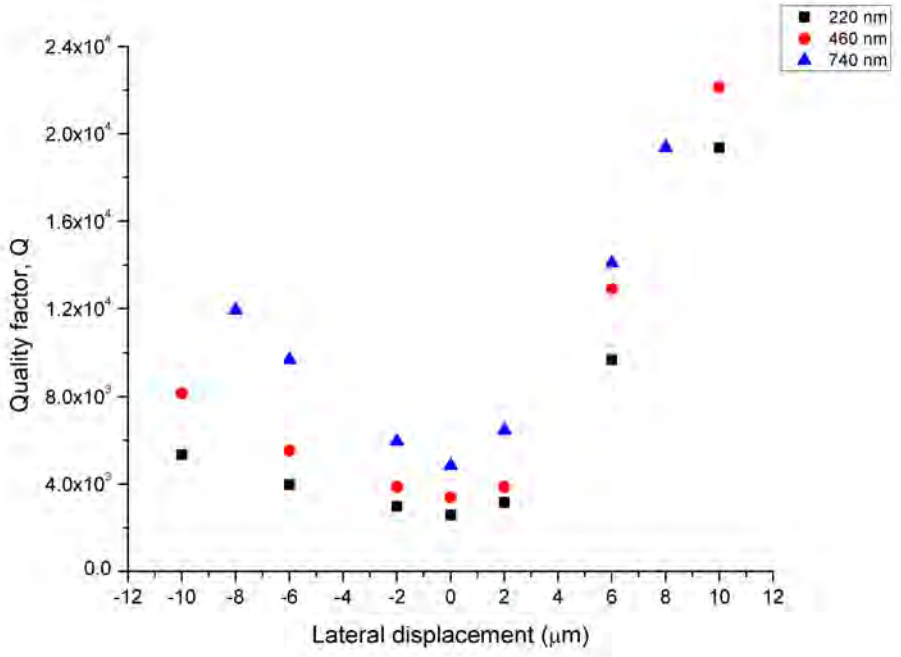

FIGURE 4.20: Q: Microsphere located at 220 nm, 460 nm, 740 nm away from waveguide surface in vertical direction, as a function of lateral displacement from -10 μm to +10 μm from centre of waveguide, at $\lambda = 1550$ nm

obtained. It can be seen as shown in Figure 4.20 that the Q-factors are not the same in the left and right hand side, this is probably because the WGM propagation in the microsphere was disrupted with the flattened area of the microsphere, or the fibre stem, as the microsphere attached to the fibre-stem was translated across the waveguide to the left, thus, Q values with respect to the microsphere position on the left-hand-side to the waveguide centre were found to be smaller than the ones on the right-hand-side. Figure 4.20 shows that Q-factors at 220 nm separation are smaller than the case of 460 nm and 740 nm separations, respectively, as expected. The section on theoretical modelling to extract the microsphere diameter and mode assignment for these sets of data will be included in Section 4.5.

4.5 Theoretical modelling for fitting experimental data and sphere mode assignment

In this section, the procedure for fitting the width of the resonant peaks from the experimental data to the Lorenzian relation [3] and mode assignment to the experimental results obtained from the previous section, are discussed. The determination of the resonant wavelength for each mode can be obtained with the use of the characteristic equation, Equation 2.4, that relates the wavelengths to the sphere mode numbers, and microsphere diameter [4]. The fitting procedure is presented in Section 4.5.1 and examples for illustrating the fitting procedure are given in Section 4.5.2. The amplitude and width of the resonant peaks, $\delta\lambda$, are related to total loss in the cavity, α, and coupling factor, κ. Information such as microsphere diameter, D, circulation loss factor, α, and coupling factor, κ, will be extracted by the fitting process from the free spectral range, FSR, that can be determined from the experimental data.

4.5.1 Algorithm

Precise assignment of mode numbers to the experimental data and extraction of the physical diameter of the microsphere from these data requires matching theoretically predicted resonant wavelengths with all the experimentally measured resonances, using the characteristic equation, Equation 2.4. Each solution of the characteristic equation yields the field distribution of a WGM. l is the azimuthal mode number and is equal to the number of wavelengths taken to travel around the microsphere for a particular resonance. For a particular value of sphere mode number l for a particular sphere radius and index, there are many solutions of the characteristic equation. These solutions correspond to a different radial mode numbers n. The sphere mode numbers m (m is the polar mode number) are degenerate and they have the same value of l and n. For a perfect sphere $m = l$. The fundamental has $m = l$ and $n = 1$. Depending on the coupling between the sphere cavity and the waveguide, several n modes may be excited.

Figure 4.21 shows example plots of the field distributions of the fundamental ($l = 83$, $n = 1$) and the second order ($l = 77$, $n = 2$) modes as a function of radial position, for a microsphere that has a refractive index of 1.50 and a diameter of 30 μm. These solutions exist at wavelengths of $\lambda_{83,1} = 1551$ nm and $\lambda_{77,2} = 1549$ nm, respectively. The field distributions shown in Figure 4.21 are normalised so that equal power is carried in both whispering gallery modes.

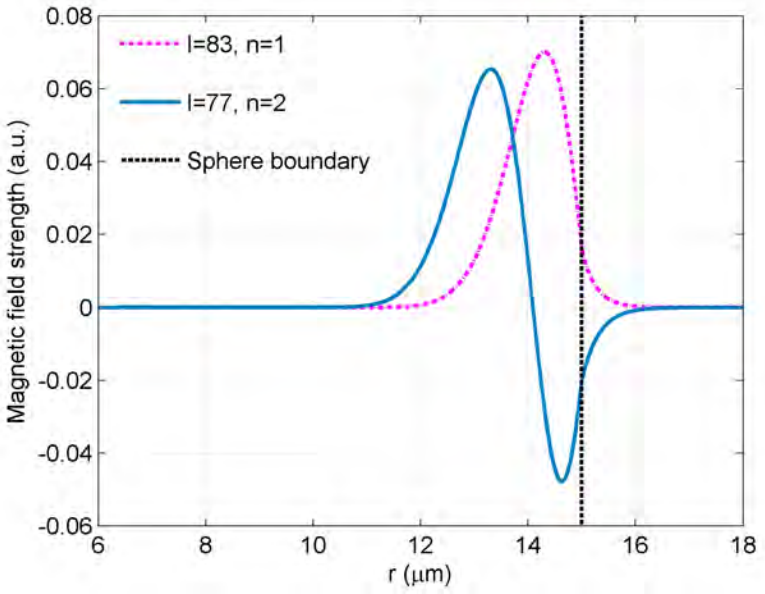

FIGURE 4.21: WGM radial field distributions for the 30 μm diameter microsphere

The refractive index of the BK7 microspheres obtained using the Schott datasheets and the Sellmeier equation [5] and is shown in Figure 4.22.

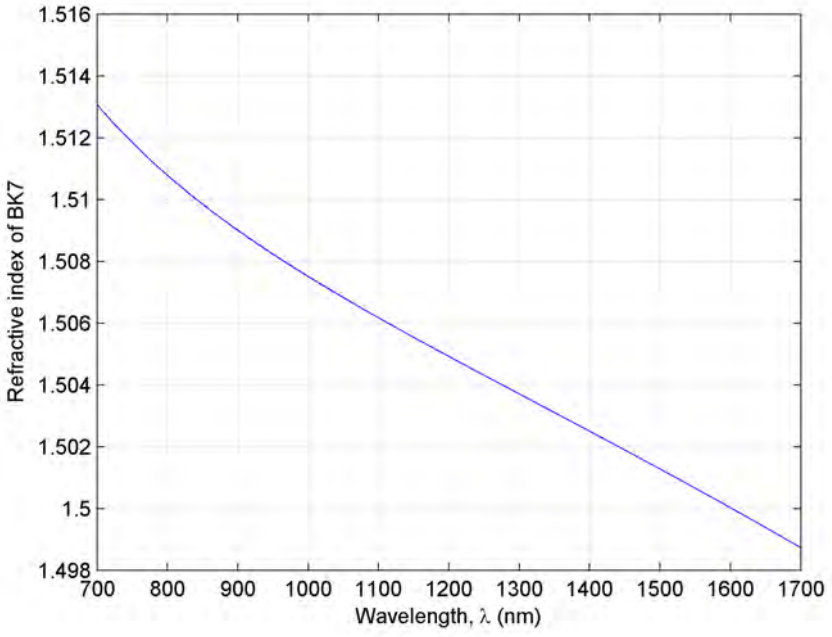

FIGURE 4.22: Refractive index of BK7 as a function of wavelength

Starting with this refractive index, the resonant wavelengths corresponding to zeroes of the characteristic equation for specific mode numbers l, are found for radial mode numbers at wavelengths between 1520 nm and 1610 nm. The microsphere diameter is then adjusted until the best agreement between the experimental and theoretical resonant wavelengths is achieved.

The justifications for assigning the sphere mode numbers $n = 1$ and $n = 2$, respectively, to the "strong" and "weak" families of peaks are determined as the following. In an experiment limited by surface roughness, the measured scattered power will depend upon the circulating power in the mode and upon the scattering efficiency from that mode which, in turn, depends upon the surface intensity of that mode for a given modal power. The solutions to the characteristic equation can be used to calculate the intensity distribution in the microsphere for a given modal power, as shown in Chapter 2, and it is found that the surface intensity for the $(l, n) = (83, 1)$ mode is 60% of that for the $(l, n) = (77, 2)$ mode, so that the fundamental mode would be expected to scatter less, for equal modal power. However, for the expected values of κ, which are 0.044 for the fundamental and 0.014 for the $n = 2$ mode (see Figure 4.23), it can be concluded from Figure 4.24 that for the low circulation loss factors observed here ($\alpha \leq 0.93$), the circulating power increases rapidly with coupling factor, κ, and so will be much higher in the fundamental mode than in the second-order mode. This will result in the highest scattered power for the fundamental mode despite the lower normalised

surface intensity for this mode, justifying the assumption that the mode exhibiting the strongest scattering is the fundamental mode.

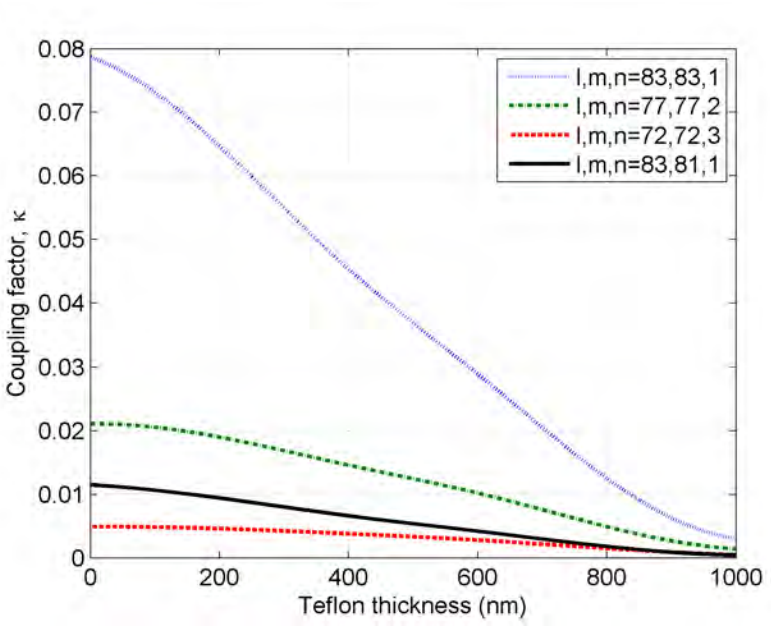

FIGURE 4.23: Coupling factor vs separation for the 30 μm diameter microsphere

The scattered power as a function of wavelength, from the results obtained in the previous section, can be fitted to the circulating power, that is obtained from the relation described below [3],

$$\left|\frac{\mathrm{E}_r}{\mathrm{E}_i}\right|^2 = \left|\frac{a_2}{a_1}\right|^2 = \frac{\alpha^2\kappa^2}{1-2\alpha[1-|\kappa|^2]^{1/2}\cos(\varphi+\varphi_t)+\alpha^2(1-|\kappa|^2)}, \tag{4.4}$$

where α is the circulation loss factor, κ is the coupling factor, φ_t is a phase offset due to coupling to the waveguide and φ is the circulation phase shift, which can be described with,

$$\varphi = \frac{2\pi^2 n_{\mathrm{eff}}\mathrm{D}}{\lambda}, \tag{4.5}$$

where n_{eff} is the effective index of a mode and D is the microsphere diameter.

The free spectral range for each radial mode is determined from the experimental data. The FSR is related to the effective index of a mode by,

$$\mathrm{FSR} = \frac{\lambda^2}{\pi n_{\mathrm{eff}}\mathrm{D}}. \tag{4.6}$$

The FSR is used with $\varphi = \frac{2\pi^2 n_{\mathrm{eff}}\mathrm{D}}{\lambda}$ to determine the circulation phase shift, φ. The optical path length for each radial mode, OPL, can be obtained with a straightforward

relation to the corresponding n_{eff} values for each radial mode, as seen in the relation below,

$$\text{OPL} = \pi n_{\text{eff}} \text{D}. \tag{4.7}$$

In order to match the width of the resonant lobe in the theoretical model to the experimental data, the coupling factor, κ, and the circulation loss factor, α, are then adjusted so that the widths are well matched. If is is assumed that the coupling factors, κ, may be calculated using Equation 2.20 described in Chapter 2, the width of the resonant peaks are determined by α.

Figure 4.24 shows a plot of circulating power as a function of coupling factor, κ, for several circulating loss factors, α. It can be seen that, for low coupling factors, the circulating power is increasing as κ gets larger, whereas at the larger values of κ the value of circulating power is decreasing. The power circulating in the microsphere in each mode at its resonance is dependent upon the coupling factor and the circulation loss factor, α. As shown in Figure 4.24, for $\alpha = 0.9946$, the circulating power is maximum at κ~0.1, which corresponds to $\kappa_c = \left[1 - |\alpha|^2\right]^{1/2}$ from Equation 4.4. This corresponds to critical coupling where the lost power per round trip is equal to the coupled power. For $\kappa < \kappa_c$, the microsphere is undercoupled and the circulating power increases with coupling factor. The opposite behaviour is observed in the overcoupled case where $\kappa > \kappa_c$.

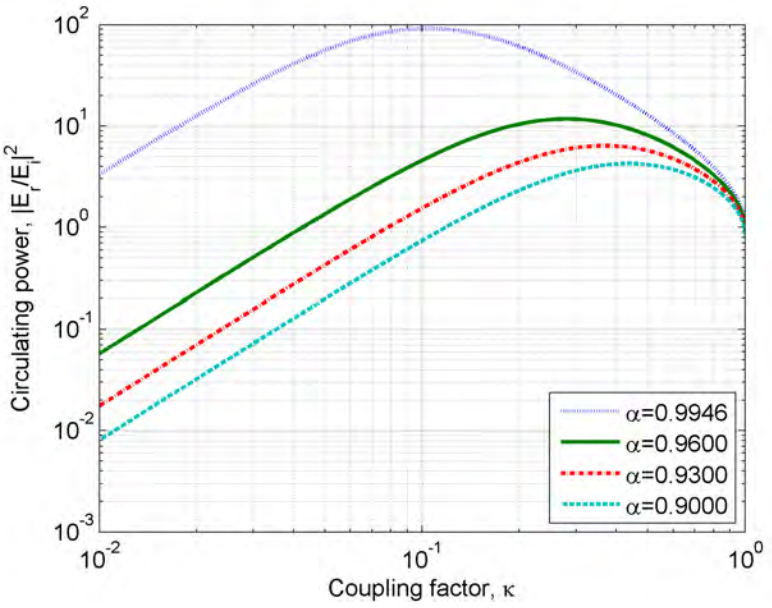

FIGURE 4.24: Circulating power vs coupling factor

4.5.2 Examples of fitting experimental data and mode assignment

In this section, three sets of examples will be included to illustrate the data fitting and mode assignment procedures. The detailed explanation of the graph fitting and mode assigning on the experimental results obtained from the commercial Nd-doped BK7 microspheres of 30±3 μm in diameter [1], the in-house made Nd-doped BK7 microspheres with the nominal size of 200 μm diameter, and the in-house made Er-doped BK7 microspheres of 130 μm diameter, will be discussed. These sets of data are chosen because the results have small wavelength scan resolutions of 5 pm, which has a minimum of inaccuracy during the measurement process. The commercial Nd-doped BK7 microsphere exhibits two family peaks, while the data obtained from the larger microsphere (internally made in-house) show strong evidence of the three families of resonant peaks. The sphere mode numbers will be assigned to each of these family of peaks. At the end of the section, the comparison of the surface quality of these microspheres will be made.

4.5.2.1 30 μm diameter Nd-doped BK7 microsphere

Figure 4.25 shows the scattered power collected through the microscope by the InGaAs detector as a function of wavelength, with fitted theoretical curves for circulating power, for the case of the 30 μm diameter BK7 microsphere.

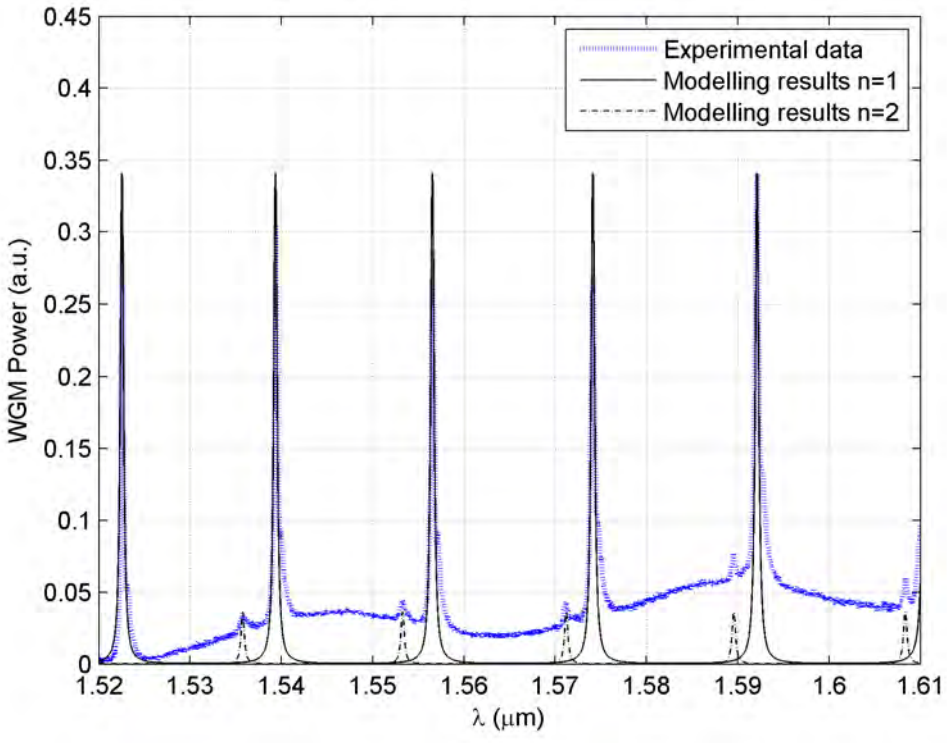

FIGURE 4.25: Resonance spectrum of the commercial Nd-doped BK7 microsphere of 30±3 μm in diameter [6]

The experimental data show high amplitude "strong" resonances with a free spectral range of 17.380±0.005 nm at the centre wavelength and a family of "weak" resonances with a free spectral range of 18.138±0.002 nm at the centre wavelength ($\lambda \approx 1565$ nm). Assigning the major peaks to fundamental WGMs with $n = 1$ yields azimuthal WGM numbers ranging from $l = m = 87$, for the resonance with the shortest wavelength shown in Figure 4.25, to $l = m = 83$ for the longest wavelength resonance. Similarly, assigning the weaker peaks to the higher order radial mode, $n = 2$, yields azimuthal mode numbers ranging from 80 to 76. The values of physical diameter of the microsphere that provides the best match for all wavelengths for the two families of modes are n_s =1.5004 and D = 30.774±0.014 μm. The full set of measured and theoretically predicted resonant wavelengths and assigned mode numbers, l and n, are shown in Table 4.3, with the deviation between the experimental and theoretically fitted values, $\Delta\lambda_{\text{res}}$. The estimated tolerance on the deduced diameter of the microsphere reflects the range of modelled diameters required to fit each resonance, in turn.

Experimental results		Theoretical fit		
λ_{res} (nm)	FSR (nm)	Sphere mode numbers, (l, n)	λ_{res} (nm)	$\Delta\lambda_{\text{res}}$ (nm)
TM polarisation				
1522.55	16.622	(87,1)	1522.50	0.05
1539.35	17.997	(86,1)	1539.00	0.35
1556.55	17.380	(85,1)	1556.55	0.00
1574.10	17.772	(84,1)	1573.50	0.60
1592.10	18.174	(83,1)	1591.50	0.60
1535.75	17.308	(80,2)	1535.80	0.05
1553.25	17.718	(79,2)	1553.35	0.10
1571.20	18.138	(78,2)	1571.15	0.05
1589.50	18.568	(77,2)	1589.35	0.15
1608.35	19.010	(76,2)	1608.00	0.35

TABLE 4.3: Experimental and theoretical resonant wavelengths and assigned mode numbers (l, n), D = 30.774±0.014 μm

The theoretical curves in Figure 4.25 are plots of Equation 4.4 fitted to the experimental data separately for the $n = 1$ and $n = 2$ modes, as follows. The experimental data has been normalised so that the magnitudes of the resonances of the fundamental modes match the theoretical results. The main peaks are found to exhibit a Q-factor of 4×10^3 and a circulation loss factor of $\alpha = 0.93$, using the calculated coupling factor of 0.044 obtained from coupling factor equation in Chapter 2 in Figure 4.26. The theoretical plot for the second-order ($n = 2$) mode, using the same circulation loss factor and a calculated coupling factor of 0.014 show resonance magnitudes relative to the fundamental ($n = 1$) mode which are well matched with the experimental data. The fluctuating background is probably due to non-resonant scattering of light from the laser source. The attempt to match the weaker family of peaks to TE excitation was done with no success, confirming that this family was not due to spurious TE excitation.

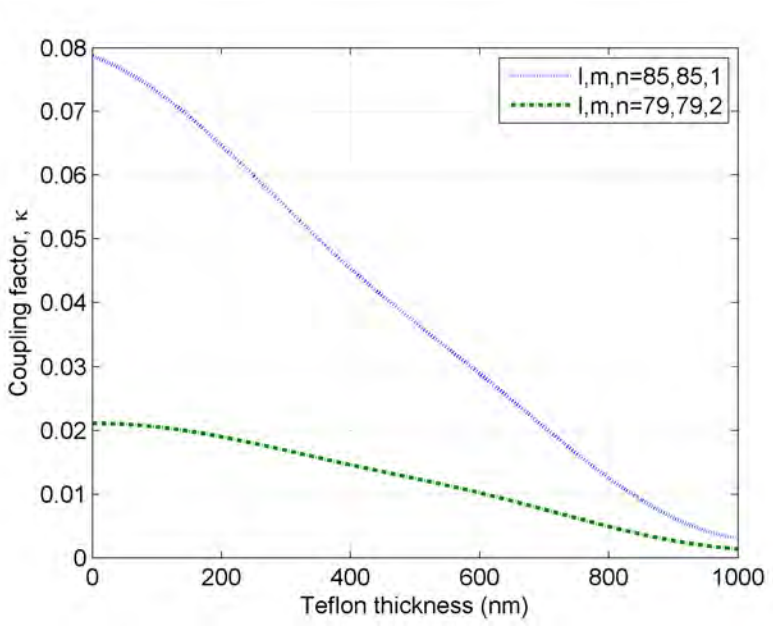

FIGURE 4.26: Coupling factor vs separation at $\lambda = 1550\pm1$ nm, D = 30.774±0.014 μm microsphere

Good agreement between experimental and theoretical resonant wavelengths is achieved, so that mode numbers and microsphere diameter and index may be deduced with confidence, and the diameter is found to be within the manufacturer's tolerance of 30±3 μm. The relative magnitudes of the resonances for the fundamental and second order families of radial modes give confidence in the theoretical estimation of coupling factors, and the spectral widths of the resonances allow the deduction of the circulation loss factor for the fundamental mode. The effective refractive index n_{eff} for each mode can be obtained by using Equation 4.6 using the value of FSR found from the experimental data. The n_{eff} of the fundamental and the second order radial modes around a wavelength of 1550 nm are found to be 1.441 and 1.407 respectively. This is in line with the fact that the $(l, n) = (83, 1)$ mode is more confined inside the microsphere than the $(l, n) = (77, 2)$ mode. The corresponding optical path lengths for each of the modes are 139.315±0.063 μm and 136.028±0.062 μm, respectively, where the circumference of the microsphere is found to have the value of 145.058±0.066 μm. The OPL of each radial mode is found to be smaller than the circumference of the microsphere times its refractive index, as expected. The loss factor of 0.93 is rather low for microspheres, representing a round-trip loss of 0.63 dB, and leading to a Q-factor of only 4×10^3.

4.5.2.2 200 μm diameter Nd-doped BK7 microsphere

The same fitting procedures were carried out for the three families of modes ($n = 1, 2, 3$) in the data for an in-house Nd-doped BK7 microsphere with the nominal diameter of 200 μm, as for the 30 μm diameter microsphere.

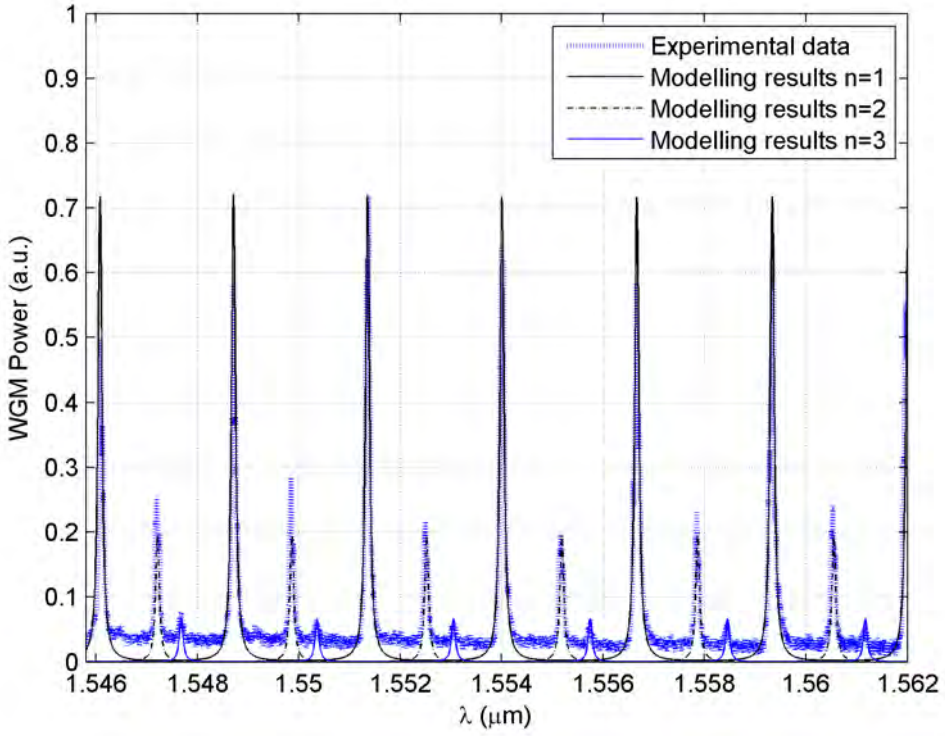

FIGURE 4.27: Resonance spectrum of in-house made Nd-doped BK7 microsphere with the nominal size of 200 μm in diameter [6]

The experimentally observed resonant wavelengths were fitted to the characteristic equation and mode numbers l and n were assigned to each resonant wavelength, as before, by adjusting the microsphere diameter. Table 4.4 shows the full set of experimental and theoretical resonant wavelengths for the fundamental, second and third order radial modes ($n = 1, 2, 3$), for the best-fit values of D = 198.62±0.06 μm and $n_s = 1.5006$. The discrepancies between the theoretical and the experimental resonant wavelengths are less than 0.5 nm for all modes. Sphere mode numbers (l, n) of (590,1) to (585,1) are assigned to the major peaks, corresponding to fundamental radial WGMs. The sphere mode numbers of (578,2) to (573,2) and (568,3) to (563,3) are assigned to the second and third order radial WGMs.

The coupling factors calculated for a microsphere of diameter 198.62±0.06 μm separated from the waveguide by a 400 nm Teflon film are calculated to be $\kappa = 0.0935$, $\kappa = 0.0473$, and $\kappa = 0.0274$, for the $n = 1, 2, 3$ modes (see Figure 4.28), respectively, so that, as before, the $n = 1$ mode is expected to show the strongest peaks, and the $n = 2$ and $n = 3$ modes are expected to show correspondingly lower scattered power. The field distributions of the field in radial dependence are shown in Figure 4.29. The surface intensity of the first order mode is at 70% of the second order mode, but the coupling factor values suggest, as similarly described in the previous section for the microsphere of 30 μm diameter case, that the scattered power of $n = 1$ is larger than $n = 2$. The

Experimental results		Theoretical fit		
λ_{res} (nm)	FSR (nm)	Sphere mode numbers, (l, n)	λ_{res} (nm)	$\Delta\lambda_{\text{res}}$ (nm)
TM polarisation				
1546.09	2.623	(590,1)	1546.20	0.11
1548.71	2.634	(589,1)	1548.80	0.09
1551.37	2.645	(588,1)	1551.38	0.01
1553.99	2.655	(587,1)	1553.99	0.00
1556.66	2.667	(586,1)	1556.66	0.00
1559.34	2.678	(585,1)	1559.21	0.13
1547.20	2.643	(578,2)	1547.00	0.20
1549.84	2.652	(577,2)	1549.58	0.26
1552.50	2.662	(576,2)	1552.20	0.30
1555.17	2.671	(575,2)	1554.80	0.37
1557.84	2.681	(574,2)	1557.40	0.44
1560.53	2.690	(573,2)	1560.20	0.33
1547.69	2.683	(568,3)	1548.18	0.49
1550.33	2.688	(567,3)	1550.70	0.37
1553.06	2.695	(566,3)	1553.35	0.29
1555.74	2.700	(565,3)	1555.99	0.25
1558.44	2.707	(564,3)	1558.53	0.09
1561.16	2.713	(563,3)	1561.28	0.12

TABLE 4.4: Experimental and theoretical resonant wavelengths and assigned mode numbers (l, n), D = 198.62±0.06 μm

surface intensity of $n = 3$ is the smallest, corresponding to the weakest family of peaks. Fitting the transfer function obtained in Yariv et al. [3] (see Equation 4.4) to the fundamental family of resonances results in a circulation loss factor of 0.90, and the relative magnitudes of the theoretically calculated circulating powers for this value of α and the calculated values of κ are in good agreement with the experimental results. A circulation loss factor of 0.90 corresponds to a round-trip loss of 0.87 dB, a Q of 2.3×10^4 is obtained. Q is higher than for the smaller microspheres because the larger microsphere has more stored energy at resonance and the relation of Q and α can be found by $\text{Q} \approx \frac{\pi^2 n_{\text{eff}} \text{D}}{\lambda(1-\alpha)}$ [7], where Q is large when α is small.

The corresponding values of n_{eff} at a wavelength of 1550 nm for the fundamental, second, and third order radial modes are 1.457, 1.450 and 1.435, respectively. This is again in agreement with the fact that higher radial number modes extend further into the surrounding air. The corresponding optical path lengths, OPL, for each of the modes are 909.14±0.27 μm, 904.78±0.27 μm and 895.42±0.27 μm, respectively, where the circumference of the microsphere multiplied by an actual microsphere refractive index is found to have a slightly larger value of $\pi\text{D} \cdot n_s = 936.35\pm0.28$ μm, as expected. The attempts at matching the peaks with TE excitation have failed, validating that they were not due to TE excitation.

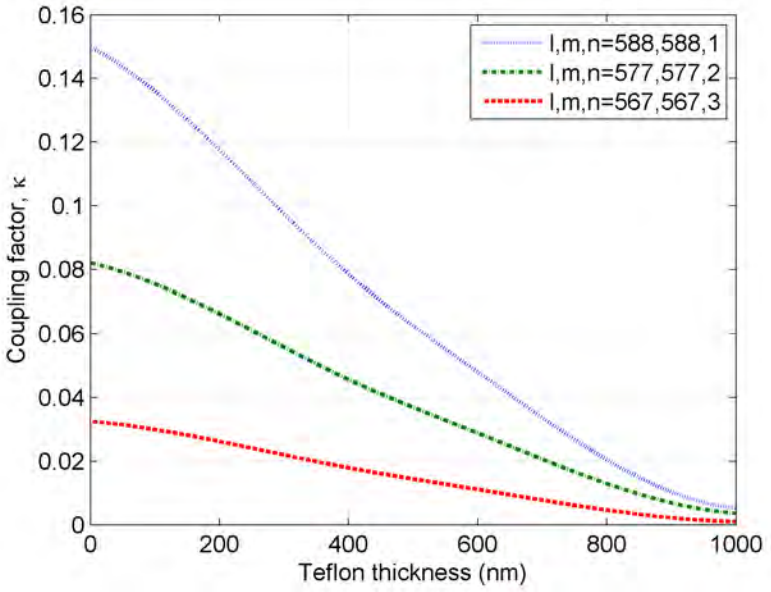

FIGURE 4.28: Coupling factor vs separation at $\lambda = 1550 \pm 1$ nm, D = 198.62±0.06 μm

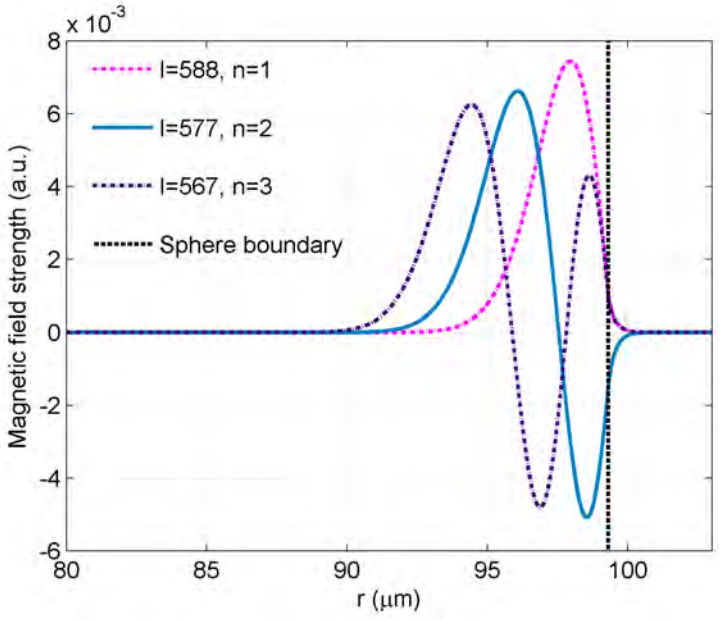

FIGURE 4.29: WGM radial intensity distributions, D = 198.62±0.06 μm

4.5.2.3 130 μm diameter Er-doped BK7 microsphere

In this section, the theoretical fitting procedure of the experimental data in Section 4.4 is described, uses the same fitting procedures as in the previous sections. Figure 4.30 shows the resonance spectrum of an in-house made Er-doped BK7 microsphere at 1440 nm to 1460 nm. It can be seen in Figure 4.30 that there are three prominent families of modes. However, as the wavelength gets larger (1560 nm to 1640 nm), these modes start to merge, making mode assigning difficult. Thus, the mode assignment was carried out at wavelengths between 1440 nm and 1560 nm, where the modes are easy to distinguish. It is to be noted that the spectrum obtained from the microsphere located off-waveguide centre shows promising modal separation, as the widths of the lobes are narrower than at the ones obtained when the microsphere was located at the centre of the waveguide, as the coupling efficiency between the microsphere and waveguide is smaller. Thus, data that is used for fitting in this section is that obtained from the microsphere located 6 μm off-centre from the waveguide.

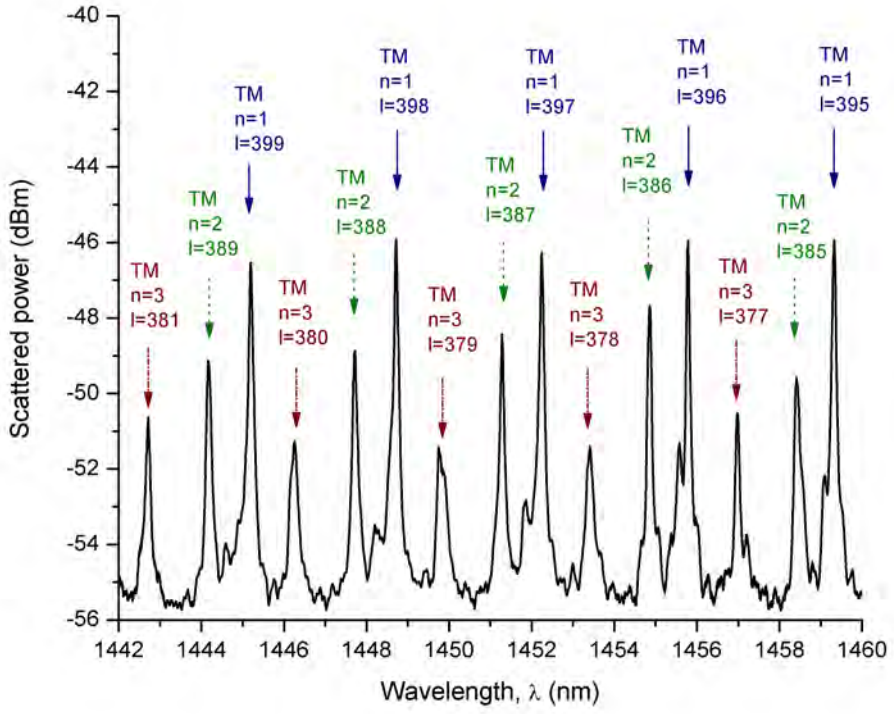

FIGURE 4.30: Resonance spectrum of in-house made Er-doped BK7 microsphere, D = 126.40±0.03 μm in diameter, when the microsphere is located at 6 μm off-waveguide centre

The coupling factors of the microsphere located at 460 nm away from the waveguide surface are calculated to be $\kappa = 0.0975$, $\kappa = 0.0489$, and $\kappa = 0.0216$, for the $n = 1, 2, 3$ modes (see Figure 4.31), respectively. The modal assignment was justified as in the previous section, where the prominent peaks that have the strongest amplitude

correspond to $n = 1$, the weaker family peaks correspond to $n = 2$, and the weakest family peaks correspond to $n = 3$, as according to the calculated values of κ. Even though, the field distribution in radial dependency in Figure 4.32, shows that the surface intensity of all the modes have similar values.

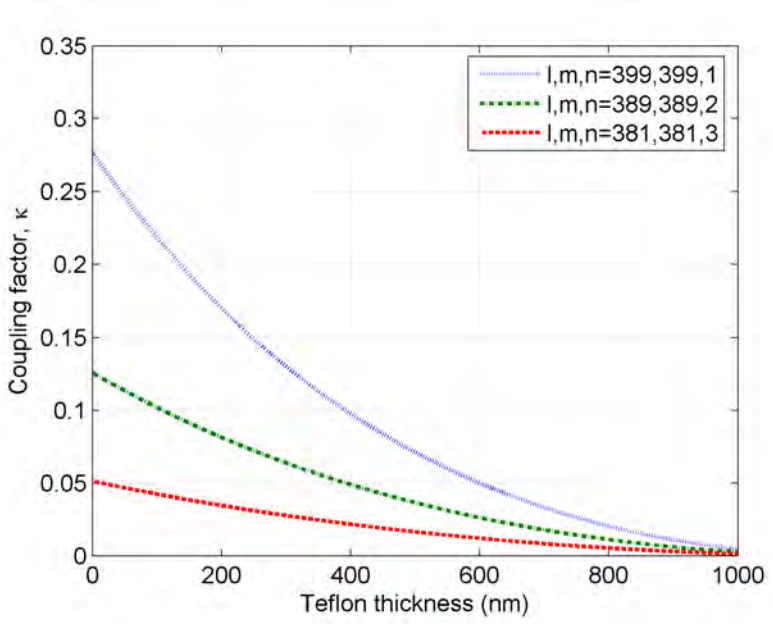

FIGURE 4.31: Coupling factor vs separation at $\lambda = 1444 \pm 1.5$ nm, D = 126.40±0.03 μm

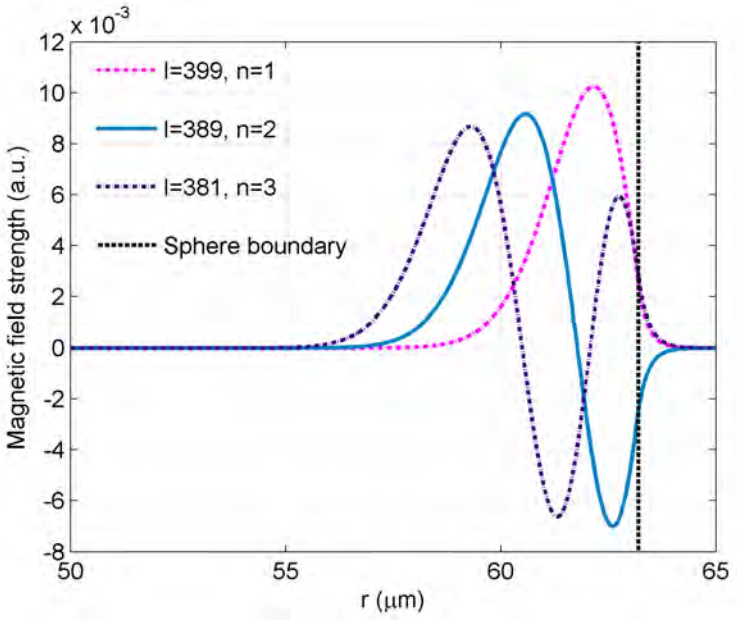

FIGURE 4.32: WGM radial intensity distributions, D = 126.40±0.03 μm

Figure 4.33 shows the experimental and the fitted theoretical resonance spectra of the 126.40±0.03 μm diameter Er-doped BK7 microsphere. In order to fit the widths of the resonances, a circulation loss factor of $\alpha = 0.89$, which corresponds to a round-trip loss of 0.98 dB, is used. The refractive index of the microsphere of $n_s = 1.502$ is

used, and the microsphere diameter of D = 126.40±0.03 μm is found to be the best fit to the experimental data. The effective refractive index of the modes are found to be 1.5017, 1.4906 and 1.4747 for $n = 1, 2$, and 3 respectively. The corresponding OPL for each of the modes are 596.32±0.3 μm, 591.91±0.3 μm and 585.60±0.3 μm, respectively, which are, as expected, slightly smaller than $\pi D \cdot n_s$ = 596.44±0.3 μm. Table 4.5 - 4.7 show the theoretical and the experimental values of the resonant wavelengths, and the corresponding microsphere mode numbers l, for $n = 1, 2$, and 3, respectively.

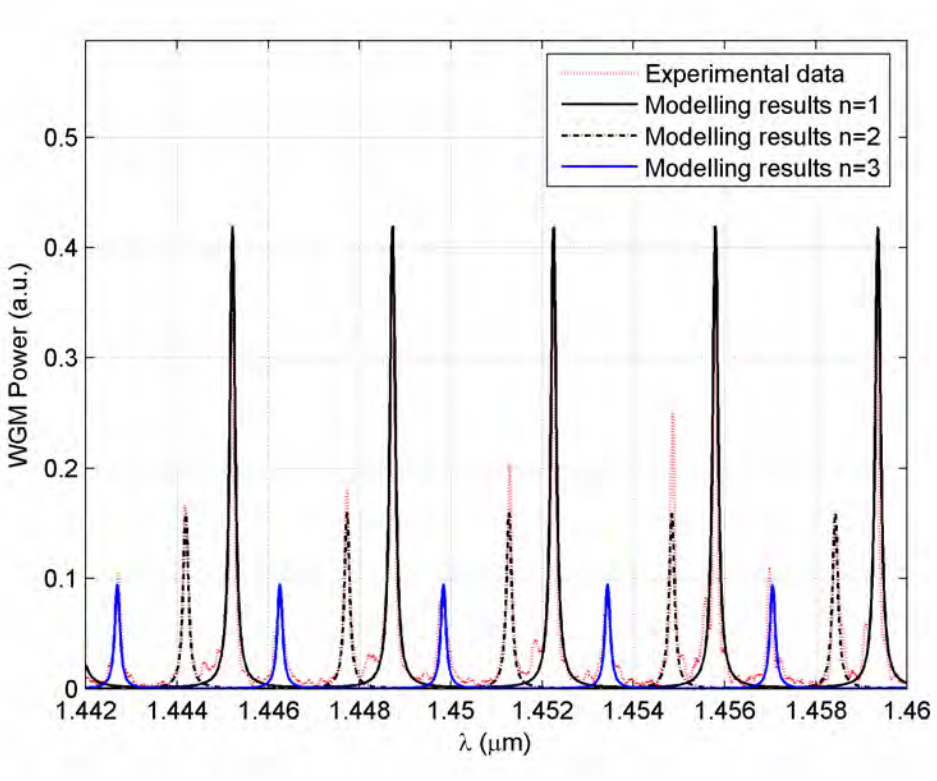

FIGURE 4.33: Experimental and theoretical resonance spectra of Er-doped BK7 microsphere, D = 126.40±0.03 μm

It has been found that Q factors of the in-house made microspheres with the nominal diameter of 200 μm are significantly improved, as they exhibited Q of 2.3×10^4 at 1550 nm, compared with the as-supplied microspheres (Q = 4×10^3 at 1550 nm), due to improved surface quality. The circulation loss factor, α, of 0.93, 0.90 and 0.89 have been obtained for microspheres of 30 μm, 200 μm and 130 μm diameters, respectively. It can be concluded that the circulation loss factor is lower for the larger microspheres, because of the longer WGM path length.

Experimental results		Theoretical fit		
λ_{res} (nm)	FSR (nm)	Sphere mode numbers, (l)	λ_{res} (nm)	$\Delta\lambda_{res}$ (nm)
TM polarisation, sphere mode number $n = 1$				
1445.20	3.49	399	1445.24	0.04
1448.72	3.51	398	1448.76	0.04
1452.24	3.53	397	1452.29	0.05
1455.79	3.55	396	1455.83	0.04
1459.32	3.57	395	1459.39	0.07
1462.93	3.58	394	1462.97	0.04
1466.54	3.60	393	1466.56	0.02
1470.08	3.62	392	1470.19	0.11
1473.75	3.64	391	1473.81	0.06
1477.40	3.66	390	1477.47	0.07
1481.07	3.68	389	1481.11	0.04
1484.76	3.70	388	1484.81	0.05
1488.48	3.72	387	1488.51	0.03
1492.20	3.74	386	1492.24	0.04
1495.94	3.75	385	1495.98	0.04
1499.72	3.77	384	1499.74	0.02
1503.50	3.79	383	1503.56	0.06
1507.30	3.81	382	1507.32	0.02
1511.12	3.83	381	1511.14	0.02
1514.96	3.85	380	1514.97	0.01
1518.83	3.87	379	1518.83	0.00
1522.70	3.89	378	1522.70	0.00
1526.60	3.91	377	1526.60	0.00
1530.52	3.93	376	1530.51	0.01
1534.47	3.95	375	1534.46	0.01
1538.43	3.97	374	1538.42	0.01
1542.41	4.00	373	1542.39	0.02
1546.39	4.02	372	1546.40	0.01
1550.41	4.04	371	1550.40	0.01
1554.48	4.06	370	1554.44	0.04
1558.55	4.08	369	1558.51	0.04

TABLE 4.5: Experimental and theoretical resonant wavelengths and assigned sphere mode numbers l, $n = 1$, D = 126.40±0.03 μm

Experimental results		Theoretical fit		
λ_{res} (nm)	FSR (nm)	Sphere mode numbers, (l)	λ_{res} (nm)	$\Delta\lambda_{res}$ (nm)
TM polarisation, sphere mode number $n = 2$				
1444.16	3.53	389	1444.22	0.06
1447.72	3.55	388	1447.77	0.05
1451.28	3.57	387	1451.28	0.00
1454.86	3.59	386	1454.89	0.03
1458.41	3.60	385	1458.47	0.06
1462.05	3.62	384	1462.08	0.03
1465.65	3.64	383	1465.69	0.04
1469.32	3.66	382	1469.35	0.03
1472.99	3.68	381	1473.00	0.01
1476.63	3.69	380	1476.69	0.06
1480.34	3.71	379	1480.36	0.02
1484.07	3.73	378	1484.09	0.02
1487.80	3.75	377	1487.82	0.02
1491.56	3.77	376	1491.58	0.02
1495.32	3.79	375	1495.35	0.03
1499.12	3.81	374	1499.13	0.01
1502.94	3.83	373	1502.99	0.05
1506.78	3.84	372	1506.78	0.00
1510.64	3.86	371	1510.63	0.01
1514.50	3.88	370	1514.49	0.01
1518.40	3.90	369	1518.38	0.02
1522.34	3.92	368	1522.29	0.05
1526.28	3.94	367	1526.22	0.06
1530.20	3.96	366	1530.17	0.03
1534.17	3.98	365	1534.15	0.02
1538.21	4.00	364	1538.14	0.07
1542.13	4.02	363	1542.15	0.02
1546.17	4.04	362	1546.19	0.02
1550.24	4.06	361	1550.23	0.01
1554.31	4.08	360	1554.31	0.00
1558.39	4.10	359	1558.40	0.01

TABLE 4.6: Experimental and theoretical resonant wavelengths and assigned sphere mode numbers l, $n = 2$, D = 126.40±0.03 μm

Experimental results		Theoretical fit		
λ_{res} (nm)	FSR (nm)	Sphere mode numbers, (l)	λ_{res} (nm)	$\Delta\lambda_{res}$ (nm)
TM polarisation, sphere mode number $n = 3$				
1442.71	3.55	381	1442.76	0.05
1446.26	3.49	380	1446.32	0.06
1449.75	3.66	379	1449.89	0.14
1453.41	3.57	378	1453.47	0.06
1456.98	3.66	377	1457.07	0.09
1460.64	3.61	376	1460.70	0.06
1464.25	3.68	375	1464.34	0.09
1467.93	3.70	374	1468.01	0.08
1471.63	3.74	373	1471.69	0.06
1475.37	3.76	372	1475.39	0.02
1479.13	3.74	371	1479.08	0.05
1482.87	3.72	370	1482.84	0.03
1486.59	3.73	369	1486.59	0.00
1490.32	3.78	368	1490.37	0.05
1494.10	3.75	367	1494.16	0.06
1497.85	3.89	366	1497.97	0.12
1501.74	3.84	365	1501.85	0.11
1505.58	3.90	364	1505.65	0.07
1509.48	3.92	363	1509.52	0.04
1513.40	3.84	362	1513.42	0.02
1517.24	3.94	361	1517.33	0.09
1521.18	3.96	360	1521.26	0.08
1525.14	3.98	359	1525.21	0.07
1529.12	3.99	358	1529.18	0.06
1533.11	4.00	357	1533.19	0.08
1537.11	4.08	356	1537.20	0.09
1541.19	4.04	355	1541.24	0.05
1545.23	4.10	354	1545.31	0.08
1549.33	4.10	353	1549.37	0.04
1553.43	4.14	352	1553.48	0.05
1557.57	4.14	351	1557.60	0.03

TABLE 4.7: Experimental and theoretical resonant wavelengths and assigned sphere mode numbers l, $n = 3$, D = 126.40±0.03 μm

4.6 Conclusions

The scattered power measurement of the glass microspheres on the diffused-ion exchanged waveguide as a function of wavelength has been demonstrated for the first time. The experimental work to observe the scattered signal, which is proportional to the intensity of the light circulating in the microsphere as a function of wavelength, has been described. The equipment, experimental setup, techniques, and the experimental procedures, which related to the experiment for obtaining the scattered signal from the microspheres have been introduced. The basic analysis has been completed by a straightforward image processing method. A signal proportional to the intensity of the light circulating in the microsphere has been obtained from the intensity integration over the surrounding area.

The algorithm of the theoretical modelling for fitting experimental data and sphere mode assignment have been discussed. The theoretical work in this chapter allows determination of the sphere diameter and assignment of sphere mode numbers to the experimental data. The experimental work with the 1550 nm light source was successfully completed, as fine wavelength tuning resolution was obtained and the comparison of experimental data could be completed with minimal errors. Data fitting allows the determination of the resonant wavelength as well as the microsphere diameter from the information of the free spectral range obtained from the experimental data. The individual mode numbers have been identified with confidence, the physical diameters of the microspheres have been confirmed, and waveguide coupling to each mode is in agreement with theory. The optical path length of the WGM propagation in the microsphere, which depends on the mode that light is travelling in, has been determined, it has a slightly smaller value than the circumference of the microsphere. This theoretical modelling for fitting experimental data and sphere mode assignment will be used throughout the rest of the thesis, with the experimental results from microsphere lasers experiment that will be obtained in Chapter 6.

The variations of Q-factor of the microsphere on the channel waveguide, as a function of vertical and lateral displacements with respect to the waveguide surface and centre of the waveguide, have been observed. The measurements of the scattered power of microspheres have been carried out for various thicknesses of the Teflon buffer layer to achieve a varying vertical displacement, and the measurements in lateral displacement have been completed by translating the microsphere across the waveguide surface with respect to the centre of the waveguide. The results of the Q have been discussed, Q of the system at the larger separation is large due to the small coupling efficiency into the sphere. As the microsphere was shifted away from the waveguide surface the coupling efficiency has been found to be smaller and the system exhibited high Q.

Experimental work on light coupling into microspheres in the 800 nm region has been completed, and the WGM characteristics from the waveguide-coupled microsphere have

been observed, this wavelength region is a useful region for pumping in the laser experiment to be described in Chapter 6.

4.7 References

[1] http://www.mo-sci.com.

[2] http://www.dukescientific.com.

[3] A. Yariv. Universal relations for coupling of optical power between microresonators and dielectric waveguides. *Electronics Letters*, 36:321–322, 2000.

[4] B. E. Little, J. P. Laine, and H. A. Haus. Analytic theory of coupling from tapered fibers and half-blocks into microsphere resonators. *Journal of Lightwave Technology*, 17:704–715, 1999.

[5] http://www.schott.com.

[6] Y. Panitchob, G. S. Murugan, M. N. Zervas, P. Horak, S. Berneschi, S. Pelli, G. Nunzi Conti, and J. S. Wilkinson. Whispering gallery mode spectra of channel waveguide coupled microspheres. *Optics Express*, 16:11066–11076, 2008.

[7] A. E. Siegman. *Lasers*. Univerity Science Books, California, 1986. ISBN 0-935702-11-3.

Chapter 5

Theory of waveguide-coupled microsphere lasers

5.1 Introduction

In this chapter, the theoretical characteristics of microsphere lasers will be presented. The derivation of loss and gain of the cavity will be discussed, in Section 5.2 and Section 5.3, respectively. The gain and loss of the system are important because they are the key parameters for threshold pump power calculation. In Section 5.4, the value of maximum gain and the minimum required Q for a 1.5-wt% Nd_2O_3-doped BK7 microsphere of 30 μm diameter, will be calculated, to ensure that the microsphere is suitable for lasing action. Section 5.5 will include the calculation of threshold pump power at the microsphere, $P_{\text{th-sphere}}$, which refers to the pump power in the microsphere where the laser starts to oscillate. In Section 5.6, the derivation of the pump power in the microsphere, $P_{\text{th-sphere}}$, as a function of the microsphere-waveguide separation will be described. At the end of the section, the threshold pump power in the input waveguide, $P_{\text{th-wg}}$, as a function of the microsphere and waveguide separation, will be determined. In the final part of this chapter, the calculation of pump power threshold for a 1.5-wt% Nd_2O_3-doped BK7 microsphere of 190 μm in diameter, will be carried out, followed by a detailed discussion. A microsphere with the same Nd concentration and diameter will be used in the experimental work in Chapter 6. Thus, the aim of the theoretical work in this section is to provide the knowledge of the pump power threshold which will be required for the microsphere laser when pumped from a waveguide. It is to be noted that the thermal characteristics of the system will not be included in the calculation in this chapter, however the discussion will be covered in Chapter 6.

5.2 Cavity loss

Total round-trip loss of the cavity, δ_c, can be obtained from the quality factor of the system, as follows [1]:

$$\delta_c = 1 - \alpha = \frac{2\pi^2 n_{\text{eff}} \mathrm{D}}{\mathrm{Q}_{c_s} \lambda_s}, \tag{5.1}$$

where α is the circulation loss factor as described in Chapter 2, Q_{c_s} is the quality factor of the system at the signal wavelength, λ_s is the signal wavelength, D is the microsphere diameter and n_{eff} corresponds to the effective refractive index of the mode that propagates along a circular path within the cavity. The power loss of the cavity in nepers is obtained from the exponential of the total loss in the cavity, δ_c, as follows:

$$\mathrm{L} = \exp(-\delta_c). \tag{5.2}$$

5.3 Cavity gain

Calculation of gain within the cavity is presented below, following reference [2]. The gain per unit length at the signal wavelength at a single point in the cavity can be found from Equation 5.3.

$$g(z) = \frac{d\mathrm{P}_s(z)}{dz} = \iint \mathrm{N}(x, y, z)\mathrm{I}_s(x, y)\sigma_s \, dx \, dy, \tag{5.3}$$

where $\mathrm{I}_s(x, y, z)$ is the signal intensity obtained by multiplying the signal power, $\mathrm{P}_s(z)$, by the normalised signal mode distribution, $\mathrm{S}_s(x, y)$, as shown in Equation 5.4.

$$\mathrm{I}_s(x, y, z) = \mathrm{P}_s(z)\, \mathrm{S}_s(x, y), \tag{5.4}$$

σ_s is the stimulated emission cross-section, which may be calculated according to Equation 5.5 [3].

$$\sigma_s = \frac{\lambda_f^4}{8\pi c n_s^2 \tau \Delta\lambda}, \tag{5.5}$$

where λ_f is the peak wavelength of the fluorescence emission spectra, c is the speed of light, n_s is the microsphere refractive index, τ is the fluorescence lifetime, $\Delta\lambda = \int_0^\infty \frac{\mathrm{I}(\lambda)\, d\lambda}{\mathrm{I}_p}$ and $\mathrm{I}(\lambda)$ is the fluorescence line shape with a maximum I_p at λ_p. Figure 5.1

shows a typical fluorescence spectrum of BK7 glass doped with 1.5-wt% of neodymium oxide [4].

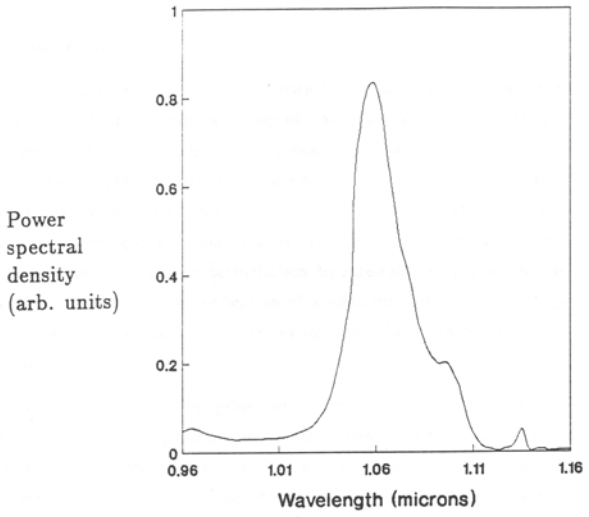

FIGURE 5.1: Typical fluorescence spectrum of BK7 glass doped with 1.5-wt% neodymium oxide [4]

and $\mathrm{N}(x, y, z)$ is the excited-state population of the cavity, which can be calculated from the incident pump intensity $\mathrm{I}_p(x, y, z)$ [2]:

$$\mathrm{N}(x, y, z) = \frac{\tau \mathrm{N}_o \sigma_p \eta_q}{h\nu_p} \mathrm{I}_p(x, y, z), \tag{5.6}$$

where N_o is the number of active ions per unit volume, σ_p is the pump absorption cross-section, η_q is the quantum efficiency, ν_p is the pump frequency, h is Planck's constant, and $\mathrm{I}_p(x, y, z)$ is the incident pumping intensity that can be obtained by multiplying the pumped power, $\mathrm{P}_p(z)$, by the normalised pump mode distribution, $\mathrm{S}_p(x, y)$:

$$\mathrm{I}_p(x, y, z) = \mathrm{P}_p(z)\, \mathrm{S}_p(x, y). \tag{5.7}$$

In a rare-earth-ion-doped microsphere cavity, the rare-earth ions introduced into the cavity caused pump attenuation, and as propagation loss also attenuates the pump power along path length of the cavity, the pump power decays according to Equation 5.8.

$$\mathrm{P}_p(z) = \mathrm{P}_p(0) \exp\left[-(\mathrm{a}_p + \beta_p)z\right], \tag{5.8}$$

where β_p is the absorption coefficient per unit length at the pump wavelength. For negligible ground-state depletion the absorption coefficient, β_p, is obtained by multiplying N_o with σ_p. If N_o is known, then σ_p can be obtained from the absorption spectrum shown in Figure 5.2. a_p is the microsphere propagation loss per unit length, α_p is a loss factor associated with a_p, where $\alpha_p = \mathrm{a}_p \pi \mathrm{D}$.

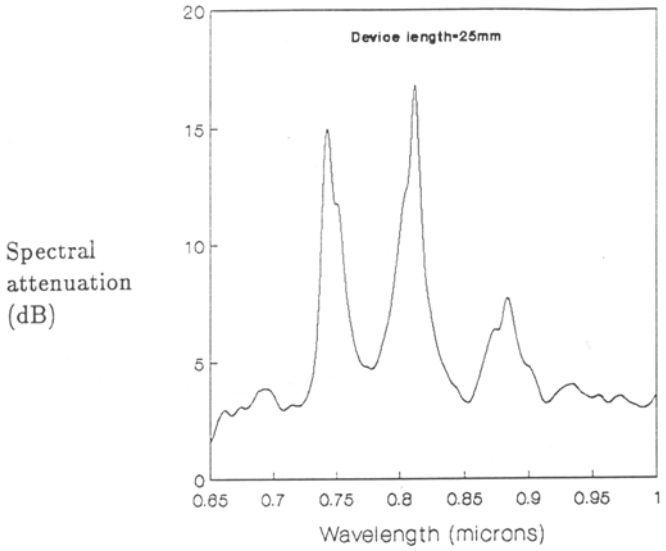

FIGURE 5.2: Typical loss spectrum of BK7 glass doped with 1.5-wt% neodymium oxide [4]

The cavity round-trip gain can be determined by integrating Equation 5.3 over the total length of the sphere cavity, πD, $\left(\mathrm{G} = \int_0^{\pi \mathrm{D}} \frac{d\mathrm{P}_s(z)}{dz}\right)$, as shown in Equation 5.9;

$$\mathrm{G} = \exp\left[\iint \mathrm{S}_s(x,y)\mathrm{S}_p(x,y)\,dx\,dy \left(\frac{\tau\eta_q\sigma_s}{h\nu_p}\right)\mathrm{P}_p(0)\left(\frac{1-\exp[-(\mathrm{a}_p+\beta_p)\pi\mathrm{D}]}{1+\frac{\mathrm{a}_p}{\beta_p}}\right)\right], \quad (5.9)$$

where $\mathrm{S}_s(x,y)$ and $\mathrm{S}_p(x,y)$ are the normalised mode distributions at the signal and pump wavelengths, respectively. They are normalised such that $\iint \mathrm{S}_s(x,y)\,dx\,dy = 1$ and $\iint \mathrm{S}_p(x,y)\,dx\,dy = 1$ per unit area, respectively. Note that $\frac{1}{\iint \mathrm{S}_s(x,y)\mathrm{S}_p(x,y)\,dx\,dy}$ corresponds to the effective mode area of the overlapped signal and pump fields.

The pump power which makes the cavity gain, G, equal to the round-trip loss, L, in the cavity is the threshold power of the system, and will be derived in Section 5.5.

5.4 Minimum required quality factor for microsphere laser

In this section, the minimum value of Q factor which is required for lasing action to occur and the maximum gain for a 1.5-wt% Nd_2O_3-doped BK7 microsphere of 30 μm in diameter, are derived. The assumption is made that all Nd^{3+} ions are in the excited state, thus, the gain coefficient, g, can be found by multiplying the emission cross-section, σ_s, with the total Nd^{3+} ion density, N_o.

$$g_{\max} = \sigma_s \mathrm{N}_o. \quad (5.10)$$

The round-trip loss of the micro-cavity can be found from Equation 5.1. For lasing to occur, the gain must be greater than the loss of the system, yielding:

$$\mathrm{Q} > \frac{2\pi}{\sigma_s \mathrm{N}_o \lambda_s}, \tag{5.11}$$

For a 30 μm diameter BK7 microsphere doped with 1.5-wt% Nd_2O_3, $\sigma_s = 1.9 \times 10^{-24}$ m^2 and $N_o = 1.68 \times 10^{26}$ m^{-3}; $g_{\max} = 319.2$ m^{-1}. Thus, by using Equation 5.11, the value of Q must be greater than 1.86×10^4 at $\lambda_s = 1060$ nm for lasing to occur.

This estimation of the minimum Q required depends upon achieving the theoretically predicted gain. To check the plausibility of the calculation, the gain achieved experimentally by Miliou et al. [5] for Nd-doped BK7 glass is used instead of the calculated value of $g_{\max}$ above. Miliou et al. obtained a maximum gain of 216 m^{-1}, which would require a Q factor of 2.74×10^4 at $\lambda_s = 1060$ nm to achieve lasing in the microsphere configuration described here. Thus, it may be assumed that a worst-case Q to allow lasing for this material in a microsphere configuration is 3×10^4.

In Chapter 3, the value of Q measured from the commercial sphere has been found to be about 4×10^3, whereas the in-house fabricated spheres exhibited larger Q of up to 6.2×10^4 at 1550 nm. The value Q obtained from the in-house fabricated spheres is larger than the minimum Q that would require for lasing. Thus, it can be confirmed that the microspheres that are fabricated in-house are good candidates for microsphere laser experiment.

5.5 Microsphere threshold power calculation

In this section, the pump power required in the fundamental WGM of a microsphere for lasing action to be achieved is derived. The pump power threshold calculation is derived based on negligible ground-state depletion. At threshold, total gain, G, must equal loss, L. Power threshold in the spherical cavity, $\mathrm{P_{th\text{-}sphere}}$, can be found by equating Equation 5.2 to Equation 5.9 and the corresponding pump power is the pump power threshold of the system, see Equation 5.12.

$$\mathrm{P_{th\text{-}sphere}} = \frac{\left(\frac{2\pi^2 n_{\mathrm{eff}} \mathrm{D}}{\mathrm{Q}_{c_s}\lambda_s}\right)}{\iint \mathrm{S}_s(x,y)\mathrm{S}_p(x,y)\,dx\,dy}\left(\frac{h\nu_p}{\tau\eta_q\sigma_s}\right)\left(\frac{1+\frac{\mathrm{a}_p}{\beta_p}}{1-\exp[-(\mathrm{a}_p+\beta_p)\pi\mathrm{D}]}\right), \qquad (5.12)$$

The power threshold calculation requires information on the total loss of the cavity at the signal wavelength, δ_c, which can be obtained from Q_{c_s} as shown in Equation 5.1. As described in Chapter 2, the Q factor of the cavity depends upon the separation of the sphere from the waveguide and is found by carrying out an overlap integral of the fields of the microsphere and the evanescent field of the waveguide at signal wavelength.

For a 1.5-wt% Nd_2O_3-doped BK7 microsphere of 30 μm diameter and refractive index of $n_s = 1.51$, the expected resonant wavelengths within the pump absorption band, λ_p, and within the emission band, λ_s, the corresponding sphere mode numbers l for the fundamental radial mode ($n = 1$) in the TM polarisation are shown in Table 5.1 and 5.2 respectively.

λ_p (nm)	Sphere mode number, (l, n)
803	(167, 1)
808	(166, 1)
812	(165, 1)
817	(164, 1)
822	(163, 1)

TABLE 5.1: Pump wavelengths and the sphere mode number l, n for 1.5-wt% Nd_2O_3-doped BK7 microsphere of 30 μm in diameter, $n_s = 1.51$

λ_s (nm)	Sphere mode number, (l, n)
1043	(127, 1)
1051	(126, 1)
1059	(125, 1)
1068	(124, 1)
1076	(123, 1)

TABLE 5.2: Signal wavelengths and the sphere mode number l, n for 1.5-wt% Nd_2O_3-doped BK7 microsphere of 30 μm in diameter, $n_s = 1.51$

The threshold pump power for each of the resonant signal wavelengths for each pump wavelength are shown in Figure 5.3. Specific values used in the calculation are $\tau = 470$ μs, $\eta_q = 0.8$, $\sigma_{\mathrm{peak}_s} = 1.9 \times 10^{-24}$ m^{-2}, $\sigma_{\mathrm{peak}_p} = 1.0 \times 10^{-24}$ m^{-2} and $\mathrm{N}_o = 1.68 \times 10^{26}$ m^{-3}. The loss due to spurious attenuation is assumed to be negligible. The approximation of $n_{\mathrm{eff}} \cong n_s = 1.51$ is made for simplicity of the calculation, because the value of n_{eff} of the fundamental mode is close to the actual microsphere refractive index n_s.

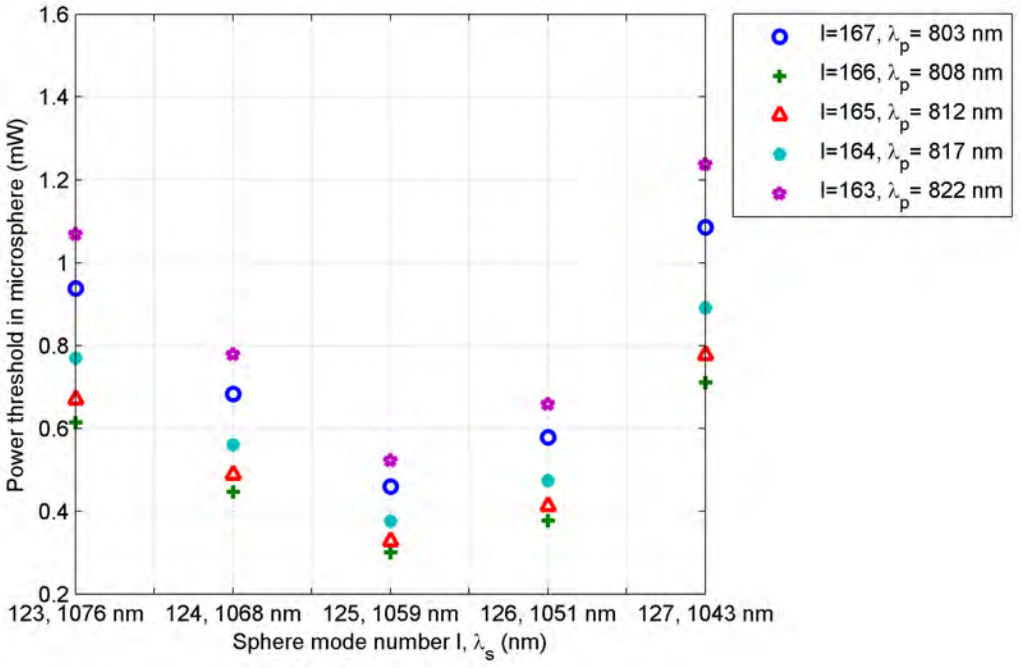

FIGURE 5.3: Calculated threshold pump power circulating in the fundamental WGM, $P_{\text{th-sphere}}$, for all possible resonant signal wavelengths, λ_s, for each resonant pump wavelength, λ_p, of 1.5-wt% Nd_2O_3-doped BK7 microsphere of 30 μm in diameter and $n_s = 1.51$, at zero separation from waveguide surface

Figure 5.3 shows that the lowest threshold pump power at the microsphere, $P_{\text{th-sphere}}$, was approximately 0.3 mW at the zero separation of microsphere from a waveguide surfaces. It can be seen that the lasing threshold is lowest at a pump wavelength of $\lambda_p = 808$ nm, and a signal wavelength of $\lambda_s = 1059$ nm, because the peak absorption of 1.5-wt% Nd_2O_3-doped BK7 glass is maximum at a wavelength near 808 nm and the peak of the fluorescence spectrum is located close to 1059 nm, thus the pump power that is needed in the system in order to overcome the total loss in the cavity is the lowest.

5.6 Calculation of threshold pump power as a function of microsphere-waveguide separation

In this section, the calculation of the threshold pump power as a function of the microsphere separation from a channel waveguide surface is carried out. A Teflon layer of refractive index $n_{\text{Teflon}} = 1.29$ is used as a means to separate the microsphere from waveguide surface. First, the threshold pump power within the microsphere, $P_{\text{th-sphere}}$, of a 1.5-wt% Nd_2O_3-doped BK7 microsphere of 30 μm diameter, is calculated, and then the threshold pump power within the coupled waveguide, $P_{\text{th-wg}}$, is derived. The last section includes the calculations of $P_{\text{th-sphere}}$ and $P_{\text{th-wg}}$ for a 1.5-wt% Nd_2O_3-doped BK7 microsphere of 190 μm diameter, represents practical values used in the next chapter.

The calculation of $P_{\text{th-sphere}}$ at $\lambda_p = 808$ nm and $\lambda_s = 1059$ nm is selected, because it provides the lowest threshold pump power as previously shown. Fields of the waveguide which were used in this calculation were obtained from a homogeneous channel of W $\times$ H of 5 μm by 3 μm with the substrate refractive index and the step refractive index of 1.51 and $\Delta\lambda = 0.0094$, respectively (for K^+-ion exchanged substrate on BK7). The separation of the microsphere from the waveguide surface was varied from 0 nm to 1000 nm. The calculation is based on the fundamental modes in both the microsphere ($l = m, n = 1$) and waveguide.

The overlap integration of the fields of the microsphere and the evanescent field of the waveguide at the signal wavelength at different microsphere-waveguide separations are carried out, to obtain Q_{c_s} as a function of the microsphere separation from the waveguide surface according to Equation 2.35a, where t can be obtained from the calculated κ (Equation 2.20) and the loss factor due to spurious attenuation at the pump wavelength, α_s is arbitrary chosen to be 0.99. By substituting Q_{c_s} into Equation 5.12, the values of $P_{\text{th-sphere}}$ as a function of microsphere separation from the waveguide surface are obtained. Table 5.3 shows Q_{c_s} at $\lambda_s = 1059$ nm for a 30 μm and a 190 μm diameter microspheres, which will be used in the power threshold calculation in the following sections.

Next, the calculated values of threshold pump power of a 1.5-wt% Nd_2O_3-doped BK7 microsphere of 30 μm diameter, and a 1.5-wt% Nd_2O_3-doped BK7 microsphere of 190 μm diameter, are determined. Detailed discussion on the results of $P_{\text{th-sphere}}$ and $P_{\text{th-wg}}$ for a 1.5-wt% Nd_2O_3-doped BK7 microsphere of 30 μm diameter, and a 1.5-wt% Nd_2O_3-doped BK7 microsphere of 190 μm diameter, will be elaborated.

Separation (nm)	Q_{c_s} of 30 μm microsphere	Q_{c_s} of 190 μm microsphere
0	5.97×10^4	3.51×10^4
100	6.48×10^4	393×10^4
200	7.00×10^4	4.34×10^4
300	7.48×10^4	4.71×10^5
400	7.85×10^4	4.98×10^5
500	8.09×10^4	5.15×10^5
600	8.25×10^4	5.25×10^5
700	8.34×10^4	5.29×10^5
800	8.37×10^4	5.31×10^5
900	8.39×10^4	5.32×10^5
1000	8.40×10^4	5.33×10^5

TABLE 5.3: Q_{c_s} of 30 μm and 190 μm diameter microspheres, $\alpha_s = 0.99$, at $\lambda_s = 1059$ nm

5.6.1 30 μm-diameter microsphere

The results for threshold circulating pump power as a function of microsphere separation from the waveguide surface, for the 1.5-wt% Nd_2O_3-doped BK7 microsphere of 30 μm in diameter that has the refractive index of 1.51 at the pump and signal wavelengths of $\lambda_p = 808$ nm and $\lambda_s = 1059$ nm, are shown in Figure 5.4 for separations of the microsphere from the waveguide surface of 0 nm to 1000 nm.

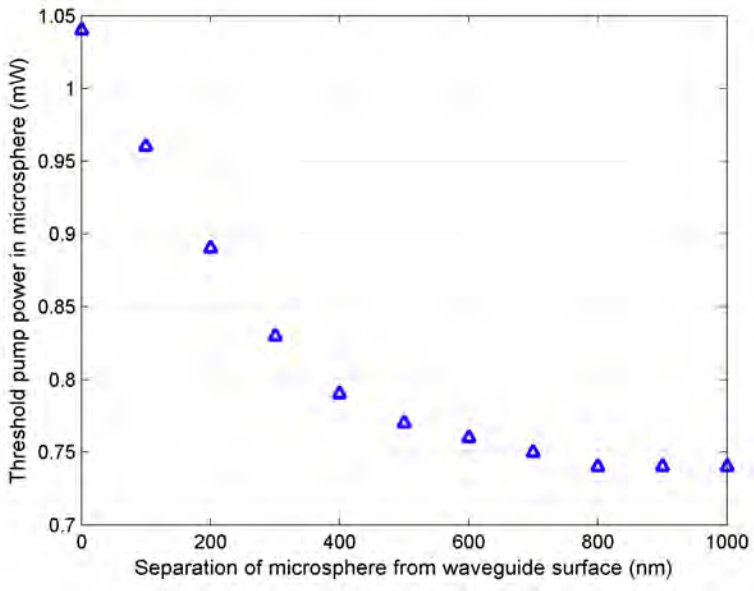

FIGURE 5.4: Calculated threshold power in the microsphere, $P_{\text{th-sphere}}$, as functions of separation of a 30 μm diameter Nd-doped BK7 microsphere from the waveguide surface

The threshold pump power in the microsphere at zero separation is found to be 1.04 mW, where the pump power threshold at the 1000 nm separation is found to be 0.74 mW. The threshold pump power decreases as the separation increases, because, as the separation gets larger, the quality factor of the system at the signal wavelength increases.

The pump power required in the waveguide for lasing action, $P_{\text{th-wg}}$, can be determined from $P_{\text{th-sphere}}$, by dividing the pump power required in the microsphere by the enhancement factor, ϵ, which relates P_{sphere} to P_{wg} as shown in Equation 5.13, as described in Chapter 4,

$$\left| \frac{P_{\text{sphere}}}{P_{\text{wg}}} \right| = \epsilon. \tag{5.13}$$

Thus, the pump power threshold at the waveguide, $P_{\text{th-wg}}$, can be expressed as follows:

$$\mathrm{P_{th\text{-}wg}} = \frac{1}{\epsilon} \cdot \frac{\left(\frac{2\pi^2 n_{\mathrm{eff}} \mathrm{D}}{\mathrm{Q}_{cs}\lambda_s}\right)}{\iint \mathrm{S}_s(x,y)\mathrm{S}_p(x,y)\,dx\,dy} \left(\frac{h\nu_p}{\tau\eta_q\sigma_s}\right) \left(\frac{1+\frac{\mathrm{a}_p}{\beta_p}}{1-\exp[-(\mathrm{a}_p+\beta_p)\pi\mathrm{D}]}\right), \quad (5.14)$$

where $\epsilon = \frac{\alpha^2(1-t^2)}{(1-\alpha t)^2}$ and $t = \sqrt{1-|\kappa|^2}$.

At the pump wavelength, the value of loss due to the Nd absorption, α_{Nd}, is selected to be 5.2 dB/cm following the practical value obtain from the prior work [6]. The loss factor due to spurious attenuation at pump wavelength, α_p, is selected to be 0.99. Thus, the total round-trip loss-factor in the cavity is found to be 0.9789 ($\alpha_{\mathrm{total}} = \alpha_{\mathrm{Nd}} \cdot \alpha_p$). Figure 5.5 shows the theoretical plots of enhancement factor which relates the power in the microsphere to the power in the input waveguide, as a function of coupling factor, when $\alpha_{\mathrm{total}} = 0.9789$.

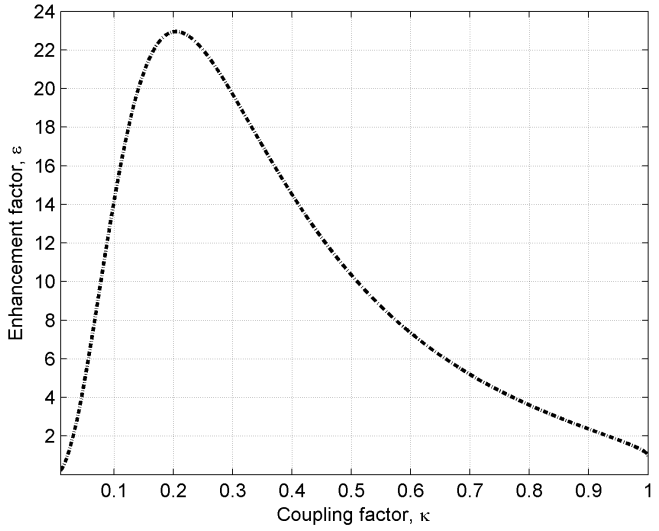

FIGURE 5.5: Enhancement factor as a function of coupling factor, with a loss due to Nd absorption of 5.2 dB/cm and attenuation loss, $\alpha_p = 0.99$ ($\alpha_{\mathrm{total}} = 0.9789$), for a 1.5-wt% Nd_2O_3-doped BK7 microsphere of 30 μm in diameter

Table 5.4 shows the calculated values of $1/\epsilon$ as according to the coupling factor at the pump wavelength at each microsphere and waveguide separation from 0 nm to 1000 nm. It can be seen that, the value of $1/\epsilon$ increases as the separation of the microsphere/waveguide increases due to the decrease of the coupling factor. Because, as the separation becomes larger, coupling efficiency at the pump wavelength significantly decreases.

$\mathrm{P_{th\text{-}wg}}$ are obtained by multiplying $\mathrm{P_{th\text{-}sphere}}$ with $1/\epsilon$. Figure 5.6 shows theoretical plots of the calculated threshold power in the waveguide, $\mathrm{P_{th\text{-}wg}}$, and $\mathrm{P_{th\text{-}sphere}}$, as a function of microsphere separation from the waveguide surface, with the value of attenuation loss factor of $\alpha_p = 0.99$ ($\alpha_{\mathrm{total}} = 0.9789$). It can be seen that, for zero microsphere/waveguide

Separation (nm)	Coupling factor, κ_p	$1/\epsilon$ $\alpha_{\text{total}} = 0.9789$
0	0.1245	0.06
100	0.1006	0.07
200	0.0774	0.10
300	0.0572	0.16
400	0.0413	0.29
500	0.0291	0.57
600	0.0197	1.22
700	0.0125	2.99
800	0.0077	7.86
900	0.0033	42.74
1000	0.0009	573.72

TABLE 5.4: Coupling factor at pump wavelength and $1/\epsilon$ as a function of microsphere separation from the waveguide surface, with a loss due to Nd absorption of 5.2 dB/cm and attenuation loss, $\alpha_p = 0.99$ ($\alpha_{\text{total}} = 0.9789$), for a 1.5-wt% Nd_2O_3-doped BK7 microsphere of 30 μm diameter

separation, $P_{\text{th-wg}}$ is the smallest, while it is increasing as the separation gets larger. In the low-coupling regime, where the microsphere is located at a far distance away from the waveguide surface, κ is relatively small, thus more of the required pump power for lasing is needed, compared with the stronger coupling cases. The minimum value of $P_{\text{th-wg}}$ is found at 0 nm separation and it has a value of 0.06 mW, while the maximum $P_{\text{th-wg}}$ is 425 mW at 1000 nm separation.

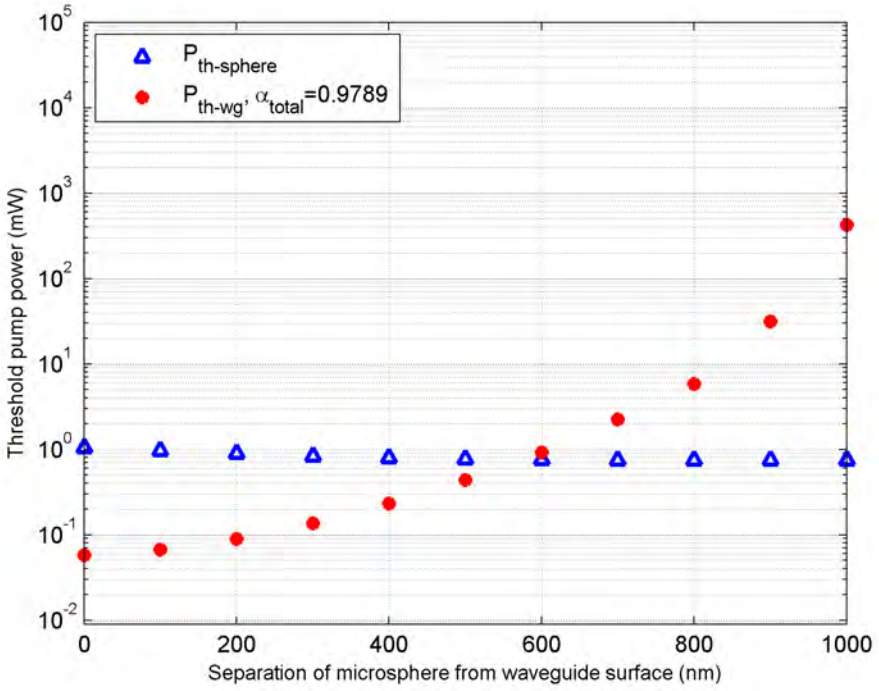

FIGURE 5.6: Calculated threshold power in the microsphere, $P_{\text{th-sphere}}$, and threshold power in the waveguide input, $P_{\text{th-wg}}$, as functions of separation of a 30 μm diameter Nd-doped BK7 microsphere from waveguide surface, with a loss due to Nd absorption of 5.2 dB/cm and attenuation loss, $\alpha_p = 0.99$ ($\alpha_{\text{total}} = 0.9789$), for $\alpha_s = 0.99$

5.6.2 190 μm-diameter microsphere

In this section, calculation of the power threshold in the waveguide for a 1.5-wt% Nd_2O_3-doped microsphere of 190 μm diameter is carried out, as in the previous section. Table 5.5 shows the parameters used for the calculations in this section. Microspheres of 190 μm diameter and refractive index of 1.51 are used in this calculation, and the corresponding sphere mode numbers l of 1096 and 833 are obtained at $\lambda_p = 808$ nm and $\lambda_s = 1059$ nm respectively. The loss due to the Nd absorption and the loss due to the attenuation of the microsphere cavity at the pump and signal wavelengths of 0.9310, 0.99 and 0.99, are included, respectively.

Parameters	Values
Microsphere diameter, D (μm)	190
Microsphere refractive index, n_s	1.51
Pump wavelength, λ_p (nm)	808
Sphere mode number l at λ_p	1096
Signal wavelength, λ_s (nm)	1059
Sphere mode number l at λ_s	833
Loss factor due to Nd absorption, α_{Nd}, (5.2 dB/cm)	0.9310
Loss factor due to attenuation at pump wavelength, α_p	0.99
$\alpha_{\mathrm{total}} = \alpha_{\mathrm{Nd}} \cdot \alpha_p$	0.9217
Loss factor due to attenuation at signal wavelength, α_s	0.99
Quality factor at λ_s, Q_{c_s}	3.51×10^5
Coupling factor at λ_p, κ	0.1602
Power threshold at sphere, $P_{\text{th-sphere}}$	0.66 mW
Enhancement factor, ϵ	2.679
1/Enhancement factor, $1/\epsilon$	0.3733
Power threshold at waveguide, $P_{\text{th-wg}}$	0.25 mW

TABLE 5.5: Parameters that are used for power threshold calculation for a 1.5-wt% Nd_2O_3-doped BK7 microsphere of 190 μm diameter

A Q_{c_s} of 6.62×10^4 is obtained from coupling factor at the signal wavelength calculated by overlapping the field at the signal wavelength 1059 nm with the evanescent field of the waveguide. The power threshold in the microsphere is found to have a value of 0.66 mW. Figure 5.7 shows the calculated plot of the enhancement factor of the microsphere with $\alpha_{\mathrm{total}} = 0.9217$. A coupling factor, κ, of 0.1602 at the pump wavelength is calculated. For a coupling factor of 0.1602 and $\alpha_{\mathrm{total}} = 0.9217$, $1/\epsilon = 0.3733$ is obtained. Consequently, the corresponding power threshold at the input waveguide of $P_{\text{th-wg}} = 0.25$ mW is obtained. $P_{\text{th-sphere}}$ of the smaller sphere (30 μm diameter) is found to be larger compared to the $P_{\text{th-sphere}}$ from the sphere in this case, this because of Q_{c_s} for the larger sphere is greater than the smaller one. As it can be seen from Equation 5.12 that $P_{\text{th-sphere}}$ is inversely proportional to Q_{c_s}.

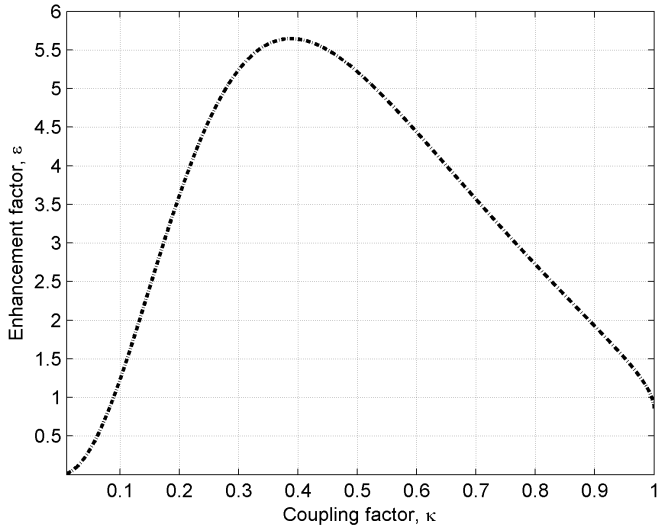

FIGURE 5.7: Enhancement factor as a function of coupling factor, with a loss due to Nd absorption of 5.2 dB/cm and attenuation loss, $\alpha_p = 0.99$ ($\alpha_{\text{total}} = 0.9217$), for a 1.5-wt% Nd_2O_3-doped BK7 microsphere of 190 μm in diameter

The calculation of the pump power threshold as a function of the microsphere and waveguide separation are now described. Table 5.6 shows values of $1/\epsilon$ and coupling factors at the 808-nm-pump wavelength as a function of microsphere and waveguide separation from 0 nm to 1000 nm. It can be seen that the value of $1/\epsilon$ is increasing rapidly as the separation gets larger in the same manner as shown in previous section.

Separation (nm)	Coupling factor, κ_p	$1/\epsilon$ $\alpha_{\text{total}} = 0.9217$
0	0.1602	0.37
100	0.1272	0.54
200	0.0962	0.87
300	0.0695	1.58
400	0.0487	3.13
500	0.0329	6.75
600	0.0211	16.29
700	0.0125	46.27
800	0.0071	143.25
900	0.0024	1252.98
1000	0.0003	80192.46

TABLE 5.6: Coupling factor at pump wavelength and $1/\epsilon$ as a function microsphere separation from the waveguide surface, with a loss due to Nd absorption of 5.2 dB/cm and attenuation loss, $\alpha_p = 0.99$ ($\alpha_{\text{total}} = 0.9217$), for a 1.5-wt% Nd_2O_3-doped BK7 microsphere of 190 μm diameter

Figure 5.8 shows the plots of the calculated threshold power in the microsphere, $P_{\text{th-sphere}}$, and the threshold power in the waveguide input, $P_{\text{th-wg}}$, as functions of separation of a 190 μm diameter Nd-doped BK7 microsphere from the waveguide surface.

It can be seen that the power threshold within the microsphere and the power threshold in the waveguide have the same trends as the previous section. The pump power thresholds in the sphere are found to have smaller values than the ones in the 30-μm-case. The minimum of $P_{\text{th-sphere}}$ is 0.44 mW at 1000 nm separation, while for the maximum $P_{\text{th-sphere}}$, the value of about 0.66 mW was obtained at the zero separation. Because Q_{c_s} obtained with the 30 μm diameter sphere are larger than the 190-μm-case. However, the pump power thresholds in the waveguide are found to have larger values than the ones in the 30-μm-case. The minimum of $P_{\text{th-wg}}$ is 0.25 mW at the zero separation, while for the maximum $P_{\text{th-wg}}$, the value of about 3.5×10^4 mW was obtained at 1000 nm separation. Thus, it can be concluded that the microsphere of a larger size requires more pump power in the waveguide for lasing action; because round-trip attenuation at the pump wavelength is expected to be higher, as it can be seen in Equation 5.1. In this case ϵ becomes smaller, hence higher $1/\epsilon$ and $P_{\text{th-wg}}$.

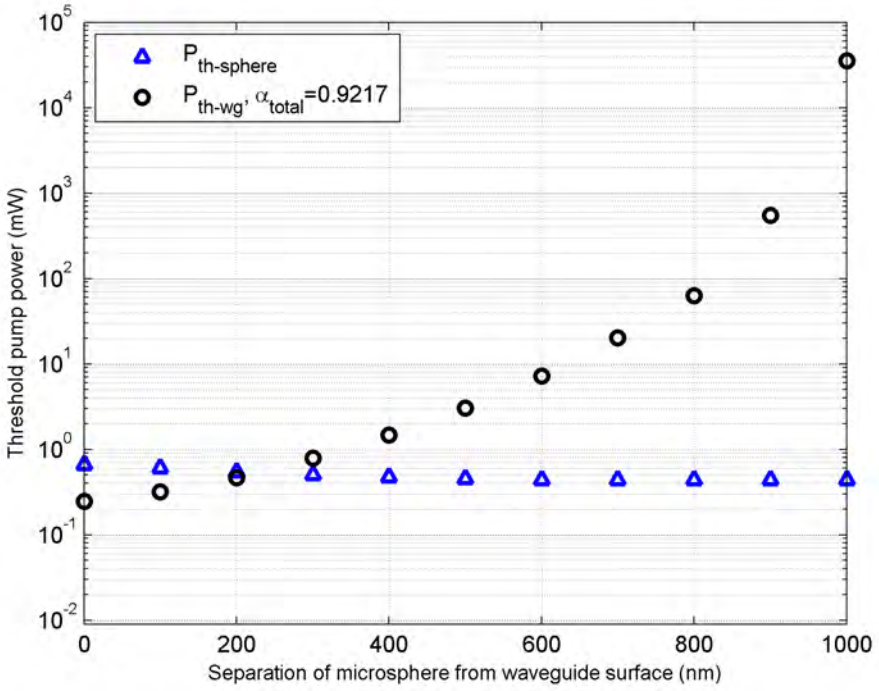

FIGURE 5.8: Calculated threshold power in the microsphere, $P_{\text{th-sphere}}$, and threshold power in the waveguide input, $P_{\text{th-wg}}$, as functions of separation of a 190 μm diameter Nd-doped BK7 microsphere from waveguide surface, with a loss due to Nd absorption of 5.2 dB/cm and attenuation loss, and $\alpha_p = 0.99$ ($\alpha_{\text{total}} = 0.9217$), for $\alpha_s = 0.99$

5.7 Conclusions

The theoretical basis of microsphere lasers has been described. The expressions of loss and gain of the laser cavity for a microsphere have been derived. The derivation of the minimum Q which is required for the lasing action to occur has been obtained. The minimum Q factor that would be required for the lasing action to occur for a 1.5-wt% Nd_2O_3-doped BK7 microsphere of 30 μm diameter, has been found ($Q = 3 \times 10^4$). The Q factor obtained with the microspheres fabricated in-house by dropping through the vertical furnace (as described in Chapter 3) are higher than the minimum Q required for lasing (6.2×10^4 @ 1550 nm), thus, it is confirmed that the lasing action can be achieved with these microspheres, with sufficient pump power.

Threshold pump power at the microsphere, $P_{\text{th-sphere}}$, for each possible excited mode according to each pump wavelength in the Nd-doped glass absorption band for a 1.5-wt% Nd_2O_3-doped BK7 microsphere of 30 μm diameter at a zero separation from the waveguide surface, have been calculated. For simplicity, the calculations have been carried out for the fundamental modes for both the microsphere ($l = m$, $n = 1$) and waveguide, and the assumption has been made that the loss due to spurious attenuation is negligible. Loss due to Nd absorption was chosen to be 5.2 dB/cm. It has been found that the lowest threshold pump power obtained from a 30 μm diameter Nd-doped BK7 microsphere is about 0.3 mW at $\lambda_p = 808$ nm and $\lambda_s = 1059$ nm.

Threshold pump power at the waveguide, $P_{\text{th-wg}}$, must be calculated since the measurement can be done straightforwardly. $P_{\text{th-wg}}$ for a 1.5-wt% Nd_2O_3-doped BK7 microsphere of a 30 μm diameter and a 190 μm diameter as a function of the sphere separation from the waveguide surface at $\lambda_p = 808$ nm and $\lambda_s = 1059$ nm, have been calculated. The comparison of $P_{\text{th-wg}}$ for a 30 μm and a 190 μm diameter microspheres has been done. The loss due to Nd absorption of 5.2 dB/cm and loss due to spurious attenuation of $\alpha_p = \alpha_s = 0.99$ were included in the calculation. The laser threshold pump power at the waveguide, $P_{\text{th-wg}}$, for the 30 μm diameter microsphere has been determined to have the minimum value, which is about 0.06 mW, at zero separation from waveguide surface. $P_{\text{th-wg}}$ significantly increased as the separation increased from 0 nm to 1000 nm, because $1/\epsilon$ increased rapidly. $P_{\text{th-wg}}$ of a 190 μm diameter 1.5-wt% Nd_2O_3-doped BK7 microsphere of $P_{\text{th-wg}} = 0.25$ mW at zero separation, has been obtained. It has been found that a microsphere of a larger size requires more pump power at the waveguide for lasing, as expected, because the total round-trip attenuation at the pump wavelength in a larger sphere is higher than in the smaller sphere. The results indicate that, at the large separation, the power threshold at the microsphere is smaller, however the required power at the input waveguide is larger, because the value of the reciprocal of the enhancement factor at the pump wavelength increases rapidly as the separation becomes larger. In order to obtain the minimum threshold pump power at the input waveguide of the system, $P_{\text{th-wg}}$, the microsphere must be placed at the critical coupling

regime, where the enhancement factor is maximum. By reducing the loss in the sphere cavity and increasing the coupling efficiency of the microsphere and waveguide to the point where $\kappa = \sqrt{1 - |\alpha|^2}$, the critical coupling can be obtained. The thermal effect to the shift of WGM in microspheres will be discussed in the following chapter.

5.8 References

[1] A. E. Siegman. *Lasers*. Univerity Science Books, California, 1986. ISBN 0-935702-11-3.

[2] L. M. B. Hickey, V. Apostolopoulos, R. W. Eason, J. S. Wilkinson, and A. A. Anderson. Diffused Ti:sapphire channel-waveguide lasers. *Jounal of the Optical Society of America B*, 21:1452–1462, 2004.

[3] C. H. Huang, L. McCaughan, and D. M. Gill. Evaluation of absorption and emission cross sections of Er-doped $LiNbO_3$ for application to integrated optic amplifiers. *Jounal of Lightwave Technology*, 12:803–809, 1994.

[4] E. Mwarania. *PhD thesis on Planar ion-exchange waveguide lasers in glass*. University of Southampton, Southampton, 1992.

[5] A. N. Miliou, X. F. Cao, R. Srivastava, and R. V. Ramaswamy. 15-dB amplification at 1.06 μm in ion-exchanged silicate glass waveguides. *IEEE Photonics Technology Letters*, 4:416–418, 1993.

[6] E. K. Mwarania, J. Wang, J. Lane, and J. S. Wilkinson. Neodymium-doped ion-exchanged waveguide lasers in BK-7 glass. *Journal of Lightwave Technology*, 11: 1550–1558, 1993.

[7] M. Rosenblit, P. Horak, S. Helsby, and R. Folman. Single-atom detection using whispering-gallery modes of microdisk resonators. *Physical Review A*, 70:053808–1–053808–10, 2004.

Chapter 6

Experimental characteristics of neodymium-doped microspheres

6.1 Introduction

In this chapter, details of work on Nd-doped BK7 microsphere lasers will be explored. Lasing and fluorescence behaviours of commercial Nd-doped BK7 microspheres [1] and in-house made neodymium-doped BK7 microspheres, for which details of fabrication were described in Section 3.4 in Chapter 3, will be characterised. The neodymium-doped BK7 microsphere laser exhibits a 4-level lasing system, at the $^4F_{3/2}$ - $^4I_{11/2}$ transition at wavelengths in the 1060 nm region, where a sufficient population inversion is obtained, with free-space pumping.

Section 6.2 includes a detailed discussion of experimental work on confocal fluorescence studies. The objective of Section 6.2 is to study the fluorescence lifetime and fluorescence characteristics of the Nd-doped microspheres. The experiments on the observation of fluorescence emission at wavelengths near 1060 nm from a single Nd-doped BK7 microsphere and the measurement of the fluorescence lifetime will be carried out. Methods and procedures of fluorescence emission and fluorescence lifetime measurements for a single microsphere, will be discussed. In Section 6.3, the experimental work on fluorescence emission from the Nd-doped microsphere, when it is evanescently coupled from a potassium-sodium-ion exchanged channel waveguide, will be described, and mode assignment to the families of the WGMs spectra will be elaborated. Section 6.4 describes experimental work on a microsphere laser by free-space light excitation. The aim of this section is to characterise lasing behaviour of a single Nd-doped microsphere as a function of pump power and wavelength, independently of waveguide excitation which imposes more constraints on lasing. The aim of Section 6.5 is to determine whether Nd-doped microspheres, excited by the evanescent field of the waveguide, exhibit lasing action at a lower threshold power compared to the free-space excitation. Section 6.5 includes

discussion of experimental procedures to obtain the lasing oscillation by evanescently exciting a single Nd-doped BK7 microsphere with a channel waveguide. A suggested plan for further work will be addressed at the end of the section.

6.2 Confocal fluorescence measurements

In this section, the confocal microscopy technique is used to visualise the fluorescence behaviour from the Nd-doped samples. The detailed discussion of the experimental work of using the confocal microscopy technique to obtain the information of fluorescence emission from a single Nd-doped BK7 microsphere and a Nd-doped BK7 bulk glass, are included. The work is in collaboration with Dr. Daniel Jaque and Mr. Antonio Benayas, at Departmento de Física de Materiales, Universidad Autónoma de Madrid, Madrid, Spain [2].

The experimental apparatus that is used to observe the spectroscopic properties of Nd-doped BK7 microspheres, results and discussion of fluorescence lifetime measurement and fluorescence measurement of Nd-doped microspheres, are described in this section. The confocal microscopy technique is an appropriate method for a localised study of the behaviour of the fluorescence emission from the Nd-doped microspheres, where the tight beam spot size is locally focused onto the desired location of the microsphere. The illumination from the Nd-doped microsphere is detected and the WGM emission spectra from the sample are observed. The comparisons of the WGM characteristics of the microsphere with obvious defects on the surface with those of a perfect microsphere are described in this section. The experimental work in this section includes two types of microspheres: commercial 2.2-wt% concentration of Nd_2O_3-doped BK7 microspheres from Mo-Sci [1] with diameter of 30±3 μm, and in-house made 1.5-wt% Nd_2O_3-doped BK7 microspheres with a range of sizes from 30 μm to 200 μm diameter, fabricated on the carbon substrate as described in Section 3.4.1.

6.2.1 Experimental apparatus

The apparatus used for a confocal fluorescence characterisation is shown in Figure 6.1. A fibre coupled 808 nm diode laser was launched to focus onto a Nd-doped BK7 microsphere, located on a XYZ translation stage. The 808-nm laser beam was reflected and tilted downward by a dichroic mirror which transmits light in the 1060 nm region, and the focused onto the microsphere by a 50× microscope objective lens, resulting in a laser spot size of about 5 μm in diameter. The laser spot size can be adjusted by using a different microscope objective lens. The fluorescence emitted from the microsphere was collected with the same objective lens, as shown in Figure 6.1. The emitted light was directed to a 1060-nm-pass-dichroic mirror and fluorescence light was passed through the

mirror and launched into the fibre connected to spectrometer, via a lens. The fluorescence emission obtained from the microsphere was launched into the spectrometer, and the spectrum was recorded. For lifetime measurements, the emitted light was launched into the fibre connected to a photomultiplier tube and the signal was recorded using a digital oscilloscope (Lecroy, 500 MHz).

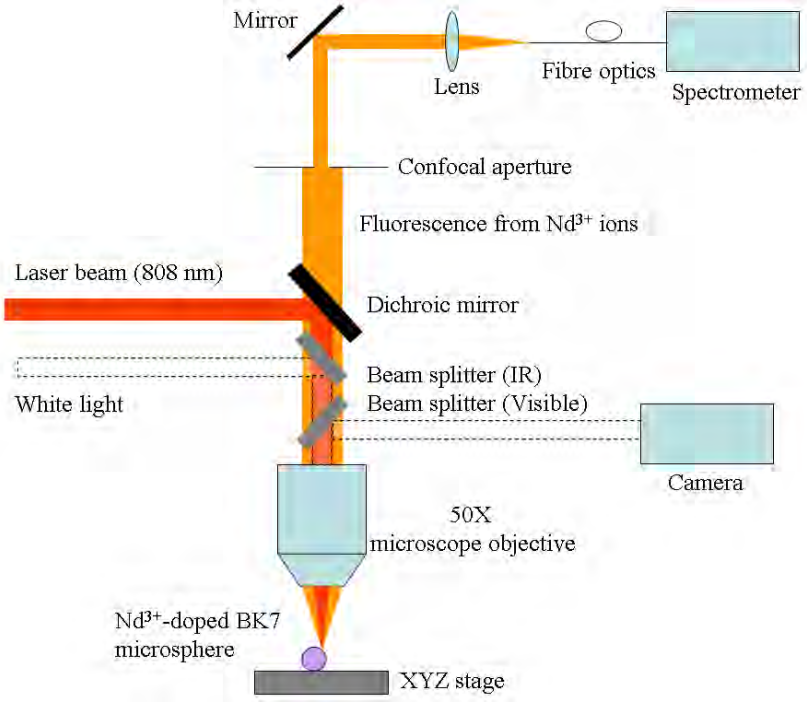

FIGURE 6.1: Experimental apparatus: Luminescence measurement

6.2.2 Fluorescence lifetime measurements

The aim of the experimental work in this section is to obtain the fluorescence lifetime measurements of Nd-doped BK7 bulk glass and microspheres, to compare with the value from similar material used in the theoretical section, described in Chapter 5. The experimental work on fluorescence lifetime measurements of Nd-doped BK7 bulk glass and microspheres are described.

The fluorescence lifetime refers to the average amount of time atoms stay in the excited state. The fluorescence lifetime can be determined by the fluorescence intensity. The fluorescence intensity, at time t, is defined by [3],

$$\mathrm{I}(t) = \mathrm{I}_o \exp\left(\frac{-t}{\tau}\right), \tag{6.1}$$

where I_o is the intensity before decaying and τ is the lifetime at the time where $\mathrm{I} = \mathrm{I}_o/\mathrm{e}$.

The measurement of the fluorescence lifetime for a bulk BK7 glass doped with 1.5-wt%

of Nd_2O_3 was carried out. An 808-nm-pulse laser beam, which has a repetition rate of 2.5 kHz and pulse width of 50 ps, was launched to focus onto a bulk BK7 glass that is doped with 1.5-wt% of Nd_2O_3. The emission light was collected with a photomultiplier tube via a fibre optics, the fluorescence signal was averaged and recorded with a 500 MHz digital oscilloscope. The fluorescence lifetime for a bulk BK7 doped with 1.5-wt% of Nd_2O_3 was recorded.

The pulsed-laser beam with the same repetition rate and pulse width as were used for the bulk glass, was then used to study the microsphere. The measurements of the fluorescence lifetime for a commercial 30±3 μm diameter BK7 microsphere doped with 2.2-wt% of Nd_2O_3 and an in-house made 100±5 μm diameter BK7 microsphere doped with 1.5-wt% of Nd_2O_3, that was fabricated on glassy carbon plate as described in Section 3.4.1, and an in-house made 1.5-wt% Nd_2O_3-doped BK7 microsphere of 170 μm diameter fabricated by dropping through a vertical furnace as described in Section 3.4.2, were carried out.

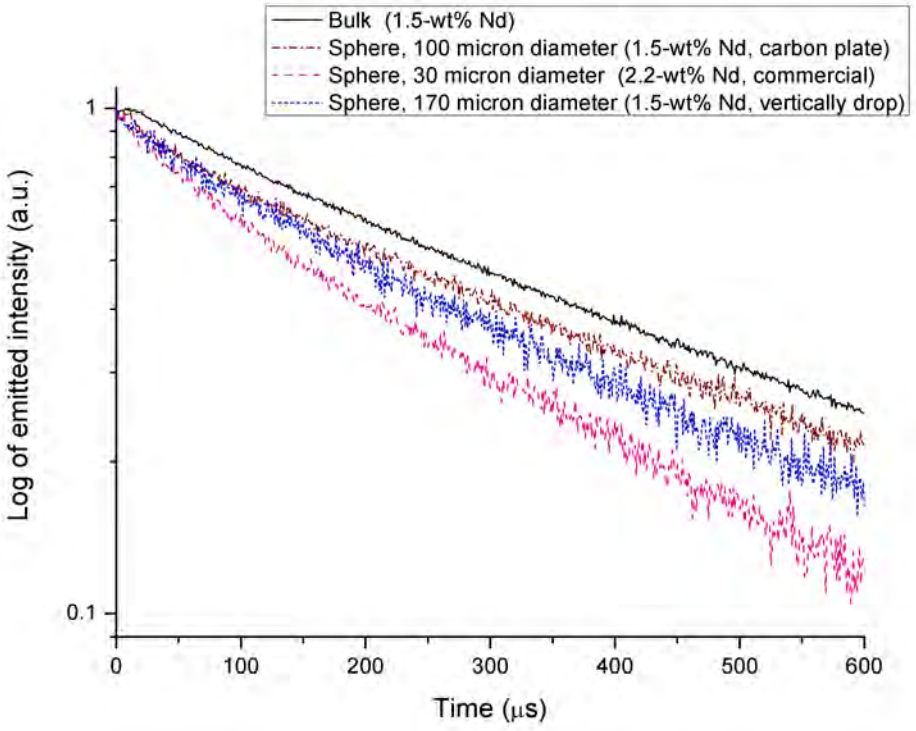

FIGURE 6.2: Fluorescence decay curve of a 1.5-wt% Nd_2O_3-doped BK7 bulk glass (solid line), a commercial 2.2-wt% Nd_2O_3-doped BK7 microsphere of 30 μm diameter (dashed line), an in-house made 1.5-wt% Nd_2O_3-doped BK7 microsphere of 100 μm diameter fabricated on glassy carbon plate (dash-dotted line) and an in-house made 1.5-wt% Nd_2O_3-doped BK7 microsphere of 170 μm diameter fabricated by dropping through a vertical furnace (dotted line)

Figure 6.2 shows fluorescence decay curves of a 1.5-wt% Nd_2O_3-doped BK7 bulk glass, a commercial 30±3 μm diameter BK7 microsphere doped with 2.2-wt% of Nd_2O_3, an

in-house made 1.5-wt% Nd_2O_3-doped BK7 microsphere of 100±5 μm diameter and an in-house made 1.5-wt% Nd_2O_3-doped BK7 microsphere of 170±5 μm diameter. The fluorescence lifetime for a 1.5-wt% Nd_2O_3-doped BK7 bulk glass is found to have a value of $\tau = 431.99 \pm 0.88$ μs, for a 2.2-wt% Nd_2O_3-doped BK7 microsphere of 30±3 μm diameter is found to be $\tau = 281.01 \pm 1.58$ μs, for an in-house made 1.5-wt% Nd_2O_3-doped BK7 microsphere of 100±5 μm diameter fabricated on glassy carbon plate is found to be $\tau = 393.59 \pm 1.55$ μs and for an in-house made 1.5-wt% Nd_2O_3-doped BK7 microsphere of 170 μm in diameter fabricated by dropping through a vertical furnace is found to be $\tau = 344.48 \pm 1.25$ μs. The microsphere exhibits a lower lifetime compared to a bulk glass with the same concentration, this may be due to the heating process of the sphere formation during the fabrication altering the local environment of the Nd ions in a microsphere compared to the bulk [4]. Fast decay at the beginning of the decay time might correspond to the energy transfer between the high density Nd-ions in the metastable state due to the high excitation rate. The lifetime reduction with microsphere size reduction may be due to a high pump density and/or high density of possible defects introduced in a small sphere, hence a shorter lifetime [2]. To further investigate the fluorescence lifetime as a function of the microsphere and bulk material including the lifetime on sphere size dependence, a detail experimental work to characterise microsphere size dependence of the fluorescence lifetime for sphere and bulk is required.

6.2.3 Fluorescence measurement from a microsphere with variation of the position of the pump beam

In this section, measurements of the fluorescence spectra of commercial 2.2-wt% Nd_2O_3-doped BK7 microsphere of 30±3 μm [1] with respect to the location of the excited beam, is described. In order to observe the fluorescence WGM behaviour of a single microsphere with respect to the location of the excited beam, the continuous wave excitation from a fibre coupled 808 nm diode laser was focused onto the 2.2-wt% Nd_2O_3-doped BK7 microsphere of 30±3 μm on the edge and centre of the microsphere. The emitted light was collected and recorded.

Figure 6.3 shows the WGM spectrum obtained when the position of the focused beam onto the microsphere was altered. It shows that, at the edge-excitation, the fluorescence WGM is more prominent compared to the WGM from the centre-excitation. Q of 2.5×10^3 at $\lambda = 1055.68$ nm for the edge excitation is obtained, while the spectrum obtained from the centre excitation exhibits Q of 1.9×10^3 at $\lambda = 1055.68$ nm. Thus, it can be concluded that the edge-excitation is desirable since it causes an enhancement of WGM characteristics from the microsphere [5].

It is to be noted that, the resonant peaks of the fundamental TM modes are located at 1048.48 nm, 1055.68 nm, 1063.18 nm, and 1070.36 nm, which comprises the FSR of 7.35±0.10 nm at 1055.68 nm. The other peaks correspond to the higher radial modes

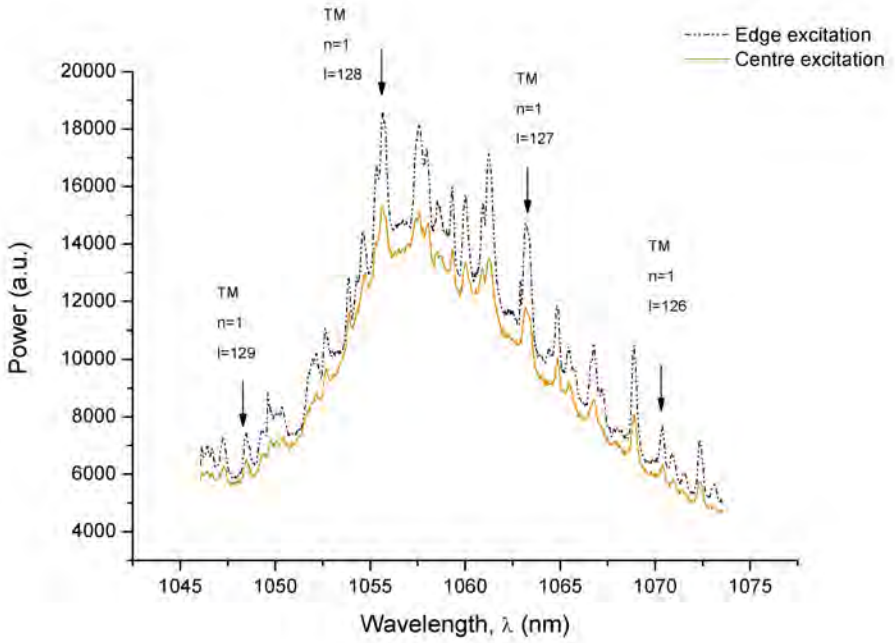

FIGURE 6.3: Fluorescence spectra of a 2.2-wt% Nd_2O_3-doped BK7 microsphere, microsphere diameter of 30±3 μm, pump power 69.54 mW

in the TM polarisation. The resonant wavelengths fit to the TE polarisation are not matched to the other families of peaks, thus these peaks are not associated with the TE modes, which agree with the discussion in Chapter 4. Finally, when the mode assignment is performed to this data, with the same method as described in Chapter 4, the microsphere diameter of 30.64±0.04 μm is obtained. The spectrum shows the good WGM characteristics, where the resonance peaks yield the microsphere diameter to be within the manufacturer tolerance.

6.2.4 Pump power dependence of fluorescence spectra

In this section, the measurement of the fluorescence spectra obtained from an in-house made 1.5-wt% Nd_2O_3-doped microsphere as a function of pump power level is described. The microsphere of about 40±3 μm diameter, measured by optical microscope, was characterised. The pump power was varied from 69.54 mW to 260.45 mW. The emission spectrum for each pump power was recorded.

The fluorescence spectra obtained from a 1.5-wt% Nd_2O_3-doped microsphere as a function of pump power level are shown in Figure 6.4. It can be seen that, as the pump power level increases, the intensity level of the emitted fluorescence spectrum increases as expected. Figure 6.5 shows the fluorescence peak power at $\lambda = 1057.39$ nm as a function of input power. It can be seen that the peak power is increasing as the pump power is increasing.

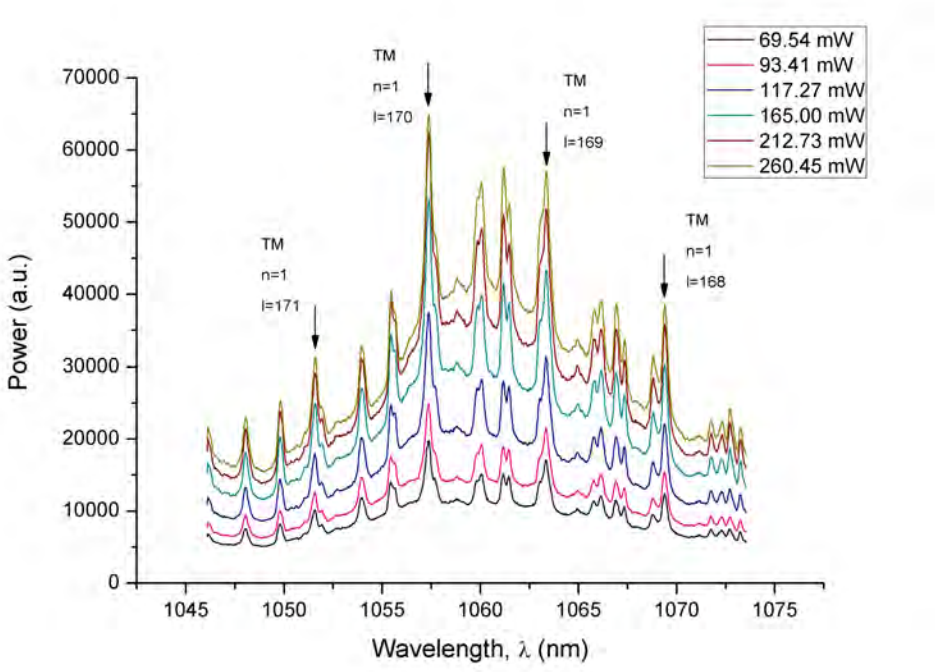

FIGURE 6.4: Fluorescence spectra of 1.5-wt% Nd_2O_3-doped BK7 microsphere as a function of pump power from 69.54 mW to 260.45 mW

The spectrum shows WG fluorescence in the wavelength range from 1045 nm to 1075 nm. The spectrum shows a strong evidence of WGM, where it exhibits Q of 2.5×10^3 at $\lambda = 1057.39$ nm. The locations of the major resonant peaks are at 1051.56 nm, 1057.39 nm, 1063.32 nm and 1069.40 nm. Comparison with the model in Chapter 2 shows that these resonances, with a free-spectral range of about 5.88±0.10 nm at $\lambda = 1057.39$ nm, correspond to the sphere mode number $n = 1$ and the sphere mode number l from 171 to 168, see Figure 6.4, and a diameter of 40.28±0.08 μm is obtained. The other families of peaks correspond to the higher radial modes in the TM polarisation. The tolerance

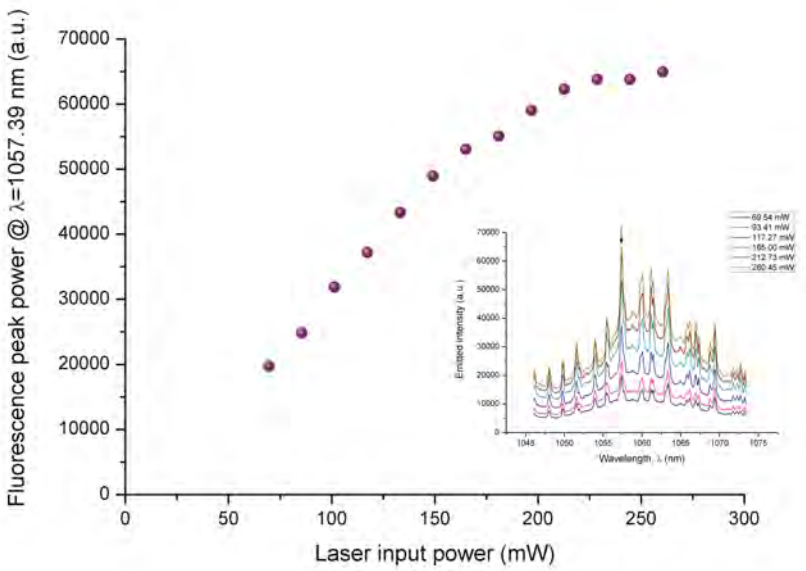

FIGURE 6.5: Fluorescence peak power of 1.5-wt% Nd_2O_3-doped BK7 microsphere at 1057.39 nm as a function of input power. Inset: Fluorescence spectra of 1.5-wt% Nd_2O_3-doped BK7 microsphere as a function of pump power from 69.54 mW to 260.45 mW

value of the diameter of the microspheres is found such that the maximum discrepancy of the theoretical and experimental resonant wavelength, $\Delta\lambda_{res}$, is found to be less than 0.01 nm.

Figure 6.5 shows the collected fluorescence power as a function of pump power. The curve displays evidence of saturation at above 200 mW. The pumping configuration of the tight-focus excitation spot is not appropriate for lasing action to occur, because of the small excited area.

6.2.5 Fluorescence measurements on microspheres containing defects

In this section, an experiment is derived on the observation of the fluorescence spectra emitted from a microsphere with defects in order to study the WGM behaviour of a microsphere containing a defect compared to a "perfect" microsphere which refers to the microsphere that has no obvious defects on its surface. The commercial 2.2-wt% Nd_2O_3-doped BK7 microspheres, with a nominal diameter of 30 μm [1], were selected such that the sizes were similar, so that the direct comparison of the WGM characteristics of the scattered intensity obtained from both microspheres could be straightforward to make. Figure 6.6 and 6.7 show the images of the microspheres that were chosen for this experiment, the diameters of microspheres are 30.70 μm and 31.90 μm, respectively. The microsphere in Figure 6.6 represents a "perfect" surface microsphere, because there are no obvious defects on the surface. In contrast, Figure 6.7 shows an image of a microsphere with large air traps located on the outer region of microsphere on its surface. The experiment was done such that the pump power (77.5 mW), the laser spot size (5 μm), and the position of the focused beam onto the microsphere (at the edge of the microsphere) were maintained the same for both cases.

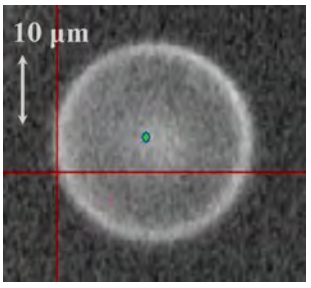

FIGURE 6.6: 2.2-wt% Nd_2O_3-doped microsphere 30.70 μm in diameter, with no defect on the surface

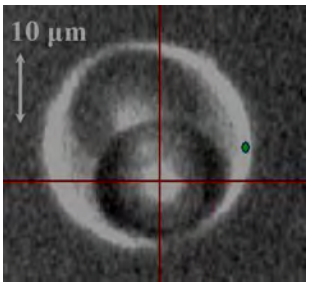

FIGURE 6.7: 2.2-wt% Nd_2O_3-doped microsphere 31.90 μm in diameter, with air traps located near the surface

Figure 6.8 shows the fluorescence spectra obtained from the microspheres in both cases, showing that the fluorescence spectrum obtained from the microsphere with defects on its surface exhibits no evidence of resonant peaks, whereas for the "perfect" microsphere case, the fluorescence spectrum exhibits strong WGM characteristics with a Q factor of 1.3×10^3 at $\lambda = 1056.55$ nm. The defects due to air traps that are located on the microsphere surface distorted the WG path propagation of the light, these prevent the resonant condition from occurring.

The fluorescence lifetime of a 1.5-wt% Nd_2O_3-doped BK7 microsphere was obtained, and it can be used to compare with the theoretical section in Chapter 5. The measurement of the fluorescence from the microsphere, by the evanescent light excitation, is the next step to explore the behaviour of the Nd-doped microsphere.

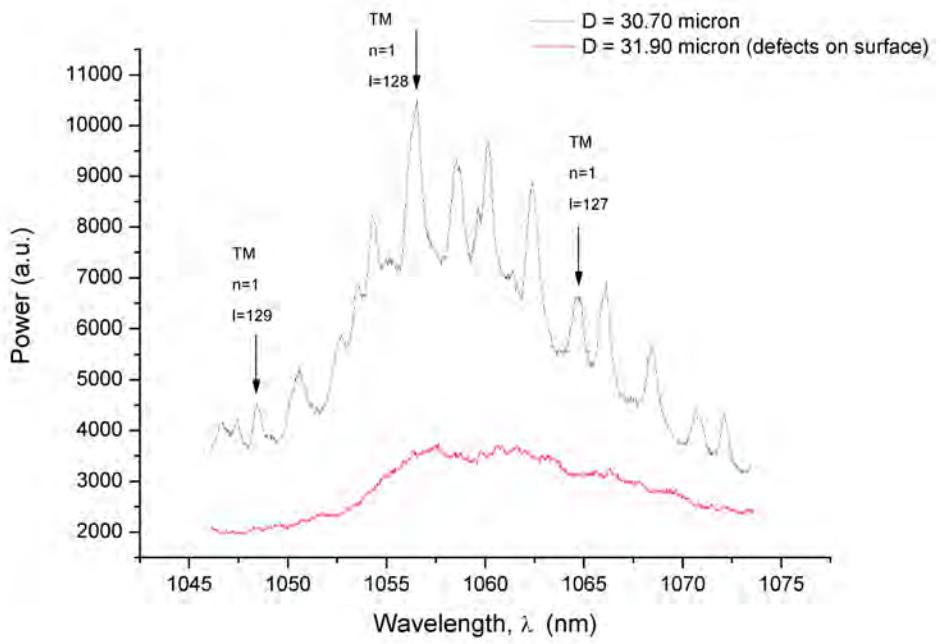

FIGURE 6.8: Fluorescence spectra of a 2.2-wt% Nd_2O_3-doped BK7 microsphere, comparison with a defected microsphere

6.3 Microsphere fluorescence measurements: Waveguide excitation

The purpose of the experimental work in this section is to couple light into a microsphere by using a channel waveguide, so the evanescent light coupling into the microsphere can be obtained. The fluorescence measurements of the 1.5-wt% Nd_2O_3-doped BK7 microspheres, fabricated based on the detailed discussion in Section 3.4.2, in Chapter 3 coupling with a potassium-sodium-ion exchanged waveguide are carried out. These microspheres are chosen for characterisation in this section, as they have a good surface quality, where Q of about 6×10^4 at wavelength near 1550 nm was observed, and they will be used later on in this thesis in the microsphere laser experiment.

6.3.1 Experimental apparatus

Figure 6.9 shows the experimental apparatus used for measuring fluorescence spectra from microspheres when excited from a waveguide. Light from Ti:sapphire laser was coupled into the K^+-Na^+-ion exchanged waveguide channel, which was fabricated as described in Section 3.2, by a 10× microscope objective lens. The evanescent light from the waveguide was coupled into the microsphere, and the emitted light from the microsphere was collected with a multimode fibre. A variable attenuator was used to alter the input power. The fluorescence spectrum of the emitted light from the microsphere was monitored with an optical spectrum analyser. The power at the output of the waveguide was monitored with a power meter.

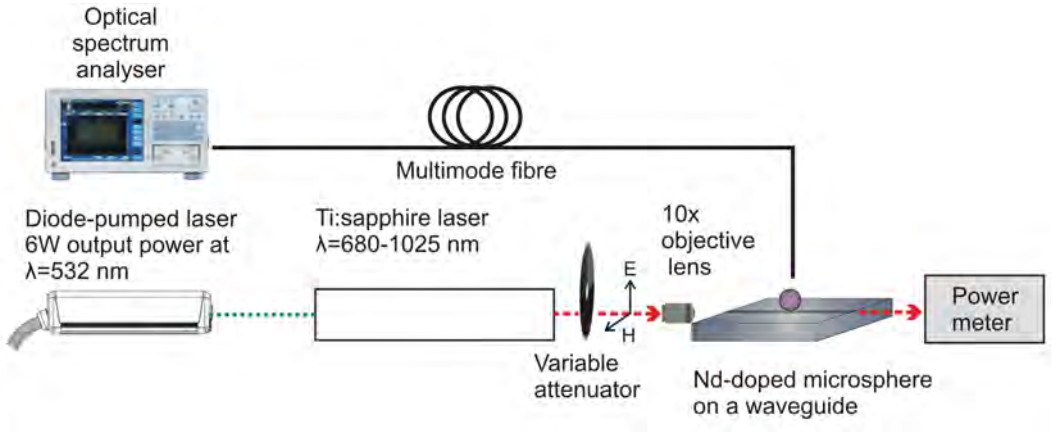

FIGURE 6.9: Experimental apparatus for fluorescence measurement of a microsphere coupling with a channel waveguide

6.3.2 Fluorescence spectra

The pump light in the TM polarisation of about 80 mW before the microscope objective lens was launched into a channel waveguide. The emission spectrum was recorded with

an optical spectrum analyser. The output power at the waveguide is about 65 mW. Figure 6.10 shows the fluorescence spectrum obtained from a BK7 microsphere doped with 1.5-wt% of Nd_2O_3 that has a diameter of 105±3 μm. Q of about 6×10^3 at λ = 1058.76 nm was obtained. The WGM spectrum obtained from the microsphere when excited with the evanescent field of an optical waveguide, shows two prominent families of peaks. The resonant wavelengths of the "strong" family are 1051.90 nm, 1054.16 nm, 1056.46 nm, 1058.76 nm, 1060.08 nm, 1063.40 nm, 1065.72 nm and 1068.01 nm, which correspond to FSR of 2.28±0.40 nm at λ = 1058.76 nm. The peaks of the "weak" resonance are located at 1050.74 nm, 1053.00 nm, 1055.36 nm, 1057.62 nm, 1059.98 nm, 1062.30 nm, 1064.60 nm, 1066.96 nm, and 1069.30 nm, which comprise FSR of 2.32±0.02 nm at λ = 1059.98 nm.

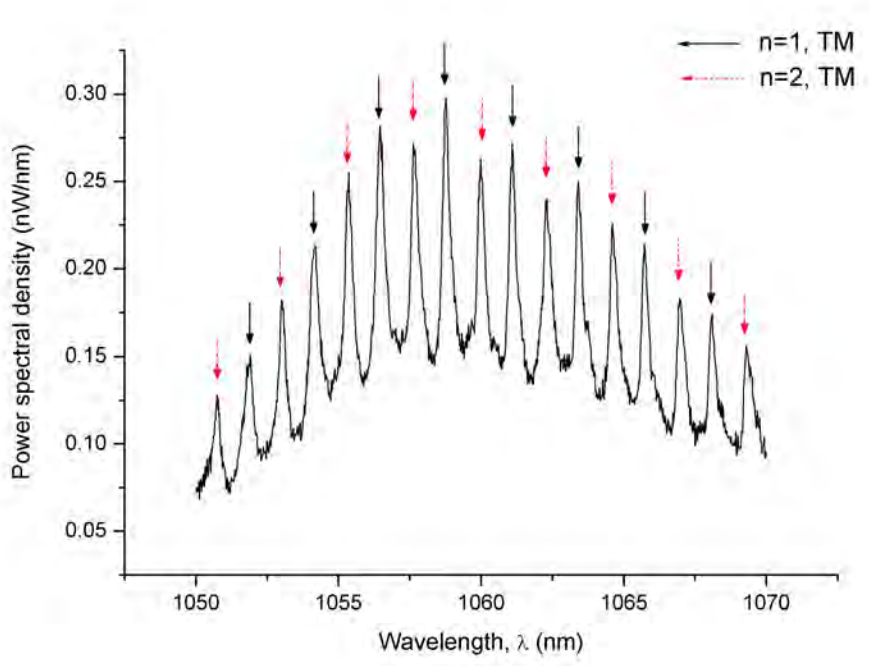

FIGURE 6.10: Fluorescence spectrum of a 1.5-wt% Nd_2O_3-doped BK7 microsphere on a K^+-Na^+-ion exchanged channel waveguide

The mode assignment procedure will be discussed in detail in the next section.

6.3.3 Mode assignment

The aim of the work in this section is to identify and assign the sphere mode numbers to the resonance spectrum obtained from the previous section, so that the corresponding microsphere diameter can be obtained. The method that is used is the same as described in Chapter 4. Input light in the TM polarisation was used to launch into the waveguide, thus, the "strong" resonant family should correspond to $n = 1$ in the TM polarisation. Because, as it was described in Chapter 4, it is found that $n = 1$ has the strongest coupling efficiency to the waveguide compared to other high order modes. Then, the "weak" family is assigned to $n = 2$ in the TM polarisation. The microsphere diameter was determined to be 103.18±0.03 μm. It is to be noted that the discrepancy of 0.03 μm relates to the value of the microsphere diameter which makes the maximum difference between the theoretical and experimental wavelengths less than 0.1 nm.

The sphere mode number l corresponding to the two families of resonant peaks are shown in Table 6.1.

Experimental results		Theoretical fit		
λ_{res} (nm)	FSR (nm)	Sphere mode numbers, (l, n)	λ_{res} (nm)	$\Delta\lambda_{res}$ (nm)
TM polarisation				
1051.90	2.09	(450,1)	1052.10	0.20
1054.16	2.15	(449,1)	1054.38	0.16
1056.46	2.22	(448,1)	1056.67	0.21
1058.76	2.28	(447,1)	1058.95	0.19
1061.08	2.31	(446,1)	1061.26	0.14
1063.40	2.41	(445,1)	1063.58	0.18
1065.72	2.47	(444,1)	1065.89	0.17
1068.01	2.53	(443,1)	1068.23	0.22
1050.74	2.30	(440,2)	1050.48	0.26
1053.00	2.31	(439,2)	1052.78	0.22
1055.36	2.31	(438,2)	1055.08	0.28
1057.62	2.32	(437,2)	1057.37	0.25
1059.98	2.32	(436,2)	1059.69	0.29
1062.30	2.33	(435,2)	1062.02	0.28
1064.60	2.33	(434,2)	1064.35	0.25
1066.96	2.34	(433,2)	1066.70	0.26
1069.30	2.35	(433,2)	1069.06	0.24

TABLE 6.1: Experimental and theoretical resonant wavelengths and assigned mode numbers (l, n) of a fluorescence spectrum of a 1.5-wt% Nd_2O_3-doped BK7 microsphere diameter of D = 103.18±0.03 μm

Figure 6.10 shows that there are only two families of excited modes observable. It has been found that the excited modes are easily distinguished and identified compared with the results obtained from the free-space light excitation. This is because the excited modes of the WGMs in a microsphere are limited when coupling with the waveguide, be-

cause the waveguide evanescent field extends only a small distance into the microsphere, resulting in weak coupling to higher order radial modes.

6.3.4 Measurement of pump power dependence of fluorescence spectrum

The aim of the experimental work in this section is to measure the fluorescence spectra from the Nd-doped microsphere coupling with the waveguide as the input pump power increases. Light in the TM polarisation was launched into the waveguide shown in Figure 6.9, the incident pump light was attenuated from about 80 mW to 1 mW corresponding to 65 mW to 0.4 mW as measured at the waveguide output. The fluorescence spectrum of the emission light from the Nd-doped microsphere at each of these input power was recorded. Figure 6.11 shows the fluorescence spectra of the waveguide-coupled microsphere as the pump power was changed.

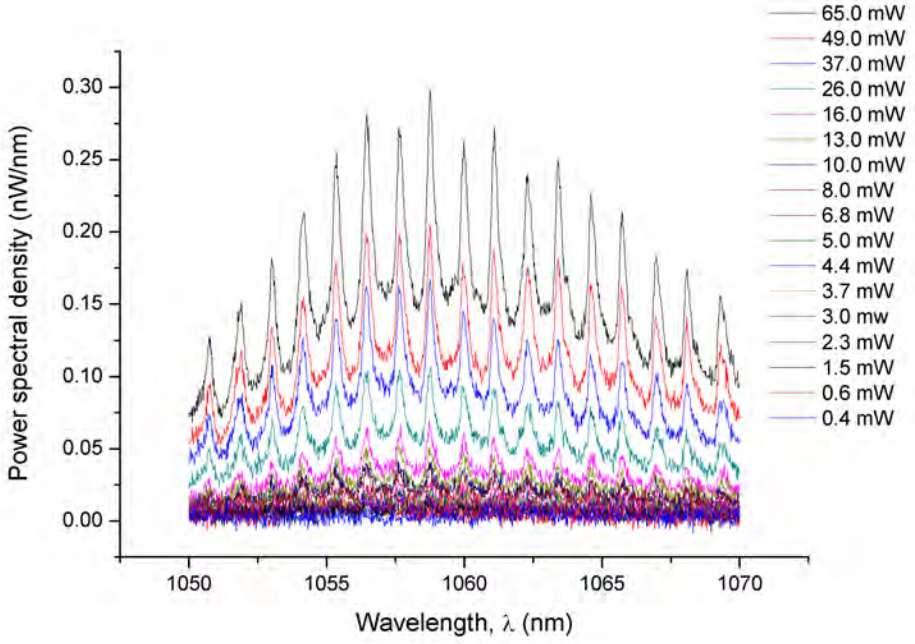

FIGURE 6.11: Fluorescence spectra of a 1.5-wt% Nd_2O_3-doped BK7 microsphere on a K^+-Na^+-ion exchanged channel waveguide as function of incident pump power

As the pump power reduces, the power in each fluorescent peak decreases, as expected. The resonant peaks are found to be located at the same positions within the experimental error, as the pump power was altered. The fluorescence power is at $\lambda = 1057.39$ nm is plotted against pump power in Figure 6.12 and shows that the peak power at $\lambda = 1057.39$ nm. The positions of the resonant peaks were found not to change, and their power is linearly increasing with pump power, indicating the behaviour of the spontaneous emission from the microsphere [6], with no evidence of saturation.

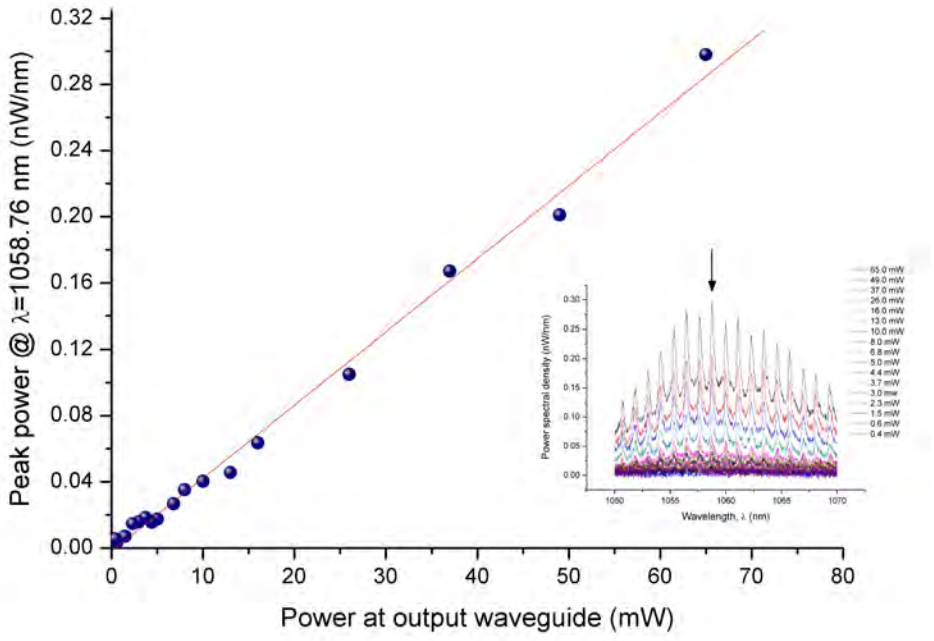

FIGURE 6.12: Fluorescence spectra of a 1.5-wt% Nd_2O_3-doped BK7 microsphere on a K^+-Na^+-ion exchanged channel waveguide as function of pump power level. Inset: Fluorescence spectra of a 1.5-wt% Nd_2O_3-doped BK7 microsphere on a K^+-Na^+-ion exchanged channel waveguide as function of incident pump power

In summary, experimental studies of the WGM from the Nd-doped microsphere coupled with the evanescent field from the ion-exchanged waveguide were carried out. In this configuration, the WGMs of the emission light are found to be more prominent compared to the free-space pump configuration, where Q of 6×10^3 near the wavelength of 1058 nm was obtained. In the waveguide coupling configuration, the WGMs in microsphere were excited with a fixed path along the waveguide channel, and the WGM scattered power observed is found to be more clear. While in the confocal pumping configuration, pump light was focused to a tight spot to excite the WGMs, which could excite more radial modes in various planes. Pumping by waveguide excitation will be extended in the experimental work described in Section 6.5.

6.4 Microsphere laser operation: Free-space excitation

The aim of the experimental work in this section is to study the microsphere lasing characteristics when excited with a free-space excitation before moving on to the waveguide excitation. Experimental work on the observation of lasing oscillation by free-space excitation onto a 1.5-wt% Nd_2O_3-doped BK7 microsphere is described. The experimental apparatus is setup to observe the lasing action of the 1.5-wt% Nd_2O_3-doped BK7 microspheres that were fabricated according to Section 3.4 in Chapter 3. These microspheres as known to exhibit low losses which should allow lasing to occur, because Q factors as high as 6.2×10^4 have been observed at wavelengths near 1550 nm. Detailed discussions on the experimental setup, observation, results and discussion on the measurement of lasing spectra, lasing threshold pump power and the lasing spectra obtained from different pump wavelengths follow.

6.4.1 Experimental apparatus

Light from a tunable titanium: sapphire laser was focused onto a microsphere that was located on a sodalime glass slide coated with a 1 μm thick Teflon layer. The Teflon layer is used to prevent the evanescent field of WGM at the signal wavelength from penetrating into the substrate. A horizontal input beam was focused with a lens and launched onto a tilted mirror, where the beam was reflected and vertically illuminated the microsphere. The position of the microsphere and the mirror were optimised such that the desired pump beam spot size, was achieved. A multimode fibre was horizontally aligned close to the microsphere in order to collect the fluorescence emission from the microsphere. The spectrum of the emitted light was monitored with an optical spectrum analyser (OSA). A variable attenuator was used to vary the power input, and 8% of the light was tapped for power monitoring.

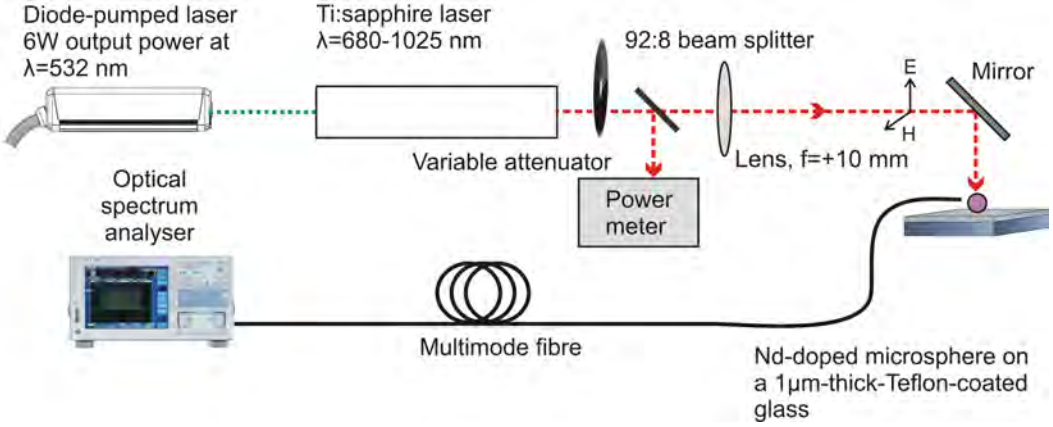

FIGURE 6.13: Experimental apparatus for free-space excitation of microsphere laser

6.4.2 Threshold power measurement

The measurement of threshold power, P_{th}, from a single Nd-doped microsphere was carried out. The titanium:sapphire laser was tuned to 808 nm, where the absorption of the neodymium-doped glass is a maximum, and the beam was launched to excite a Nd-doped microsphere on the Teflon coated glass substrate, see Figure 6.13. The microsphere size was measured using an optical microscope and was found to be about 190 μm in diameter. The position of the lens was adjusted such that the pump beam spot size at full-width of half maximum of 78.5 μm was obtained, this value was chosen because the maximum collected power was obtained. The pump power was varied with a variable attenuator so that the observation of the lasing spectrum as a function of pump power can be obtained. The spectra as a function of the pump power (prior to the lens) from 2 mW to 20 mW were recorded.Figure 6.14 shows the lasing spectra as a function of input pump power from a 190 μm diameter 1.5-wt% Nd_2O_3-doped BK7 microsphere.

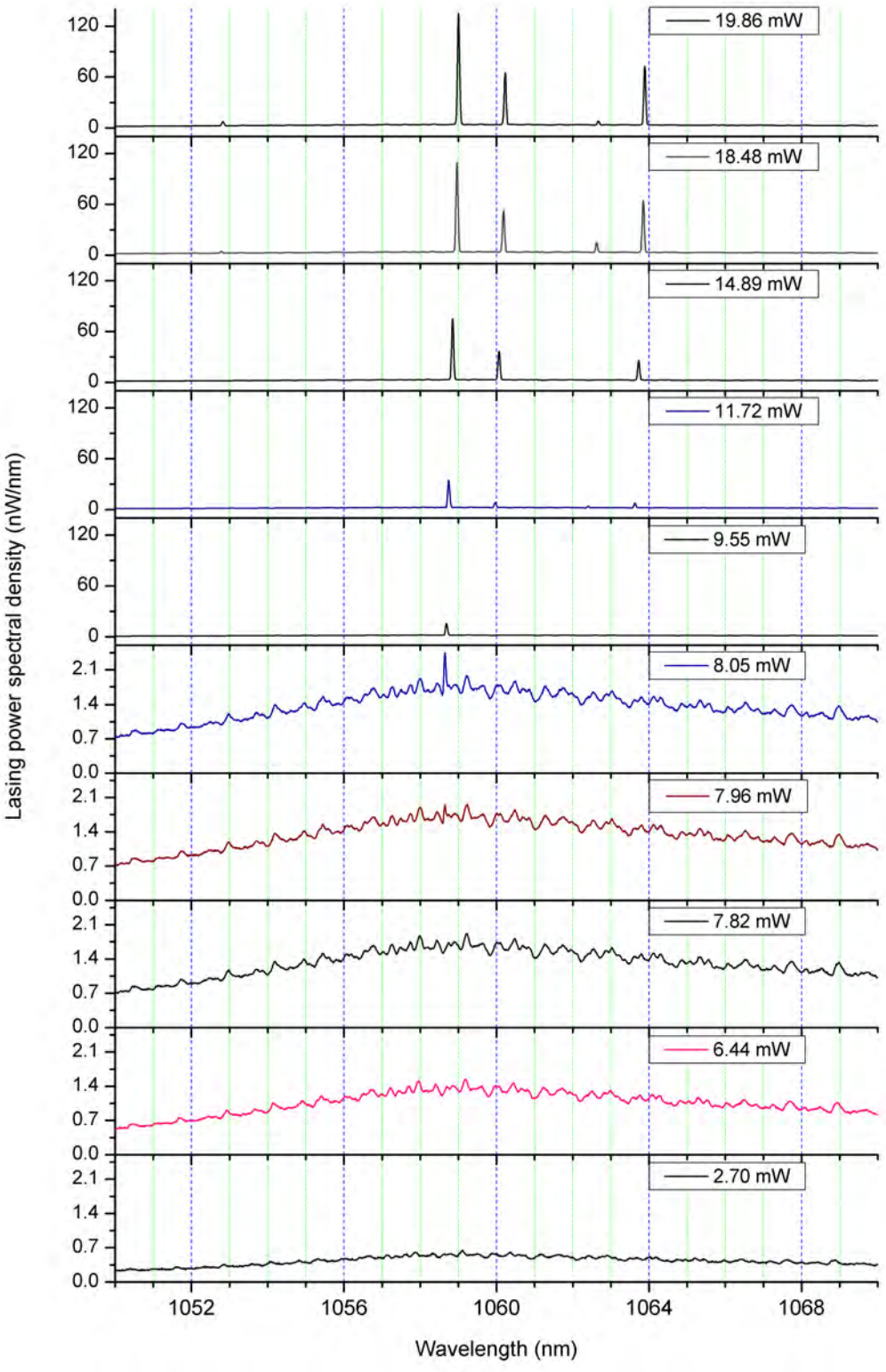

FIGURE 6.14: Lasing spectra as a function of input pump power from a 190 μm diameter 1.5-wt% Nd_2O_3-doped BK7 microsphere (wavelength resolution 10 pm) ***note the PSD scale change*

It can be seen from Figure 6.14 that the power density of the spectra is increasing as the pump power increases. Lasing oscillation starts to occur at an input pump power of 7.96 mW, which is identified as the threshold pump power, P_{th}. At pump power of 19.86 mW, the laser linewidth at full-width of half-maximum of the lasing peak wavelength near 1059 nm of about $\delta\lambda_{FWHM} = 65$ pm was obtained (wavelength resolution 10 pm). Figure 6.15 shows the plot of lasing power spectral density at the signal peak wavelength near 1059 nm as a function of incident pump power.

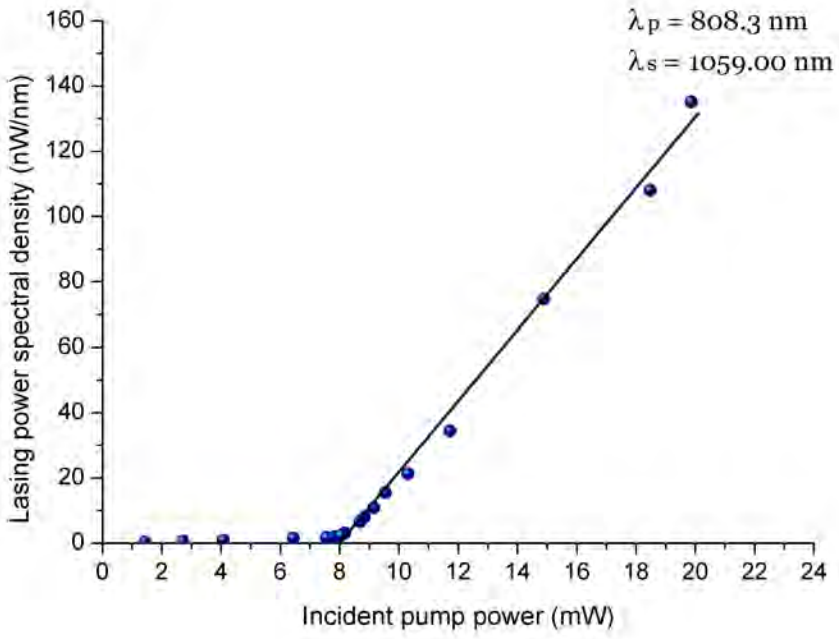

FIGURE 6.15: Lasing power spectral density vs incident pump power

It can be seen from Figure 6.15 that above the lasing threshold, the curve can be fitted to a straight line, this indicates that losses in the cavity are the same. The figure shows the sudden increasing of the emission power above the threshold point, where the slope efficiency is found to be 0.0005%. This value is very low because an overlap of the pump radiation and the signal is poor; and the large pump beam size was large and most of the light was radiated into the surrounding medium, thus the collection efficiency was low.

6.4.3 Mode assignment

This section includes the mode assigning results for the spectra from the lasing results obtained in Section 6.4. The aim of the work in this section is to identify the sphere mode numbers to the lasing spectrum and to extract the physical microsphere diameter from the experimental data. It will be shown in the following section that lasing wavelengths

shift with the pump power. The modal assignment in this section is focused on the two sets of data, which are the data that were obtained with the pump power of 7.96 mW and 19.86 mW.

Figure 6.16 shows the WGM characteristics over the entire wavelength range. The justification of the mode assignment was done such that the major peaks which carry a "strong" resonance characteristic at the low pump power under the lasing threshold level ($P_{in} < 7.96$ mW) correspond to the fundamental mode of TM polarisation radial direction $n = 1$, where the lasing peaks correspond to the $n = 1$, TE mode. The TE mode is found to be oscillated at above threshold level, because of the higher losses in the TM mode. It has been found by Féron et al. that for the larger separation of the microsphere from the substrate (prism), TE and TM modes oscillated simultaneously [7]. According to the current setup in this work, there is no gap between the microsphere and the substrate, thus the TE and TM modes are not expected to oscillate simultaneously.

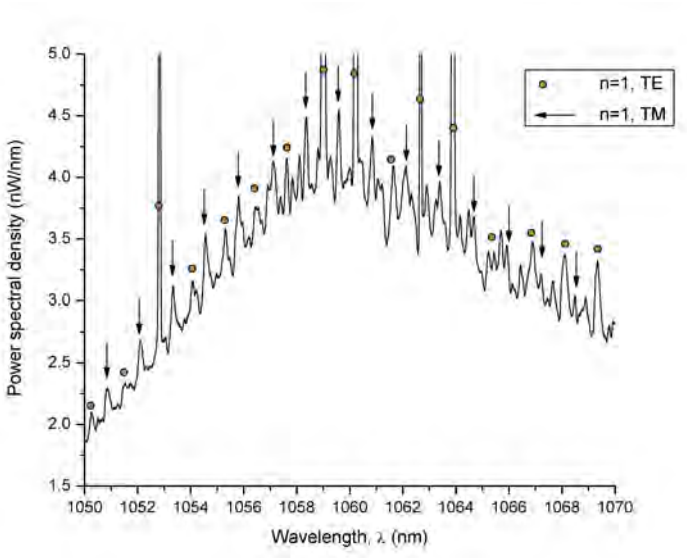

FIGURE 6.16: Lasing spectrum at pump power of 19.86 mW (wavelength resolution 10 pm)

In the current configuration, the polarisation of the light after the mirror might have been altered from a reflection via a mirror [8, 9]. Thus, when launching the TM light to reflect onto a mirror, the TE polarised light was reflected from the mirror onto the microsphere, and laser emission obtained correspond to the TE polarisation.

Lists of families of resonant peaks from the spectrum, obtained at a pump power of 19.86 mW, are shown in Table 6.2. The method, as described in Section 4.5 in Chapter 4, was applied, and the microsphere diameter of D = 188.12±0.06 μm was obtained. The discrepancy of the sphere diameter is found when fit sphere diameter to minimise the maximum discrepancy of the theoretical and experimental wavelengths of the entire values list in Table 6.2. The same method was applied to the data obtained at a pump power of 7.96 mW, sphere diameter is found to be 188.06±0.04 μm.

Experimental results		Theoretical fit		
λ_{res} (nm)	FSR (nm)	Sphere mode numbers, (l, n)	λ_{res} (nm)	$\Delta\lambda_{res}$ (nm)
TM polarisation				
1050.87	1.23	(830,1)	1050.84	0.03
1052.11	1.24	(829,1)	1052.08	0.03
1053.34	1.24	(828,1)	1053.32	0.02
1054.56	1.24	(827,1)	1054.57	0.01
1055.81	1.25	(826,1)	1055.82	0.01
1057.11	1.25	(825,1)	1057.06	0.05
1058.37	1.26	(824,1)	1058.32	0.05
1059.59	1.26	(823,1)	1059.58	0.01
1060.84	1.26	(822,1)	1060.84	0.00
1062.09	1.27	(821,1)	1062.12	0.03
1063.39	1.27	(820,1)	1063.36	0.03
1064.69	1.27	(819,1)	1064.63	0.06
1065.93	1.28	(818,1)	1065.91	0.02
1067.23	1.28	(817,1)	1067.17	0.06
1068.50	1.28	(816,1)	1068.45	0.05
1069.78	1.29	(815,1)	1069.74	0.04
TE polarisation				
1050.25	1.22	(831,1)	1050.51	0.26
1051.54	1.23	(830,1)	1051.75	0.21
1052.83	1.24	(829,1)	1052.99	0.16
1054.08	1.24	(828,1)	1054.24	0.16
1055.30	1.25	(827,1)	1055.49	0.19
1056.55	1.26	(826,1)	1056.73	0.18
1057.62	1.26	(825,1)	1057.99	0.37
1059.00	1.27	(824,1)	1059.25	0.25
1060.23	1.28	(823,1)	1060.51	0.28
1061.63	1.28	(822,1)	1061.76	0.13
1062.72	1.29	(821,1)	1063.03	0.31
1063.89	1.29	(820,1)	1064.30	0.41
1065.44	1.30	(819,1)	1065.57	0.13
1066.89	1.31	(818,1)	1066.84	0.05
1068.10	1.32	(817,1)	1068.12	0.02
1069.34	1.32	(816,1)	1069.40	0.06

TABLE 6.2: Experimental and theoretical resonant wavelengths and assigned mode numbers (l, n) of lasing spectrum of a Nd-doped BK7 microsphere diameter of D = 188.12±0.06 μm with a 808.30 nm-pump input power of 19.86 mW

6.4.4 Thermal shift of WGMs in a microsphere

It can be seen from the lasing spectra shown in Figure 6.14 that the location of the lasing wavelengths and the fluorescence peaks shift as the pump power is altered. This wavelength shift may occur due to thermal-induced expansion as the pump power is increasing, which causes the change in the diameter of the microsphere, and the thermal coefficient of index change, which causes the change in the sphere index [10]. Thermal changes in the optical path length of the cavity relate to a change of the product of sphere refractive index and the microsphere diameter with respect to a change in temperature. The plot of wavelength shifts of the lasing peak near $\lambda = 1059$ nm, as a function of pump power, is shown in Figure 6.17.

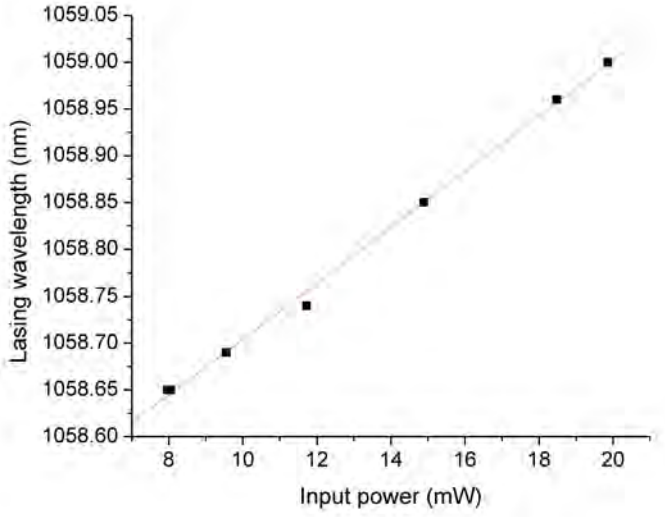

FIGURE 6.17: Emission wavelength as a function of pump power for the lasing peak near $\lambda = 1059$ nm

The value of the peak wavelength shift, $d\lambda_{\text{shift}}$, as the input power was varied from 7.96 mW to 19.86 mW, is $d\lambda_{\text{shift}} = 0.35$ nm, corresponding to $d\lambda/d\text{P} = 3 \times 10^{-8}$ m/W, where P is the input power.

An estimate of the temperature change of the microsphere, due to the change in pump power, is carried out as follows. For a microsphere of diameter D with the corresponding sphere mode number l at wavelength λ, the change of peak wavelengths, $d\lambda$, over the change of product of refractive index and sphere diameter, $d(n\text{D})$, $d\lambda/d(n\text{D})$ can be obtained as shown in Equation 6.2,

$$\frac{d\lambda}{d(n\text{D})} = \frac{\pi}{l}. \tag{6.2}$$

The change of product of refractive index and sphere diameter, $d(n\text{D})$, over the input power change, dP, $d(n\text{D})/d$P can be expressed as follows;

$$\frac{d(n\mathrm{D})}{d\mathrm{P}} = \frac{l}{\pi} \cdot \frac{d\lambda}{d\mathrm{P}}, \tag{6.3}$$

thus, for a 188 μm diameter microsphere, with a refractive index of 1.507 at $\lambda = 1059$ nm and $l = 824$, $d(n\mathrm{D})/d\mathrm{P}$ of 7.87×10^{-6} m/W is obtained from Equation 6.3 and the experimentally determined $d\lambda/d\mathrm{P}$.

The change of product of refractive index and sphere diameter, $d(n\mathrm{D})$, for a temperature change, $d\mathrm{T}$, $d(n\mathrm{D})/d\mathrm{T}$ can be described as,

$$\frac{d(n\mathrm{D})}{d\mathrm{T}} = \frac{\mathrm{D}dn}{d\mathrm{T}} + \frac{nd\mathrm{D}}{d\mathrm{T}}. \tag{6.4}$$

The linear thermal expansion coefficient, $\epsilon_{\mathrm{thermal}}$, for BK7 is found to have a value of 7.1×10^{-6}/K, where $\epsilon_{\mathrm{thermal}} = \frac{1}{\mathrm{D}} \cdot \frac{d\mathrm{D}}{d\mathrm{T}}$, thus, the corresponding $d\mathrm{D}/d\mathrm{T} = 1.33 \times 10^{-9}$m/K. And the value of temperature coefficient of refractive index, $dn/d\mathrm{T}$, is found to have a value of $dn/d\mathrm{T} = 1.17 \times 10^{-6}$/K at 1059 nm [11, 12].

Thus,

$$\Delta\mathrm{T} \approx \frac{d(n\mathrm{D})}{d\mathrm{P}} \cdot \left(\frac{1}{\frac{\mathrm{D}dn}{d\mathrm{T}} + \frac{nd\mathrm{D}}{d\mathrm{T}}} \right) \cdot \Delta\mathrm{P}, \tag{6.5}$$

thus, the $\Delta\mathrm{T}$ of 42 K was obtained for $\Delta\mathrm{P} = 12$ mW.

This value of the temperature change obtained is believed to be justified. It has been observed that with a very tight focused of the pump intensity, the microspheres were found to be destroyed by a heat damaged. In this experiment, the focused beam size is relatively large, thus, the results of the temperature change of 42 K is believed to be reasonable.

6.4.5 Measurement of the pump wavelength dependence of lasing spectrum

In this section, measurement of the lasing spectra obtained from the 1.5-wt% Nd_2O_3-doped BK7 microsphere as a function of input pump wavelength, λ_p, is described. A microsphere is free-space excited with an input pump power of 80 mW, while the pump wavelength is altered. The pump wavelengths at which the lasing spectra are recorded were chosen as they are the resonant wavelengths of the microsphere at the pump wavelength. The pump wavelength of 808.3 nm, 809.1 nm, 809.9 nm, 810.6 nm, 811.4 nm, 812.4 nm and 812.9 nm were used to excite the lasing oscillation in the microsphere. The free-spectral range of these resonant wavelengths is found to be FSR = 0.79±0.09 nm near λ_p = 810 nm. Figure 6.18 shows the lasing spectra of the 190 μm diameter BK7 microsphere doped with 1.5-wt% of Nd_2O_3, as a function of pump wavelength, λ_p, from 808.3 nm to 812.9 nm. At the pump wavelength of 808.3 nm, there are four lasing peaks which are located at 1053 nm, 1059 nm, 1060 nm and 1064 nm, where the maximum amplitude is at wavelength of 1059 nm. At the pump wavelength of 809.1 nm, the lasing peaks are reduced in amplitude. At the pump wavelength of 809.9 nm, a lasing peak at 1063 nm is emerging, where its amplitude increases as the pump increases to 810.6 nm and it starts to accordingly drop when the pump wavelength increases to 812.4 nm. At the pump wavelength of 810.6 nm, the lasing peak at 1060 nm has completely vanished, where the lasing amplitude at 1064 nm is maximised. The 1064 nm lasing peak then accordingly drops to vanish as the pump wavelength increases to 812.9 nm. The lasing peak at 1066 nm starts to occur at a pump wavelength of 811.4 nm, and it progressively increases as the pump power increases to 812.9 nm. At the pump wavelength of 812.9 nm, the lasing peak at 1066 nm is maximised. It can be seen that amplitude of the each lasing amplitude is altered as the pump wavelength is changed, and the overall peak amplitude of the lasing spectra are shifted to higher wavelengths as the pump wavelength increases.

To better understand this behaviour, the fluorescence spectra of the microsphere as a function of pump wavelength were recorded by lowering the pump level to under the threshold power. The variation of the pump light from 808.3 nm to 812.9 nm, was used and the fluorescence spectra as a function of pump input wavelength were recorded. Figure 6.19 shows the fluorescence spectra, it can be seen that the peak fluorescence shifts to a longer wavelength as the pump wavelength increases. The plot of the average peak wavelength of lasing spectra, $\lambda_{\text{Lasing-avg}}$, as a function of peak wavelength of fluorescence spectra, $\lambda_{\text{Fluorescence-peak}}$, is made and shown in Figure 6.20. It can be seen that the average peak wavelength of lasing increases approximately linearly with peak wavelength fluorescence. Thus, the laser emission wavelengths are expected to be increased as the pump wavelength increases. The change of the lasing peak positions as a function of pump wavelength may be due to the transition of different pairs of the energy levels of the neodymium ions in glass medium. Ion distributions in glass do not only depend

on dopant concentration but also the host material. The Nd^{3+} distributions in glass medium are randomly distributed and the energy transfer process is dependent on the excitation wavelength, thus the energy transfer of the random distributed ions in the glass medium might cause a change in lasing wavelength when the pump wavelength was altered [13, 14].

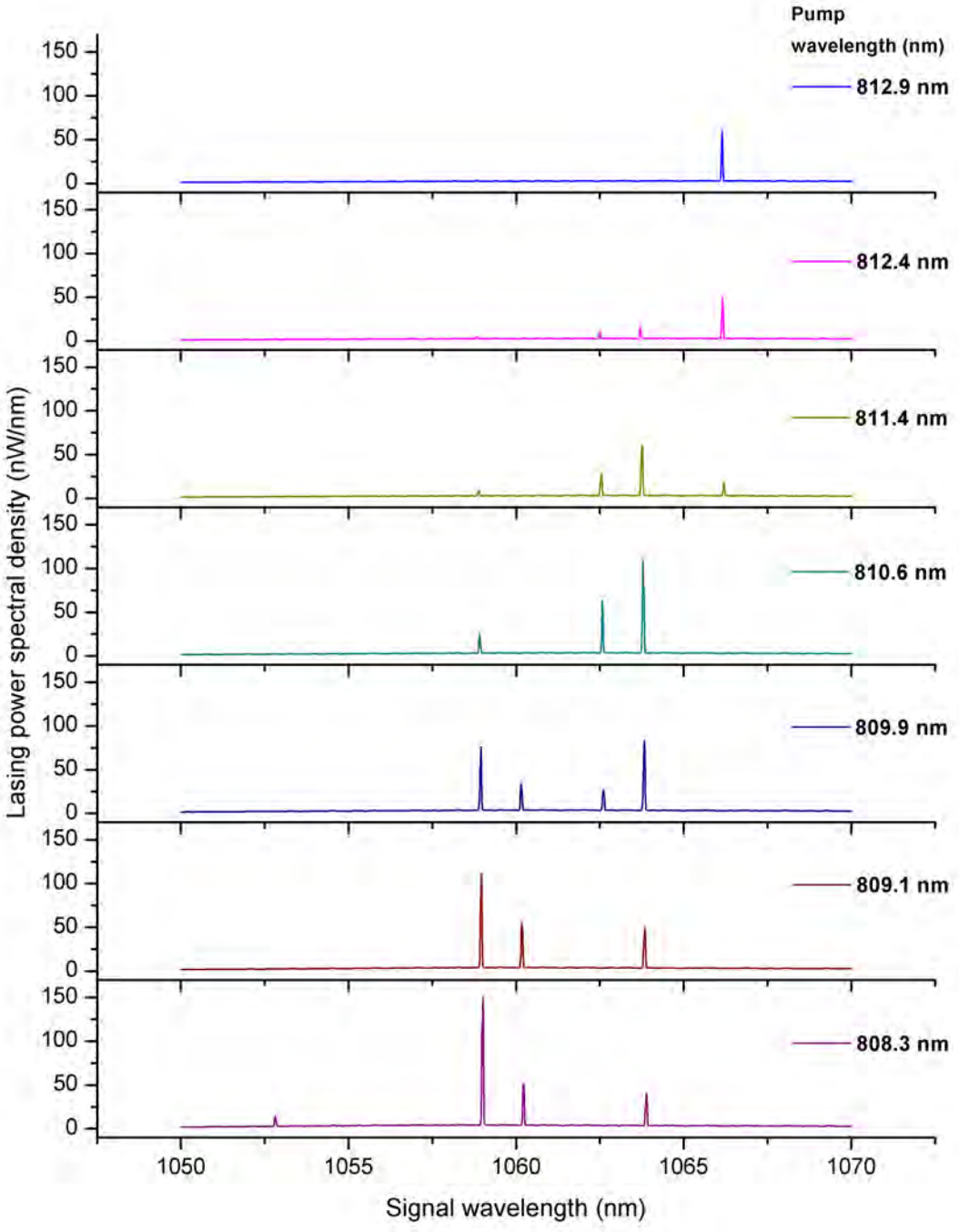

FIGURE 6.18: Lasing spectra of 1.5-wt% Nd_2O_3-doped BK7 microsphere as a function of pump wavelength, λ_p, from 808.3 nm to 812.9 nm (wavelength resolution 4 pm)

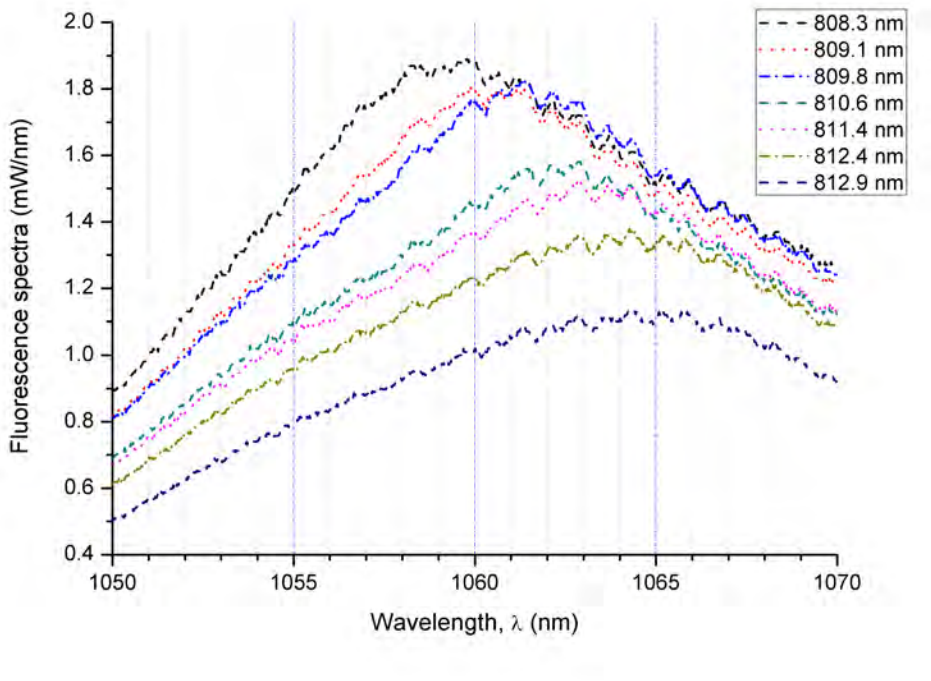

FIGURE 6.19: Fluorescence spectra 1.5-wt% Nd_2O_3-doped BK7 microsphere as a function of pump wavelength, λ_p, from 808.3 nm to 812.9 nm (P_{in} = 80 mW)

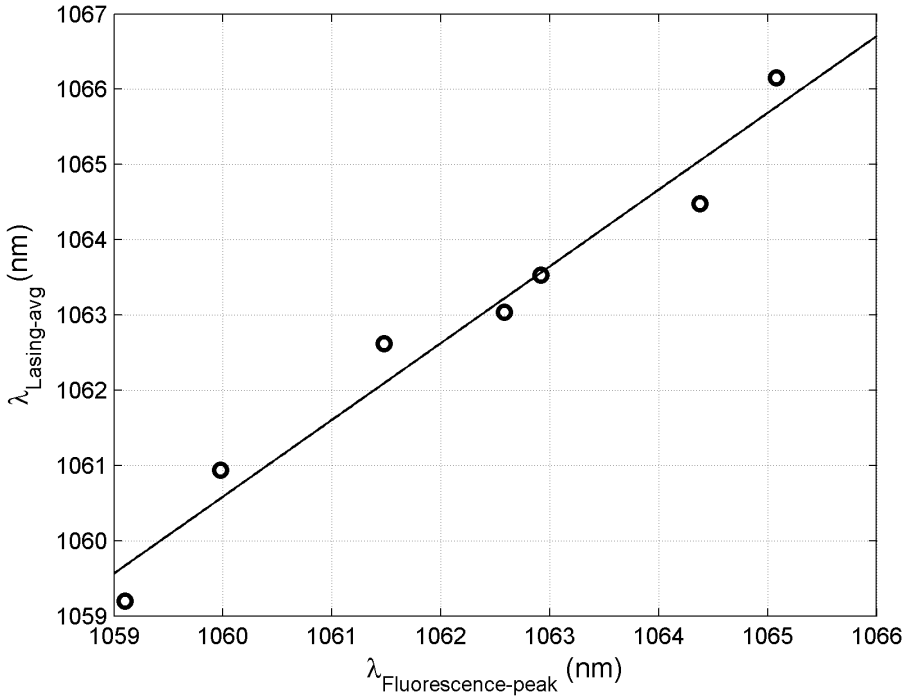

FIGURE 6.20: Average peak wavelength as a function of fluorescence peak wavelength

6.5 Microsphere laser operation: Waveguide excitation

The aim of the work in this section is to couple the light evanescently into the Nd-doped microsphere, so that laser oscillation can be obtained with more efficient use of the pump radiation. The approach in Figure 6.9 was used to attempt to observe the laser oscillation of the Nd-doped microsphere when excited via an evanescent field from the optical waveguide. The potassium-sodium-ion exchanged waveguide, fabricated according to Section 3.2 in Chapter 3, was used. 1.5-wt% of Nd_2O_3-doped BK7 microspheres that were fabricated in Section 3.4.2 in Chapter 3, were used because these microspheres are found to have good surface quality as they exhibited Q-factors of as high as 6×10^4 at a wavelength near 1550 nm.

The fluorescence power versus pump power measurement was carried out by observing the lasing spectra from a 100±5 μm diameter microsphere on the waveguide, when the pump power increased. The spectra at each pump level were recorded. However, as it can be seen from Figure 6.12, there is no evidence of lasing.

To investigate the possible reasons that limited the lasing to occur, the power threshold calculation is needed to be explored. Equation 5.14 shows that the power threshold in the waveguide can be varied with Q_{c_s}, α, κ, τ, A_{eff}, η_q, σ_s and β_p. To explore the reasons that lasing characteristics were not successfully achieved with the experimental setup in this configuration, the comparison of the values obtained from the literature with estimated values from the present experiment for a 100 μm diameter sphere at $\lambda_p = 808$ nm (sphere mode number $l = 572$) $\lambda_s = 1059$ nm (sphere mode number $l = 434$), are made and the values are listed in Table 6.3.

Parameters	Calculated values from theory	Estimated values in experiment
Loss factor at signal wavelength, α_s	0.99	0.90
Q at signal wavelength, Q_{c_s}	1.45×10^5	2.45×10^4
Loss factor at pump wavelength, α_p	0.99	0.90
Loss factor due to Nd absorption, α_{Nd}	0.9631	0.9631
$\alpha_{\mathrm{total}} = \alpha_{\mathrm{Nd}} \cdot \alpha_p$	0.9535	0.8668
Coupling factor at pump wavelength, κ_p	0.1970	0.1970
Effective area, $A_{\mathrm{eff}} = \frac{1}{\iint S_s(x,y) S_p(x,y)\, dx\, dy}$	7 μm^2	7 μm^2
Fluorescence lifetime, τ	470 μs	345 μs
Quantum efficiency of the pumping, η_q	0.8	0.8
Nd^{3+} ion density, N_o	1.68×10^{20} $\frac{\mathrm{atoms}}{\mathrm{cm}^3}$	1.68×10^{20} $\frac{\mathrm{atoms}}{\mathrm{cm}^3}$
Absorption coefficient per unit length, β_p	1.57 cm^{-1}	1.57 cm^{-1}
Stimulated emission cross-section, σ_s	1.9×10^{20} cm^2	1.9×10^{20} cm^2
Power threshold at sphere, $P_{\text{th-sphere}}$	1.21 mW	10 mW
1/enhancement factor, $1/\epsilon$	0.12	0.77
Power threshold at waveguide, $P_{\text{th-wg}}$	0.15 mW	7.8 mW

TABLE 6.3: Parameters and values from theory and estimated values from experiment on waveguide-coupled microsphere laser for a 100 μm diameter BK7 microsphere doped with 1.5-wt% of Nd_2O_3 at zero separation from potassium-sodium-ion exchanged waveguide

Figure 6.21 shows the plot of enhancement factor as a function of coupling factor, with a loss due to Nd absorption of 5.2 dB/cm and attenuation loss, $\alpha_p = 0.90$ ($\alpha_{\text{total}} = 0.8668$), and $\alpha_p = 0.99$ ($\alpha_{\text{total}} = 0.9535$), for a 1.5-wt% Nd_2O_3-doped BK7 microsphere of 100 μm in diameter.

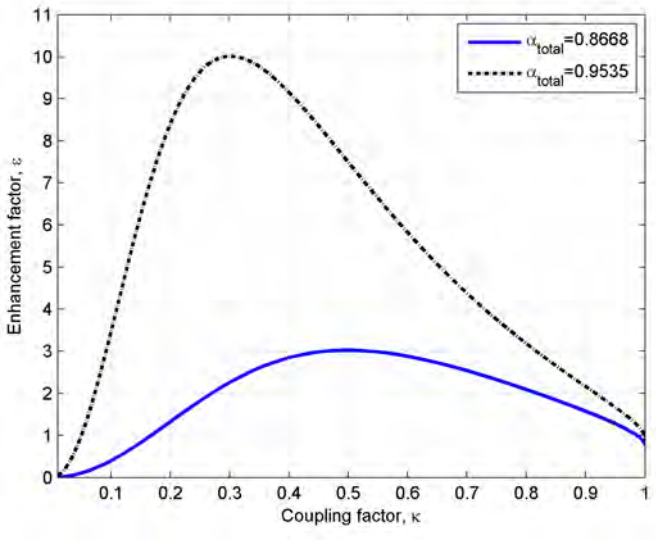

FIGURE 6.21: Enhancement factor as a function of coupling factor, with a loss due to Nd absorption of 5.2 dB/cm and attenuation loss, $\alpha_p = 0.90$ ($\alpha_{\text{total}} = 0.8668$), and $\alpha_p = 0.99$ ($\alpha_{\text{total}} = 0.9535$), for a 1.5-wt% Nd_2O_3-doped BK7 microsphere of 100 μm in diameter

When loss due to spurious attenuation in a sphere at the signal wavelength is high, Q at the signal wavelength becomes small. As a result, the threshold power in the sphere becomes large, as according to Equation 5.12 where it shows that power threshold at the sphere is inversely proportional to Q of the system at the signal wavelength. In the experimental work, assuming that the value of α_s is estimated to be 0.90, this is chosen based on an approximate value of the actual attenuation of the cavity obtained from the discussion in Section 4.5. Q of 2.45×10^4 is obtained and when combined with the others values listed in column 3 in Table 6.3, $P_{\text{th-sphere}}$ of about 10 mW is predicted for lasing to occur.

At low κ, when the typical value of $\alpha_{\text{Nd}} = 0.9631$ and loss factor at pump wavelength of 0.90 ($\alpha_{\text{total}} = 0.8379$) are combined, the power required in the waveguide for lasing to occur is large because of small enhancement factor value. At the calculated value of coupling factor of $\kappa = 0.1970$, the estimated threshold power in the waveguide is expected to be about 7.8 mW. With a larger value of the enhancement factor, the value of the threshold power at the waveguide can be reduced. As it can be seen from Figure 5.7 that the enhancement factor for a total loss factor of 0.8668 (solid line) is maximum at $\kappa = 0.5$ ($\epsilon = 3.02, 1/\epsilon = 0.33$), at this point, the predicted pump threshold at the waveguide can be reduced to 3.3 mW. However, if the coupling factor at the pump wavelength is lower than the calculated values, for example at 80% of 0.1970

($\kappa = 0.1576$), the corresponding $1/\epsilon$ is found to be 1.11, this makes the power required in the waveguide equal to 11 mW. And for the lower coupling efficiency, which is at 70% of 0.1970 ($\kappa = 0.1379$), the value of the power threshold at the waveguide becomes 14 mW ($1/\epsilon = 1.4$). Thus, it can be concluded that, at low κ, a small change in κ makes significant change of power threshold in the waveguide.

Despite the fact that a predicted threshold pump power in the waveguide in this configuration is 7.8 mW, lasing oscillation was not observed for pump power up to 65 mW. Thus, each parameters that are involved with the power threshold calculation will be discussed in turn to ascertain potential reasons. It is important to be note that, in the current model, the assumption of the negligible depletion of the ground-state has been made. In the high loss cavity, more ions are needed to be excited to achieve lasing action, thus, the pump power required for lasing to oscillate is expected to be high when the cavity loss is high.

The fluorescence lifetime from the experimental work in Section 6.2.2 of the 170 μm diameter microsphere was found to be about 345 μs. The calculation of power pump threshold in the waveguide according to this lifetime is carried out with the value of the parameters listed in column 3 in Table 6.3, the threshold pump power in the waveguide is found to be about 7.8 mW. Whereas the pump power threshold in the waveguide for a 470-μs-case is about 5.7 mW. Thus, it can be concluded that the reduction in lifetime brings the power threshold up as can be seen in Equation 5.14.

The value of the A_{eff}, which is the normalised interaction cross-sectional area between the pump and signal modes [16], is proportional to the threshold pump power. A_{eff} is found to be about 7 μm^2 for a sphere of 100 μm diameter, $n_s = 1.51$, pump wavelength of 808 nm and signal wavelength of 1059 nm. The calculation was completed based on the entire area of sphere mode including the evanescent field contribution, however, the expected effective area in the experimental work should be slightly (about less than 0.01%) larger compared with 7 μm^2, due to the small field distribution of the evanescent field should be excluded. However, this change in the effective area is very small, thus the effect of the change in pump threshold power is expected to be very small.

Quantum efficiency, η_q, is defined as ratio of number of fluorescent photons emitted to the number of photons absorbed on the pump transition [6]. η_q plays an important role in the threshold pump power as can be seen in Equation 5.14. For η_q of 0.8 [17], the calculated value of the required pump power at the waveguide is 7.8 mW. For $\eta_q = 0.5$, the required pump power at the waveguide of 12 mW is obtained. The required pump power at the waveguide increases as η_q increases.

The other parameters that determine the pump power required for lasing are the absorption coefficient per unit length at the pump wavelength, β_p, and stimulated emission cross-section, σ_s. As discussed in Chapter 5, β_p can be obtained by multiplying N_o with σ_p. For Nd^{3+} ion density, $N_o = 1.68 \times 10^{20}$ atoms/cm^3, $\beta_p = 1.57$ cm^{-1}. The power

threshold calculation as a function of β_p and σ_s are carried out and the parameters that are used in the calculation are from column 3 in Table 6.3. The pump power required at the waveguide is about 7.8 mW at $\beta_p = 1.57$ cm^{-1} and $\sigma_s = 1.9 \times 10^{20}$ cm^2, and it increases as β_p or σ_s decrease. If β_p or/and σ_s are small, the lasing oscillation cannot be obtained due to the high $P_{\text{th-wg}}$.

As a conclusion, Q at the signal wavelength, Q_{c_s}, is estimated to be at marginal compared to the minimum Q required for lasing, found in Section 5.4 ($\sim 2 \times 10^4$). Thus, if the actual Q_{c_s} in the experiment was less than the minimum Q required for lasing, the laser oscillation cannot occur. To reduce the threshold pump power, the coupling efficiency at pump wavelength should be increased by increasing the field intensity of the evanescent field at the surface of the waveguide coupler. The surface intensities of the evanescent field can be increased with a high refractive index thin-film waveguide. Moreover, the improvement of the model is needed to be done such that the ground state-depletion is taken into account.

6.6 Conclusions

Confocal microscopy was applied for lifetime measurements and fluorescence studies of the Nd-doped BK7 bulk glass and BK7 microspheres. This method provides local information on the light emission from the microsphere. Fluorescence measurements from various microspheres have been carried out with edge-excitation of the microsphere exciting the WGMs in microspheres most efficiently. Microspheres which contain obvious defects on the WGM path, have been found to exhibit extremely low Q.

Mode assignments and the microsphere diameter extraction methods described in Chapter 4 have been applied to the results in this chapter. It has been found that mode assignments are difficult for the results obtained from the free-space excitation compared with the set of results obtained from the waveguide coupling method, because the WGMs have been found to be more distinguishable in the waveguide coupling method. Moreover, in the waveguide coupling method, a limited number of WGMs were excited, whereas in the free-space pumping case, many WGMs of higher order were excited. It has been experimentally confirmed that microspheres with good surface qualities exhibit higher Q.

The laser oscillations have been successfully observed in a single 1.5-wt% Nd_2O_3-doped BK7 microsphere, fabricated as in Section 3.4.2, by free-space excitation. A laser linewidth of about 65 pm was obtained. The threshold pump power and the slope efficiency of 7.96 mW and 0.0005%, were obtained. The experiment for observing the change of lasing signal as a function of pump wavelength has been completed. It has been found that, as the microsphere was excited with a different value of pump wavelength, the lasing spectrum was altered.

The discussion of the results observed from the laser experiment by waveguide excitation has been discussed, where the reasons that have prevented the laser cavity to oscillate in that configuration have been outlined. The quality of the microspheres must be improved to enhance Q of the system at the signal wavelength. Moreover, it has been discussed that, large coupling efficiency of the system at pump wavelength can bring down the threshold pump power required in the waveguide, due to a large surface enhancement. The detailed discussion to assess this problem will be covered in Chapter 7.

6.7 References

[1] http://www.mo-sci.com.

[2] A. Benayas, G. S. Murugan, Y. Panitchob, D. Jaque, and J. S. Wilkinson. Time resolved confocal luminescence of Nd^{3+} doped BK7 glass microspheres. In *The 15th International Conference on Luminescence and Optical Spectroscopy of Condensed Matter*, Lyon, France, July 2008.

[3] D. Q. Hoa, T. Uchimura, T. Imasaka, and N. D. Hunga. Fluorescence lifetime measurement of dibenzofuran and monochlorodibenzofuran. *Science and Technology of Advanced Materials*, 7:714–717, 2006.

[4] G. Nunzi Conti, A. Chiasera, L. Ghisa, S. Berneschi, M. Brenci, Y. Dumeige, S. Pelli, S. Sebastiani, P. Feron, M. Ferrari, and G. C. Righini. Spectroscopic and lasing properties of Er^{3+}-doped glass microspheres. *Journal of Non-Crystalline Solids*, 352:2360–2363, 2006.

[5] Y. Z. Wang, B. L. Lu, Y. Q. Li, and Y. S. Liu. Observation of cavity quantum-electrodynamic effects in a Nd:glass microsphere. *Optics Letters*, 20:770–772, 1995.

[6] A. E. Siegman. *Lasers*. Univerity Science Books, California, 1986. ISBN 0-935702-11-3.

[7] P. Féron. Whispering gallery mode lasers in erbium doped fluoride glasses. *Annales de la Foundation Louis de Broglie*, 29:317–329, 2004.

[8] S. C. Tidwell, D. H. Ford, and W. D. Kimura. Transporting and focusing radially polarized laser beams. *Optical Engineering*, 31:1527–1531, 1992.

[9] B. P. S. Ahluwalia, X. C. Yuan, K. J. Moh, and J. Bu. Experimental transfer of torque induced by localized polarization of radially polarized vector beams to anisotropic microparticles. *Applied Physics Letters*, 91:171102–1–3, 2007.

[10] T. Carmon, L. Yang, and K. J. Vahala. Dynamical thermal behavior and thermal self-stability of microcavities. *Optics Express*, 12:4742–4750, 2004.

[11] http://www.schott.com.

[12] N. A. Sanford, K. J. Malone, and D. R. Larson. Integrated-optics laser fabricated by field-assisted ion exchange in neodymium-doped soda-lime-silicate glass. *Optics Letters*, 15:366–368, 1990.

[13] J. Azkargorta, I. Iparraguirre, R. Balda, J. Fernández, J. L. Adam, E. Dénoue, and J. Lucas. Site-effects on the laser emission of Nd^{3+} ions in a new fluoride glass. *Journal of Non-Crystalline Solids*, 213–214:271–275, 1997.

[14] J. Azkargorta, I. Iparraguirre, R. Balda, and J. Fernández. On the origin of bichromatic laser emission in Nd^{3+}-doped fluoride glasses. *Optics Express*, 16:11894–11906, 2008.

[15] G. L. Duveneck, A. P. Abel, M. A. Bopp, G. M. Kresbach, and M. Ehrat. Planar waveguides for ultra-high sensitivity of the analysis of nucleic acids. *Analytica Chimica Acta*, 469:49–61, 2002.

[16] E. Mwarania. *PhD thesis on Planar ion-exchange waveguide lasers in glass.* University of Southampton, Southampton, 1992.

[17] V. I. Arbuzov, N. B. Brachkovskaya, I. A. Zhmyreva, V. P. Kolobkov, P. I. Kudryashov, A. K. Przhevuskiĭ, V. A. Savost'yanov, and M. N. Tolstoĭ. Absolute quantum efficiency of the luminescence emitted from neodymium-actived glasses. *Soviet Journal of Quantum Electronics*, 6:1091–1095, 1976.

Chapter 7

Conclusions and further work

7.1 Conclusions

In this thesis, the basic concepts of microspheres and optical planar waveguides and the integrated waveguide-coupled microsphere, have been studied. The spherical resonator has a high Q when a good surface quality is achieved. In this work, the evanescent field from an ion-exchange waveguide has been used to excite the WGMs in BK7 glass microspheres. Despite the obvious applications of these microspheres coupled to waveguides, such as optical filters or optical sensors, microsphere lasers are also of interest. In this work, a microsphere laser based on a waveguide coupling configuration has been studied. Apart from the study of waveguide-coupled microsphere lasers, waveguide-coupled passive microspheres, confocal microscopy and microsphere lasers by free-space excitation, have also been studied.

Ion diffused waveguides used in the present study were fabricated by photolithography followed by ion-exchange. Aluminium mask with open channels of desired widths was produced using the photolithography on BK7 substrates and the ion-exchange was performed with an appropriated molten salt for a suitable diffusion time to obtain monomode waveguides at the desired operating wavelength. Commercial Nd-doped BK7 microspheres were found to have high losses due to significant surface roughness. Higher-quality Nd-doped BK7 microspheres have been prepared in-house. Crushed and sieved glass particles (within a short range of particle size) were annealed on a glassy carbon plate to produce microspheres. Glass particles were heated just above the softening temperature and cooled down slowly. The surface tension of the softened glass produced a spherical shape which was retained during cooling. However, it has been found that microspheres larger than 80 μm in diameter formed a flattened surface in the contact area with the carbon plate. Moreover, the amount of microspheres produced in this technique is also limited by the area of the carbon substrate. Thus, heating the micro-particles while they are dropped through a vertical tube furnace to allow surface

tension to form microspheres before reaching a cool zone, has been chosen to be a good alternative method for the microspheres fabrication. Microspheres with good sphericity were obtained in significantly larger amounts from this technique. Q-factors of the commercially available microspheres were found to be around 4×10^3 in the 1550 nm region. Whereas the microspheres fabricated from both techniques in-house have been found to have a good surface quality. The experimental results show a significantly improved Q-factor of about 2.2×10^4 for the 130 μm diameter Er-doped BK7 microsphere fabricated on a carbon plate as shown in Section 4.4 and 6.2×10^4 for the 160 μm diameter Nd-doped BK7 microsphere fabricated by the dropping technique as shown in Section 3.4.3, at wavelengths in the 1550 nm region.

The mode and field distribution in the spherical cavity has been studied. Sphere mode numbers l, m, n for each of the microsphere modes were described with the spherical Bessel and Hankel functions [1, 2]. The example of the calculation of mode and field for a microsphere of 30 μm diameter, was established. The contour plots of sphere modes and fields in the $\hat{\phi}$-$\hat{r}$ and $\hat{\theta}$-$\hat{r}$ planes of the spherical coordinates have been shown. The continuity of the field at the microsphere surface was obtained when the relation of the sphere mode number and the wavelength for each particular mode was related with the characteristic equation. Waveguide mode fields and effective indices were obtained by the beam propagation method, where the appropriate values of the waveguide geometry and refractive indices have been carefully chosen accordingly for each waveguide fabricated. Theoretical modelling of waveguide-coupled microspheres has been developed to obtain a coupling factor, κ, for the system by integrating the overlapping field [3]. Q-factors due to coupling to the waveguide, Q_{ext}, and coupling factors, κ, for a specific system have been derived. Moreover, the calculation of the effect upon Q-factors of material absorption, Q_{matl}, radiative loss, Q_{WGM}, and surface roughness, Q_{surf} [4], have been carried out. Q-factors as a function of microsphere separation have been calculated, quantifying how Q varies with microsphere-waveguide separation, useful for subsequent device design.

A detailed experimental and theoretical study of the coupling of ion-exchanged optical waveguides coated with a low-index isolation layer to WGM of Nd-doped BK7 microspheres of different diameters has been carried out. The experimental work has been done by allowing the light to couple to the microsphere via the waveguide evanescent field. The experimental results demonstrated WGM propagation in the microsphere cavity, and the resonance peaks were identified and assigned to the mode numbers l and n, by comparison with the characteristic equation for microsphere resonators. By fitting the experimentally observed resonance spectra to universal coupled microresonator theory, the extraction of the physical microsphere diameter, D, and cavity loss factor, α, have been obtained [5]. Excellent agreement has been achieved between theory and experiment, in terms of mode position, spacing, width and amplitude, and the precise fitting of all modes.

Nd-doped microspheres have been characterised to observe fluorescence WGM characteristics and fluorescence lifetime by confocal microscopy. The advantage of this method is that it provides a localised study of the emission spectra as the sphere was excited with a tightly confined laser beam. Lifetimes of about 345 μs have been found for the sphere of 170 μm diameter fabricated by dropping through a vertical furnace, and about 435 μs for a bulk glass of the same dopants. The reduction of fluorescence lifetime may be due to the stress introduced during the sphere formation process. A further study on the size dependence of the lifetime is recommended. The emission spectrum of the microsphere when excited at the edge suggested that there is more coupling to high-Q modes compared to the excitation at the centre of the microsphere. It was clear from the WGM fluorescence spectra that various WGM were excited in this manner.

A theoretical model on waveguide-coupled microsphere lasers has been developed. Loss and gain of the spherical cavity and the minimum Q-factor of the system that would be required for the lasing oscillation have been derived. For a microsphere of 190 μm in diameter, Q_{min} have been found to be about 2×10^4. The calculation of the power threshold at the microsphere, $P_{th\text{-}sphere}$, and the power threshold at the input waveguide, $P_{th\text{-}wg}$, have been derived. The lowest pump threshold obtained from a 1.5-wt% Nd_2O_3-doped BK7 microsphere was found when $\lambda_p = 808$ nm and $\lambda_s = 1059$ nm. $P_{th\text{-}wg}$ has been found to be minimum at a zero separation from the waveguide surface. $P_{th\text{-}wg}$ of 0.25 mW for a 190 μm diameter sphere has been found, when the value of spurious loss factors at pump and signal wavelengths of 0.99 and loss due to Nd absorption of 5.2 dB/cm were used. With the same loss parameters, $P_{th\text{-}wg}$ of 0.15 mW for a 100 μm diameter sphere was obtained. $P_{th\text{-}wg}$ of larger spheres have been found to be larger compared with the smaller spheres, this is because the total round-trip attenuation at the pump wavelength higher in the larger spheres.

In-house made Nd-doped microspheres have been characterised and laser oscillation has been observed with the pump wavelength in the 800 nm region. A microsphere laser obtained by a free-space excitation, has been successfully demonstrated. A beam spot size of 80 μm diameter at FWHM, was used to excite the microsphere to achieve lasing characteristics. The threshold pump power of 8 mW has been obtained. Evidence of thermal shifts in the Nd-doped BK7 microsphere, has been found when the pump power was increased, the corresponding temperature change in the sphere cavity has been identified. The lasing spectra as a function of the pump wavelength have been obtained. It has been found that the lasing wavelength shifted toward the high wavelength regime and the lasing amplitude and lasing peaks are different, as the the pump wavelength is changed within the absorption region, this may be due to the transition from the different pairs of energy levels of neodymium ions. Lastly, in order to obtain lower threshold lasers, evanescent light from an ion-exchanged waveguide has been used. However, the lasing oscillation based on this configuration has been not been successfully demonstrated, this is believed to be due to the low pump coupling efficiency of the microsphere to the

waveguide combined with insufficiently high sphere Q-factor.

7.2 Further work

The work described in this thesis provides a good foundation to design a complex integrated circuit of microspheres and optical waveguides. Proposed work to demonstrate waveguide-coupled laser performance and further work on a potential waveguide integrated circuit structure, are briefly presented as follows.

It is proposed that, improvement on microlasers' performance based on the evanescent light coupling from an optical waveguide should be pursued as follows:

The waveguide that was used in this work is believed to provide a low coupling efficiency to the pump, and this structure introduced significant light leakage at the signal wavelength into the substrate. Thus, in order to obtain more efficient light to couple into a microsphere via an optical waveguide, optimisation of the geometrical shape and refractive indices of the waveguide structure, should be developed.

A high-index (~ 2.1) waveguide could provide the potential for strong coupling efficiency into the microsphere.

A tantalum pentoxide, Ta_2O_5, rib/ridge waveguide may be a promising candidate to couple the light more efficiently into the microsphere. The strength of the evanescent field increases with decreasing the thickness of the waveguide, however, the attenuation losses due to scattering caused by surface roughness would increase, which reduces the field intensity at the waveguide surface. In Duveneck et al., the optimum of the waveguide film thickness of around 100 nm to 200 nm with a refractive index around 2 for visible light operation has been found [6]. To compare the coupling efficiency of the sphere to a rib tantalum pentoxide waveguide with the ion-exchange waveguide, the calculation of the coupling factors of the microsphere coupling to a 5 by 3 μm potassium-sodium-ion exchanged waveguide and a 200-nm-thick rib Ta_2O_5 waveguide were carried out. It has been found that the coupling efficiency of a microsphere coupled with a Ta_2O_5 waveguide is about 5-6 times greater than the ion-exchanged waveguide. This result confirms that the evanescent field that extends from the Ta_2O_5 waveguide surface is greater than that in potassium-sodium-ion exchanged waveguide. Thus, the field enhancement at the waveguide surface can be achieved with a 200-nm-thick Ta_2O_5 rib/ridge waveguide.

The structure of rib/ridge waveguide could allow the fundamental WGM to propagate in a microsphere in a direction along the plane parallel to the substrate, which could prevent light leakage into the substrate. By placing a microsphere next to the rib/ridge to allow the lateral light coupling from the waveguide, light leakage to the substrate can be reduced, see Figure 7.1.

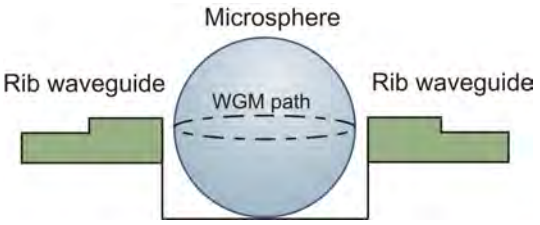

FIGURE 7.1: Schematic of rib/ridge waveguide-coupled microsphere

In conclusion, with a properly aligned microsphere to a tantalum pentoxide rib/ridge waveguide, the demonstration of the laser oscillation should be possible. The microsphere could be precisely positioned to a micro-well structure by self-assembly technique [7]. Further work on lasing oscillation by coupling the light into the improved surface quality microsphere with the Ta_2O_5 waveguide is recommended, where the lasing oscillation may be achievable.

Good surface quality microspheres have been obtained as described in Chapter 3, however, it is proposed that further improvements of sphere surface quality should be addressed by a detailed optimisation of the fabrication procedure.

The construction of more complex waveguide-coupled microspheres structures, are expected to lead to novel devices including integrated microsphere laser circuits as a laser light source, sensors, or filter applications. The accurate positioning of microspheres on the waveguide could be achievable with the cooperated method of chemical surface patterning [7, 8]. Microspheres doped with other rare-earth ions such as erbium or erbium-ytterbium can be fabricated with the improved method described in Chapter 3. By pumping these microspheres with a light source in the 980 nm region, laser emission in the telecommunication band in the 1550 nm region can be obtained. The waveguide coupling technique is very suitable for making complex circuit of the miniature sphere laser as an array of spheres can be readily patterned onto the waveguide with precise alignment. The chip-based microlasers could allow novel low-cost optical and/or electronic circuit applications for telecommunication and sensing.

7.3 References

[1] http://mathworld.wolfram.com/SphericalBesselFunctionoftheFirstKind.html.

[2] http://mathworld.wolfram.com/HermitePolynomial.html.

[3] B. E. Little, J. P. Laine, and H. A. Haus. Analytic theory of coupling from tapered fibers and half-blocks into microsphere resonators. *Journal of Lightwave Technology*, 17:704–715, 1999.

[4] M. Rosenblit, P. Horak, S. Helsby, and R. Folman. Single-atom detection using whispering-gallery modes of microdisk resonators. *Physical Review A*, 70:053808–1–053808–10, 2004.

[5] Y. Panitchob, G. S. Murugan, M. N. Zervas, P. Horak, S. Berneschi, S. Pelli, G. Nunzi Conti, and J. S. Wilkinson. Whispering gallery mode spectra of channel waveguide coupled microspheres. *Optics Express*, 16:11066–11076, 2008.

[6] G. L. Duveneck, A. P. Abel, M. A. Bopp, G. M. Kresbach, and M. Ehrat. Planar waveguides for ultra-high sensitivity of the analysis of nucleic acids. *Analytica Chimica Acta*, 469:49–61, 2002.

[7] E. Tull, P. Bartlett, and K. Ryan. Controlled assembly of micrometer-sized spheres: Theory and application. *Langmuir*, 23:7859–7873, 2007.

[8] S. M. Ganapathy, Y. Panitchob, E. J. Tull, P. N. Bartlett, and J. S. Wilkinson. Micropositioning of microsphere resonators on planar optical waveguides. In *The 5th International Conference on Optics-photonics Design Fabrication*, Nara, Japan, December 2006.